Error Analysis of near-field High Energy Diffraction Microscopy

by

David B. Menasche

Submitted in partial fulfillment of the
requirements for the degree of
Doctor of Philosophy
at
Carnegie Mellon University
Department of Physics
Pittsburgh, Pennsylvania

Advised by Professor Robert M. Suter

June 2, 2016

Abstract

Among non-destructive characterization techniques able to probe the properties of bulk polycrystals, High Energy Diffraction Microscopy (HEDM) has become the method of choice for researchers seeking spatial resolution of grain orientations and strain states. From HEDM data collected in the near field, the forward modeling method (FMM) of reconstruction is capable of producing micro-scale resolution of the orientation field, despite complex grain morphologies and significant plastic strains. In this thesis, the accuracy of the FMM reconstruction is examined through direct comparison with an Electron Backscatter Diffraction (EBSD) measurement of a pure gold specimen. The sensitivity of the FMM reconstruction to its inputs is probed through a series of simulations. Given raw diffraction data collected under optimum experimental conditions, spatial resolution is found to be accurate to within intrinsic limits set by the experimental equipment. Resolution of reconstructed crystallographic orientations is found to be $< 0.05°$. Input parameters most likely to cause reconstruction errors are identified, and a novel method is proposed to determine proper values for experimental inputs. Two case studies are also presented.

Acknowledgments

It takes a village to write a thesis. With that in mind, I'd like to take this opportunity to thank those without whom this endeavor would not have been possible. Beginning with the academic domain, I would like to extend a special thank you to my committee members, Professor Randall Feenstra, Professor Anthony Rollett, Dr. Jun-Sang Park, and my advisor, Professor Robert Suter. I greatly appreciate your collective willingness to provide feedback and advice in order to better the quality of this work and your generosity in acting in what is sometimes an overlooked but challenging role.

I am greatful that Jun arrived at the beam during my tenure at CMU. Perhaps the only job more thankless than that of a committee member is that of the beamline scientist, and I'd like to extend further thanks both to Jun and Dr. Peter Kenesei, both of whom contributed uncountable hours toward the success of so many projects. Additional thanks are in order too, for Tony, to whom I owe a debt of gratitude for educating me about both materials science and pipe organs, neither of which I knew anything about before our dealings.

There are many colleagues deserving of individual recogonition. To Jon Lind, I'd like to offer a special thanks for advising me closely during my first year in the group during the sabbatical. That year might easily have been lost if not for his willingness to show me the ropes. I owe so much of what I know to that early training. I want to thank Chris Hefferan, for continuing to mentor me professionally, despite the fact that our overlapping time in the group was short. Thanks for looking out for me, it means a lot. Our dinners and sports outings were always highlights. I must thank Sid Maddali with whom it was often helpful to talk through problems when I became stuck. Thanks to Frankie Li are in order, who provided constant motivation to avoid the fate of mediocrity. I'd like thank Reeju Pokharel, my copilot at the synchrotron for many, many beamruns. Without you there, 1ID wouldn't have been the same. I want to especially thank Tugce Ozturk, whose assitance and company kept me sane down the home stretch.

To my whole host of professional mentors: Joel Bernier, Mike Sangid, Ashley Spear, and Euan Wielewski among others, thank you all for providing advice and insights along the way. I wish all the best and good luck to Rulin Chen and He Liu, the students poised to continue development of HEDM.

Many individuals contributed to the shocked copper work presented in Chapter 4. I would like to thank: C.M. Hefferan and R. Pokharel (CMU) for assisting with HEDM measurements at APS, S. Maddali (CMU) for boundary smoothing code, M. Prijatelj (CMU) for image artifact removal, R. Randolph (LANL) for micro-machining, M.F. Lopez (LANL) for heat treating, G.T. Gray III (LANL) for providing material, M. Tucker (LANL) for APS assistance, D. Martinez (LANL) for experimentation, A.D. Rollett (CMU), R.A. Lebensohn (LANL), and C.A. Bronkhorst (LANL) for useful discussions, and E.K. Cerreta and C.A. Bronkhorst whose collaborations helped secure APS beamtime.

While we have collaborated with many outstanding scientists, I need to especially highlight the incredible efforts of Paul Shade at the Air Force Research Laboratory, under whose leadership along with T.J. Turner the PUP program continuted to grow and mature. Paul both prepared and performed EBSD on the calibration specimen described in this work—without him it would not be possible. I need to thank Ulrich Lienert, whose vision shaped my time at CMU.

To Bob Suter, thank you so much for advising me. Your dedication to advancing the field is unmatched and I'm proud to have learned under you these past few years. Thank you for humoring my frequent visits to your office and for being such a darn nice guy.

A little more personally, I'd like to thank some friends at CMU without whom I wouldn't have made it through the program. Paul and Sergio, you guys have been there from $t = 0$, and I've learned so much from both of you. You made both the bad times and good times a lot better and things wouldn't have been the same without you. Bai-Cian, thanks for tutoring all of us. Sam, Stephan, thanks for being there too, guys. To my puffins, ca-caw! To Fracky, thanks. To Cindy Suter, thank you so much for all of your hospitality. I've always felt so welcomed, and I won't forget that. I want to thank my high school wrestling coach John Lowe, for sending me out into the world ready to meet and overcome its inevitable setbacks.

I'm proud to thank my parents Kathy and Isaac Menasche. Your love and guidance put me on this path from the very beginning, and I know without all you've done for me, I would never have made it here. This holds true for the rest of my loving family, too.

To Gabriella, you've been by my side for the entirety of this process, blowing wind into my sails when the waters seemed still. Thank you for all of your love and support.

Contents

List of Tables

List of Figures

Chapter 1

Background and Introduction

1.1 Scope

Study of material microstructure is a endeavor that quietly underpins much of modern structural and engineering technology. Simply put, material microstructures influence macroscopic material properties and *in operendo* performance. The Materials Genome Initiative[1] [4] was created in part because incremental improvement in material performance has the potential to both save billions of dollars per year and dramatically improve safety for the many citizens whose well being depends on reliable material performance. Examples range from obvious, like bridges and buildings and aircraft bearing loads in the way they were designed to do so and thereby protecting their inhabitants, to subtle, like reducing auto-body weight consequently improving gas mileage or developing fabrication methods that minimize waste and energy expenditure. Such industrial-scale improvements happen usually only after significant advancement of understanding occurs first in academic regimes or others that emphasize basic science, and it is toward this goal that this endeavor begins.

Modern structural and engineering materials have been developed using phenomenological principles discovered over thousands of years of metalworking and materials investigation, but precise and validated theories of many fundamental processes critical to understanding material performance (like crack propagation, fatigue dynamics, plasticity, and other forms of dislocation dynamics) remain elusive. Even more clearly founded theories like those explaining polycrystalline grain growth and coarsening phenomena [5, 6], often fail to capture the seemingly exotic evolution of real physical systems. Arguably, these theories should be in place before meaningful materials engineering, the development of materials and microstructures with specific properties for a specific purpose, can begin in earnest. In part, these shortcomings remain because of the lack of representative data with which to compare and validate

---

[1] This federal initiative designed to dramatically shorten the time to commission and implement a commercially viable new material product was announced by President Obama at CMU's Robotics Center in 2011.

models and theories. But this is changing.

With the significant increase in x-ray brilliance made by the conversion to 3^{rd} generation synchrotron light sources, penetrative hard x-rays (energies $\mathcal{O}(10)$ keV) have emerged as a valuable probe to study bulk polycrystalline microstructures. A portfolio of experimental techniques have emerged that make use of the high flux and low emittance of these sources to perform bulk characterization in various regimes and under different conditions. Among them, High Energy Diffraction Microscopy (HEDM) (also sometimes referred to as 3D X-ray Diffraction or 3DXRD) utilizes Bragg diffraction to map crystallographic orientations with either a high degree of spatial information (in the near-field regime, nf-HEDM) or with grain averaged strain information (in the far-field regime, ff-HEDM). Often performed concurrently with these diffraction measurements, micro-computed tomography (μCT), in phase and/or absorption contrast modes, provides a probe of material density in volumes of interest. Highlighting the utility of combining these techniques will be one byproduct of this work.

The past 10 years have seen considerable development of these techniques, with applications once considered to be *tours-de-force* becoming commonplace. More and more, competent experimentalists are creating exactly the type of data sets needed to validate models of complicated but vital-to-understand processes. Data collection capabilities at Argonne National Laboratory's Advanced Photon Source 1-ID beamline (APS 1ID) in particular, have evolved from piecemeal truncated 2D or 3D polycrystalline orientation field volumes to fully registered 4D material phase, orientation, and strain fields created on the fly during experimentation. These considerable advancements will be discussed briefly, as their development has been fundamental background to much of the work contained in this thesis. Indeed, future works will contain more directly the fruits of those labors.

The works covered in this thesis will span the latter part of this transitional period. Beginning around the point where the fusion of micro-computed tomography-based material phase field information and full cystallographic orientation field information was becoming routine, the need to fully understand the sources of error inherent in the reconstruction of polycrystalline orientation field information from raw nf-HEDM data became apparent. After covering background information necessary for proper digestion of the work as a whole in this chapter, the next chapter of this thesis will introduce an experiment designed to identify fundamental limits of the nf-HEDM technique. The following chapter will highlight reconstruction-space sensitivities to perturbations of the reconstruction parameters and suggest a method of controlling the effects of these sensitivities. Following these discussions, proper application of the nf-HEDM technique will be employed to examine two case studies where accurate reconstruction of the microstructure in question is critical: the first, identifying nucleation sites of micro-scale voids within ballistically shocked copper, and the second, correlation of thermally induced pores with the microstructural topology of a sintered nickel superalloy. Concluding remarks will highlight future work that will leverage

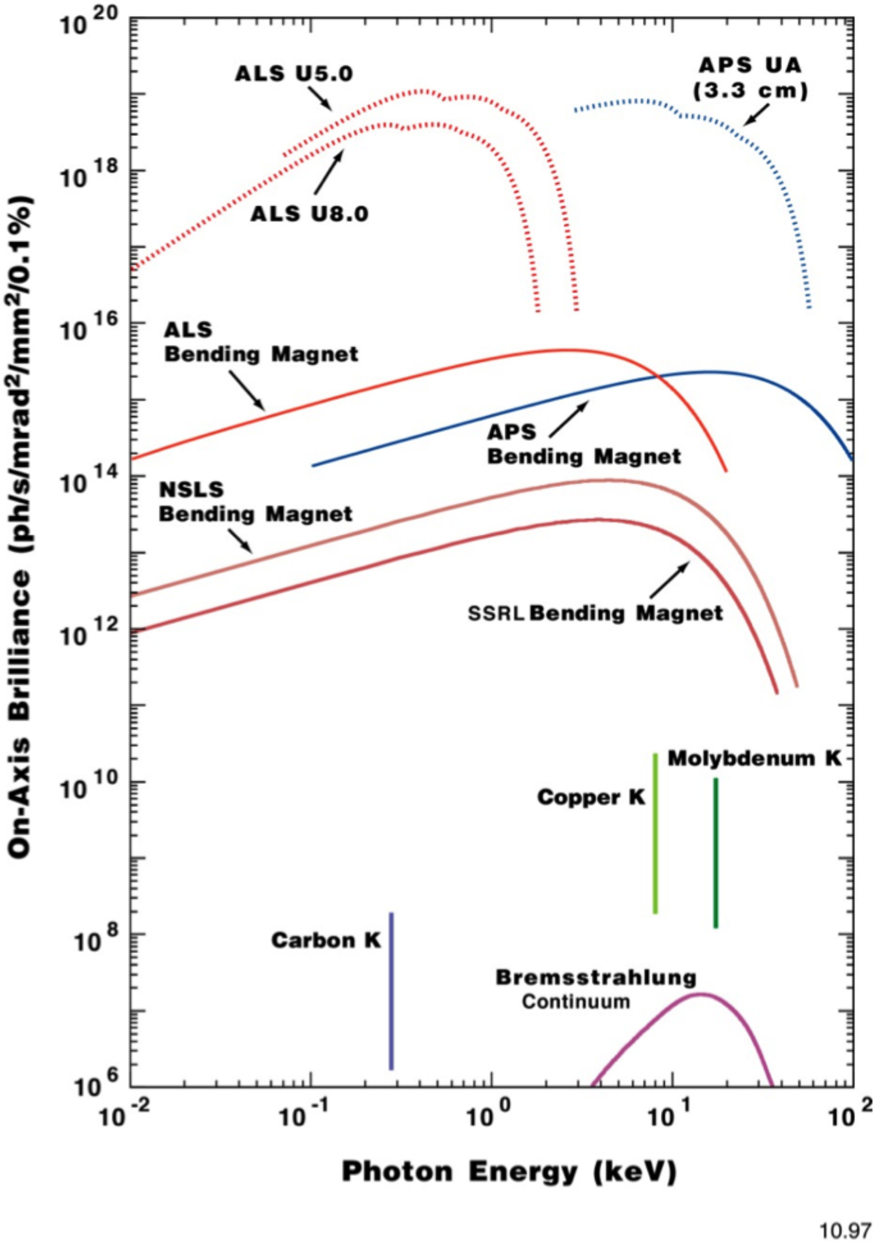

Figure 1.1: Brilliance of third generation light sources like the Advanced Photon Source (APS) at Argonne National Laboratory and the Advanced Light Source (ALS) at Lawrence Berkeley National Laboratory are about five orders of magnitude greater than the brilliance of second generation light sources like the National Synchrotron Light Source (NSLS) at Brookhaven National Laboratory and the Stanford Synchrotron Radiation Lightsource (SSRL). The photon flux from these machines is sufficient to facilitate novel bulk materials characterization techniques like HEDM and also to transform the capabilities of existing techniques like x-ray computed tomography. Image taken from the APS website.

the lessons learned.

1.2 X-ray Techniques Used and Relevant Definitions

We will begin by explaining the techniques used in this work quite briefly and generally; other necessary details will be included and explored throughout as they become salient, but these techniques and their implementations are explained thoroughly in the included references.

1.2.1 HEDM

As currently implemented, HEDM uses monochromatic x-rays in the $\mathcal{O}(10)$ keV spectral range to penetrate and interrogate the crystallographic orientation fields of macroscopic volumes of polycrystalline material [7, 8, 9, 10]. High energies are required to ensure adequate penetration of the volume, as the $1/e$ lengths for many materials of interest extend into the mm range at these energies. As mentioned, synchrotron sources are currently utilized to provide the photon flux sufficient for reasonable image integration times. Samples are illuminated with the x-ray beam and rotated to bring crystalline regions within into the Laue condition [11, 12]. During rotation, an area detector is exposed to collect diffracted intensity. Adjusting the distance between the rotation axis and the area detector changes the nature of the data collected.

nf-HEDM employs multiple area detector configurations < 10 mm from the sample rotation axis. By placing the detector 'near' to diffracting crystallites, the scattering does not emanate from a point source in the detector frame, instead encoding spatial information about the diffracting element as well as information about its orientation. Focusing optics are used to line-focus the x-ray beam into a profile roughly 1.2 mm wide by ~ 2 μm high [13]. Because a single planar cross section of microstructure is illuminated, the diffraction peaks collected are projections of the illuminated cross sections. The diffracted beam is a two dimensional projection onto the area detector of a two dimensional cross section. Analyzing the geometry of this projection shows that a grain of diameter d will be compressed along the $\hat{k}$ direction by a factor of $1/\tan 2\theta$. Accordingly, peaks at higher 2θ values encode more of this spatial information. This setup is depicted schematically in Fig. 1.2. Data is collected at $N_L \geq 2$ rotation axis to detector distances to resolve the origin of diffracted intensity, where we denote the total number of detector positions N_L. These detector positions are colloquially termed L-distances, and will be denoted in this thesis $L_i, i \in \{0, 1, 2, \ldots, N_L\}$. At APS-1ID, where the data used within this work were collected, the nf-HEDM CCD detector is of size 2048×2048 pixels, with an effective pixel pitch of 1.48 μm for a field of view of approximately 3 mm × 3 mm. The nf-HEDM detector is typically arranged *vis-a-vis* the sample diffraction plane as depicted in Fig. 1.2, with the in-

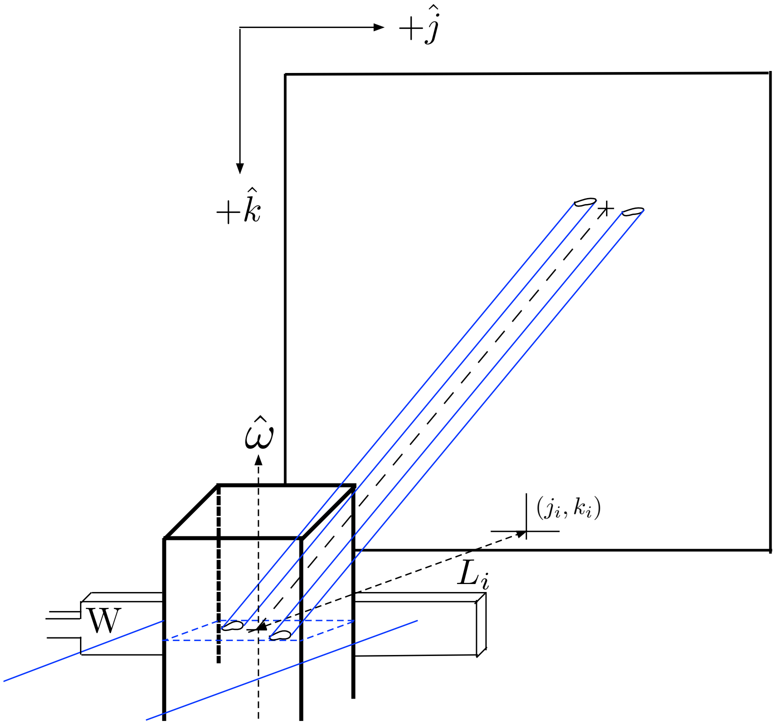

Figure 1.2: This schematic depicts the nf-HEDM setup. A rectangular sample, in the foreground, is illuminated by an incoming line-focused x-ray beam, shown in blue. While passing through the cross section of the sample shown in blue dashed lines, two grains with identical orientation diffract onto the detector, placed a distance L_i away. The portion of the beam passing directly though the sample is attenuated by a single crystal Tungsten beam-block labeled here W. Because the two grains have the same orientation they diffract along identical outgoing vectors. Because the distance between them is not negligible relative to L_i, we observe separation of the diffracted peaks on the detector. Here, the transformation between the laboratory reference frame and the sample reference frame is given by the rotation interval where the diffraction is observed.

tersection of the rotation axis with the line-focused beam projected onto the bottom of the detector. In this manner, an image of the direct beam is usually captured, and while this need not be the case for successful reconstruction of nf-HEDM data [14], we will argue later there are definite benefits to this placement.

Images are collected by integrating the detector while simultaneously rotating the sample about the axis parallel to detector coordinate $\hat{k}$, so that a single illuminated specimen cross section stays within the line-focused beam. While rotating through an angle $\Delta\omega$ about this axis of rotation, $\hat{\omega}$, grains within the specimen may fulfill the Laue condition and diffract, as will be discussed in more detail in the following section. These diffracted beams couple to the CCD via a scintillating crystal which produces visible light when struck with x-rays. This visible light is then imaged by the CCD. Typically images from 180° of rotation around $\hat{\omega}$ are collected, either in $N_{\Delta\omega} = 180$ divisions with $\Delta\omega = 1°$ or $N_{\Delta\omega} = 360$ divisions with $\Delta\omega = 0.5°$. The implications of these choices will also be later examined. Following the collection of these $N_L \times N_{\Delta\omega}$ images, the sample is translated along $\hat{\omega}$ to illuminate a new cross-sectional layer. If data for a total of N_z layers are collected, the total number of images is then $N_z \times N_L \times N_{\Delta\omega}$.

A significant challenge to any subsequent science is then deducing the underlying microstructure from these images. The reconstruction method utilized throughout this thesis is the forward modeling method (FMM) [8, 10, 15]. This technique grids a particular cross sectional layer into sample space elements (voxels), and then performs a virtual diffraction experiment on each voxel that searches orientation space for a crystallographic orientation that will maximize overlap between simulated projected scattering and experimentally observed scattering. As currently implemented, peak intensities are ignored in favor of binary segmentation of the raw images into so-called 'reduced data'. These reduced data contain an image field of pixels lit by diffracted intensity, and the methods of producing this information and their implications have been well explained in [1] and [16]. When each cross-sectional layer is reconstructed, the microstructures are integrated vertically to form a 3D volume which is then analyzed.

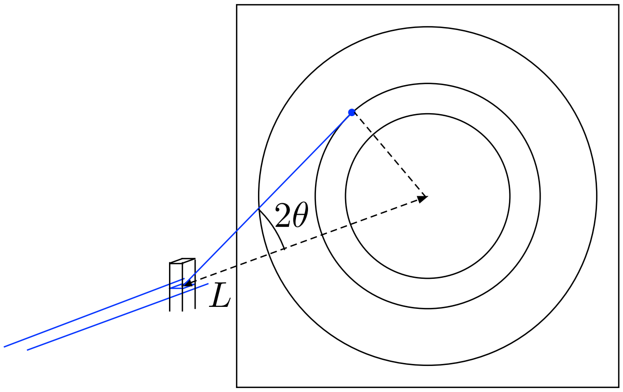

Figure 1.3: This diagram illustrated the ff-HEDM setup. A sample with square cross section is illuminated in the foreground by a line-focused x-ray beam, but in general the beam need not be focused. Because the sample dimensions are small relative to L, grains diffract onto Debye-Sherrer rings. Statistical deviations of peak position from the theoretical ring position are ascribed to changes in a grain's average lattice parameter, *i.e.* a grain-averaged strain, and the position of the grain centroid in the polycrystalline bulk.

The ff-HEDM is similar in that it utilizes the same rotating crystal geometry, but the detector is placed in the 'far field,' approximately 1 m away from the illuminated sample. In this regime, the separation between grains is small compared to L, the rotation axis to detector distance, and because of this diffraction spots fall on the Debye-Sherrer rings [11] defined by the 2θ values compatible with the selection rules given by the structure factor discussed in the next section. Data are collected in a manner similar to the collection of nf-HEDM data, with a major difference being that diffraction spots are collected at only one L-distance. For relatively coarse grained samples without too much deformation, peak overlap is not prohibitive. ff-HEDM may be conducted with a line-focused beam as depicted in Fig. 1.3, or with a partially focused beam with finite height, colloquially called a 'box-beam.' Because 2θ may easily be determined for a given diffraction peak, differences in peak centroid in the radial direction are attributed to changes in the diffracting grain's lattice parameters, *i.e.* elastic strains and the center of mass of the grain with respect to the rotation axis. By indexing consistent groups of peaks and associating them as consistent with diffraction from a single orientation, one can statistically examine these radial deviations and derive grain averaged strains [9, 17, 18, 19, 20, 21] from which stresses may be inferred.

1.2.2 μCT

Micro-computed x-ray tomography (μCT) is a for non-destructively determining the material density within a specimen. A volume of sample is illuminated with a box beam and rotated about $\hat{\omega}$ while radiographs are collected on the detector. This collection of radiographs may be reconstructed through a number of well known algorithms (*e.g.* filtered back projection, algebraic inversion, iterative methods, etc. [22, 23, 24]) to recover the relative material density values within the volume of interest. To the extent that unique material phases within the specimen have unique characteristic absorption values, these phases may be segmented or identified within these reconstructions. As an example, the left of Fig. 1.4 depicts a cross-sectional layer of the reconstructed material density field of a nickel base superalloy that will be discussed later. Viewed as an image in this way, pixel intensity is proportional to material density. As a result, pores within the structure are clearly viewed as regions of reduced density (darker regions). At right, we depict the material density along the red line in the upper left corner of the sample, beginning at the red point labeled $\mathcal{O}$. Crossing into the pore we see the material density fall to the background level of the surrounding air indicating the pore region absorbs x-rays of this energy like air within this region.

1.3 Fundamentals of Scattering Critical to HEDM

Given that later chapters will utilize some analysis of diffracted intensity, it is important to discuss the physics underpinning the scattering process. We will start from scattering fundamentals and proceed to more target issues specific to HEDM.

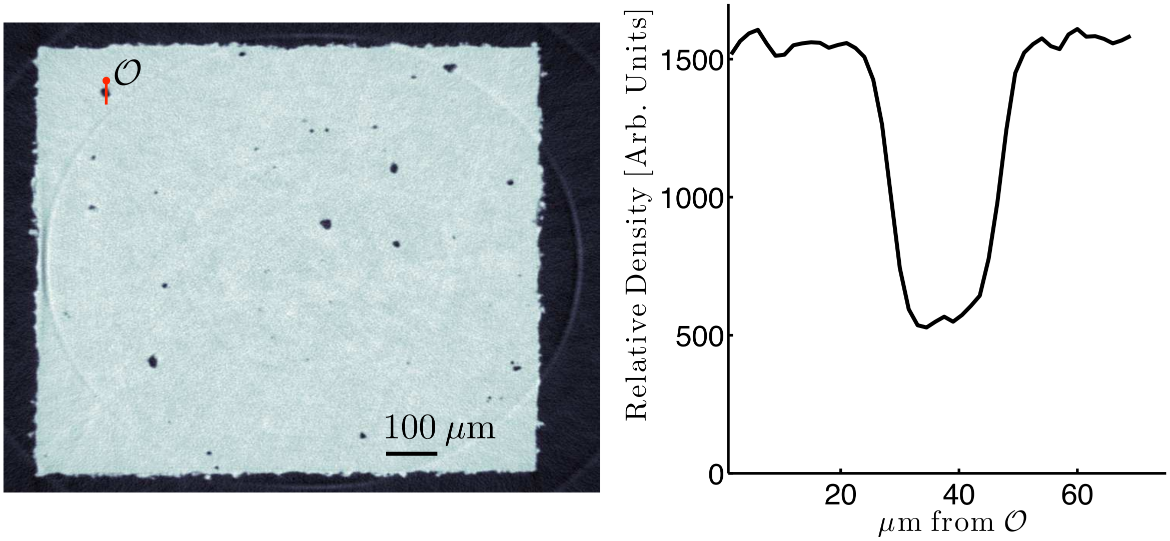

Figure 1.4: At left, a cross section of reconstructed material density from raw μCT data. Darker pixels correspond to regions of comparatively lower material density. The sample shown is a nickel base superalloy which contains significant porosity. These pores are visible within the sample as connected regions of lower material density. Starting at the red point labeled $\mathcal{O}$ in the upper left corner of the specimen, the plot at right depicts the reconstructed material density along the red line. The ratio of density between air and material is not 1/3; this ratio would be more physical if the raw radiographs collected were exposed longer, however detector saturation acts as an effective upper bound on this quantity. Regardless, the dynamic range pictured is sufficient for phase segmentation.

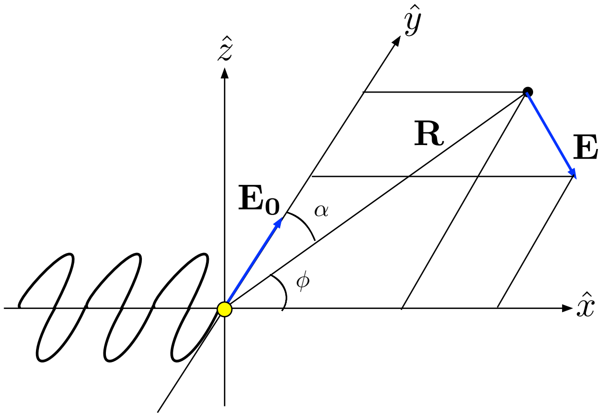

Figure 1.5: Here, an electron at the origin, is impinged on by an incoming monochromatic plane wave along $\hat{x}$ with polarization E_0 lying along $\hat{y}$. At an observation point in the xy plane a distance $\mathbf{R}$ from the origin, the electric field from the accelerating charge points along $\mathbf{E}$, perpendicular to $\mathbf{R}$ but in the xy plane.

1.3.1 The Form Factor - Scattering From a Single Atom

First, to build understanding of the scattering problem, we consider the case of elastic scattering of a linearly polarized plane wave with electric field $E = E_0 e^{i(\omega t + \mathbf{k}\cdot\mathbf{r})}\hat{r}$ by a free electron at the origin. The explanation to follow is adapted from [25]; further detail is available there. We choose the propagation direction of the plane wave to be $\hat{x}$ and the polarization direction to be $\hat{y}$, consistent with beam profiles at synchrotron sources. This geometry is depicted in Fig. 1.5. Classically, an electron at rest subject to a propagating electric field will accelerate and radiate; this radiation is the scattered x-ray signal. Given a force on the electron, $\mathbf{f} = e\mathbf{E}$, this acceleration may be given by $\mathbf{a} = \mathbf{f}/m_{\mathrm{e}}$, or in this case,

$$a_y = \frac{eE_0}{m_{\mathrm{e}}} \operatorname{Re}\left[e^{i\omega t}\right], \tag{1.1}$$

where $kx = 0$ at the origin. The resulting motion of the charge has harmonic time dependence and choosing proper initial conditions gives

$$y(t) = \frac{eE_0}{m_{\mathrm{e}}(\omega^2)} \operatorname{Re}\left[e^{i\omega t}\right]. \tag{1.2}$$

Invoking the Larmour formula for the electric field due to an accelerating charge,

$$|E(\mathbf{r})| = \frac{ea_{\perp}\sin\alpha}{c^2|\mathbf{r}|}, \tag{1.3}$$

then allows for the computation of the electric field at observation point $\mathbf{R}$ from $a_{\perp}$, the component of acceleration perpendicular to $\mathbf{R}$. The angle between $\mathbf{a}$ and $\mathbf{R}$ is α.

The direction of this field is perpendicular to $\mathbf{r}$ and in the plane of $\mathbf{R}$ and $\mathbf{a}$. Plugging 1.1 into 1.3 gives an expression for the magnitude of the electric field at $\mathbf{r}$,

$$E(\mathbf{R}) = \frac{e^2 E_0}{m_\mathrm{e} c^2 |\mathbf{R}|} \sin\alpha \,\mathrm{Re}\left[e^{i(\omega t)}\right]. \tag{1.4}$$

For a y-polarized x-ray, the electron acceleration is purely in the $\hat{y}$-direction. For an observation point sitting in the xy plane which makes an angle ϕ with the x axis, we identify $\sin\alpha = \cos\phi$ and the magnitude becomes

$$E(\mathbf{R}) = \frac{e^2 E_0}{m_\mathrm{e} c^2 |\mathbf{R}|} \cos\phi \,\mathrm{Re}\left[e^{i\omega t}\right]. \tag{1.5}$$

On a detector, the intensity $\mathcal{I} \propto |E|^2$ is the observable, so we are concerned with the square modulus of this quantity, specifically its spatial dependence given by ϕ. Wrapping the time dependence in $\tilde{E}(t) = E_0 \,\mathrm{Re}[e^{i\omega t}]$ allows

$$\mathcal{I} \propto |E|^2 = \frac{e^4 |\tilde{E}|^2}{m_\mathrm{e}^2 c^4 |\mathbf{R}|^2} \cos^2\phi \tag{1.6}$$

where $\cos^2\phi$ is recognized as the polarization factor for a polarized incident beam.

For multiple scatterers in a region small compared with the observation distance, the path length differences of the contributions from each scatterer add to phase development and modulation of the intensity signal. Aside from the previously derived factors, the electric field at location $\mathbf{r}'$ will vary as given by the geometry of scatterers at positions $\mathbf{r}_i$ from the origin. If we define $\mathbf{Q} = \mathbf{k}_f - \mathbf{k}_i$ to be the so-called scattering vector, this field is given by

$$E(\mathbf{r}') \propto e^{i(\omega t + \mathbf{k}\cdot\mathbf{r}')} \sum_i e^{i\mathbf{Q}\cdot\mathbf{r}_i}, \tag{1.7}$$

with the phase differences from the various scattering contributors tracked by the scalar product $\mathbf{Q}\cdot\mathbf{r}_i$. It would seem such considerations are wholly insufficient to develop any theory of scattering from atoms or ensembles of atoms. We have assumed our scatterers are free and not bound by any potential damping their radiative motions. We have assumed our scatterers do not interact with one another and interact only classically and non-relativistically with the incoming plane wave. No quantum phenomena were considered. Consequently, we have entirely neglected the inelastic (Compton) scattering. While these restrictions may seem limiting, our intuitive arguments lead to expressions which are able to explain the Bragg scattering necessary to the aforementioned techniques, so we will not consider further corrections.

This being the case, to consider scattering from a spatial distribution of electrons $\rho(\mathbf{r})$, as in an atom, we need only apply the reasoning of 1.7 to a delocalized distribution of charge. In this manner, at observation point $\mathbf{r}$ the electric field goes as

$$E(\mathbf{r}) \propto \int \mathrm{d}^3\mathbf{r}' \rho(\mathbf{r}') e^{i\mathbf{Q}\cdot\mathbf{r}'}, \tag{1.8}$$

where we have suppressed the constant terms and the overall phase lost when measuring the intensity. The RHS of 1.8 is called the atomic form factor, $f(\mathbf{Q})$ and depends on the electronic density and the scattering vector. Of course, one must point out that one can view $f(\mathbf{Q})$ as the Fourier transform of the electronic density. Another important observation is that $f(\mathbf{0}) = Z$, for an individual atom with Z electrons. Practically, $f(\mathbf{Q})$ is measured and tabulated and the National Institute of Standards and Technology maintains a database of form factors for use by the scientific community [26]. The form factor for gold, $Z = 79$, is shown in Fig. 1.6; we see that

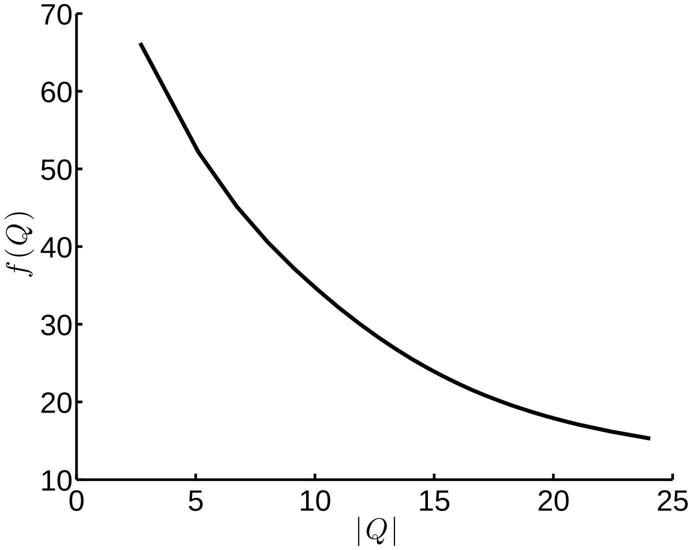

Figure 1.6: The atomic form factor, $f(\mathbf{Q})$, for gold as a function of $|Q|$, computed from data compiled by NIST. The form factor attenuates the relative intensity observed from the scattering at higher $|Q|$ values, that scattering which encodes the most information about peak shape.

for $2 \leq |\mathbf{Q}| \leq 10$, $f(\mathbf{Q})$ changes by about a factor of two. Recalling that ultimately the intensity is what one measures, this factor of two reduction becomes a reduction of four in the measured diffracted intensity. All else equal, we expect higher order scattering to be weaker, even at zero temperature. In reality, $f(\mathbf{Q})$ also depends on $|k|$, proportional to the energy of the incident x-rays. Our considerations were completely classical, so we did not account for the effect of the atom's quantized energy levels on x-ray absorption or damping of the electronic response. While we will not treat these corrections here, qualitatively one can note that at energies low compared the binding energy of the inner electronic states, the response of these electrons is weakened by that potential, and the scattering cross sections are smaller. At high x-ray energies, bound electrons behave as if they are free. At synchrotron sources it is not unusual for these energy scales to be comparable, so one must take care experimentally to avoid unwanted resonance and absorption. For further exposition, an interested reader could consult [27].

1.3.2 The Structure Factor - Scattering from an Ensemble

In the limit of one atom scattering an x-ray signal, there is no lattice orientation and thus nothing for HEDM to measure. If there are an ensemble of atoms arranged in some configuration, however, the integrated intensity may be sufficient for extraction of information about the configuration. If this configuration of atoms is a lattice, we observe Bragg diffraction from the periodicity of the underlying lattice. To aid the discussion, we introduce a Bravais lattice $R = n_1 a_1 + n_2 a_2 + n_3 a_3$, decorated by unit cells with atoms at positions $\mathbf{r}_i$ relative to each Bravias lattice point. The scattered amplitude, I, where $\mathcal{I} = |I^* I|$ from just one unit cell is the sum of the contributions from each scatterer:

$$I = \sum_i f_i(\mathbf{Q}) e^{i\mathbf{Q}\cdot\mathbf{r}_i} \tag{1.9}$$

As in 1.7, the quantity $\mathbf{Q} \cdot \mathbf{r}_i$ tracks the phase difference of the scattered plane wave from each contributing atom. If each atom in the lattice is identical, $f(\mathbf{Q})$ factors and we identify the remaining sum as the structure factor, $S(\{\mathbf{r}_i\})$, so that for the unit cell,

$$I = f(\mathbf{Q}) S(\{\mathbf{r}_i\}). \tag{1.10}$$

If this unit cell repeats throughout a volume at sites $\mathbf{R}_j$, we sum this is as well to acquire the full amplitude

$$I = f(\mathbf{Q}) S(\{\mathbf{r}_i\}) \sum_j e^{i\mathbf{Q}\cdot\mathbf{R}_j} \tag{1.11}$$

simply the product of the scattering contribution at the various length scales. In the absence of thermal vibration 1.11 is sufficient to explain the variation in scattered intensity.

1.3.3 Bragg Diffraction, The Rotating Crystal, and The Lorentz Factor

Associated with our direct lattice, we have a dual reciprocal lattice defined in the usual way [11]. For reciprocal lattice basis vectors, $\mathbf{b}_i$, reciprocal lattice points are defined at locations

$$\mathbf{G}_{\mathrm{hkl}} = h\mathbf{b}_1 + k\mathbf{b}_2 + l\mathbf{b}_3 \tag{1.12}$$

where $\mathbf{G}_{\mathrm{hkl}}$ is a reciprocal lattice vector. By definition,

$$\mathbf{a}_1 + \mathbf{a}_2 + \mathbf{a}_3 \cdot \mathbf{G}_{\mathrm{hkl}} = 2\pi(h + k + l), \tag{1.13}$$

so we see that we get constructive additions of phase in 1.11 for $\mathbf{Q} = \mathbf{G}_{\mathrm{hkl}}$. This is the Laue condition, and describes the condition for coherent Bragg diffraction. Coupling this condition with the geometry given by

$$|Q| = 2|k| \sin\theta \tag{1.14}$$

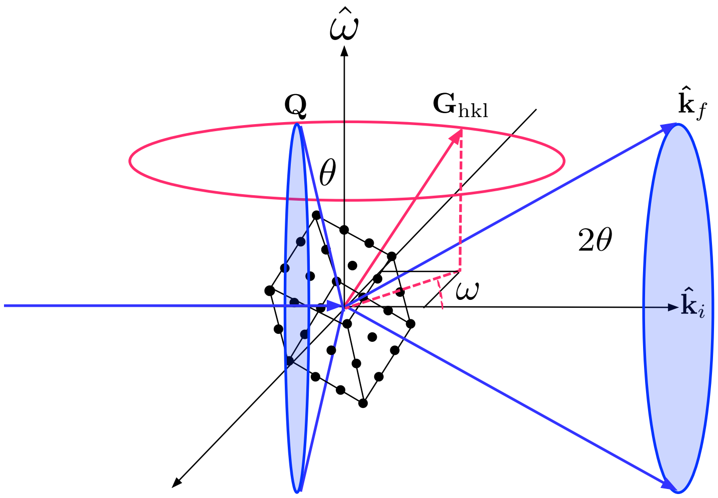

Figure 1.7: Depicted here, we have a graphical depiction of the Laue condition for an experiment in the rotating crystal geometry. A crystallite centered at the origin with a particular reciprocal lattice vector, $\mathbf{G}_{\mathrm{hkl}}$, is illuminated by a monochromatic plane wave incoming along $\hat{\mathbf{k}}_{\mathbf{i}}$. The crystallite rotates about $\hat{\omega}$ by an angle ω. When $\mathbf{G}_{\mathrm{hkl}}$ lies along the conical locus of $\mathbf{Q}$ points at fixed angle θ, diffraction is observed along $\hat{\mathbf{k}_{\mathbf{f}}}$ at scattering angle 2θ.

for $\theta = \frac{1}{2}\cos^{-1}(\mathbf{k}_f \cdot \mathbf{k}_i)$ (easily derived from $\mathbf{k}_i + \mathbf{Q} = \mathbf{k}_f$ and our elastic scattering condition $|k_i| = |k_f|$), we identify the relationship between the reciprocal lattice vectors of a crystal and the outgoing scattered signal.[2]

The above analyses have been general to scattering. To consider the scattered intensity particularly generated by HEDM, we must also consider experimental geometry. We will again consider a case as in Fig. 1.7 with $\hat{\mathbf{k}}_i$ along $\hat{x}$ with a volume of crystalline material at the origin. At fixed $\mathbf{Q}$, by 1.14 2θ is also fixed and given the geometry implied by $\mathbf{k}_f = \mathbf{k}_i + \mathbf{Q}$, there exists a conical locus of reciprocal vector positions that will satisfy the Laue condition and cause scattering. This cone is depicted in blue in Fig. 1.7 and represents the points where the condition $\mathbf{Q} = \mathbf{G}_{\mathrm{hkl}}$ is achievable. A reciprocal lattice vector satisfies this condition when it sits in coincidence with this conical locus. The reciprocal lattice vectors of the crystallite, however, are fixed in space by the crystal's orientation relative to the laboratory frame. In fact, for an arbitrary orientation, when illuminated by the incoming x-rays, it is possible that none of the reciprocal lattice vectors with appreciable form factor will intersect this cone and diffract. For this reason, rotation of the sample is necessary to observe the diffracted beams. In the HEDM experiment, this rotation is about the axis labeled $\hat{\omega}$ in Fig. 1.7, and causes the reciprocal vectors to precess. The precession rotates the reciprocal vector into coincidence with the Laue condition provided $\chi > \theta$, for

---

[2] It is typical to consider 2θ as the scattering angle, as opposed to θ which is sometimes cleaner mathematically.

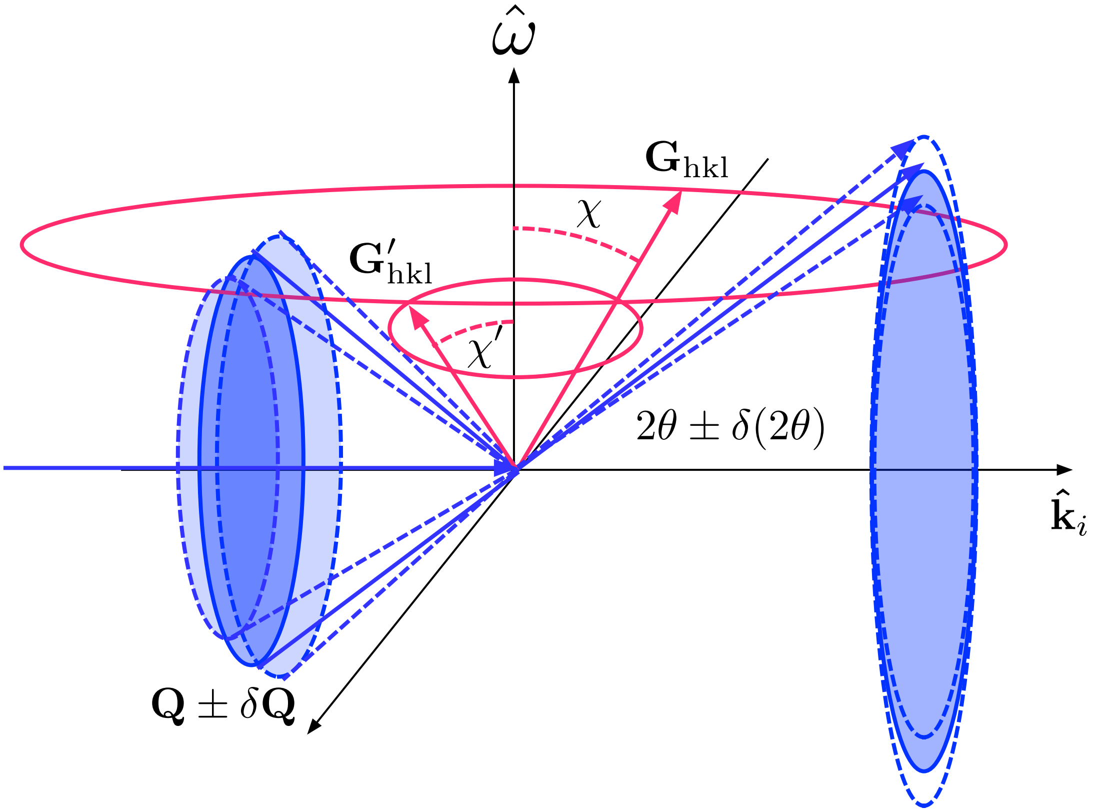

Figure 1.8: Even for perfect crystals, the Laue condition is satisfied for finite time because of the finite energy bandwidth of the plane wave. Peaks diffract for a time period that depends on χ.

$\chi = \cos^{-1}(\mathbf{G}_{\text{hkl}} \cdot \hat{\omega})$. One such path for a particular reciprocal lattice vector of the crystallite is highlighted in magenta in Fig 1.7.

The above reasoning considers the Bragg diffraction event as transient, existing only as long as $\mathbf{G}_{\text{hkl}}$ is coincident with the $\mathbf{Q}$-locus. If the incident beam energy is perfectly monochromatic and the lattice perfectly ordered and infinite, this is true, however, in practice neither of these assumptions hold. In the case there is some finite energy bandwidth, the $\mathbf{Q}$-locus is broadened. This effect is depicted in Fig. 1.8. The diffraction peaks associated with each $|G_{\text{hkl}}|$ intersect the $\mathbf{Q}$-locus for a length of time given by χ; at larger values of χ, the radial velocity of $\mathbf{G}_{\text{hkl}}$ is greater for fixed angular rotation, ω. In Fig. 1.8, $\chi > \chi'$ so $\mathbf{G}'_{\text{hkl}}$ will satisfy the Laue condition longer than for $\mathbf{G}_{\text{hkl}}$. As a result the diffracted intensity collected over the rotation interval will be correspondingly greater. Let us assume that k_i lies along the laboratory $\hat{x}$ direction. Quantitatively, if we wish to calculate this factor, we need to examine $\dot{G}_x$, because by inspection of Fig. 1.7, we can see that the Laue condition is satisfied

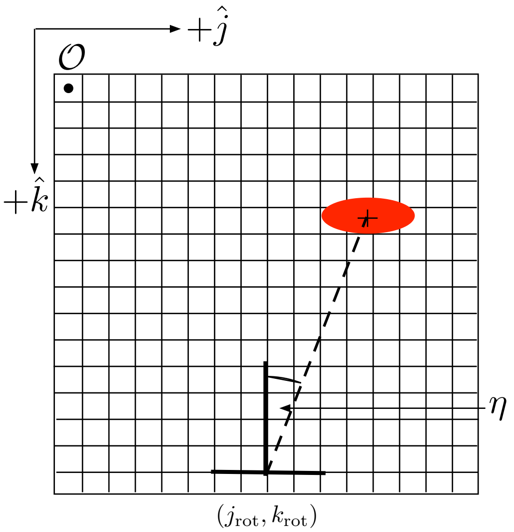

Figure 1.9: These conventions will be used throughout the thesis to talk about positions of or on the detector. The point marked $\mathcal{O}$ is the detector origin. $(j_{\mathrm{rot}}, k_{\mathrm{rot}})$ is the projection of the rotation axis onto the detector. For a grain centered on the rotation axis, a diffracted peak makes an angle η with $\hat{k}$ from the projection of the rotation axis.

when $|G|\sin\theta = |G|\sin\chi\sin\omega$.[3] It's noteworthy to point here that this allows for easy computation of the observation angle for a given $\mathbf{G}_{\mathrm{hkl}}$, namely

$$\omega = \sin^{-1}\left(\frac{\sin\theta}{\sin\chi}\right). \tag{1.15}$$

Recalling that at the Laue condition, $k_{x,f} = k_{x,i} + G_x$, we have

$$G_x = |G|\sin\chi\cos\omega, \tag{1.16}$$

and we have

$$\dot{G}_x = \frac{\partial G_x}{\partial\omega}\dot{\omega} = \dot{\omega}\frac{\partial}{\partial\omega}(|G|\sin\chi\cos\omega) = -2|k|\dot{\omega}\sin\theta\sin\chi\sin\omega. \tag{1.17}$$

To interpret this expression in terms of observable quantities we first define a parameter η as in Fig. 1.9, with the example detector depicted sitting in the xy plane of Fig. 1.7. By geometry, we then can associate $\sin\chi\cos\omega = \sin(2\theta)\sin\eta$, thus

$$\dot{G}_x = -|G|\dot{\omega}\sin(2\theta)\sin\eta, \tag{1.18}$$

and normalizing for the non-constant factors requires a Lorentz factor, L,

$$L \propto \frac{1}{\sin(2\theta)\sin\eta}. \tag{1.19}$$

---

[3] The following discussion is adapted from [28].

Here, we've assumed a constant integration rate, $\dot{\omega}$, but this is controllable by the experimenter. Notably, L contains divergences; these divergences may be tamed by considering second order corrections to $\delta\mathbf{G}$ [28], but 1.19 models experimental data quite well, as we will later show.

1.3.4 Effect of Atomic Displacements

1.3.4.1 Thermal Excitation of the Crystal Lattice

Having imposed the experimental geometry on our scattering discussion, we return now to address a more general feature of Bragg scattering at finite temperature, namely computation of the Debye-Waller effect of thermal lattice excitation. Qualitatively, at finite temperature, phonon modes are excited in the crystalline structures. (We leave aside the zero point fluctuations at zero temperature.) These phononic oscillations perturb the constituent atoms from their ideal positions and result in reduction of the scattered amplitude. We may treat this effect quantitatively by assuming atoms are generally close to their ideal positions, but perturbed by some $\vec{\delta}$. For a single unit cell with a single atomic species then,

$$I = f(\mathbf{Q}) \sum_i e^{i\mathbf{Q}\cdot(\mathbf{r}_i+\vec{\delta}_i)}, \tag{1.20}$$

with $\mathcal{I}$ given by the expectation of the square modulus,

$$\mathcal{I} = \langle I^* I \rangle = \left\langle f^*(\mathbf{Q}) f(\mathbf{Q}) \sum_i \sum_j e^{-i\mathbf{Q}\cdot(\mathbf{r}_i+\vec{\delta}_i)} e^{i\mathbf{Q}\cdot(\mathbf{r}_j+\vec{\delta}_j)} \right\rangle. \tag{1.21}$$

Simplifying,

$$\mathcal{I} = f^*(\mathbf{Q}) f(\mathbf{Q}) \sum_i \sum_j e^{i\mathbf{Q}\cdot(\mathbf{r}_j-\mathbf{r}_i)} \left\langle e^{i\mathbf{Q}\cdot(\vec{\delta}_j-\vec{\delta}_i)} \right\rangle \tag{1.22}$$

where only the lattice vibrations expectation must be evaluated. Assuming the $\vec{\delta}$s are normally distributed in space (an isotropic crystal) permits us Baker Campbell Hausdorff simplification of the expectation

$$\langle e^{ix} \rangle = e^{-\frac{1}{2}\langle x^2 \rangle}, \tag{1.23}$$

for a normally distributed variable x. (The difference of two normal random variables is also normally distributed.) Inspired by [27], we denote the components of δ parallel to $\mathbf{Q}$ by $\delta_{||}$ so that we may drop the scalar product in favor of

$$\langle e^{i|Q|(\delta_{||,j}-\delta_{||,i})} \rangle = e^{-\frac{1}{2}|Q|^2\langle(\delta_{||,j}-\delta_{||,i})^2\rangle} \tag{1.24}$$

after we apply 1.23. Having one atomic species ensures $\langle\delta_{||,j}^2\rangle = \langle\delta_{||,i}^2\rangle = \langle\delta_{||}^2\rangle$, so altogether for the expectation we have

$$\langle e^{i|Q|(\delta_{||,j}-\delta_{||,i})}\rangle = e^{-|Q|^2\langle\delta_{||}^2\rangle}e^{|Q|^2\langle\delta_i\delta_j\rangle}. \tag{1.25}$$

In standard notation, $\frac{1}{2}|Q|^2\langle\delta_{||}^2\rangle \equiv M$, so that

$$\mathcal{I} \propto e^{-2M}e^{|Q|^2\langle\delta_i\delta_j\rangle}. \tag{1.26}$$

Typically, e^{-2M} is referred to a the Debye-Waller Factor, while the second term encodes information about the correlations between displacements among nearby lattice sites. These correlations result in thermally diffuse scattering, TDS, which may be analyzed to probe phononic effects. Substituting 1.14 for into M gives a form that is easily applied experimentally, namely,

$$M = 8\pi^2\Big(\frac{\sin\theta}{\lambda}\Big)^2\langle\delta_{||}^2\rangle \tag{1.27}$$

where the dependence on the scattering angle is explicit. Defining the temperature-dependent B-factor, $B(T) = \frac{8pi^2}{3}\langle\delta^2\rangle$, for $\langle\delta^2\rangle = \langle\delta_x^2+\delta_y^2+\delta_z^2\rangle = 2\langle\delta_{||}^2\rangle$. We can then write $M = B(T)\Big(\frac{\sin\theta}{\lambda}\Big)^2$ where B depends only on the squared amplitude of the thermal atomic displacements over all phonon modes. The results of this calculation may be found in [27], [11], or [12], and under the Debye model, (Linear phonon dispersion up to a frequency cutoff) the B-factor is found to be

$$B(T) = \frac{6h^2}{mk_B\Theta}\left[\frac{\phi(\Theta/T)}{\Theta/T}+\frac{1}{4}\right], \tag{1.28}$$

for

$$\phi(x) \equiv \frac{1}{x}\int_0^x \frac{x'}{e^{x'}-1}\mathrm{d}x', \tag{1.29}$$

m, the atomic mass, k_B Boltzmann's constant, h Planck's constant, and Θ, the Debye temperature, a material-dependent parameter proportional to the dispersion cutoff frequency. In useful units of Å^2,

$$B(T) = \frac{11492T}{A\Theta^2}\phi(\Theta/T) + \frac{2873}{A\Theta}, \tag{1.30}$$

for A the atomic mass number and the temperatures expressed in Kelvin. Using these expressions, we plot e^{-2M} as a function of $|Q|$ for gold ($A = 196$ u) at room temperature (300 K) in Fig. 1.10.

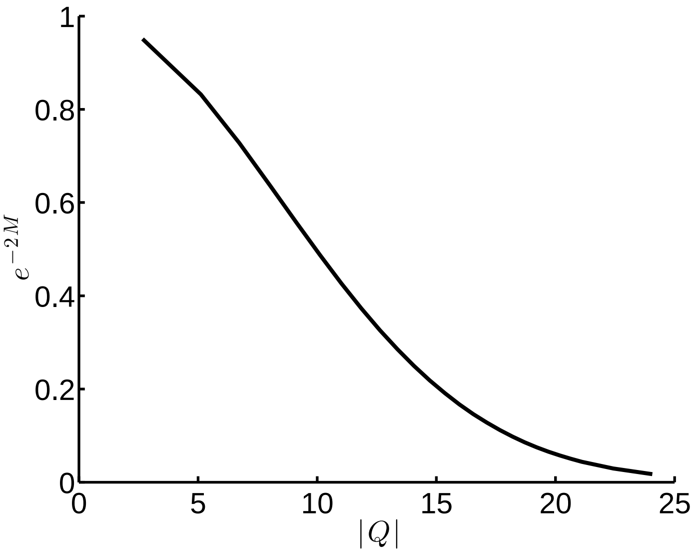

Figure 1.10: Here we plot the Debye Waller factor, computed for gold, as a function of $|Q|$. The TDS term we set to unity, approximating that $\langle\delta_i\delta_j\rangle = 0$.

1.3.4.2 Prospects for Probing Defect structure

Examining the intensity variations within a Bragg peak associated with a specific $\mathbf{G}_{\text{hkl}}$ provides a possible method for resolving defect accumulation within crystallites. Returning to examine 1.11, we can separate $\mathbf{R}$ into components parallel to and perpendicular to $\mathbf{Q}$ of which only the former contributes to the phase development. If we extend the lattice sum sufficiently in space to approximate the sum as an integral, but not larger than the coherence length of the beam, we have an expression for the scattered amplitude,

$$I = f(\mathbf{Q})S(\{\mathbf{r_i}\}) \int_{L_{||}} \mathrm{d}r'_{||} \int_{A_\perp} \mathrm{d}^2 r'_\perp \rho(\mathrm{r}') e^{i|Q|r'_{||}}. \tag{1.31}$$

Performing the perpendicular integration gives an overall factor of the illuminated area perpendicular to $\mathbf{Q}$ leaving the remaining factor a one dimensional Fourier transform of the scattering density along $\mathbf{Q}$:

$$I = A_\perp f(\mathbf{Q})S(\{\mathbf{r_i}\}) \int_{L_{||}} \mathrm{d}r'_{||} \rho(\mathrm{r}') e^{i|Q|r'_{||}}. \tag{1.32}$$

Provided our length scale assumptions are satisfied, it should then be possible to compare a peak's intensity as a function of deformation to determine defect accumulation. Indeed, a similar technique is already being employed by Bragg coherent diffraction imaging (CDI) [29, 30, 31, 32], where an entire crystallite is illuminated by the x-ray beam and the Fourier transform directly imaged. Phase retrieval methods then recover the scattering density, ρ.

Alternatively, one could also examine variations in intensity associated with $\mathbf{Q}$ vectors in various directions to identify strain-effective Debye Waller signatures that may quantify strains. Ordinarily, we consider normally distributed thermal perturbations $\vec{\delta}_i$ around each atom's equilibrium position such that the scattered amplitude for a unit cell with a single atomic species goes like 1.20 with $\mathcal{I}$ given by 1.21. One might wonder how elastic strains modulate the scattered intensity, given that thermal vibration causes the effect derived above. Looking at one crystal, if we assume some deviation in the lattice parameter (for now, in one direction), ϵ, and that the macroscopic strain results from the ensemble of atoms being displaced on average ϵ_0 with

$$\vec{\epsilon} \sim \begin{bmatrix} 0 \\ 0 \\ N(\epsilon_0, \sigma_\epsilon^2) \end{bmatrix}_{\text{lab}} \tag{1.33}$$

as in Fig. 1.11, then an expression analogous to 1.20 could be written by

$$I = f(\mathbf{Q}) \sum_i e^{i\mathbf{Q}\cdot(\mathbf{r}_i + \vec{\epsilon}_i)}. \tag{1.34}$$

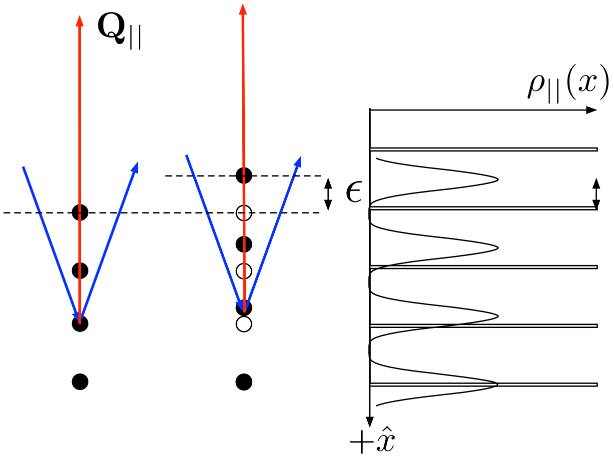

Figure 1.11: Here we illustrate the sensitivity of the component of $\mathbf{Q}$ along $\vec{\epsilon}$, $Q_{||}$, to the strain. By examining the diffracted intensity associated with peaks with symmetry well aligned along strained axes, lattice strains should be detectable within the near field. On the right is a schematic illustrating the average effect of elastic strains on a pristine lattice; periodic scatterers become displaced to with position probability distribution $\rho_{||}(x)$.

Resimplifying, this would leave an expectation term of

$$\left\langle e^{i\mathbf{Q}\cdot(\epsilon_j-\epsilon_i)}\right\rangle. \tag{1.35}$$

Because we chose 1.33 for $\vec{\epsilon}$, $\mathbf{Q}\cdot(\epsilon_j-\epsilon_i)$ simplifies to $Q_z(\epsilon_j-\epsilon_i)$ with both ϵ_j and ϵ_i given by $\sim N(\epsilon_0,\sigma_\epsilon^2)$. Further, we know $Q_z=\mathcal{O}\mathbf{G}_{\mathrm{hkl}}\cdot\hat{z}_{lab}$, for $\mathcal{O}$ an active rotation from the lab frame into the crystal frame. Taken all together with the Baker Campbell Hausdorff expression from the previous section,

$$\left\langle e^{i\mathbf{Q}\cdot(\epsilon_j-\epsilon_i)}\right\rangle = e^{\frac{1}{2}(\mathcal{O}\mathbf{G}_{\mathrm{hkl}}\cdot\hat{z}_{lab})^2\langle(\epsilon_j-\epsilon_i)^2\rangle}, \tag{1.36}$$

or, in directly observable quantities,

$$\left\langle e^{i\mathbf{Q}\cdot(\epsilon_j-\epsilon_i)}\right\rangle = e^{\frac{1}{2}(\cos^2\eta)\langle(\epsilon_j-\epsilon_i)^2\rangle}, \tag{1.37}$$

so we're left only to simplify the expectation. Expanding

$$\langle(\epsilon_j-\epsilon_i)^2\rangle = \langle\epsilon_j^2-2\epsilon_i\epsilon_j+\epsilon_i^2\rangle, \tag{1.38}$$

and recalling that $\sigma^2=\langle x^2\rangle-\mu^2$ for normal random variables, we have the scattered intensity modulated by the strain by

$$\mathcal{I}\propto e^{-[\epsilon_0^2+\sigma_\epsilon^2][\mathcal{O}\mathbf{G}_{\mathrm{hkl}}\cdot\hat{z}_{lab}]^2}e^{\langle\epsilon_i\epsilon_j\rangle[\mathcal{O}\mathbf{G}_{\mathrm{hkl}}\cdot\hat{z}_{lab}]^2} \tag{1.39}$$

where the second term includes the correlations between neighboring strains. This is analogous to a term resulting in TDS.

One might reasonably wonder how such a signal would manifest in the collected nf-HEDM data. Because the strain-effective Debye term maintains dependence on $\mathbf{Q}$, the first effect would be preferential weakening of the intensity of peaks with high $\mathbf{Q}$. Given these strains are elastic, this intensity variation occurs before the smearing in η commonly observed when grains within a polycrystal break into subdomains of different orientations. Through careful calibration, this strain effective term may then provide another probe to gauge elastic strain.

Chapter 2

Calibration of nf-HEDM

2.1 Motivation

It has been long been noted anecdotally by practitioners of nf-HEDM that the reconstructed microstructures derived from experimentally collected data are not uniquely defined by those data. The FMM reconstruction itself (as currently implemented in [15]) is an optimization process that is a function of both the binarized experimental data and the geometry of the virtual experiment modeled by the software; reasonable[1] perturbations in either of these quantities will still result in the reconstruction of *a* microstructure, though in general, the experimental practitioner does not know whether the reconstruced microstructure is *the* microstructure that was physically manifest during the experiment. By binarizing the peaks rather than looking directly at diffracted intensities, there is necessarily some uncertainty as to the precise peak extent. These types of errors have been examined and characterized to a certain extent in [1], but are generally considered to be second order corrections for microstructures with grain sizes above a certain threshold and without highly re-entrant morphologies. Without the knowledge of the precise geometry of physical experiment that produced the collected scattered signal, the physical geometry within the virtual experiment may be approximate at best.

Fig. 2.1 shows an illustration of the non-unique solution space. In this figure, we show the reconstruction of a simulated microstructure. The microstructure was constructed by discretizing a sample space into voxels and assigning crystallographic orientations to the various voxels to simulate polycrystalline grains. These orientations are mapped to an RGB colorspace so that in this depiction regions of continuous color have like orientation. From this synthetic structure, scattering was simulated onto a known detector configuration. This simulated scattering was then used to reconstruct the microstructures depicted, with the caveat being that the geometry of the detector configuration within the virtual experiment was perturbed by some small amount. The left column of images depicts the reconstructed crystallographic

---

[1] What is reasonable will be a later topic of some discussion.

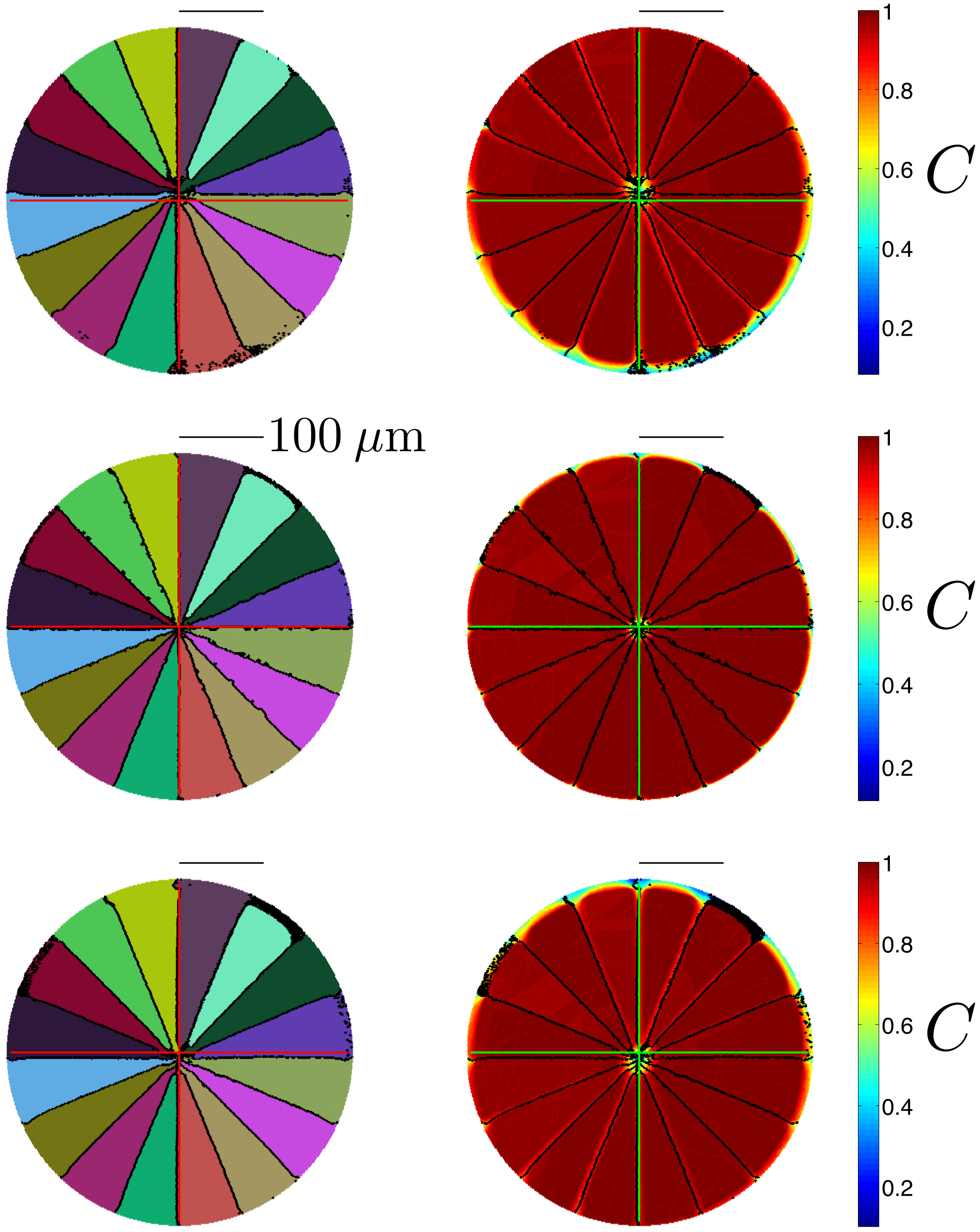

Figure 2.1: Reconstructed cross sections of simulated microstructure illustrating the effects of reconstructing with a perturbed virtual detector geometry. The rotation axis is aligned along the intersection of the red or green lines in the left and right figures, respectively. These reconstructions are produced from synthetic data generated from a phantom gold polycrystal. Reconstructed grain boundaries vary in location without a characteristic signature in C, the reconstruction figure of merit. The boundaries between voxels with disorientation $\geq 5^\circ$ are highlighted in black. Here, changes are approximately rigid body translations of the boundary structure, though this is not always the case.

orientations of the synthetic sample in the RGB colorspace. Voxel boundaries of disorientation[2] $\Delta g > 5^\circ$ are highlighted in black. The simulated axis of rotation lies at the intersection of the red lines. In the right column, we have maps of a reconstruction figure of merit, the peak overlap ratio C to be discussed later. $C = 1$ refers to the case where all virtual diffraction from the reconstructed polycrystal overlaps experimentally observed scattering. Again, for this case, the 'experimentally observed' scattering was itself a simulation of an experimentally observed scattering.

The first row illustrates a case where the geometry of the detector configuration within the reconstruction is perturbed $\sim 10\,\mu$m from the correct position. The second row was achieved by a perturbation of $\sim\ 2\mu$m, and the final row's maps were reconstructed with a perturbation of $\sim 10\,\mu$m antiparallel to the detector configuration of the first row. We observe first that these changes relocate the reconstructed microstructure *vis-a-vis* the rotation axis. Additionally, there are slight variations in the reconstructed boundary positions; some boundaries also appear noticeably curved in some regions, but not in others. Interestingly, variation in C, commonly accepted to be a figure of merit for the reconstruction, is slight. Given that the solution to the FMM reconstruction is an optimization process, the reconstructed microstructure reflects changes in the input parameters as (mostly) smooth variation in the output. Without any clear variation in C, how then does an experimenter determine the physically manifest microstructure?

One might look to Fig. 2.1 and raise the point that the most dramatic changes to the reconstructed microstructures appear to be rigid body translations of the grain ensemble. Surely then, these concerns are quite minor and only concern cases where registering two or more data sets is an issue? While the output variations are comparatively well behaved for this set of perturbations, all is not well for arbitrary perturbations. By example, consider the reconstructed results from perturbations in L_i depicted in Fig. 2.2. Significant curvatures and relative motions accumulate, and while there are corresponding signatures in C and in reconstruction noise (visible as 'hashy' regions within the reconstruction where single voxels of different orientation are reconstructed within a given grain), these signatures do not appear homogeneously throughout the reconstruction. Without *a priori* knowledge of the manifest sample, how then is the experimental practitioner to determine what is physical absent these signatures? Moreover, how do these perturbations combine?

Typically, the approximations to the experimental geometry (colloquially referred to as the 'experimental parameters' within the context of the reconstruction) are obtained by naive Monte Carlo. The detector configurations must be specified relative to some fixed reference point and for the rotating crystal experiment with a line-focused incident beam, the logical choice is the intersection of $\hat{\omega}$ with the plane of the beam. For purposes of this work, we refer to this point as the rotation axis, though it is just a point. For clarity, we wil now define $\mathbf{E} = \{j_0, k_0, L_0, j_1, k_1, L_1, \ldots, j_N, k_N, L_N\}$ as

---

[2] The disorientation is defined to be the transformation between two reference frames (orientations) which aligns the two frames with the minimum possible rotation from one to another [3].

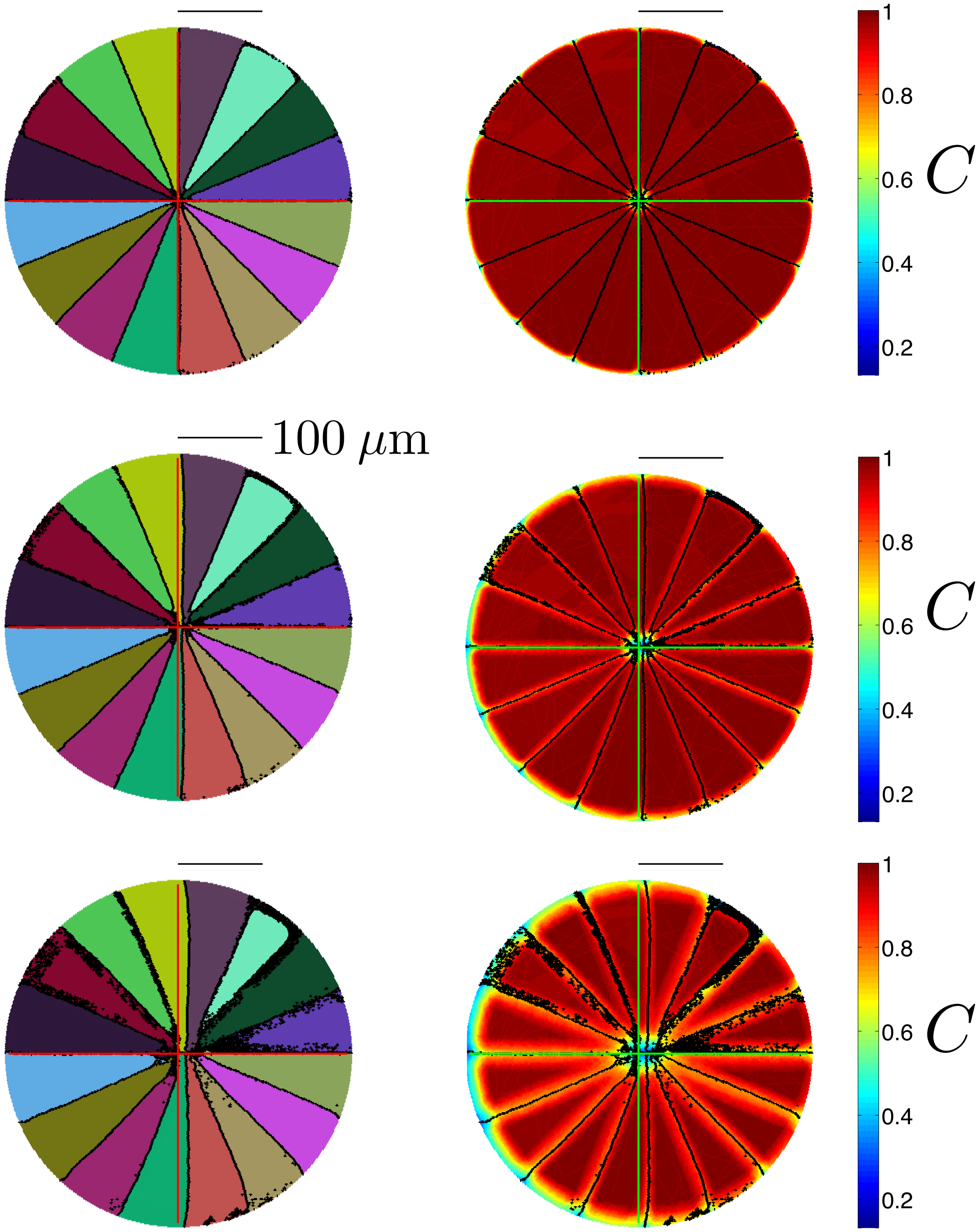

Figure 2.2: Reconstructions of simulated microstructure illustrating the effects of reconstructing with a perturbed virtual detector geometry, as in Fig. 2.1, but with detector perturbations orthogonal to 2.1. Boundary motions are not simple rigid body translations.

the collection of experimental parameters defining the virtual diffraction experiment. Here, j_i and k_i are defined as in the last chapter, respectively the horizontal and vertical projections of the rotation axis on the i^{th} detector. L_i is the distance between the projection of the rotation axis on the i^{th} detector and the rotation axis.

Performing raw image analysis typically allows the experimenter to determine preliminary estimates for $\mathbf{E}$. Proper image analysis will ensure that orientations may be determined for some sample space voxels that are consistent with the observed scattering. From this point, Monte Carlo is performed on the experimental parameters, with orientation reoptimization taking place for each instantiation of $\mathbf{E}$. Because the Monte Carlo space is high dimensional (minimum of $3 * N_L$ dimensions ignoring the detector orientation which accounts for 3 more parameters) dense sampling of the space is infeasible; to make matters worse, the effects of the elements of $\mathbf{E}$ on the scattering overlap are coupled, with cross-talk between L_i and j_i and between L_i and k_i.

The navigation through this parameter space is mediated by a cost $\mathcal{C}$ defined by the relation $\mathcal{C} = 1 - N_{\text{hit}}/N_{\text{sim}}$, where N_{hit} is the number of diffraction peaks struck by simulated diffraction from that voxel and N_{sim} counts those simulated peaks. Intuitively, $\mathcal{C} = 0$, describes perfect overlap between simulation and experiment for the peaks simulated. We refer to the ratio $C = N_{\text{hit}}/N_{\text{sim}}$ as the confidence. During the Monte Carlo optimization of E, the parameter set with the lowest $\mathcal{C}$ value is retained after orientation optimization is performed on the voxels sampled. The optimized $\mathbf{E}$ is then also a function of which voxels are sampled. Indeed different choices reflect varying degrees of senstitivity with respect to detector-space perturbations. For example, due to the coupling between the spatial extent of the diffracting element and the orientation of that element, voxels near the center of grains show less cost variation for a given detector space perturbation. This effect is shown schematically in Fig 2.3; the first row of the figure depicts simulated scattering in blue from a sample space voxel in the center of a diffracting grain. The second row shows simulated scattering from a voxel at the edge of the sample space grain. Scattering from the same grain, collected in three different angular intervals, is shown in each column.

In each row, the blue simulated scattering overlaps the experimentally observed scattering, shown in red, for all three collected intervals. During parameter Monte Carlo optimization of $\mathbf{E}$, however, the detector position may be perturbed with respect to the rotation axis projection by some $\delta\mathbf{E}$. (Similar analysis applies to out of plane perturbations parallel to L_i.) , Holding the crystallographic orientation of the diffracting voxel constant, simulated diffraction will land onto new locations highlighted in yellow. For the case of the grain-center voxel, there is no effect on $\mathcal{C}$. For the grain-edge voxel, however, in the third frame, the perterbation causes a loss of scattering overlap, giving $\mathcal{C} = 1/3$ for $\mathbf{E} + \delta\mathbf{E}$ if only these frames are used for the reconstruction. Here, we assumed the orientations of the diffracting voxels are fixed, and in reality, further orientation optimization may correct for the perturbation by correcting the crystallographic orientation. In the limit that there are many angular

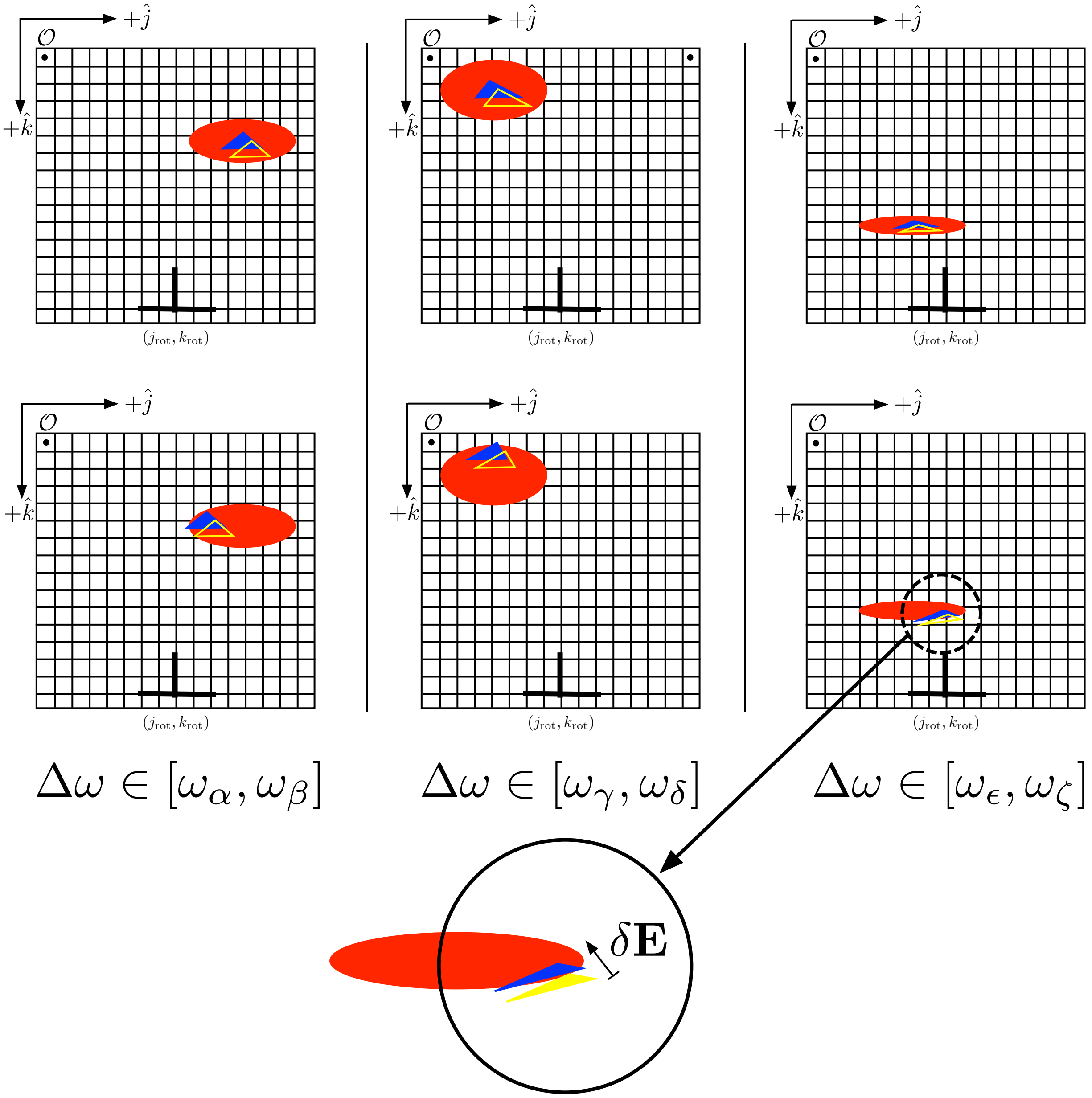

Figure 2.3: Detector schematic illustrating why voxels in the centers of grains show less variation in $\mathcal{C}$ for a given perturbation of $\mathbf{E}$. Each column represents a distinct angular integration interval in which a diffracted peak depicted in red was observed. The detector origin is labeled $\mathcal{O}$, and the projection of the rotation axis onto the detector is shown at the point labeled $(j_{\mathrm{rot}}, k_{\mathrm{rot}})$. The first row illustrates projected simulated diffraction from a voxel located near the center of a grain, at unperturbed detector configuration $\mathbf{E}$ (blue) and at perturbed detector configuration $\mathbf{E} + \delta\mathbf{E}$ (yellow). The second row illustrates projected scattering from a voxel near the grain boundary. For interval $\Delta\omega \in [\omega_\epsilon, \omega_\zeta]$ the perturbation prevents the projected intensity from striking the observed diffraction for the voxel on the grain boundary.

Table 2.1: Result of repeated Parameter Monte Carlo optimization of $\mathbf{E}$. Such optimization settings would be standard for refinement of a reconstruction under typical circumstances; sufficient iterations were conducted to consider the results 'converged'. Parameters from Monte Carlo # 1 are close to those of Monte Carlo # 2, but the differences are large enough to manifest in potentially important differences of the reconstructed microstructure, as will be discussed later.

Parameter	Monte Carlo #1	Monte Carlo #2
j_0 [μm]	926.16	925.4
k_0 [μm]	2031	2030.62
L_0[mm]	5.0976	5.0963
j_1 [μm]	935.11	934.2
k_1 [μm]	2026.9	2027.7
L_1[mm]	6.5981	6.5935
j_2 [μm]	942.67	941.30
k_2 [μm]	2023.6	2023.2
L_2[mm]	8.0945	8.0753

intervals used for the reconstruction, over-correction of the voxel orientation is limited by that orientation's consistency with other observed scattering.

The coupling between the elements of $\mathbf{E}$ creates numerous local minima in the space defined by $\mathcal{C}(\mathbf{E})$. This particular feature makes implementing common optimization schemes like gradient descent a challenge. Simulated annealing [33] has been implemented, but has been proven too computationally expensive to be a viable option. These facts taken together with the observation that dense sampling of $\mathbf{E}$ is too time consuming to be practical gives rise to extremely slow and unpredictable convergence properties for the parameter Monte Carlo. Take for example, the result of running repeated Monte Carlo optimizations on a set of parameters, $\tilde{\mathbf{E}}$, as shown in Table 2.1. Here, the optimizations were run on $\tilde{\mathbf{E}}$ using the same number of iterations, the same size search windows with no search window size-reduction scheme. The Monte Carlo converges to some relatively small region within the 9D space, but is subject to both parameter sampling coverage errors and numerous local subminima within the global minimium.

One would be remiss to ignore the extent to which this convergence region is influenced by which diffraction peaks are included during the orientation optimization. Within the particular implementation of the FMM used for this work [15], specifiying a maximum $|\mathbf{Q}|$ defines a maximum 2θ value below which all allowed scattered peaks are simulated. Increasing $Q_{\max}$ then increases the number of constraints on a particular voxel's orientation. This scaling is given by the volume of reciprocal space enclosed by a sphere of radius $Q_{\max}$ centered at the origin, namely,

$$N_{\text{peaks}}(Q_{\max}) = \lambda\rho\frac{4}{3}\pi Q_{\max}^3 \tag{2.1}$$

where $\rho = V_{\text{prim}}/(2\pi)^3$ is the number density of points in the reciprocal space for V_{prim} the volume of the crystal primitive cell. The factor λ is a constant factor that depends on how the measurement was performed: if collected as is typical for nf-HEDM, with $\omega \in [-90^\circ, 90^\circ]$,

$$\lambda \approx 2_{\text{Laue}} \times (1/2)_{\text{UHP}} \times (1/2)_{\omega}. \tag{2.2}$$

Here, the first factor of two arises from the case where a rotating reciprocal lattice vector $\mathbf{G}_{\text{hkl}}$ satisfies the Laue condition twice as it intersects the $\mathbf{Q}$-locus twice, assuming complete rotation over that interval. The first factor of 1/2 arises from the detector configuration - by collecting only upper half plane scattering, the volume of reciprocal space sampled is that with $Q_z > 0$. The second factor of 1/2 comes from measuring scattering over 180° instead of the full 360° of rotation. One should note that by performing the measurement in this way, not every $\mathbf{G}_{\text{hkl}}$ vector will satisfy the Laue condition twice, so the first factor is not exactly two.

From this analysis, we note that the number of constraining diffraction peaks has a cubic dependence on $Q_{\max}$. As a result, the convergence region within the 9D Monte Carlo space becomes smaller when using a higher $Q_{\max}$. Regardless, at common operational $\mathbf{Q}_{\max} = 10\text{Å}^{-1}$, this convergence region is typically on the order of single pixels for j_i and k_i, and about 10-20 μm for L_i. The reconstructed microstructures from these optimized **E**s, while highly similar, have subtle variations with respect to the reconstructed spatial features, and while some might not find these variations troublesome, for many precision applications they must be understood and contained. Consider the case depicted in Fig. 2.4.

In this case, we have a cross-sectional layer of synthetic microstructure of dimension 100 μm by 100 μm . Assume the microstructure extends into and out of the page exactly as pictured so that all variation in the geometry of the grain boundary is in the plane shown. The orientation of the dark blue grain on the left in ZXZ Euler angles is $(270.00^\circ, 35.26^\circ, 135.00^\circ)$ relative to the laboratory frame when reduced to the cubic fundamental zone of orientation; the lighter blue grain on the right has orientation $(90.00^\circ, 35.26^\circ, 315.00^\circ)$. The disorientation between these orientations is 60° about a common crystallographic $\langle 111 \rangle$ axis, commonly referred to as a Σ-3 boundary within the Coincident Site Lattice (CSL) classification scheme [34, 35, 36] [3]

---

[3] A seminal paper by Kronberg and Wilson in 1949 introduced to the materials community a new paradigm for quantifying microstructural texture characteristics: Coincident Site Lattice (CSL) theory. According to this model, the authors postulate that a particularly relevant quantity that should be examined is the incidence of Coincident Sites, special grain-to-grain misorientations with the property that rotation about a fixed axis by some angle ω results in $1/\Sigma$ Bravais lattice sites overlapping between the two grains, with Σ an integer. As an example, with an underlying cubic lattice, two grains with a Σ-3 boundary share 1/3 of their lattice sites after a rotation of 60° about the common $\langle 111 \rangle$ crystal axis.

Later work by Brandon extended this work by applying energetics to CSL theory. Higher internal energy configurations are associated with more broken and bent atomic bonds, i.e. frustrations within the crystalline lattice. The rationale behind CSL theory is that one can associate low reciprocal lattice density (Σ) between grains with boundaries that fit together more cleanly due to

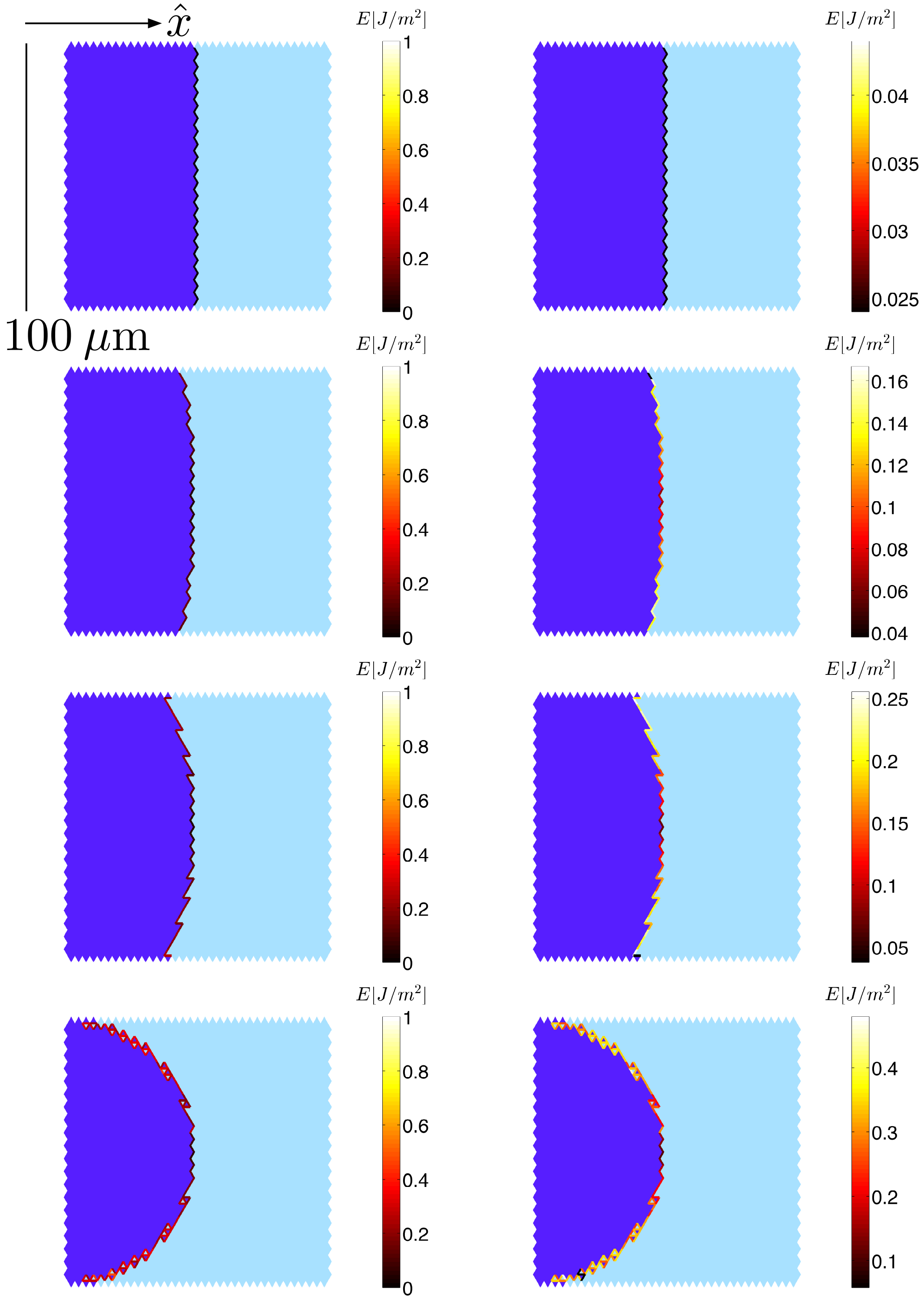

Figure 2.4: Illustration of how changes in reconstructed coherent twin geometry can dramatically change computed grain boundary energy. Microstructures depicted are simulated Σ-3 interfaces with boundary normals aligned along the mutual $\langle 111 \rangle$ crystal axes. Reading down the rows, curvatures of $\kappa = 0$, $\kappa = 1/250\ \mu\text{m}^{-1}$,$\kappa = 1/125\ \mu\text{m}^{-1}$, and $\kappa = 1/50\ \mu\text{m}^{-1}$ are added to the interface. The computed grain boundary energy at each point of the interface is colorized to illustrate the coupling between geometry and energy.

Here, we have a simulated bicrystal system, where each crystal's orientation shares a common $\langle 111\rangle$ crystal axis along the lab $\hat{x}$ direction. Assuming the grains extend as shown into and out of the page, in the first row of Fig. 2.4, the vector normal to the grain boundary, $\hat{n}_{\mathrm{GB}}$, points toward $\hat{x}$. This is an especially low energy configuration for crystals with FCC symmetry and occurs predominately because of stacking faults that occur during annealing and consequent grain growth. Sometimes this boundary configuration is referred to as a 'twin', though the term is also sometimes abused to refer to FCC grain pairs related by a Σ-3 disorientation for which $\hat{n}_{\mathrm{GB}}$ is not a common crystallographic $\langle 111\rangle$, but here we will be more precise.

Molecular dynamics simulations in [2] and [37, 38] provide computed values for the energies associated with various grain boundary characters. The energy values derived from these simulations have been interpolated semi-analytically in [39] who have graciously published code that implements this interpolation scheme. Using this tool, in Fig. 2.4, we examine the computed change in grain boundary energy for the coherent Σ-3 twin as the boundary inclination plane deviates from the crystallographic $\langle 111\rangle$, to illustrate the effect of reconstruction-space errors in precise computed quantities. Reading down the rows of the figure, we examine grain boundary curvatures of $\kappa = 0\,\mu\mathrm{m}^{-1}$, $\kappa = 1/250\,\mu\mathrm{m}^{-1}$,$\kappa = 1/125\,\mu\mathrm{m}^{-1}$, and $\kappa = 1/50\,\mu\mathrm{m}^{-1}$, respectively. Notably, because of the cusp in the FCC energy landscape around this grain boundary configuration, even errors of a few degrees in the reconstructed boundary normal can cause sizable errors in computed boundary energies to accumulate. Even with advanced boundary smoothing methods designed to minimize discretization noise inherent in the reconstruction process[40], errors in computed normal vectors still crop

---

symmetry. Configurations with more low Σ boundaries should then be more energetically favorable and thus (it was thought) have other additional desirable properties sought by materials scientists. Additionally, such a formulation is relatively simple to implement in that it ignores the atom-atom interactions at the intergranular interfaces, relying on a single integer, Σ, to describe the microstructural landscape.

In 1987, Sutton and Balluffi revisited the CSL theory developed in earlier decades with the intention of testing the predictive power of the Σ metric in determining interfacial energetics in FCC metals, those usually modeled by CSL theory. The authors placed small single-crystals on single-crystal substrates and annealed the configuration to bind them. The crystallites were randomly oriented relative to the substrate, so each crystallite experienced a diffusion-driven torque consistent with their misorientation, toward a low energy configuration. X-ray scattering was then used to infer their relative orientations. After making experimental measurements of interfacial energy on gold, they found that the CSL results have virtually no predictive power in determining boundary energetics according to the low $\Sigma \rightarrow$ low energy rule, citing, among other evidences, both high interfacial energies for Σ-13 and Σ-9 boundaries, and the especially low interfacial energy of Σ-33A.

This conceptual framework is not without utility, however, in part due to the simplification it provides. For many materials, the grain boundary character (boundary inclination degrees of freedom included) is very highly correlated to Σ. For these cases, while low energy → low energy may not be exactly true, a particular Σ will be associated with a relatively well defined energy, making Σ a useful proxy for energy in these cases. Moreover, grain boundaries with CSL misorientation can be used to create 3D periodic structures containing finite misorientation. This allows modelers the freedom to simulate structures without finite size effects [2, 37, 38].

up, making the containment of additional error integral for careful study of these phenomena. Similarly, the distribution of boundary normals for fixed disorientation (Grain Boundary Character Distribution or GBCD) will be affected by the errors in the reconstructed boundary positions. There is increasing interest in comparing experimentally observed GBCD to computed energy distributions [41, 42, 43], so again, these are errors that should be understood.

With these motivations in mind, we would like to understand the fundamental limitations and sensitivities behind the FMM reconstruction used in nf-HEDM. What exactly is the accurate spatial resolution? How do errors in simulated detector space result in errors in the reconstructed microstructure with respect to its physical manifestation? How does the orientation resolution of the measurement depend on the experimental parameters? We will answer these questions through two independent channels of analysis. The first is careful calibration. Utilizing a simple sample with a known initial microstructure, we will use the standard FMM reconstruction pipeline to attempt to reconstruct the known initial microstructure and comment on any discrepancies we observe.[4] Provided the known microstructure is well represented by the result from our standard pipeline, we will then examine possible modifications to the nf-HEDM data collection and reconstruction processes and their effects on the reconstructed microstructure. This will be possible because our initial structure is known.

Our second endeavor will be to characterize how errors in the virtual detector configuration manifest in changes to the reconstructed microstructure. Because for the case of our calibrant the true experimental detector configuration is essentially unknowable at the required precision, we will utilize simulation for this portion. By simulating a known structure onto a known detector configuration and then proceeding with our standard FMM reconstruction pipeline, we will be able to examine perturbations to the detector configuration and compare their effects to the original known structure. Performing this characterization will clarify which errors are most deleterious and will imply improvements to the experimental technique. One such suggestion will be made to improve the analysis pipeline responsible for the identification and refinement of the detector geometry configuration.

Following this work, two case studies that hinge critically on the proper use of the nf-HEDM microscope's spatial resolution will be examined. The first involves the identification and characterization of micro-scale voids formed during shock loading of a pure copper sample. Void positions within a shocked sample are identified using synchrotron-based micro-computed tomography and then mapped back into the pre-shocked sample microstructure which measured before shock loading. The void positions are interpreted in the pre-shocked state's microstructure. Following this case study, another will examine the locations of thermally induced pores in the mi-

---

[4] Special thanks here go to Dr. Paul Shade of the Air Force Research Laboratory's Materials and Manufacturing Directorate, without whom this work would surely take a simpler form. Dr. Shade is responsible for the meticulous fabrication and careful characterization of the initial structure.

crostructure of a sintered nickel-base superalloy specimen. This thesis will conclude by offering some suggestions for further work.

2.2 Calibration

2.2.1 Electron Microscopy Characterization

For our calibration sample, we require a cleanly diffracting polycrystal with a simple grain boundary network. An undeformed polycrystal will allow for careful consideration of the orientation resolution; a simple grain boundary network strikes a balance between reduced computational complexity and sufficient statistics. The necessity for rapid and frequent reconstruction of the sample as a function of various reconstruction parameters suggests a physically small sample (as computational time for a truly unbiased application of the FMM reconstruction scales with the number of voxels in the sample), and the need to register multiple data sets suggests some asymmetry would be helpful. These requirements led to the design of the specimen depicted in Fig. 2.5.

The sample was cut from 99.95% pure gold foil approximately 50 μm in thickness. After cutting, deformation was removed by annealing the specimen for 24 hours at 950° C and subsequently cooling it in the furnace. More detailed sample preparation procedures are explained in [44]. During this annealing, coarsening of the microstructure led to grains of about 20 μm in size. The sample contains about 10-20 grains. While the small antenna-like protrusion already breaks the sample symmetry, further asymmetry was incorporated by milling a trench with a focused ion beam (FIB). Images of the top surface taken at normal incidence are shown in Figs. 2.6 and 2.7. To produce Fig. 2.6, secondary electrons ejected from the sample's surface were collected on a Everhart-Thornley detector[5], enabling the collection of a topologically sensitive signal. In Fig. 2.7, backscattered electrons from the sample surface were collected, giving qualitative crystallographic sensitivity. This sensitivity results in visible orientation contrast in the imaged structure that corresponds to the underlying surface grain structure. Also visible in this image is some surface damage from errant FIB milling (triangular dark regions at fixed interval continuing on both sides of the trench) and surface oxidation from the FIB polishing of the top surface. The upside-down ("L") feature on the sample surface is a piece of fiducial dust used to adjust the focus settings of the FIB.

To perform 'ground truth' calibration for the nf-HEDM measurement and reconstruction, we must characterize the microstructure of our specimen. For this step, we require that the spatial resolution of the ground truth characterization method be better than that of nf-HEDM. Given that samples, beamtime, and man-hours are

---

[5] This detector uses careful coupling between the electron scintillator and the photomultiplier to amplify the signal of secondary electrons.

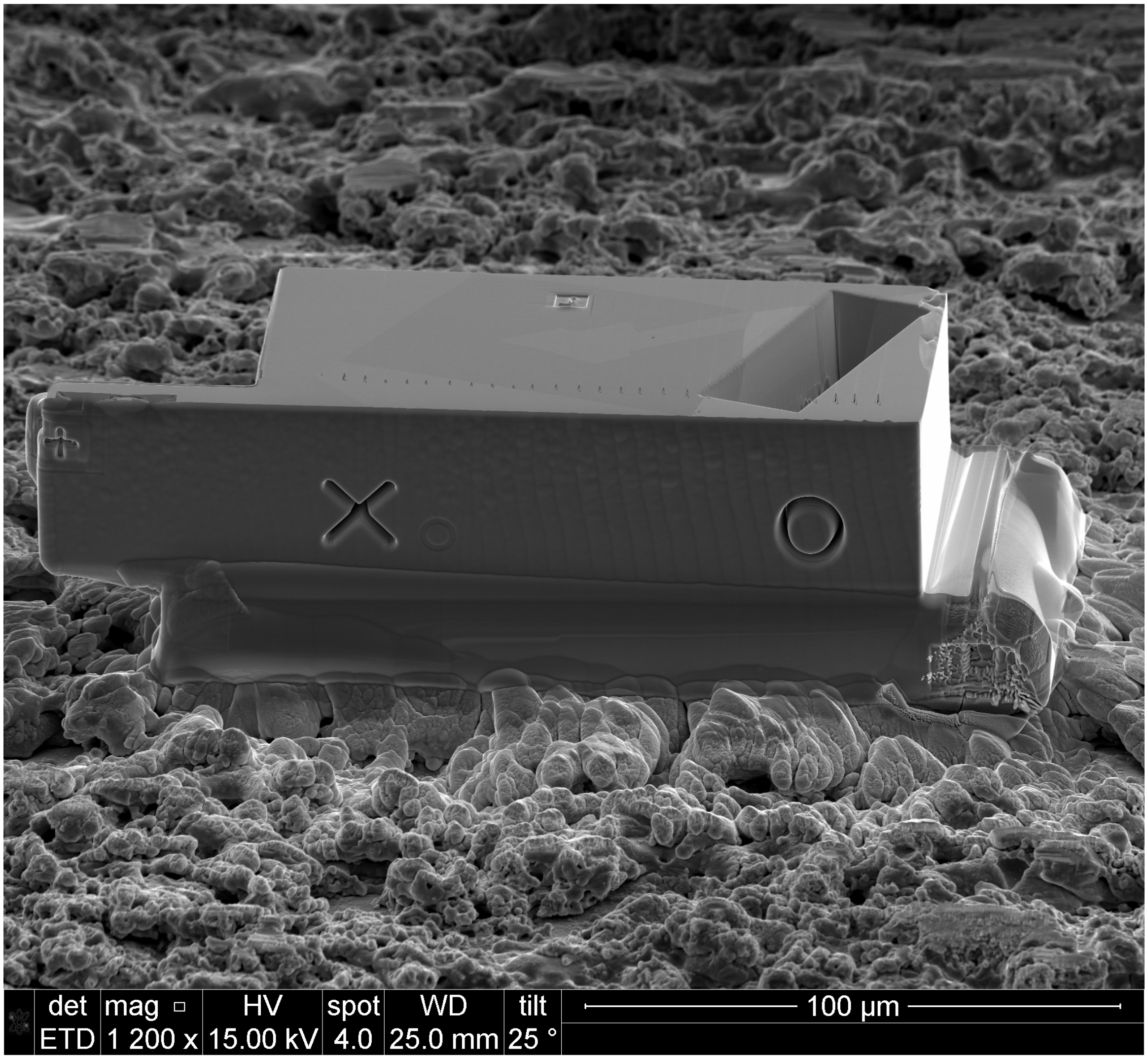

Figure 2.5: A Scanning Electron Microscope (SEM) image of the sample designed for calibration of the nf-HEDM experiment. The specimen is cut from 99.95% gold foil 50 μm in thickness and subsequently annealed at 950° C for 24 hours to coarsen the grain structure to ≈ 20 μm. The final specimen size is approximately 75 μm × 150 μm × 50 μm and contains about 10 grains. Because of the annealing treatment, the grains within the sample have low mosaic spread and may be used to calibrate the orientation degrees of freedom of the reconstruction.

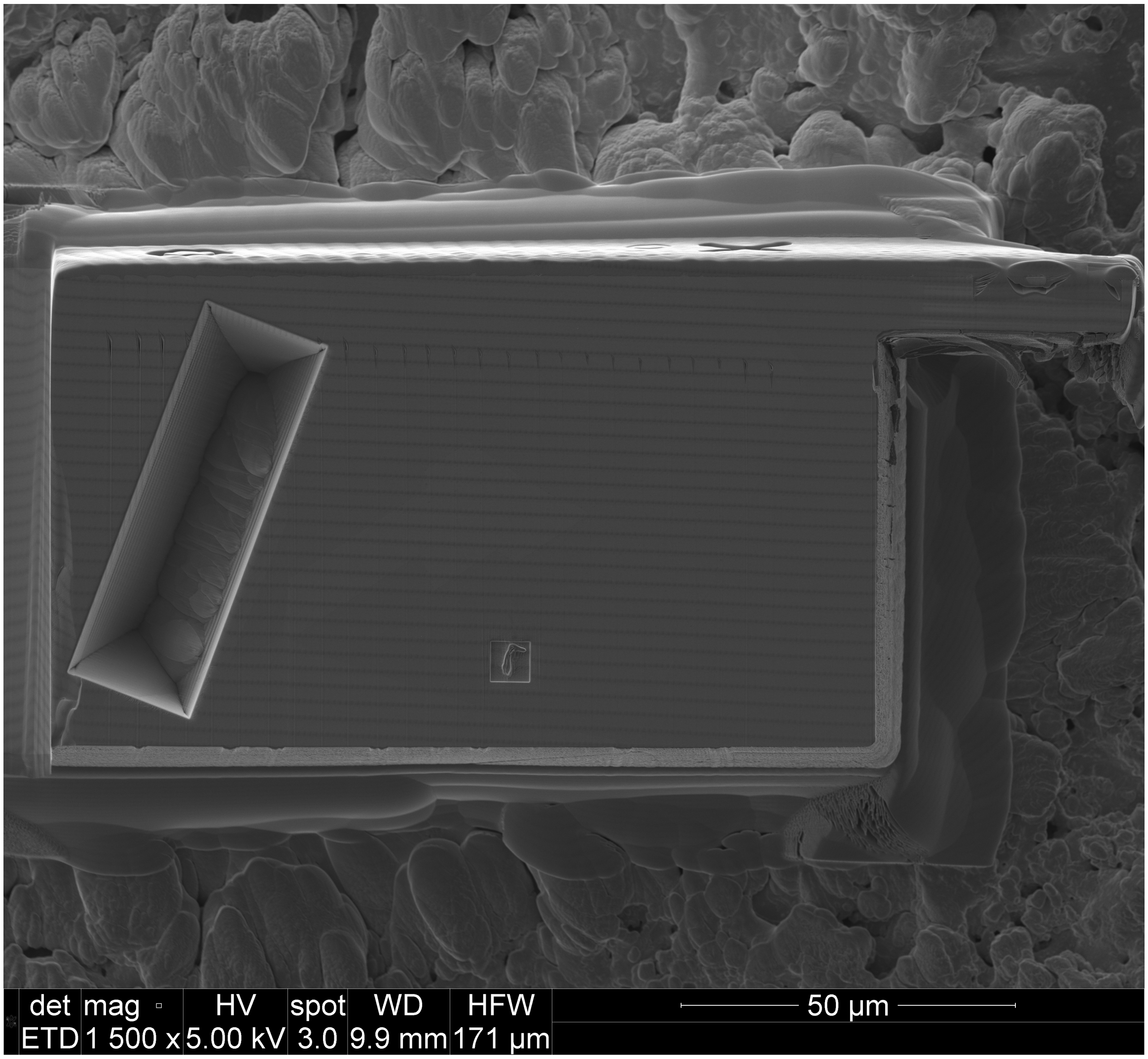

Figure 2.6: SEM image of the gold calibration sample, taken at normal incidence. Collecting secondary electrons on an Everhart-Thornley detector allows for the resolution of topological features of the sample.

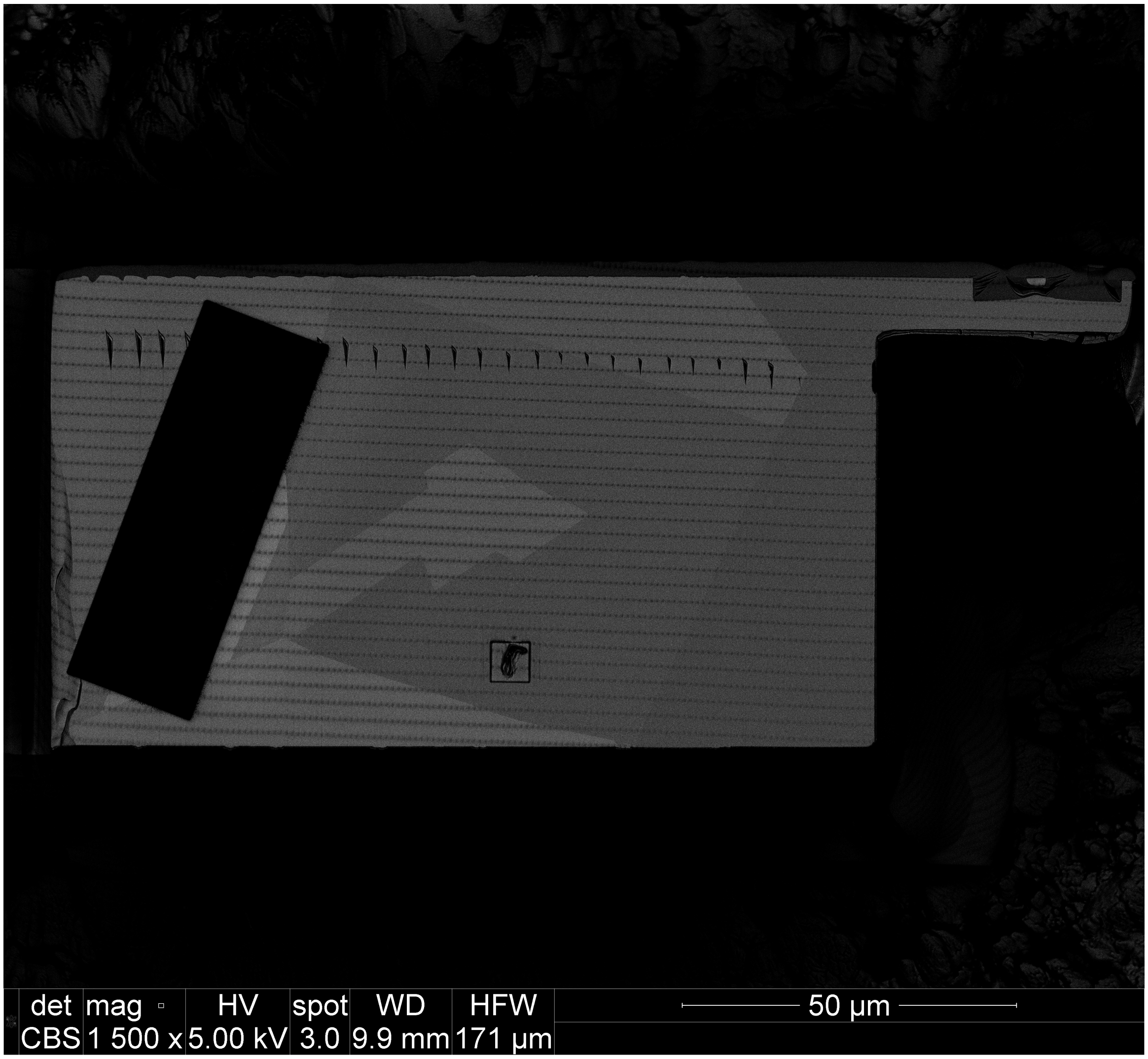

Figure 2.7: SEM image of the gold calibration sample, taken at normal incidence on a backscattered electron detector. Intensity of backscattered electrons depends on crystallographic orientation, yielding contrasts that reveal the underlying surface grain structure.

all expensive, we would also prefer a non-destructive technique, so that our sample persists to be recharacterized by other techniques or beamlines as a true calibration. Unfortunately, the requirement that the spatial resolution be better than that of nf-HEDM rules out the use of laboratory or synchrotron-based diffraction contrast tomography [45, 46, 47, 14] as with this technique direct reconstruction of grain boundaries is not possible. Differential Aperture X-ray Microscopy [48], another non-destructive x-ray technique is not suited to characterization of the comparatively large sample volume.

To best compromise a solution to these issues, electron backscatter diffraction (EBSD) was chosen to provide the ground truth characterization. EBSD is a widely used surface characterization technique that combines excellent spatial resolution (< 1 μm) with good orientation resolution ($\sim 1^{\circ}$ or less depending on the care taken by the experimenter). While the ideal scenario for this one application would be complete and destructive serial sectioning of the specimen to characterize the 3D orientation field, to maintain future use of the specimen we will restrict EBSD characterization to the surface. To calibrate nf-HEDM, a bulk charactertization technique, using just this data, considerable care must be taken to image the free surface with the nf-HEDM microscope. We will discuss these considerations as they arise.

EBSD data were collected on the sample top surface using an FEI Nova 600 Dual Beam FIB-SEM and the collected diffraction peaks were indexed using EDAX TSL software. Data were collected with an electron beam raster spacing of 150 nm. The reconstructed microstructure is shown in Fig. 2.8. This map, however, will not be what we compare to our nf-HEDM maps. While backscattered electron intensities may be probed at normal incidence, indexing the diffraction patterns produced at each spatial point required tilting the sample 70° with respect to the incoming electron beam. This tilt introduces additional distortions to the imaged surface orientation field [49] besides the distortions caused by sample drift, lens instability or stray fields common to all SEM imaging modes. One can see the distortion qualitatively by comparing Fig. 2.8 and Fig. 2.7. These distortions must be corrected in order to use the orientation-indexed EBSD image as the ground truth calibrant. The first step is then to unmap the distortions of the reconstructed EBSD image, Fig. 2.8, using the image at normal incidence, Fig. 2.7. (While one could use Fig. 2.7 directly to segment grain boundaries there are two reasons we prefer to use an undistorted version of Fig. 2.8. The first is ease of segmentation. Resolving grain boundaries in Fig. 2.7 requires an image filter sensitive to transitions between pixel intensity. While applying such a filter is manageable [1], the feature space of Fig. 2.7 is quite rich. The grain boundaries would be a small subset of other features also segmented. Denoising this signal could be an irritation. Because the reconstructed EBSD map is an orientation field, segmenting grain boundaries reduces to the problem of finding discontinuities in the disorientation above some threshold, a much more straightforward procedure. Secondly, we ultimately desire to compare the orientations reconstructed by the nf-HEDM with the reconstructed EBSD map anyway, so we might as well get

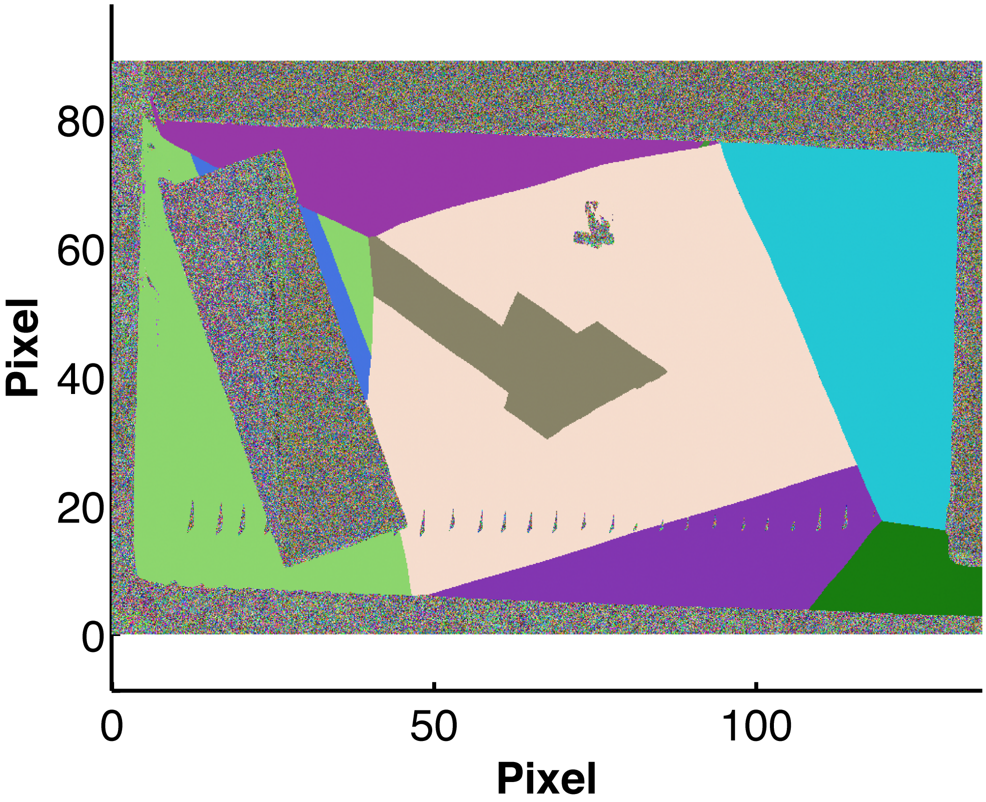

Figure 2.8: Reconstructed EBSD map of the calibrant's surface grain structure. This image was generated by indexing the backscattered diffraction pattern at each pixel point on the sample. Here, grain orientations are mapped to an RGB colorscale so solid color blocks represent individual grains. Noisy regions represent places where there is no material that produces indexable diffraction. The grid resolution used is 150 nm.

the boundaries at the same time.)

A general image distortion may be modeled with an affine transformation. In two dimensions these transformations incorporate the effects of translation, rotation, scaling, shear, and reflection; they also preserve the ratio of distances between points and colinearity of points. Removing the distortion in Fig. 2.8 then amounts to finding the affine transformation that aligns the external edges of the two sample representations. Segmenting the external edges of Fig. 2.7 is easily accomplished by thresholding the pixel intensity value at half of the average maximum intensity characteristic to the sample material. This image is 16-bit depth and has high dynamic range, so the contrast in intensity is very good. As a result, the rise width is very small, ~ 100 nm, so errors associated with this thresholding are even smaller than this and are negligible when compared to the nf-HEDM spatial errors. An illustration of this is shown in Fig. 2.9.

To extract the edges from the reconstructed EBSD grain map, first a threshold was applied on TSL's 'quality' parameter, $\mathcal{Q}$. The quality is taken to be a figure of merit for each reconstructed voxel of the EBSD scan, similar to C for the nf-HEDM reconstruction. Edges were then found by seeking EBSD voxels with fewer than four nearest neighbors on the square grid. (In practice, we sought to remove arbitrariness associated with choosing this threshold by assigning Fig. 2.7 as the ground truth for Fig. 2.8. The threshold that gave the best correspondence (lowest cost) between boundary sets after affine optimization was selected. We rastered over $\mathcal{Q}$ while iteratively performing affine optimization and ultimately $\mathcal{Q} = 0.35$ resulted in the most optimized match.) These edges are depicted in Fig. 2.10 in black and red for the SEM image and EBSD reconstruction respectively. The registered EBSD reconstruction (which will soon be discussed) is plotted also, and shows good agreement with the SEM edges. To align these edges, we used Monte Carlo optimization around a seeded guess. Initial rotation and translation parameters were selected by hand that would align the two point sets. This formed a transformation, A, of the form

$$A = \begin{pmatrix} \cos(\phi) & -\sin(\phi) & \Delta x \\ \sin(\phi) & \cos(\phi) & \Delta y \\ 0 & 0 & 1 \end{pmatrix} \tag{2.3}$$

which acts a proper rotation of angle ϕ with a translation of $(\Delta x,\ \Delta y,\ 0)$ on a point $r_i = (x_i,\ y_i,\ 0)$. Relaxing the form of A to

$$A = \begin{pmatrix} \cos(\phi) + \delta_{11} & -\sin(\phi) + \delta_{12} & \Delta x' \\ \sin(\phi) + \delta_{21} & \cos(\phi) + \delta_{22} & \Delta y' \\ 0 & 0 & 1 \end{pmatrix} \tag{2.4}$$

allows for shearing and scaling. We then generating ensembles of values for the top six components of T, and computed a cost $\mathcal{C}$, for

$$\mathcal{C} = \frac{1}{N_{\mathrm{S}}} \sum_{i=1}^{N_{\mathrm{S}}} \min_{j=1}^{N_{\mathrm{E}}} \left| \vec{r}_{i,\mathrm{S}} - \vec{r}_{j,\mathrm{E}} \right| \tag{2.5}$$

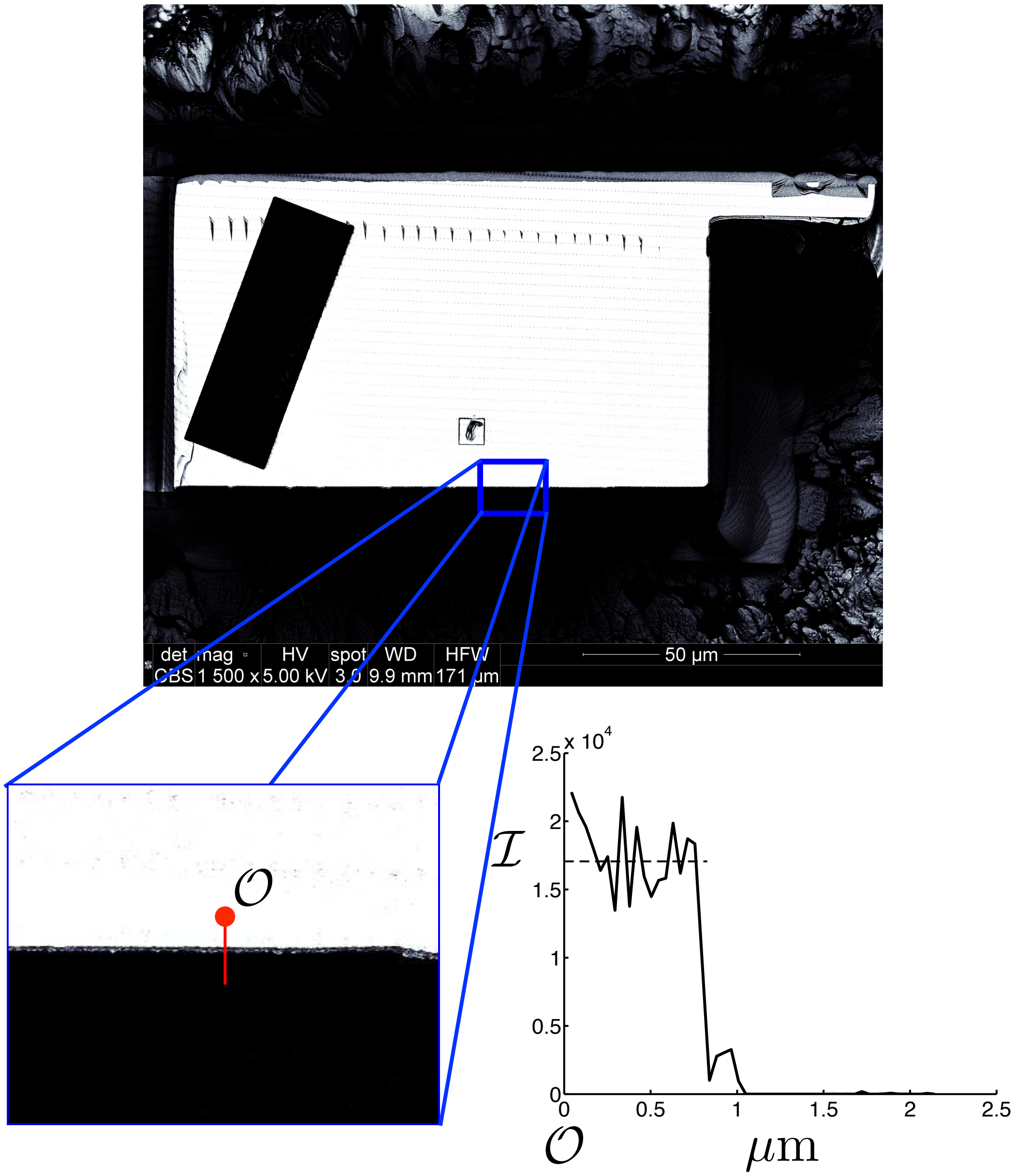

Figure 2.9: Illustration of the sharp intensity contrast used to define the specimen outline from the SEM image at normal incidence, later used to identify the distortion in the EBSD measurement. The raw SEM image taken at normal incidence is shown at the top of the figure. The plot at lower right shows the intensity of the image beginning at the point marked $\mathcal{O}$ in the enlargement in the lower left. The intensity rises 4 orders of magnitude over a distance of about 50 nm. Taking the half max points were used to define the sample edges.

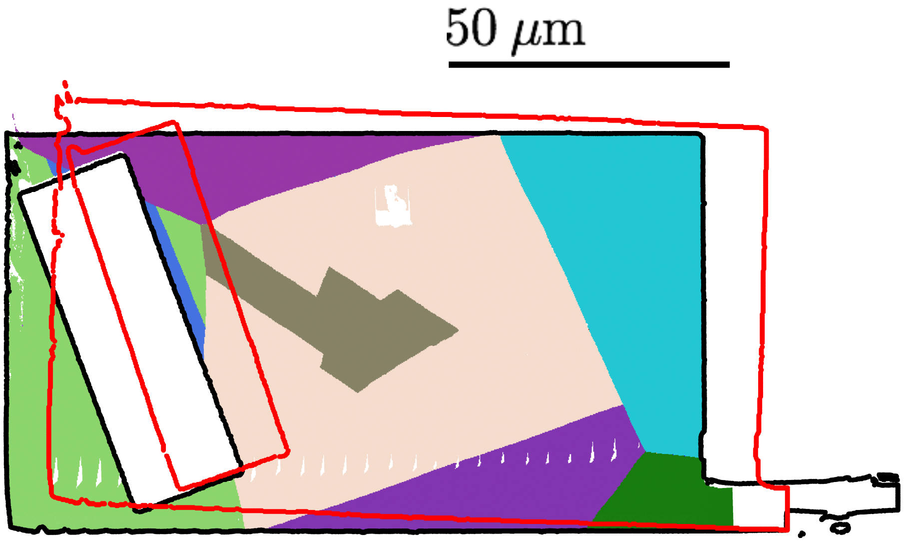

Figure 2.10: The undistorted EBSD reconstruction (colors), shown registered to the outline segmented from the normal incidence SEM edges (black). The outline of the EBSD reconstruction (depicted in red) illustrates the unregistered distorted image.

where N_{S} is the total number of edge points segmented from Fig. 2.7 and N_{E} is the total number edge points segmented from the reconstructed EBSD map. This form was chosen for C to give an of idea of the error in this registration; here $\mathcal{C}$ is the average minimum distance from a point in the SEM dataset to a point in the EBSD dataset. Performing the optimization, we find an optimal registration of

$$A_{\text{best}} = \begin{pmatrix} 0.980 & -0.026 & -0.0095 \\ 0.039 & 0.989 & -0.0028 \\ 0 & 0 & 1 \end{pmatrix} \tag{2.6}$$

depicted by component in Fig 2.11. At A_{best}, we observe $\mathcal{C} = 0.00025$ mm. For each variable component of A, we plot the value generated and the associated cost $\mathcal{C}$. Each ensemble of components is generated at one time, so a given transformation appears six times in the figure. The points representing each transformation are colored by their determinant, a proxy for the amount of shear and scale applied. Qualitatively, we see lower costs for transformations with determinant $D \approx 0.968$, more distorted than the proper rotations of $D \approx 1$ but not as distorted as those with $D < 0.968$. Viewed in a different way we can examine how $\mathcal{C}$ varies as a function of the entire transformation. For this we utilize the spectral norm n_{spec} of a transformation T,

$$n_{\text{spec}} = ||T||_2 = \left[\max \lambda(T^{\dagger}T)\right]^{\frac{1}{2}} \tag{2.7}$$

where we define $\lambda(T)$ to be a function that returns the eigenvalues of T. One can look at the spectral norm as a matrix norm, such that $||T - T'||_2$ represents the 'distance' from T to T'. Plotting these quantities for our ensemble of transformations in Fig. 2.12, we note that the bulk of transformation considered register the datasets within half a micron; A_{best} registers these datasets on average to within about 25 nm. The undistorted EBSD reconstruction in Fig. 2.10 will serve as the ground truth calibration for the subsequent nf-HEDM characterization.

2.2.2 nf-HEDM Characterization

2.2.2.1 Methods

Characterization of the calibrant using the nf-HEDM occured at APS-1ID. An incident beam energy of $E = 65.351$ keV, corresponding to the Hf K absorption edge, was selected to conduct the experiment as a balance between penetration power and overall machine efficiency. Hf foil was used to calibrate the beam energy to within ~ 10 eV of this value. Uncertainty in the energy δE, gives uncertainty in the scattering angle of $\delta\theta$, given by the differential form of Bragg's Law [11]

$$\lambda = 2d \sin\theta \tag{2.8}$$

$$\delta\lambda = \delta d \frac{\partial \lambda}{\partial d} + \delta\theta \frac{\partial \lambda}{\partial \theta} \tag{2.9}$$

$$\frac{\delta\lambda}{\lambda} = \frac{\delta d}{d} + \delta\theta \cot\theta. \tag{2.10}$$

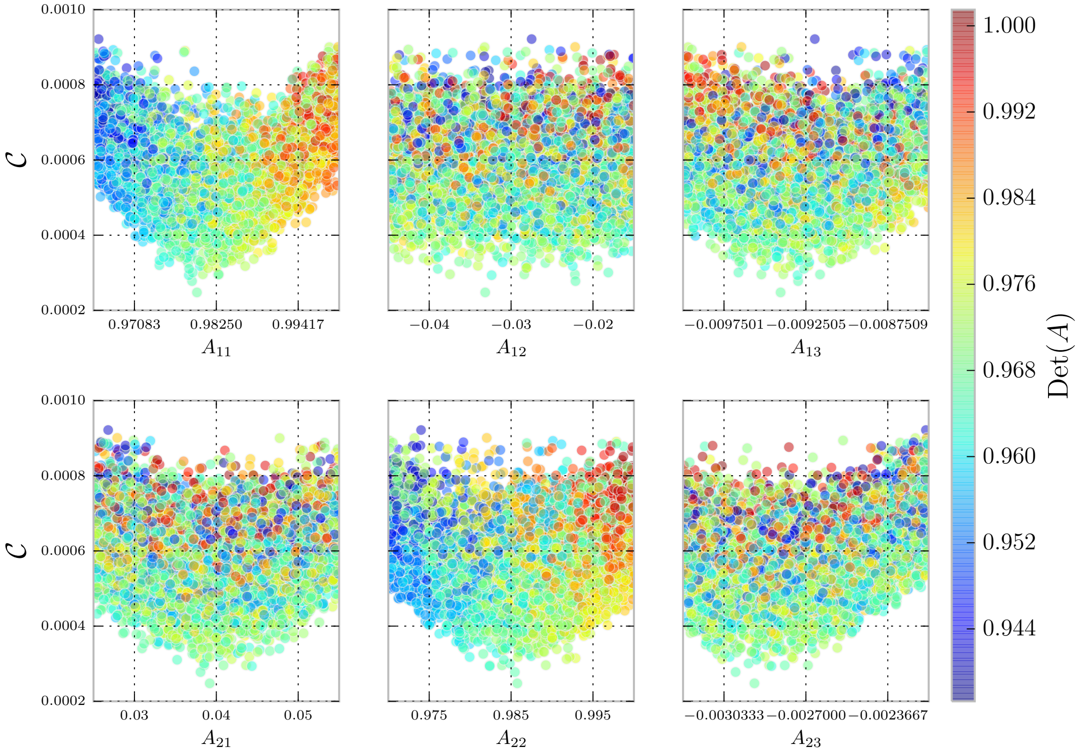

Figure 2.11: Cost landscape in each component of the affine transformation used to register the SEM and EBSD outlines. Each point in each plot represents the cost from one transformation; the x-value of the point is the value of the labeled component for that transformation. A given transformation then appears once in each subplot. Transformations are colored by the determinant of each. The units of $\mathcal{C}$ are mm. Cost minima have high dynamic range for all components except A_{12}.

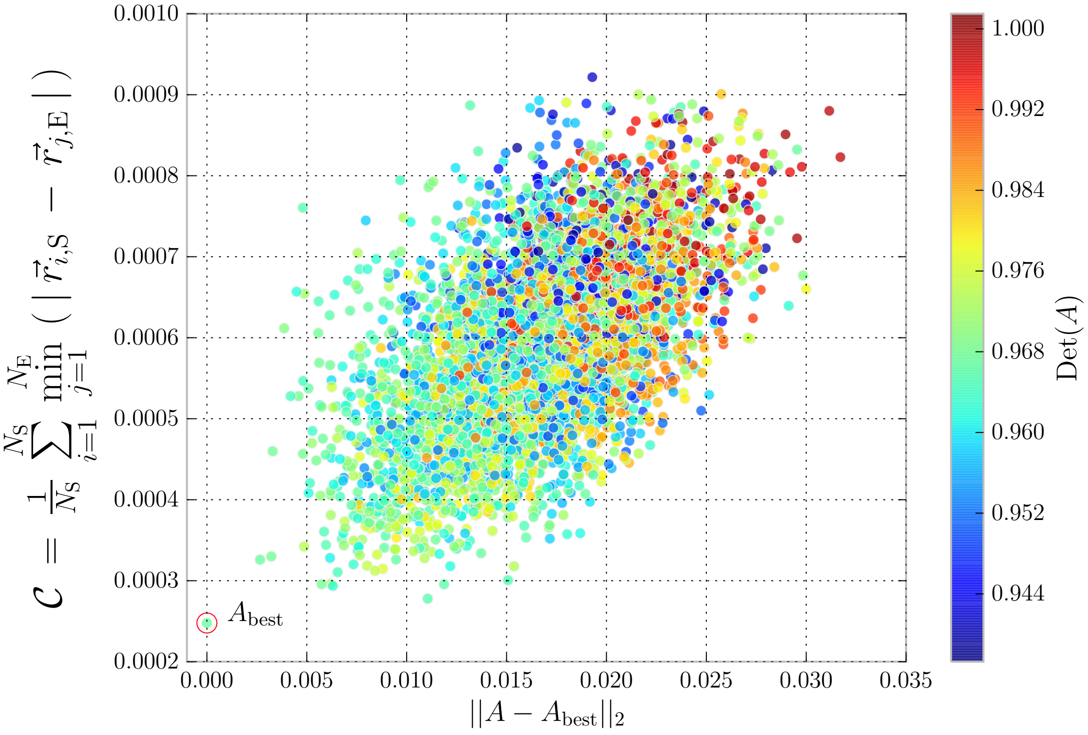

Figure 2.12: Collection of transformations considered to register EBSD and SEM datasets, plotted as a function of spectral distance from the lowest cost transformation, A_best. Each point represents one transformation and is colored by its determinant. The cost of each transformation, $\mathcal{C}$, is the average minimum distance from a boundary point in the SEM dataset to a boundary point in the EBSD dataset. Both mostly rotational ($\det(A) > 0.976$) transformations and transformation with more shearing and scaling $\det(A) < 0.960$ exhibit higher costs, when compared to transformations within this ‘Goldilocks’ zone.

Assuming an undeformed lattice, $\delta d = 0$, and

$$\delta\theta = \tan\theta\frac{\delta\lambda}{\lambda} = \tan\theta\frac{\delta E}{E}, \tag{2.11}$$

$\delta\theta \lesssim 1/4 \times 10^{-3}$ for scattering angles less than 30°. At typical $L_i \in [4, 8]$ mm, the worst case pixel motion implied by this uncertainty in θ is < 1 pixel, so these uncertainties will not be considered for the following analysis.

Before collection of experimental data, considerable care was taken to examine the geometry of the beam-sample system, so as to measure as near to the surface of the calibrant with the line-focused x-ray beam as possible. First, the beam was focused in the vertical dimension as narrowly as possible. This ensured that any effects associated with illuminating subsurface grain volume were minimized. At this point, the beam's vertical extent was measured using x-ray florescence; simultaneously, the sample's 'in beam' coordinates were recorded to note exactly the position where the beam began grazing the top surface of the sample. X-ray florescence uses an energy dispersive detector to distinguish characteristic x-rays emitted by the decay of excited atoms. In this case, the incident energy of 65 keV excited L and M shell electrons of the gold atoms, whose decays were detected while the sample was translated into the line-focused x-ray beam. The results of this scan are shown in Fig. 2.13. The monotonically increasing function shown in blue is the raw intensity registered on the energy dispersive detector as a function of sample position along $\hat{z}$ in the reconstruction coordinates, defined by the schematic of the measurement in Fig. 2.14. Gaussian and Lorentzian fits to the raw data are shown in purple and red respectively and have the parameters given in Table 2.2. Given the smaller RMS error of the Gaussian profile and tendency of the Lorentzian to overfit the tail of the raw data, the Gaussian profile with $\sigma = 0.755\mu$m was chosen to model the height of the beam. This width is an upper limit on the actual beam height; any tilt of the sample relative to the beam plane will broaden the observed transition. As discussed below, we find that such a tilt does exist. We take the full width at half maximum (FWHM) of 1.8 μm implied

Table 2.2: The values in this table characterize the width of the beam implied by fitting the results from the gold florescence scan to error and Cauchy functions. The Gaussian fit has lower RMS error and does not overfit the tail of the blue curve in Fig. 2.13. From this, we choose a Gaussian with $\sigma = 0.755\mu$m to model the beam profile in the vertical direction (height). This corresponds to a full width at half maximum (FWHM) of 1.8 μm; we take this to be the narrowest cross section we can acquire with the nf-HEDM microscope.

Functional Form	Width Parameter	Value	FWHM [m]	RMS Error [$\mathcal{I}$]
Gaussian	σ	$7.55 * 10^{-4}$	$2\sqrt{2\log 2}\sigma = 0.0018$	56.25
Lorentzian	γ	$5.70 * 10^{-4}$	$2\gamma = 0.0011$	70.12

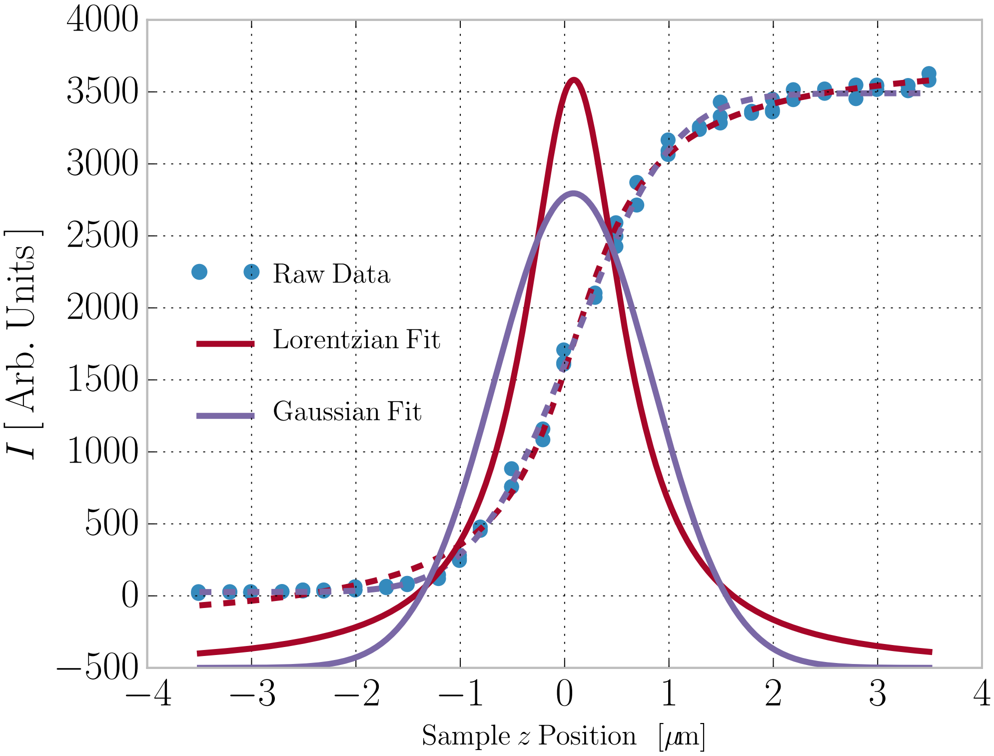

Figure 2.13: Experimental results from the florescence scan conducted using the gold specimen. The horizontal axis is scaled using relative coordinates. The vertical axis shows intensity registered on the energy dispersive detector as a function of sample position along $\hat{z}$. The raw data collected is shown in blue. Those points were fit to an error function and the cumulative distribution function of a Lorentzian (Cauchy distribution), the results of which are plotted in purple and red, respectively. The Gaussian and Lorenzian beam profiles implied by these absorption curves are also plotted in purple and red. In both cases the beam height, as measured by the FWHM, is less than 2 μm .

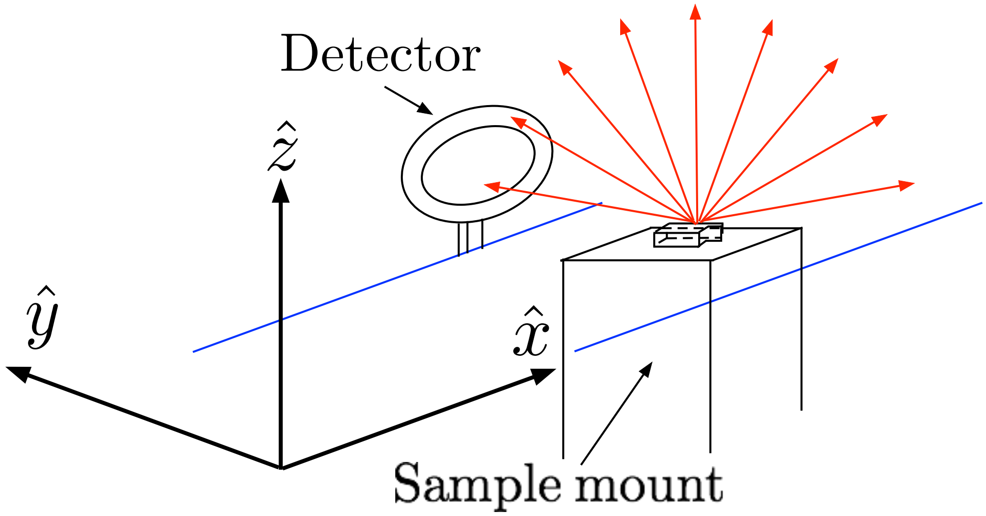

Figure 2.14: A schematic depicting the collection of the x-ray fluorescence data. The line-focused beam, depicted in blue, is incident in the $+\hat{x}$ direction. The sample is translated in the $+\hat{z}$ direction into the beam from below. Fluorescent x-rays emitted by the sample are collected on an energy dispersive detector when the sample is illuminated by the beam. This measurement was used to determine the vertical beam profile, the exact location of the specimen's top surface, and the effective point spread function of the nf-HEDM detector at normal incidence.

by this width to be the thinnest cross section we can collect using the nf-HEDM microscope with the x-ray focusing configuration achieved during this experiment. This thickness also corresponds to the limit of the approximation of a truly line-focused x-ray beam, as the best one can do with this limitation is to measure the scattering from within $\sim 2\,\mu$m of the surface sampled by the EBSD. Grain boundaries measured with nf-HEDM that have normal vectors close to $\hat{z}$ (defined by Fig. 2.14) may have comparatively large spatial errors when compared to the EBSD reconstruction, if not corrected by extrapolating them from cross sections further from the sample surface.

Performing the fluorescence scan also identified the point at which the beam began to graze the top of the sample. By recording this position, the intent was to lower the sample slightly from this position, and then to incrementally translate it into the x-ray beam, thereby measuring as close to the top surface as possible and subsequently recording the subsurface microstructure. Data collection began with the specimen at the location corresponding to a sample height of -1 μm on horizontal scale of Fig. 2.13. At this location, the specimen was thought to be just clipping the beam tail; moving +2 μm vertically would then illuminate the first 2 μm of sample surface with the $\sim 2\,\mu$m beam.

At these locations, nf-HEDM diffraction data were collected in 0.1° integration steps on the interval $\omega \in [-180°, 180°]$ at rotation-axis-to-detector distances of $L_i \in$

$\{5.0, 6.5, 8.0, 9.5, 11.0\}$. The Aerotech rotation stage was used to provide rotation about $\hat{\omega}$, in the E-hutch of Advanced Photon Source Beamline-1ID at Argonne National Laboratory. While it is typical to collect experimental data in 0.5-1° integration steps on a total angular interval of 180° at two or three values for L_i, desire for optimum orientation and spatial resolution motivated collection of more data. This extended parameter space can also be further investigated to highlight improvements to the experimental technique. At 8 MB for each raw diffraction image collected, each 144 GB cross-sectional layer of $1.8 * 10^5$ images represents considerable data volume. Five such contiguous layers including the nominal surface layer were collected with 2 μm spacing between layers. After collection of these layers, 10 bulk layers were collected with $L_i \in \{5.0, 6.5\}$.

Following data collection, data were processed using a pipeline required by the current implement of the IceNine software package [15, 10]. This pipeline is depicted schematically in Fig. 2.15. The reconstruction process begins with the determination of an approximation for $\mathbf{E}$ using the raw data. Following this step, diffraction peaks are segmented from the raw data to form binary images. These binary or 'reduced' images are then used to perform Parameter Monte Carlo (PMC) optimization to improve the match between $\mathbf{E}$ and the manifest physical setup. Following this procedure, the orientation reconstruction is performed after which its quality is evaluated. If heuristic criteria indicate that the reconstruction quality is sufficient, the PMC and reconstruction processes may be repeated after increasing $Q_{\max}$, to consider more diffraction information in the analysis. Ensuring reconstruction quality prior to iteration of the PMC and further reconstruction is necessary to maximize the likelihood of convergence. $Q_{\max}$ is increased until high-Q scattering simulated is not visible in the binarized images. Following this process, the microstructural volume is processed to build a 3D orientation field. After collecting the raw diffraction data, raw image analysis was performed to determine the parameter sets $E = \{j_0, k_0, L_0, \dots j_2, k_2, L_2\}$ that define an approximate position for the projection of the rotation axis on each detector and the detector's distance from the rotation axis. The remaining L_is will be the subject of study discussed later. Following this procedure, to manage data volume, adjacent images within 1° angular bins were summed together. The effects of reconstructing the microstructure with more finely graduated angular bins will be analyzed later. The background field associated with collecting intensity on the nf-HEDM CCD detector is relatively constant as a function of integration time. Because of this, an additional background subtraction step was performed on each integrated 1° wedge before applying Lind's method [1] to segment peaks from the raw diffraction data. Parameters used to segment peaks from the raw data are shown in Table 2.3, though these parameters have been shown to impact the segmentation only weakly.

Following segmentation, the aforementioned parameter Monte Carlo procedure was used to optimize $\mathbf{E}$. After each Monte Carlo was performed, $Q_{\max}$ was incremented, and the Monte Carlo procedure rerun. With each successive value of $Q_{\max}$, more constraining peaks were used to restrict the low-cost parameter space avail-

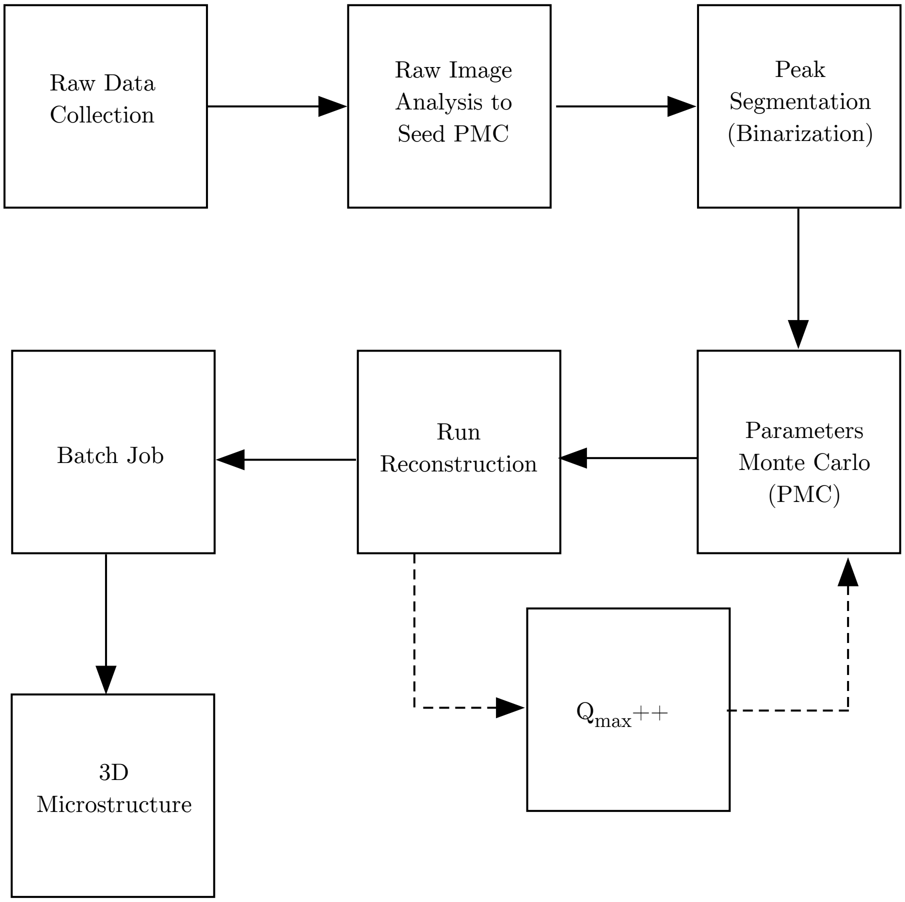

Figure 2.15: A schematic of the nf-HEDM reconstruction pipeline used in this work.

Table 2.3: The values in this table were used while performing Lind's peak segmentation method. For more information about the interpretation of these variables, see [1].

Parameter	Value
Blanket Subtraction [counts]	5.0
Peak Height Ratio	0.1
Minimum Pixels Accepted	4.0
Median Filter Radius [pixels]	1.0
Gaussian Kernal σ [pixels]	0.75

able. In this way, though the reconstruction may be non-unique, at comparatively large values of Q_{max}, the phase space available to the reconstruction is much more restricted. In this case, Q_{max} was increased until peaks were simulated that were too weak to detect and corresponding uniform decreases in C noted. Reconstructions were then performed just below this threshold. Reconstructions discussed for this specimen were performed incorporating peaks with up to $|Q| \leq 16$ Å^{-1}, which implies that each voxel was reconstructed using ~ 1100 Bragg peaks.[6] Reconstructions were performed using (equilateral) triangular voxels with side-length of 1.41 μm .

2.2.2.2 Results

Reconstructions of the top four cross-sectional layers, including the surface layer(s), are shown in Figs. 2.16 and 2.17. At first blush, we recognize the microstructure of the specimen as seen from the surface characterizations. There are several features of interest, each of which deserves some attention:

1. The surface was not captured in one cross sectional layer - during data collection the specimen surface, assumed to be parallel to the beam plane (and flat), was tilted at some small angle θ with respect to the beam.

2. Almost all grains are present in the reconstruction; notably absent is the thin grain immediately adjacent and parallel to the trench feature. This grain is depicted in blue in Fig. 2.10.

3. Reconstructed grain boundaries are mostly straight, though some curvatures exist where they appear not to in Fig. 2.10

---

[6] Typical reconstructions used for science, not calibration utilize Q_{max} values between 10-12 Å^{-1}. For a similarly collected experiment with the rotation interval $[-180°, 180°]$, this corresponds to ~ 250 and ~ 490 peaks respectively, though in practice, if the rotation interval is $[-90°, 90°]$ many of the reciprocal lattice vectors responsible for observed diffraction will intersect the **Q**-locus only once, so there will be fewer peaks than this collected.

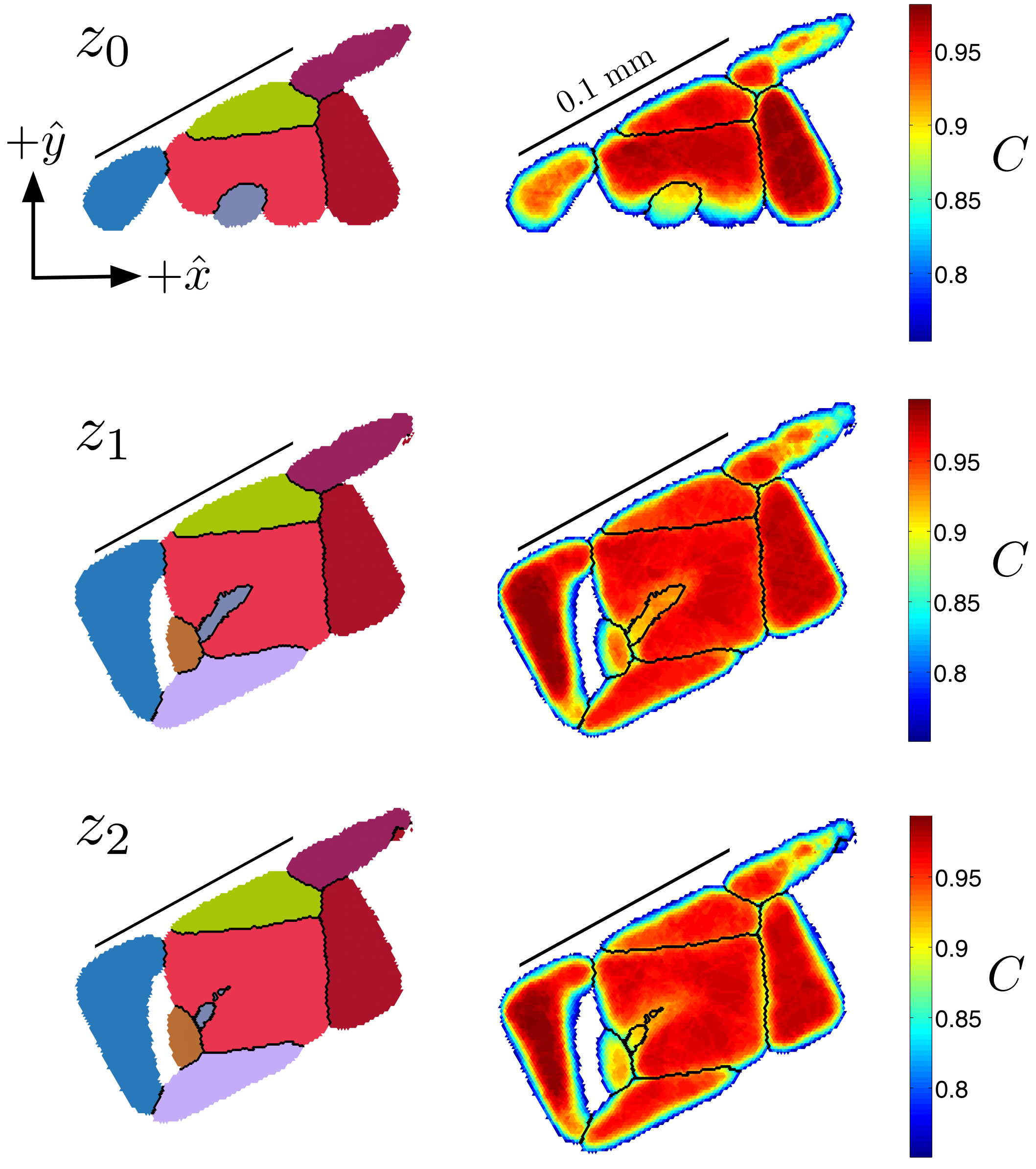

Figure 2.16: Reconstructions of the top three layers of the specimen. The first collected layer is labeled z_0 and corresponds to the data collected with the specimen at -1 μm relative to the beam in Fig. 2.13. Each subsequent cross section comes from translating the sample along $\hat{z}$ by 2 μm and re-scanning the cross section. Each reconstructed shown has been thresholded at $C = 0.8$. Reconstruction voxels are equilateral triangles with side-length equal to 1.41 μm . For reconstructions that follow, the line-focused incident beam travels along the $+\hat{x}$ direction, with the illuminated cross section depicted. $\hat{\omega}$ points out of the page.

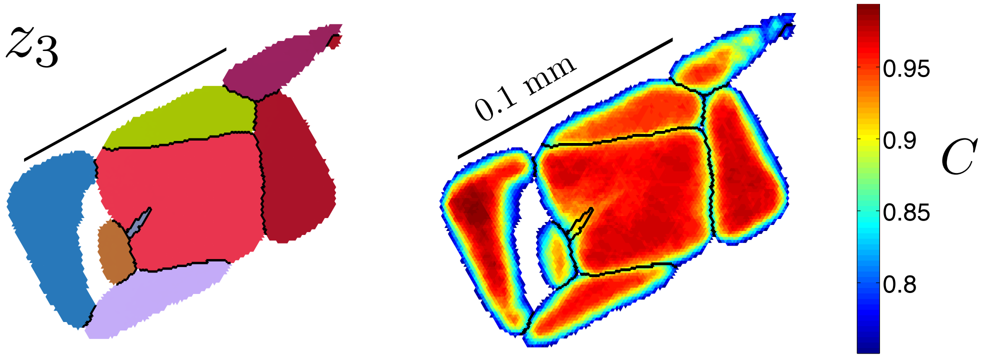

Figure 2.17: This is the fourth layer of microstructure reconstructed, counting z_0 as the first.

4. The distinctive shape of the embedded grain in Fig. 2.10, depicted brown in that map, and in lavender Fig. 2.16, (henceforth referred to as the 'embedded twin', as subsequent analysis will reveal this grain is an FCC coherent twin) is lost in the nf-HEDM reconstruction.

5. The outer edges of the specimen are rounded, with each grain extending into free space farther than its EBSD characterized counterpart; similarly the trench feature lacks definition.

6. The average C parameter of the reconstruction for most cross sections is ~ 0.95, excluding the 'antenna' protrusion. As each voxel is independently reconstructed, this means each voxel is optimized such that it overlaps ≥ 990 diffraction spots. Clearly then, all $C = 0.95$ fits are not equivalent

7. Deviations from $C \geq 0.95$ occur mostly at the free surface, at grain boundaries, and within and above the embedded twin.

To the first point, having a relative tilt of the specimen and beam plane is non-ideal. First and foremost, analyzing these results becomes complicated by the fact that the proper representation of the surface in this case is best approximated by the union of z_0 and z_1. A schematic showing why this is true is shown in Fig. 2.18. In this depiction, the (tilted sample) is illuminated by the approximately planar beam; in this case, because the cross sectional spacing is approximately equal to the beam height, we choose to show its finite extent. To the left of the dotted vertical line, the surface is illuminated at z_0 and to the right of it, the surface is illuminated at z_1. Accurately representing the surface requires taking the union of these two regions which are highlighted in dotted yellow. Added complications arise because the limits of each reconstruction are defined by specifying a value for C. Proper determination of the surface structure requires computing and minimizing some cost for each point in the space defined by (C_{z_0}, C_{z_1}). This will be discussed in more detail in the sections following. Further, the sample being tilted implies that there will be errors in locating the grain boundary surface position arising from the finite beam thickness. We consider this effect immediately following brief discussion of these results.

Regarding the absence of the thin grain immediately adjacent to the trench, the most likely culprit for this phenomenon is the size of the grain. Only $\sim 2.5\,\mu$m in width, when the grain's diffracted beams are compressed by the projection geometry the scattering is unlikely more than a single pixel row in extent. Coupled with decreased intensities due only to containing less scattering volume, these signals may easily be discarded as noise by the segmentation. Some combination of more sophisticated detector technology, increased segmentation sensitivity, and experimental care is required to resolve features of this size and smaller

The reconstructed curvatures, as we will later show, are the result of some slight discrepancies between $\mathbf{E}$ and $\mathbf{E_0}$, the physically manifest experimental geometry. These discrepancies cannot be eliminated with current technologies, but the errors

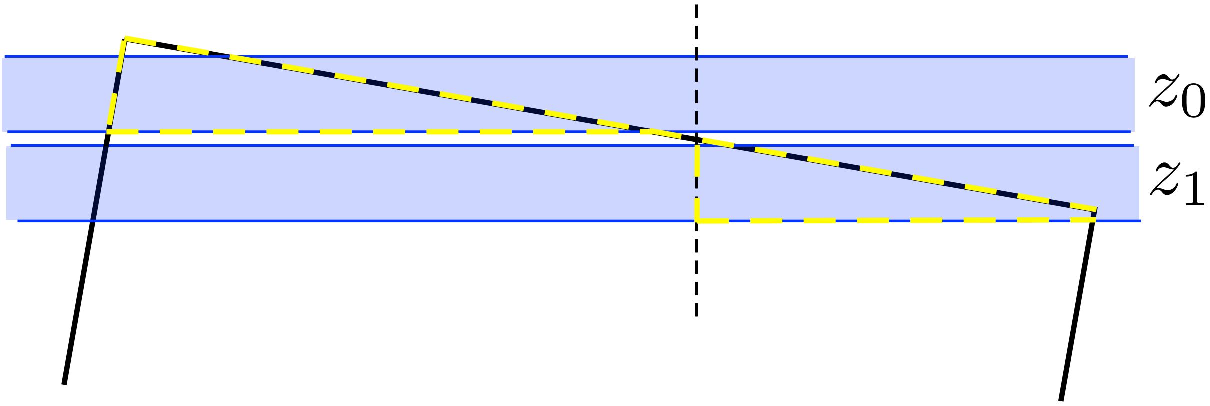

Figure 2.18: An illustration of the cross sections necessary to properly reconstruct the surface, if the entire surface is not contained in a single cross section. The proper representation should be the union of the highlighted portion of z_0 and the highlighted portion of z_1.

they cause will be explored in later sections. These factors may contribute to the lack of reconstructed shape definition of the embedded twin, but for this grain other factors are at play too. In this case, analysis from section 2.2.2.3 will show that the grain shape of the embedded twin varies considerably as a function of cross section. Any failure to illuminate the surface exactly may then result in missing the scattering required to reconstruct this distinctive shape. Further, because the twin is embedded, voxels near the grain boundary surface see two minima corresponding to parent and twin orientations in the orientation cost landscape. In that case, the details of the optimization procedure, *e.g.* size of window in orientation search Monte Carlo, or discretization noise (boundary lies within one voxel) may also result in imperfect reconstruction on the boundary.[7]

Errors in the embedded twin geometry are not the only spatial errors evident from Figs. 2.16 and 2.17. Comparing the nf-HEDM reconstructions to the undistorted EBSD ground truth, we see considerable blooming of the specimen on the free surfaces. Orientations are being reconstructed in sample space where no sample manifestly exists. This effect has been well documented [1] and has been attributed to the effective point spread function of the nf-HEDM CCD detector. As previously mentioned, the diffracting x-ray beams couple to the CCD using a crystal scintillator the emits visible light when struck with x-rays. The scintillating layer of the crystal has finite thickness t, where $t \approx 10\ \mu\mathrm{m}$, and as a result, peak edges are smeared out by a 2θ dependent distance,

$$\delta p = t \tan 2\theta. \tag{2.12}$$

Any aberrations or focusing errors of the optics that focus the scintillated light into the CCD can also contribute to this effect, even at normal incidence. At relatively small scattering angles, peak edges can be broadened by non-negligible amounts. This results in a Gaussian error function edge of finite width associated with the perimeter of each diffraction peak collected; if grain boundary voxels are reconstructed, peak dilation effects from the peaks of grains on either side of the boundary offset and the boundary position is properly located. However, on the free surface, peak dilation from the surface grain has no competition for an alternate orientation and the optimized solution includes reconstruction of orientations in free space. See [1] for a complete discussion.

It is at these free surfaces where the most variation in C takes place. We also note drops in C which are approximately one voxel in width at the grain boundaries and associate these dips with the grain boundary itself passing through these voxels. The voxel then contains both orientations and achieves a suboptimal solution for either orientation. In Figs. 2.16 and 2.17, these dips are sometimes covered by the plotted

---

[7] As implemented here, the orientation reconstruction begins with a breadth-first search of orientation space [50]. Costs are computed on a discretized grid in orientation space and candidate orientations are refined by Monte Carlo before a final orientation optimization takes place. Presented with approximately equal unoptimized costs for both parent and twin orientations, this results of this method of orientation search becoming sensitive to how the Monte Carlo is performed.

grain boundary lines. Other regions of comparatively lower C are present in the lower region of z_0; we attribute this to reduction in intensity from the scattering there resulting from illumination by the tail of the Gaussian beam. In each cross section, the embedded twin appears reconstructed at lower value of C. As previously mentioned, the comparatively small size of this grain may play some role in diffracting less intensity overall, so some peaks belonging to this grain may have been underexposed during experimental data collection.

2.2.2.3 Errors From Imperfect Sampling of the Surface - 1D Correction

Finite beam height effects will play a role as we attempt to probe the surface structure with a beam of finite height. We assume first that the microstructure reconstructed will be the region illuminated by the brightest part of the Gaussian beam that intersects that cross section. The justification for this is that the signal will be stronger for the diffraction originating from that part of the cross section. For an incoming beam intersecting a bulk sample, the cross section reconstructed will be that which intersects the peak of the Gaussian beam profile. As always, only that volume which is illuminated can diffract. If only the tail of the beam intersects the the sample surface, the brightest part of the beam will result in the dominating signal, and in that case, the volume nearest the sample surface gives the most signal. The origin of the strongest signal (thus the cross section reconstructed) is highlighted in yellow dashed in Fig. 2.19, a schematic of the geometry associated with a cross section of finite height. By these arguments, only regions where $r > 0$ require correction. In this figure, δr is the error in the assumed surface boundary position from being a height δz below the surface point relative to the planar cross section. Assuming that θ can be estimated from the first two reconstructions, then δz can be found for a given point on the reconstruction by

$$\tan\theta = \frac{\delta z}{r + \delta r}. \tag{2.13}$$

Given a grain boundary inclination (relative to the reconstruction) of ϕ, then

$$\tan\phi = \frac{\delta r}{\delta z} \tag{2.14}$$

or

$$\delta r = \frac{r \tan\theta \tan\phi}{1 - \tan\theta \tan\phi}, \tag{2.15}$$

using 2.13.

By inspection, the normal to the tilt plane of the sample with respect to the beam lays almost completely in the yz plane, thus requiring correction of the boundary locations along $\hat{y}$ only. Unfortunately, there is no good way to set the origin of $\hat{r}$, *i.e.* the location where the peak of the Gaussian beam intersects a cross section.

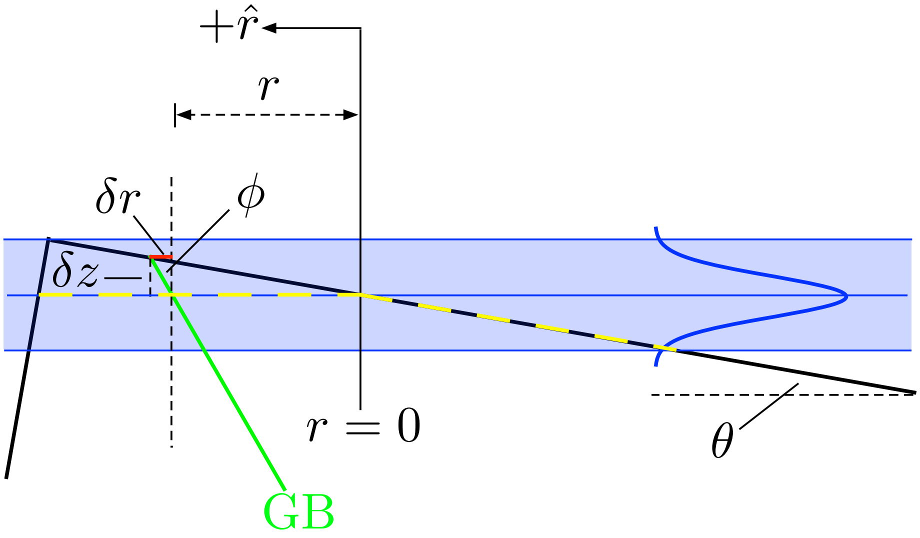

Figure 2.19: The error, δr, of interpreting the reconstructed microstructure as the surface microstructure if the bulk of the diffracted signal occurs below the surface. The reconstructed cross section appears dashed. δr depends both on the tilt of the specimen *vis-a-vis* the beam, θ, and the grain boundary inclination angle, ϕ. Here, the Gaussian beam profile is depicted in blue, with the illuminated area also in blue.

We know the point where the tail of the beam intersects z_0 because diffracted signal stops being reconstructable where there is material, at about the start of the trench feature. We do not know how far this cross section would extend, however, because of the absence of material to reconstruct beyond the 'antenna.' We do know a sure upper bound for θ, by assuming the cross section of z_0 spans only the antenna feature to the point where the reconstruction stops, a total of 91 μm along $\hat{y}$. The beam is $\sim 2\ \mu$m, so $\theta_{\max} \leq \tan^{-1}(91/2) = 1.55°$. In reality, this is probably a considerable over-estimate; there is no clipping of the 'antenna' at the top of z_0 in Fig. 2.16, and C is comparatively low at the bottom of the reconstruction, evidence that the tail of the beam illuminated that section of microstructure. We see no corresponding drop at the top of the structure, save for the 'antenna' which has reduced C values in each cross section. This implies perhaps that better initial alignment may have illuminated the entire surface volume, tilt or not, within the $\sim 2\ \mu$m beam height; the best made plans sometimes go awry.

Taking our bound for θ, we can then examine the errors δr as a function of grain boundary inclination for the 1D case. These curves are plotted in Fig. 2.20, along with the implications for reconstructions of z_0 and z_1 under the almost certainly incorrect assumption that what was reconstructed of z_0 was all that could possibly be illuminated at $\theta_{\max}$. Under these assumptions, corrections become necessary at the black solid lines on each reconstruction, with each color then corresponding to the curves at the top of Fig. 2.20. The black line corresponds to the location where the beam maximum would intersect the sample surface. In this case, δr errors are in the $\hat{y}$ direction. Because $\theta_{\max}$ is relatively small, for most boundary inclinations the errors from the finite beam height are considerably smaller than the errors associated with the sample space discretization, which we take to be on the order of half the voxel size.

The next step is to evaluate the grain boundary inclination angles along $\hat{y}$ in order to estimate the possible magnitude of these finite beam height effects. This requires examining each grain boundary at each cross sectional layer and then finding a grain boundary normal from the plane defined, either by fitting a plane or some other such operation. The projections of these boundaries onto a single plane is shown in Fig. 2.21. Qualitatively, we note the most inter-layer variation for the embedded twin. The layer spacing is only 2 μm however, so we will still need to consider what appear to be slight variations as possibly important. Estimating the range of δrs possible for each grain boundary requires estimating ϕ for each boundary, and using our upper bound for $\theta_{\max}$ to evaluate Eq. 2.15 for each boundary. To estimate ϕ, because most boundaries here are quite straight, we will use principle component analysis (PCA) to identify the grain boundary inclination and normal vectors. Qualitatively, performing PCA involves diagonolizing the covariance matrix; the eigenvector of the covariance matrix with the largest eigenvalue is the direction with the highest variance. The remaining eigenvectors are the directions of maximum variance once variations in the direction of the first and subsequent eigenvectors are removed. Performing PCA on

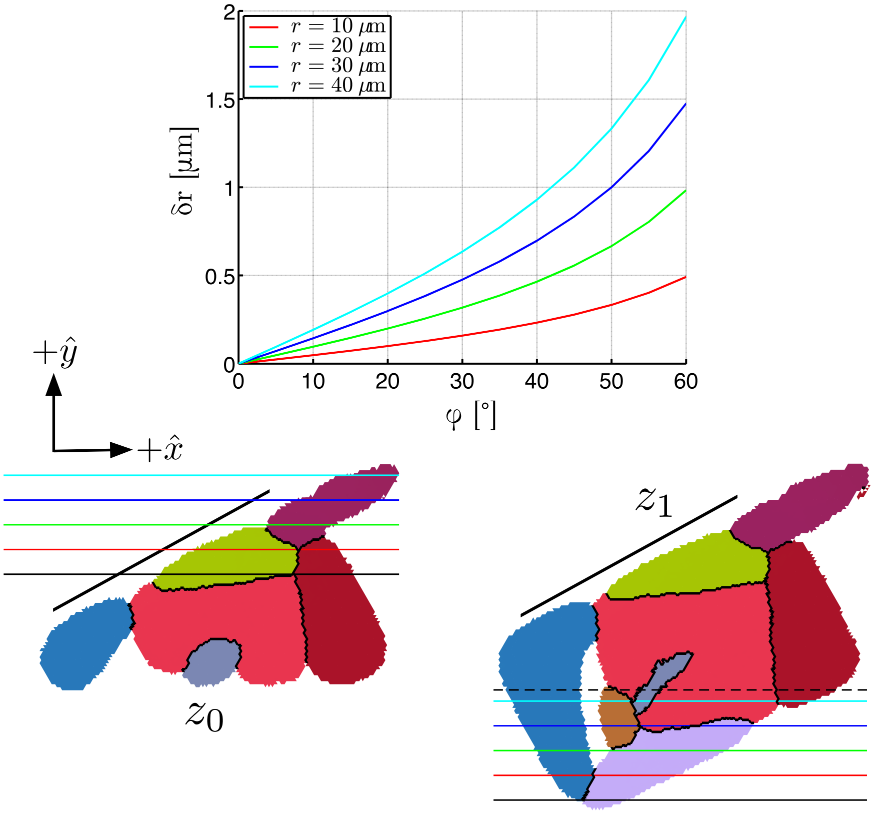

Figure 2.20: Estimation of possible errors in grain boundary position as a result of finite beam height, based on one particular set of assumptions. If the upper bound for θ is assumed, errors due to this effect accumulate past the black lines on each cross section. The multicolored curves correspond to the plot above with each a different distance from the intersection of the beam maximum with the specimen surface. At each curve, for fixed ϕ in the $\hat{y}$ direction, upper bounds for finite beam size errors are given by the value of the curve at that point.

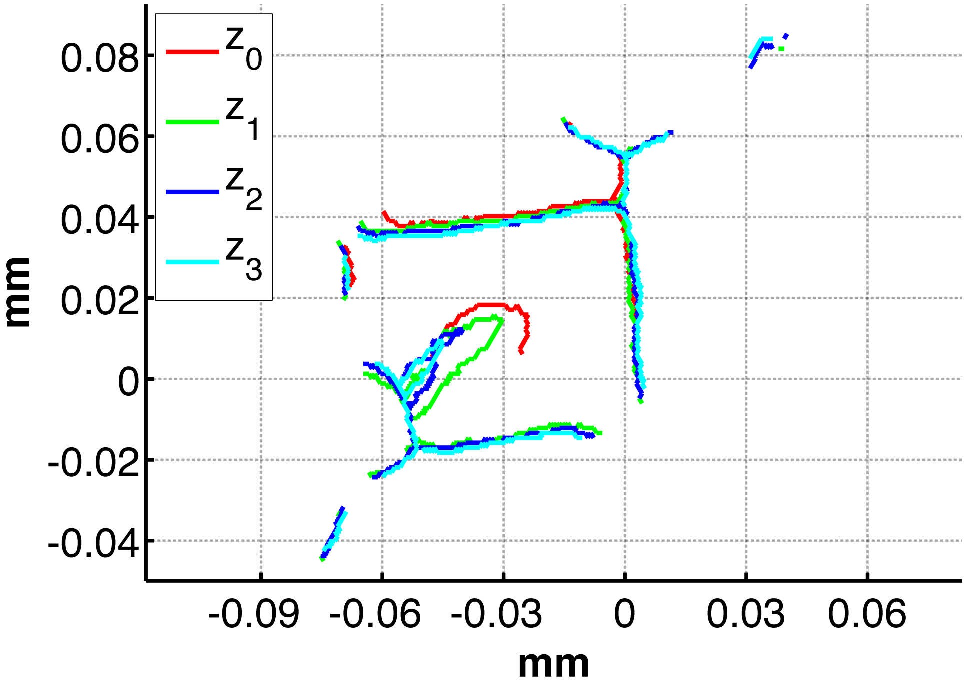

Figure 2.21: Projection of the grain boundary traces at each reconstructed cross section. Most boundary positions vary little as a function of cross section (again, cross sections are spaced at 2μm), indicating planar boundaries with one principle axis along $\hat{z}$. A notable exception is the embedded twin, whose boundary traces follow a different plane.

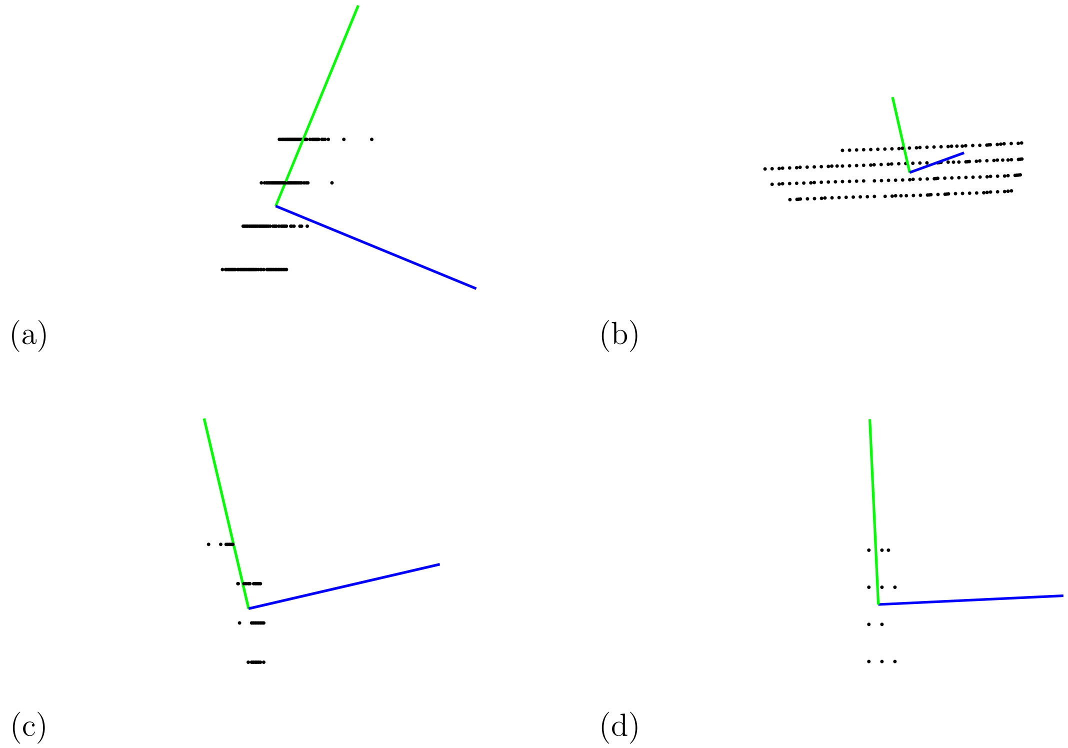

Figure 2.22: Examples of grain boundary normals (blue) and inclinations (green) found using principle component analysis. Black points are grain boundary points extracted directly from the nf-HEDM reconstructions. (a), (c), and (d) are viewed normal to the inclination and grain boundary normal directions, while (b) is tilted off axis to illustrate a different view.

points in 3D space identifies an approximate planar representation of these points with the smallest eigenvalue's eigenvector the plane's normal. While using PCA for this purpose in general is rather crude (grain boundaries are often curved patches, so finding locally flat facets that tile the space is computationally challenging), in this case, most grain boundaries are quite planar, so the approximation is acceptable. Some examples of the results of separating grain boundary points and identifying plane normals and inclination vectors in this way are shown in Fig. 2.22.

One grain boundary inclination was not found using PCA. Examining the grain boundaries depicted in Fig. 2.21, the embedded twin's boundary is comparatively noisier. The reasons for this are twofold. The first is geometry. Because the grain is thin, the overall integrated diffracted intensity is less, which results in difficulties segmenting its scattering during the binarization step. It is also completely surrounded by another orientation, so another solution to the FMM reconstruction could be reconstruction of its 'parent' grain with only minor abuse of the latter's orientation. Further, because the twin is completely embedded, removing a single boundary facet is not possible without some arbitrariness. The second reason is the twin's orientation relationship with its parent. As previously mentioned, these grains are related by a 60° around a common crystallographic $\langle 111\rangle$ axis. By plotting this axis in the laboratory frame, we can see by inspection that the it matches the boundary normal of the longer straight sections of the embedded twin. From this observation, we know that the grain is a 'coherent' twin. Because this is is a well-annealed specimen, the twin's boundary plane should then be well defined by the two orientations of parent and twin, and we can use the orientation resolution of the nf-HEDM microscope to deduce the plane normal and inclination. Doing so, the common crystallographic $\langle 111\rangle$ in the laboratory frame is

$$\hat{n}_{\text{twin}} = \begin{pmatrix} -0.71 \\ 0.38 \\ 0.60 \end{pmatrix}. \tag{2.16}$$

We can easily examine the intersection of the plane with the various cross sections and confirm that it describes the twin's inclination, as in Fig. 2.23. There, the intersection of this plane is shown in green and tracks the twin through the layers examined. Given that each boundary inclination has been found, establishing potential δr displacements for each simplifies to finding ϕ and then applying Eq. 2.15. To a good approximation, the specimen surface normal is in the yz plane, so the important component of the boundary inclination, $\hat{b}$ is the z component, so

$$\phi = \operatorname{sgn}(\hat{b}\cdot\hat{y})\cos^{-1}\hat{b}\cdot\hat{z}. \tag{2.17}$$

Plotting the boundaries while encoding each ϕ value clearly shows which boundaries may need correction. This plot is shown in Fig. 2.24. Again, higher absolute values of ϕ correspond to boundaries more susceptible to errors due to the finite beam height. Without knowing the origin of r, which boundaries satisfy $r > 0$ and could benefit by correction is unknowable. Instead, we can test each boundary's response to correction to determine the magnitude of possible corrective factors. The magnitude of one set of possible corrections are tabulated in Table 2.4 for the boundaries enumerated by Fig. 2.24. Because we do not know the lines for each reconstruction at which $r = 0$ for each reconstructed cross sectional layer, we examine only the cases here for which $r = 40\,\mu$m. From these considerations, we see potential errors of about half a μm or more for boundaries 5, 8, and 9. Boundary 9, the surface of the embedded twin, is the most susceptible to these errors, unsurprising given its ϕ value. We expect the most serious deviations in boundary position to occur for this boundary. Given the linear dependence of δr on r, the relative magnitudes of these values are constant. This scaling relative to the most susceptible boundary (9) is given in column four of Table 2.4. The errors from this effect for most boundaries grow at less than half the rate as the errors associated with boundary 9. All errors are within one reconstruction voxel side-width.

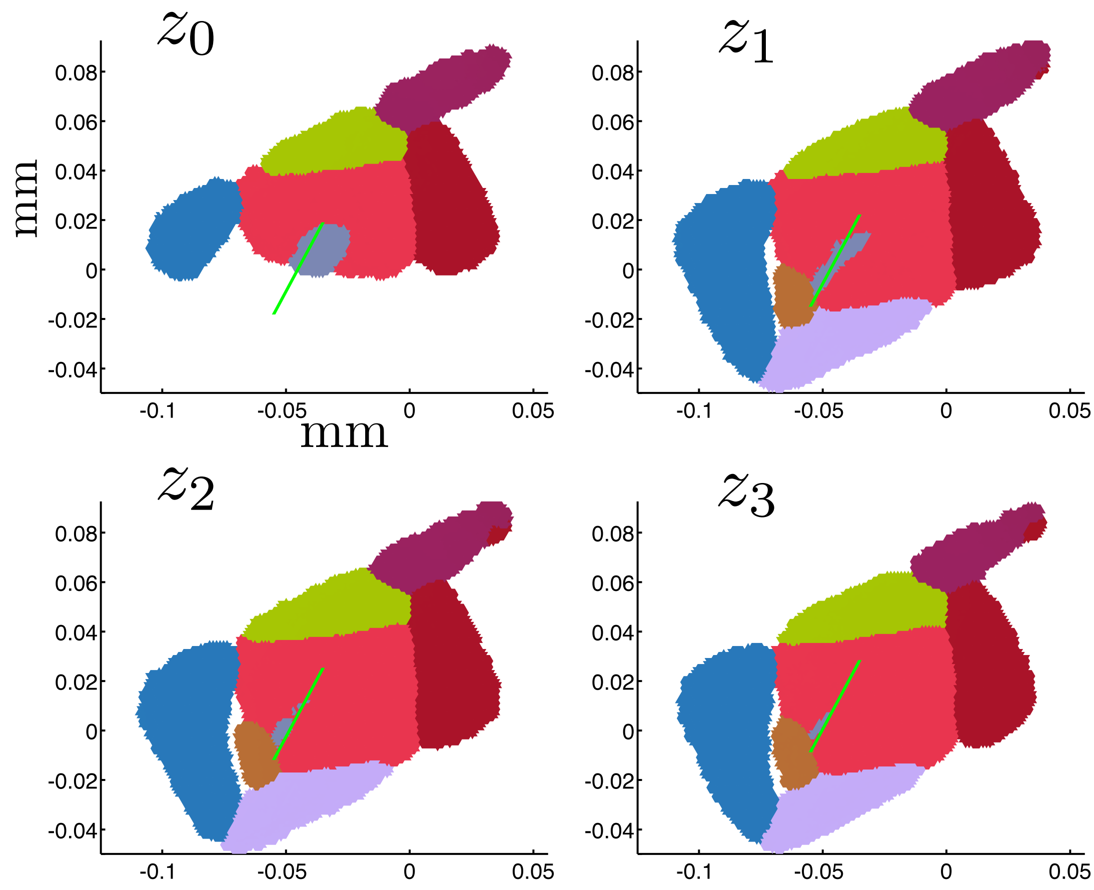

Figure 2.23: Trace of the crystallographic twin plane intersecting the reconstructed cross sections shown. This plane was determined using only the orientation relationship from the embedded twin and its parent, and is seen to track the boundary trace of the embedded twin quite well. This confirms that these Σ-3 related grains are, in fact, coherent twins, and establishes an inclination plane for this grain without using principle component analysis.

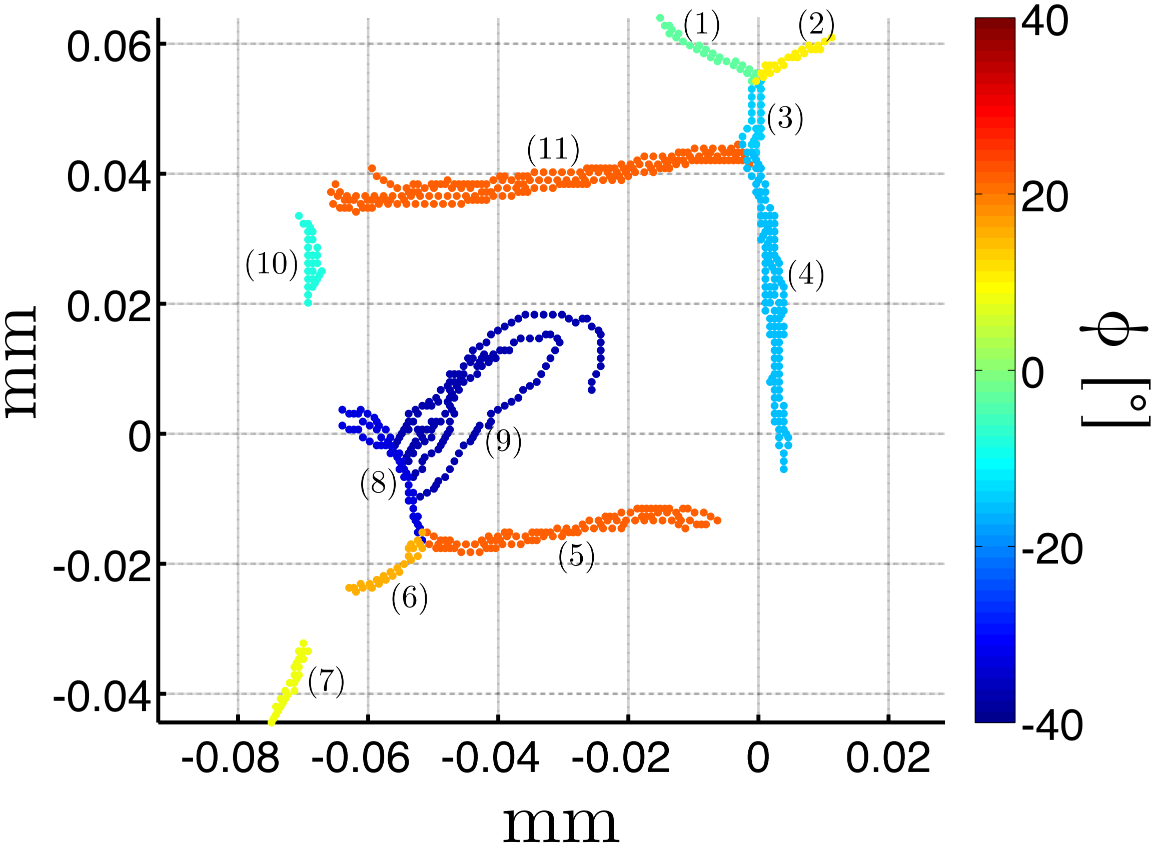

Figure 2.24: The grain boundary traces from Fig. 2.21, colored by ϕ, their grain boundary inclination angles relative to $\hat{y}$. As noted from the previous figure, most boundaries have an inclination close to parallel to $\hat{z}$; boundaries (8) and (9) deviate most strongly from this trend.

Table 2.4: Tabulation of possible errors in assumed surface boundary position due to finite beam height for each boundary depicted in Fig. 2.24. The third column lists some possible values for these errors along $\hat{y}$ assuming each boundary point is 40 μm from the point at which the beam maximum intersects the sample surface. The last column gives possible errors for each boundary as a fraction of the error on boundary (9).

Boundary Number	ϕ [°]	$\delta r\|_{r=40\,\mu\mathrm{m}}$ [μm]	$\|\delta r_i/\delta r_9\|$
1	-3.18	-0.060	0.076
2	3.70	0.186	0.237
3	-14.45	-0.277	0.352
4	-16.10	-0.309	0.393
5	22.50	0.453	0.576
6	16.28	0.319	0.406
7	8.28	0.158	0.201
8	-32.81	-0.686	0.873
9	-36.52	-0.786	1.000
10	-8.43	-0.160	0.204
11	22.38	0.451	0.574

2.2.2.4 Characterization of Errors in Boundary Position

The relative error between the grain boundary positions of the ground truth EBSD surface characterization and the surface reconstructed by nf-HEDM is of particular interest. As mentioned previously, however, deciding what combination of cross sections represents the 'surface' is not obvious. Some combination of z_0 and z_1 is the closest approximation, however, we need to determine (C_{z_0}, C_{z_1}) in order to construct this union. Intuitively, if there is material reconstructed in z_0, the reconstructed orientations from this cross section should be retained over the reconstructed orientations from z_1. Where there are orientations reconstructed in z_1, but not in z_0, these should be retained and combined with the orientations reconstructed from z_0. The proper combination should closely match the surface characterized by EBSD. Accordingly the following heuristic was employed:

Algorithm 1: Return the specimen surface.

```
Data: $z_0$, $z_1$, $C_{z_0}, C_{z_1} \in [0, 1]$, EBSD surface boundaries $\{r_{\mathrm{EBSD}}\}$
Result: Return reconstruction of sample surface, $z_{\mathrm{surface}}$
begin
    $C_{z_0} \leftarrow 0$;
    $C_{z_1} \leftarrow 0$;
    $\delta C \leftarrow 0.01$;
    $K \leftarrow \infty$;
    $C_1 \leftarrow \mathrm{NaN}$;
    $C_2 \leftarrow \mathrm{NaN}$;
    $z_{\mathrm{return}} \leftarrow \varnothing$;
    while $C_{z_0} \leq 1$ do
        while $C_{z_1} \leq 1$ do
            $z_0$_voxels $\leftarrow$ $z_0$_voxels$|_{C_i > C_{z_0}}$;
            $z_1$_voxels $\leftarrow$ $z_1$_voxels$|_{C_i > C_{z_1}}$;
            $z_{\mathrm{surface}} \leftarrow$ $z_0$_voxels $\cup$ [$z_1$_voxels $\notin$ $z_0$_voxels];
            $k$ = GetCost( $\{r_{\mathrm{EBSD}}\}$ , $z_{\mathrm{surface}}$ ) ;
            if $k < K$ then
                $K \leftarrow k$;
                $C_0 \leftarrow C_{z_0}$;
                $C_1 \leftarrow C_{z_1}$;
                $z_{\mathrm{return}} \leftarrow z_{\mathrm{surface}}$;
            end
            $C_{z_1} \leftarrow C_{z_1} + \delta C$
        end
        $C_{z_0} \leftarrow C_{z_0} + \delta C$
    end
    return $(C_0, C_1, z_{\mathrm{return}})$;
end
```

Here, GetCost() was defined to be a function returning the average minimum distance from the set of points $\{r_{\mathrm{EBSD}}\}$ and the centers of the common sides between reconstructed voxels in z_{surface} with disorientation $\geq 5°$. We illustrate these points in Fig. 2.25. Due to the relative differences in physical coordinates of the reconstructed nf-HEDM cross sections and the reconstructed EBSD surface, GetCost() also contained a physical registration step. A grid search of various translations and rotations of the reconstructed nf-HEDM boundary points was conducted and the RMS errors returned for each. The registration with the lowest cost was then returned. This process is outlined in Algorithm 2 in Appendix A. Following use of the algorithm above, C values of $(C_{z_0}, C_{z_1}) = (0.85, 0.82)$ were determined to produce the surface microstructure closest to the undistorted EBSD image. Curves showing slices of the cost space along (x, y) are shown in Fig 2.26, for the globally lowest cost C values,

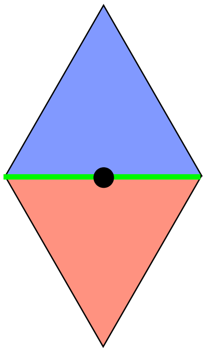

Figure 2.25: A schematic illustrating the definition of an nf-HEDM 'boundary point.' For voxels with disorientation $\geq 5°$, the common side, depicted here in green, defines the 1D boundary for a 2D cross section. The midpoint of this common side, here in black, serves as a useful proxy for the position of the boundary. For a collection of cross sections, these points may be integrated to form a 2D surface.

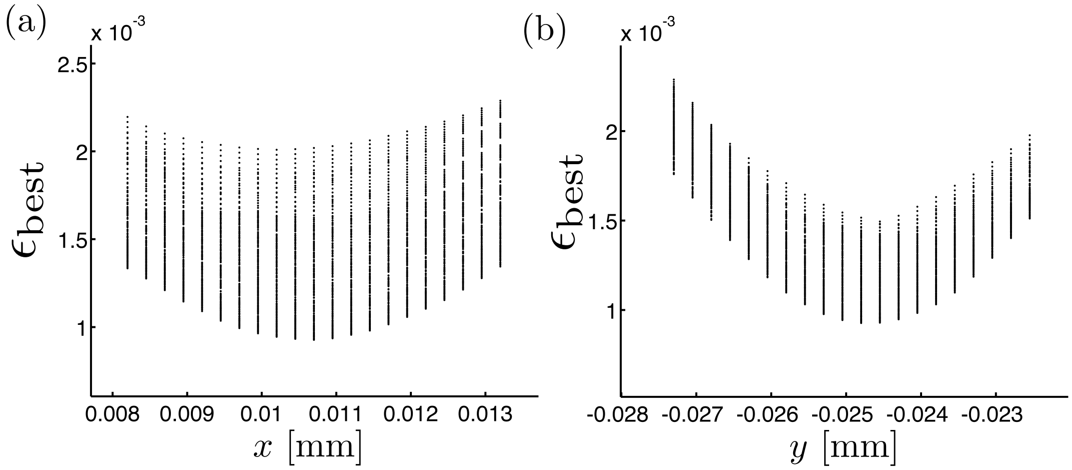

Figure 2.26: These points are values for ϵ_{best} as a function of the optimization parameters x and y, defined in Algorithm 2. Each x and y value has multiple ϵ_{best} values associated with it corresponding to different θ and y or x values respectively. The minimum in ϵ_{best} corresponds to the overall best registration between the HEDM and the EBSD datasets, at the values of C that defines give the nearest surface match.

$(C_{z_0}, C_{z_1}) = (0.85, 0.82)$. A side-by-side comparison of these surfaces is shown in Fig. 2.27, with the boundaries extracted from the HEDM plotted on top of the EBSD fit. Qualitatively, we observe good agreement for most boundaries, with the largest deviations occurring near boundaries 8 and 9, consistent with the previous analysis. Computing, $\langle \Delta \rangle$, the average minimum distance between all N_{H} nf-HEDM boundary

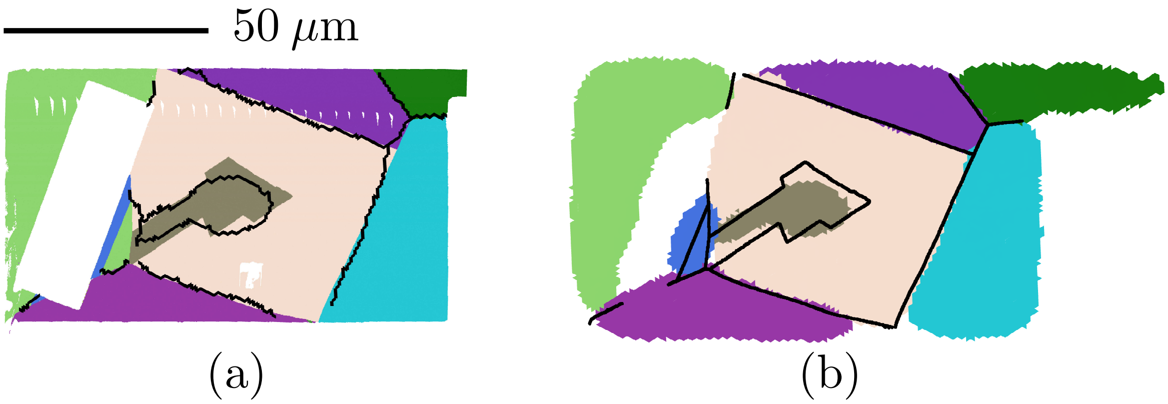

Figure 2.27: (a) EBSD orientation map with boundaries from reconstructed surface layer of nf-HEDM plotted (b) nf-HEDM surface reconstruction with EBSD boundaries plotted. Images plotted at the same scale.

$\langle\Delta\rangle_{\texttt{With Twin}}$	0.93 ± 0.83 μm
$\langle\Delta\rangle_{\texttt{No Twin}}$	0.62 ± 0.58 μm

Table 2.5: Average minimum distance from HEDM boundary center to nearest EBSD boundary pixel.

points $\vec{r}_{H,i}$ and the nearest EBSD sample point, *i.e.*

$$\langle\Delta\rangle = \frac{1}{N_{\mathrm{H}}}\sum_i \min_j |\vec{r}_{\mathrm{H},i} - \vec{r}_{\mathrm{E},j}|, \tag{2.18}$$

gives $\langle\Delta\rangle = 0.93 \pm 0.83$ μm. Of course, by definition, $\langle\Delta\rangle \geq 0$. The distribution of this quantity is shown in Fig. 2.28. Excluding the embedded twin boundary, $\langle\Delta\rangle = 0.62 \pm 0.58$ μm. The magnitude of these errors is about half the voxel side width, so given that discretization errors are on this order, this result should be taken as confirmation that statistically, the spatial measurement of the technique is limited by size of the CCD detector pixels and that boundary positions are determined to within that resolution.

2.2.2.5 Characterization of Orientation Resolution

To compare the orientations reconstructed by the two techniques, the nf-HEDM orientations were rotated into the reference frame of the EBSD sample. To find the rotation that would best achieve this, an optimization was performed that minimized the grain-averaged misorientation between like grains. To accomplish this, a guess

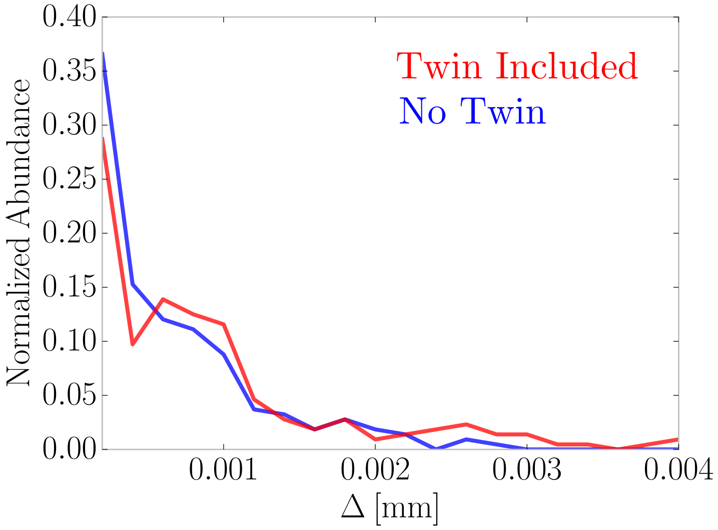

Figure 2.28: The distribution of Δ, the minimum distance from a HEDM boundary point to the nearest EBSD boundary point. The large right tail in the red colored distribution corresponds to boundary segments from grain boundaries 9.

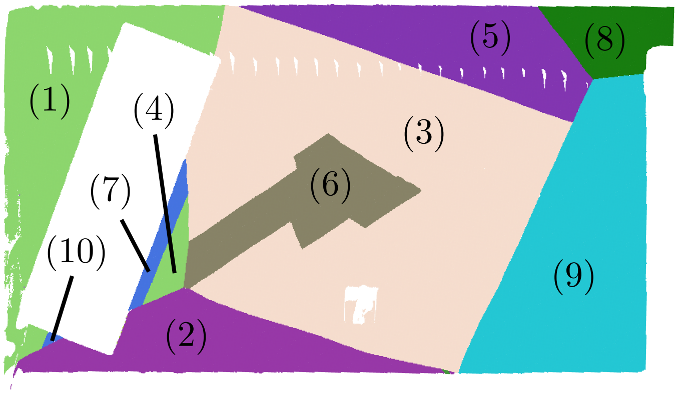

Figure 2.29: Grain identification numbers used in Table 2.6.

Table 2.6: A summary of the registered orientations reconstructed in the nf-HEDM and EBSD measurements. The orientations of the grains reconstructed by HEDM are transformed into the reference frame of the EBSD reconstructed orientations by applying a transformation that minimizes the sum of the misorientations between the two states, excluding grain 4.

Grain ID	Eulers $_{\text{HEDM}}$ (ZXZ)	Eulers $_{\text{EBSD}}$ (ZXZ)	IGM$_{\text{HEDM}}$ [°]	IGM$_{\text{EBSD}}$ [°]	Δg [°]
1	(77.63, 31.57, 275.64)	(78.07, 31.61, 275.26)	0.049 ± 0.030	0.24 ± 0.11	0.2347
2	(295.71 27.54 78.77)	(295.67 27.33 79.00)	0.043 ± 0.023	0.21 ± 0.11	0.2951
3	(52.65 50.79 335.93)	(52.59 50.65 335.90)	0.049 ± 0.030	0.24 ± 0.11	0.1664
4	(210.00 21.20 184.79)	(78.15 31.61 275.16)	0.036 ± 0.024	0.24 ± 0.11	59.91
5	(281.14 26.86 97.03)	(281.09 26.69 97.13)	0.06 ± 0.027	0.22 ± 0.10	0.1809
6	(17.42 3.23 333.42)	(18.38 3.12 332.46)	0.022 ± 0.0092	0.20 ± 0.095	0.1202
7	Not Found	(209.18 20.92 185.75)	—	0.30 ± 0.16	—
8	(161.75 35.06 158.17)	(161.54 35.06 158.53)	0.38 ± 0.20	0.26 ± 0.13	0.2284
9	(157.49 40.17 233.12)	(157.42 40.15 233.25)	0.038 ± 0.026	0.25 ± 0.11	0.0917
10	Not Found	(209.25 20.95 185.74)	—	0.36 ± 0.22	—

for the optimum transformation was made by using the known spatial registration between states. Then, 1.5 $\times 10^6$ small random rotations about random axes were generated and composed with the guess. The transformation that minimized misorientation between the grain averaged orientations for each grain pair was retained and applied to the HEDM orientations. The transformation found corresponds to a 118.15° rotation about the axis

$$\hat{n}_{\text{axis}} = \begin{pmatrix} -0.002677 \\ -0.000064 \\ -0.999996 \end{pmatrix}, \tag{2.19}$$

very close to a rotation purely about $\hat{z}$. Grain 4, as enumerated in Fig. 2.29, was not used to determine the optimum orientation transformation, because the orientation reconstructed in the HEDM measurement is that of its Σ-3 related neighbor grain. The transformed grains were then directly compared to the orientations reconstructed by the EBSD measurement.

Examining Table 2.6 shows good agreement between the two datasets. Excluding grain 4, the mean misorientation, Δg, between average grain orientations is $0.188 \pm 0.070°$. Grain 4 illustrates an interesting case in which the orientation reconstructed from the HEDM data is that of a Σ-3 connected neighbor and corresponds to a misorientation of $\sim 60°$. Intragranular misorientation (IGM) measures the average misorientation between a grain's constituent voxels and its average orientation. Generally, smaller IGM is associated with grains reconstructed from HEDM data. One outlier with particularly high IGM for the HEDM data set is grain 8, the grain forming 'antenna' feature. This grain served as the handle used by micromanipulators which were used to place the specimen on the mount, so we associate higher IGM in this region to deformation caused by gripping the specimen. Excluding that grain, average IGM for the HEDM data set was $0.0437 \pm 0.0134°$, nearly an order of magnitude smaller compared to the EBSD average IGM of $0.2530 \pm 0.0470°$. Given that these grains were well annealed during sample preparation, low IGM is expected.

2.2.2.6 Angular resolution study

The orientation resolution of the HEDM measurement depends on the size of the angular integration used to perform the reconstruction. When a diffracted peak is captured on the detector during an integration window $\Delta\omega$, it is known that the reciprocal lattice vector corresponding to that peak intersected the Q-locus and fulfilled the Laue condition at some point during $\Delta\omega$. The search for a consistent orientation during the reconstruction then simplifies to finding a lattice orientation whose reciprocal vectors, if rotated over the entire angular range considered, result in scattering within the collected $\Delta\omega$ bins. Narrowly defining these bins limits the possible lattice orientations that obey these criteria, thereby providing increased orientation resolution. But what is the dependence on this orientation resolution on the size of $\Delta\omega$?

In this section, we evaluate this question using IGM as a proxy for the orientation resolution. The specimen microstructure were reconstructed with $\Delta\omega = \{10°, 4°, 2°, 1°, 0.5°, 0.2°\}$. The speciment surface was reconstructed by unionizing z_0 and z_1 in the method previously described, and the IGM was computed for each grain. These results are tabulated in Table 2.8 and plotted in Fig. 2.31. Reconstructions with $\Delta\omega = 0.2°$ were of poor quality and were ignored for the analysis. Poor image segmentation is thought to be the cause. From Fig. 2.8, there is an approximately linear relationship between $\Delta\omega$ and the IGM. Toward the lower end of $\Delta\omega$, there is a steepening of the slope, illustrating an increased rate of angular resolution improvement per marginal change in $\Delta\omega$. This particular feature could be due to specific implementation of this FMM reconstruction, or an effect related to the density of possible states in orientation space that result in the observed scattering. Either way more work is necessary to determine the cause of this feature.

Given that below $\Delta\omega = 1°$ IGM continues to decrease, we take the natural mosaic spread of the grains measured to be below 0.05°, the IGM value at $\Delta\omega = 1°$. This measurements sets the upper bound for orientation resolution of nf-HEDM at 0.05°, for the case where grains are perfect crystals. Establishing a precise value would involve obtaining reliable reconstructions with $\Delta\omega < 0.5°$, then finding an IGM value for each grain that does not change when $\Delta\omega$ is made smaller, essentially measuring the mosaic spread. With known mosaic spread, the difference in IGM can be attributed to finite measurement resolution. Boundary position fidelity is generally better with smaller $\Delta\omega$. For each reconstructed surface, $\langle\Delta\rangle$ was computed; the results are tabulated in Table 2.7. The apparent improvement at $\Delta\omega = 10°$ compared to $\Delta\omega = 4°$ is misleading because the corresponding reconstruction lacks definition

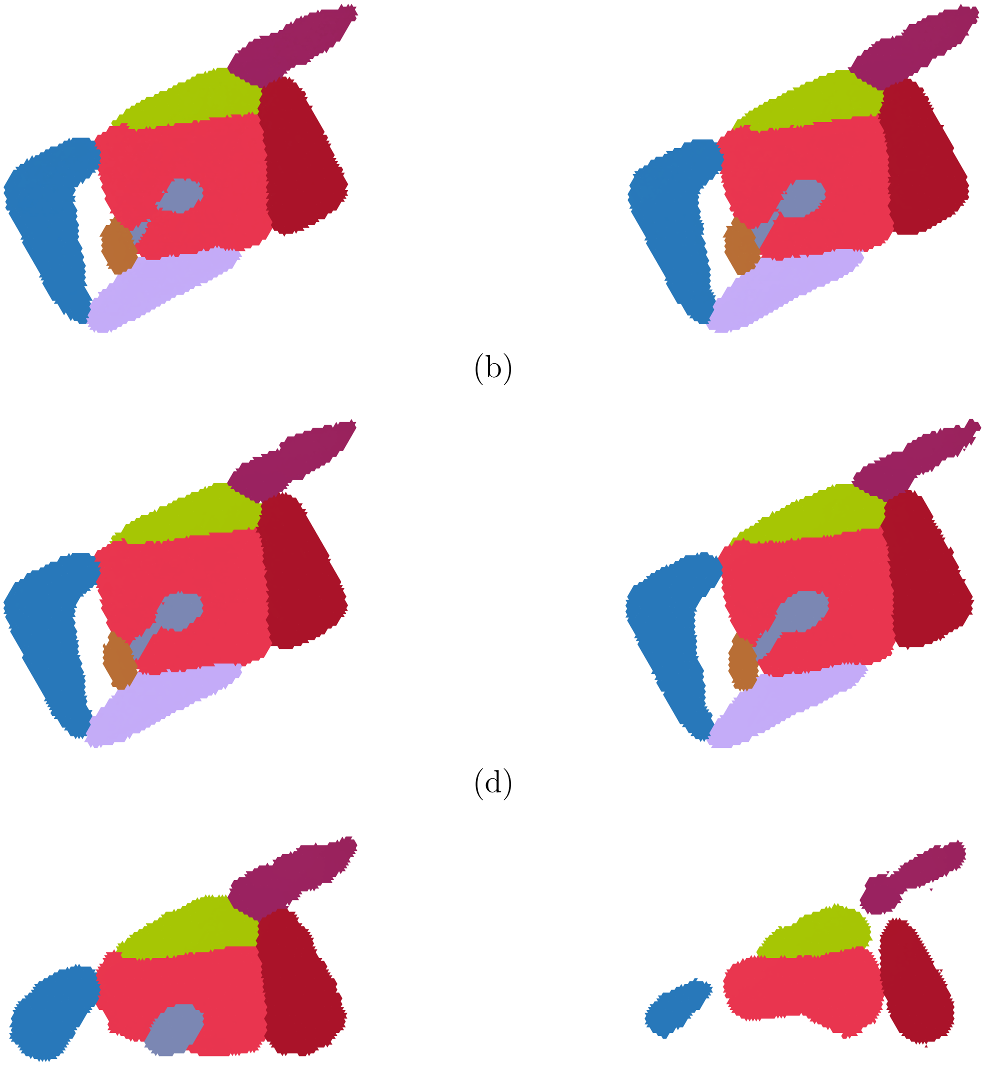

(a) (b) (c) (d) (e) (f)

Figure 2.30: Merged surface reconstructions using angular integrations of (a) 10°, (b) 4°, (c) 2°, (d) 1°, (e) 0.5°, and (f) 0.2°. Notably (e) shows only the z_0 contribution to the surface whereas all others illustrate the union of z_0 and z_1; the absence of the lower part of the reconstruction does not indicate lack of reconstruction quality. On the other hand, the reconstruction quality at (f) began to deteriorate resulting in unreconstructed features. Difficulty in peak segmentation at lower intensities is presently thought to be the culprit.

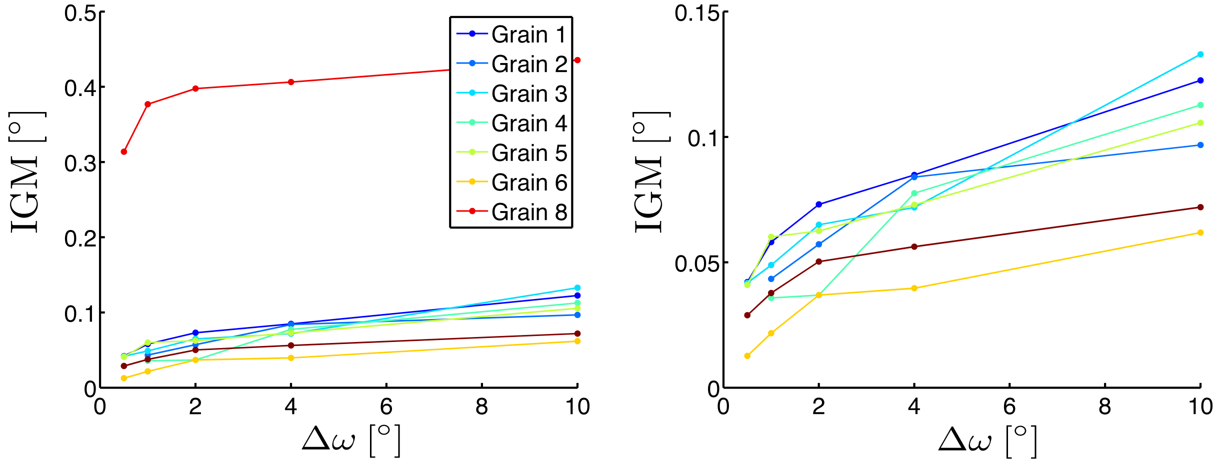

Figure 2.31: Plots of the intragranular misorientation (IGM) as a function of angular integration interval size, $\Delta\omega$. Here, IGM is a proxy for orientation resolution of the measurement, given that the reconstructed grains should have very low intrinsic mosaic spread. Grain 8 was the micromanipulator handle used to place the specimen onto the mount, so its higher IGM is ascribed to deformation accumulated by this gripping. At right, the results from grains 1 through 6 are plotted. Even at $\Delta\omega = 4°$ orientation resolution is confirmed to be $< 0.1°$. These reconstructions all used $L0$, $L1$, and L_2, at $|Q_{max}1.4| \leq 16$Å, with 1.41 μm sidewidth voxels.

Table 2.7: Average error in surface grain boundary position as a function of $\Delta\omega$. The value at 10°

$\Delta\omega$ [°]	$\langle\Delta\rangle$ [μm]
10°	0.91 ± 1.0
4°	0.99 ± 1.0
2°	0.96 ± 0.97
1°	0.93 ± 0.83

of the embedded twin, as evident from Fig. 2.30(a). The distributions of Δ for these reconstruction are quite noisy and lack statistical significance, but a general trend toward increased accuracy at lower $\Delta\omega$ can be observed.

2.2.2.7 Sparse Signal Study

The nf-HEDM measurement is quite time consuming to perform, requiring integration times on the order of 2.5-3 $\frac{\text{s}}{\circ}$, for a total collection time of

$$t = \frac{3\,\text{s}}{\circ} \times \frac{180°}{L_i} \times \frac{2 \times L_i}{\text{cross section}} \times \frac{100\text{ cross sections}}{\text{volume}} = 30\text{ hours/volume} \qquad (2.20)$$

Table 2.8: Summary of the IGM values plotted in Fig. 2.31 as a function of angular integration size. *For the 0.5° reconstruction, only z_0 was used.

Grain #	IGM [°] at $\Delta\omega = 10°$	$\Delta\omega = 4°$	$\Delta\omega = 2°$	$\Delta\omega = 1°$	$\Delta\omega = 0.5°$*
1	0.123 ± 0.089	0.085 ± 0.047	0.073 ± 0.045	0.058 ± 0.042	0.042 ± 0.020
2	0.097 ± 0.078	0.084 ± 0.044	0.057 ± 0.035	0.043 ± 0.023	—
3	0.13 ± 0.059	0.072 ± 0.035	0.065 ± 0.033	0.049 ± 0.030	0.042 ± 0.023
4	0.113 ± 0.055	0.078 ± 0.037	0.037 ± 0.033	0.036 ± 0.024	—
5	0.106 ± 0.052	0.073 ± 0.034	0.063 ± 0.030	0.060 ± 0.027	0.041 ± 0.022
6	0.062 ± 0.041	0.040 ± 0.019	0.037 ± 0.012	0.022 ± 0.0092	0.013 ± 0.0078
8	0.436 ± 0.255	0.41 ± 0.21	0.40 ± 0.22	0.38 ± 0.20	0.31 ± 0.13
9	0.072 ± 0.043	0.056 ± 0.029	0.050 ± 0.025	0.038 ± 0.026	0.029 ± 0.016

of dedicated beamtime. While improving machine brilliance can cut down image integration times, exploring the density of data required for proper reconstruction also provides a possible outlet for time savings. Toward that goal, the quality of the reconstruction as a function of the amount of input data is examined. Reconstructions were performed using 1/4, 1/10, and 1/18 of the input signal, equally sampled within the angular range $\Delta\omega \in [-180°, 180°]$. Results are tabulated in Table 2.9 and shown in Fig. 2.32. Using every fourth image collected for the reconstruction produces results very close in quality to the full signal reconstruction, with only minor increases to boundary position errors and IGM. These differences are small enough to motivate an ambitious experimenter to consider this measurement collection mode as a possibility in the future. Using every 10th image collected increases the noise of the reconstruction, both with respect to boundary localization and orientation determination. The width the boundary error distribution broadens considerably, and IGM increases from full data case by a factor two. This corresponds to a 2× decrease in orientation resolution at the worst case. Still the microstructure is reconstructed with the proper orientations, and general grain shapes are preserved. This collection mode would be a good for modelers needing an input structure without intricate orientation gradients or the need to represent non-convex or re-entrant grain shapes in a very precise way. Reconstructing using every 18th image does not provide sufficient diffraction data to reconstruct every grain, though the grains that are reconstructed have high C and match shapes well. At this level of signal sparsity, reconstruction is not guaranteed, so use of this case is not advised.

2.2.2.8 L$_i$ Study

A degree of arbitrariness exists in the choice of rotation-axis to sample distances (L_i) used in the collection of experimental data. In practice, a distance of $L_0 \in [3.0, 6.5]$ mm has been the historical range chosen as the working distance for the first detector, with subsequent detectors positions spaced at distances between 1 and 2 mm from

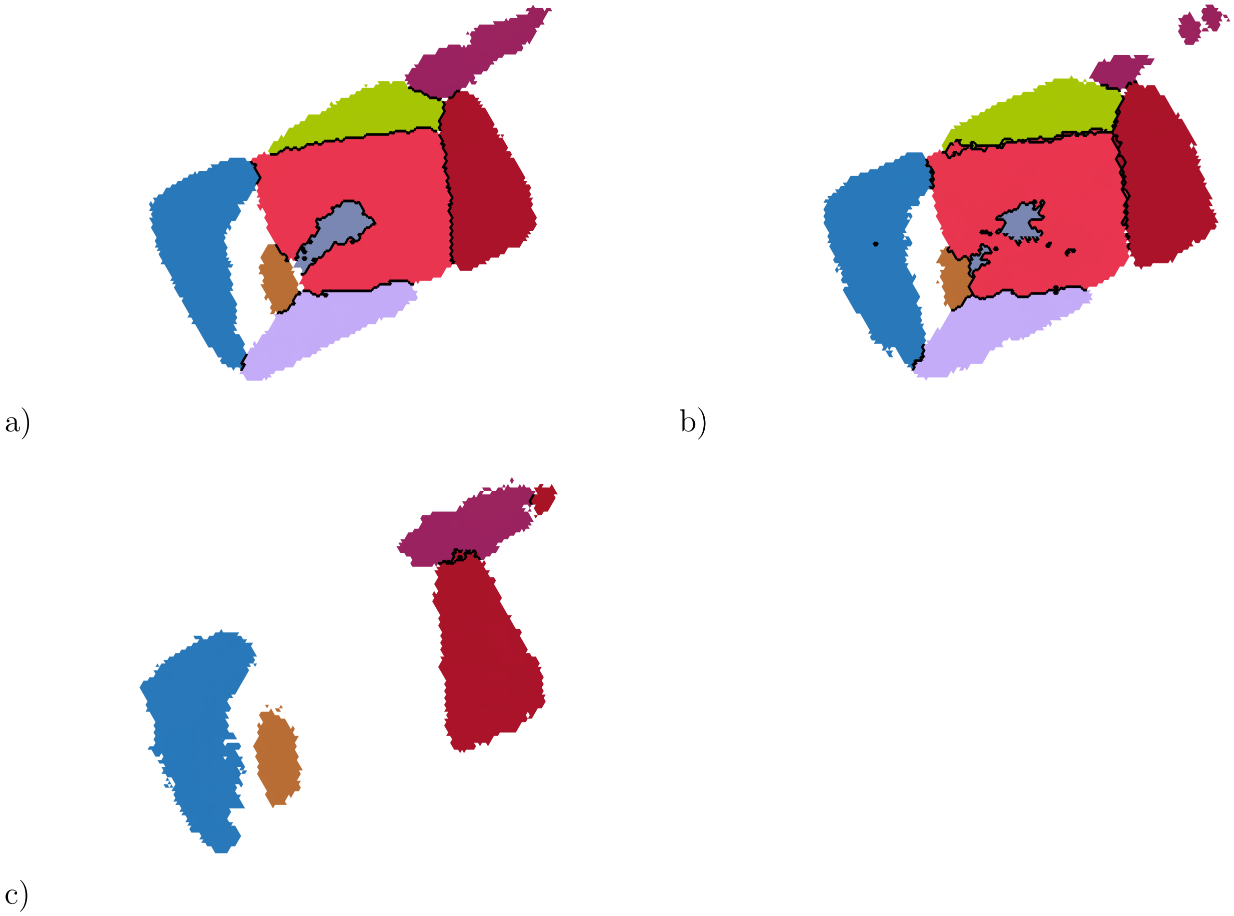

Figure 2.32: Reconstructions of the specimen using (a) every fourth $\Delta\omega$, (b) every tenth $\Delta\omega$ and (c) every eighteenth $\Delta\omega$.

the previous spacing. In the limit of an extreme near field case with the detector only a few microns from a sample, the only information encoded in the location of the diffraction on the detector is grain's position; η and 2θ information is lost. In the far field case, somr grain position information is lost in favor of more accurate η and 2θ measurement. When then is the optimal range for a spatially sensitive near field measurement?

A careful answer must depend on sample extent. Assuming a cylindrical sample of radius r centered on the rotation axis, a grain at the specimen's periphery will precess, giving an effective minimum distance of $L_i - r$ and an effective maximum distance of $L_i + r$. If r and L_i are of the same order, diffracted beams originating from various $\Delta\omega$ intervals see different L_i. Naively, one could say that a good set of L_i would be one for which a grain's diffraction still encodes η and 2θ information when it is at its closest to the detector and still encodes position information when it is at its farthest away. Such an answer, however, discounts possible situations that utilize good orientation information from some peaks and good spatial information from others. Thus, it is hard to say what a good approach should be without experimentation.

In this section we attempt to gain initial insights toward this problem's solution by evaluating reconstructions of the specimen microstructure performed using a variety of L_i configurations. Data were taken with $\{L_0, L_1, L_2, L_3, L_4\} = \{5.0, 6.5, 8.0, 9.5, 11.0\}$ mm, with the reconstructions used to produce the Fig. 2.27 utilizing $i \in \{0, 1, 2\}$. Reconstructions were also performed with fewer detectors ($i \in \{0, 1\}$), with large spacing and fewer detectors ($i \in \{0, 4\}$), with moderate spacing and fewer detectors ($i \in \{0, 2\}$), with greater initial rotation-axis-to-detector distance, ($i \in \{2, 3, 4\}$), and in a highly constrained manner ($i \in \{0, 1, 2, 3, 4\}$). Because the initial reconstruction with $i \in \{0, 1, 2\}$ was optimized many times using the iteration procedure outlined in Fig. 2.15, $\mathbf{E}$ was highly optimized for reconstruction with that parameter set. Reconstruction using any combination of detectors that included L_3 and L_4 required extending $\mathbf{E}$ to include the rotation axis projections onto these detectors and their distances to the rotation axis. To accomplish this take, the rotation axis projections were extrapolated onto L_3 and L_4 from their positions on L_0, L_1, and L_2. Each combination listed above was then independently optimized one time using the PMC method at $Q_{\text{max}} = 16$Å. These parameter sets were optimized only one time because parameter sets $i \in \{0, 1, 2\}$ were already highly optimized and provided a good initial starting point and conducting PMC steps is computationally time consuming. After reconstruction, the surface was reconstructed by unionizing z_0 and z_1 as previously described. Each reconstruction was then evaluated according to Δ and IGM metrics. Reconstructions performed that utilized only $i \in \{1, 2, 3\}$ underwent no PMC step before reconstruction and subsequent evaluation.

Resulting reconstructions are plotted in Fig. 2.33. While the results that utilize predominately pre-optimized detector geometries display high fidelity to the underlying manifest microstructure, the results of those reconstructions utilizing L_3 and L_4

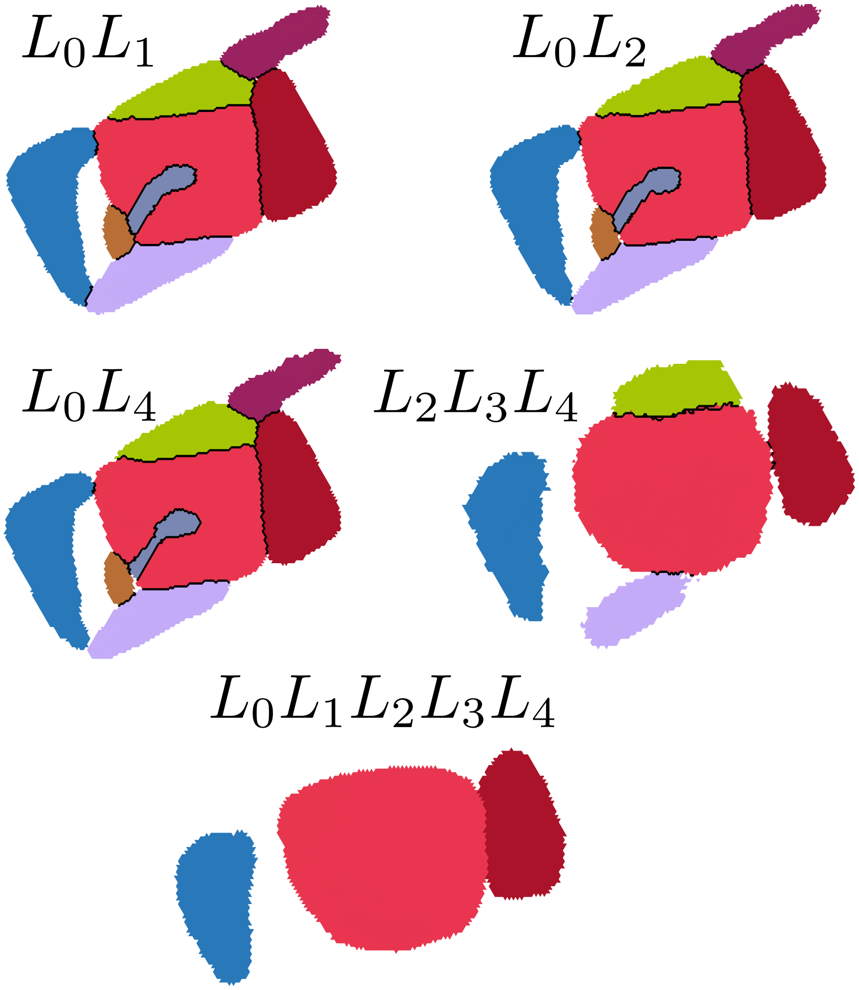

Figure 2.33: Results of the reconstruction using various combinations of L_i. As a general rule, configurations that used already optimized detector geometries (or already optimized detector geometries combined with with one singly optimized detector geometry) produced higher fidelity reconstructions.

illustrate the importance of using many optimization steps beginning at low $Q_{\max}$. For instance, speaking from this experimenter's experience, the reconstruction which utilized data from L_2, L_3 and L_4 is of poor quality when compared to historical precedents at working distances 8.0 mm through 11 mm. This reflects not the variation in L_i, but the lack of systematic optimization. Similarly, it is unclear whether the poor fidelity of the the highly constrained reconstruction represents the result of adding constraints or subpar optimization. Improving these reconstructions to the point where proper comparison can be made would require considerable man hours and computational time better spent elsewhere, and as such they will not be considered further.

Qualitatively, the differences between the remaining three reconstructions manifest most obviously in the morphology of the embedded twin. In fact, reconstructions utilizing L_0L_1 and L_0L_2 match the width of the long straight section in the middle of the twin better than the original reconstruction utilizing $L_0L_1L_2$. This may be because using fewer constrains reduces the likelihood that the weak intensity from the thin section of the twin is mis-segmented during the peak binarization or not struck by simulated scattering due to some small $\delta\mathbf{E}$ not optimized away. Increasing the distance between detectors appears to have the effect of better defining the end of the twin relative to that narrower gauge region. By incrasing the distance between detectors, small errors in reconstructed orientation can manifest in simulated scattering missing the 'intended' peak on the second detector, thereby making proper reconstruction more sensitive to $\delta\mathbf{E}$ errors. The quantiative results from these reconstructions are tabulated in Table. 2.10.

Table 2.9: Results of reconstructing the surface microstructure using subsets of the complete diffraction data.

Grain # full signal	IGM [°]	Grain # 1/4 signal	IGM [°]	Grain # 1/10 signal	IGM [°]	Grain # 1/18 signal	IGM [°]
all	$\langle\Delta\rangle = 0.93 \pm 0.83$	all	$\langle\Delta\rangle = 0.97 \pm 1.00$	all	$\langle\Delta\rangle = 1.2 \pm 1.2$	all	—
1	0.058 ± 0.042	1	0.062 ± 0.034	1	0.10 ± 0.026	1	0.11 ± 0.05
2	0.043 ± 0.023	2	0.064 ± 0.032	2	0.076 ± 0.026	2	—
3	0.049 ± 0.030	3	0.058 ± 0.039	3	0.12 ± 0.062	3	—
4	0.036 ± 0.024	4	0.031 ± 0.028	4	0.034 ± 0.021	4	0.11 ± 0.060
5	0.060 ± 0.027	5	0.061 ± 0.028	5	0.13 ± 0.038	5	—
6	0.022 ± 0.0092	6	0.027 ± 0.020	6	0.068 ± 0.032	6	—
8	0.38 ± 0.20	8	0.37 ± 0.21	8	0.49 ± 0.20	8	0.26 ± 0.16
9	0.038 ± 0.026	9	0.078 ± 0.016	9	0.093 ± 0.030	9	0.17 ± 0.23

Table 2.10: Results of reconstructing the surface microstructure using various L_i combinations.

Grain # L_0L_1	IGM [°]	Grain # L_0L_2	IGM [°]	Grain # L_0L_4	IGM [°]
all	$\langle\Delta\rangle = 1.00 \pm 0.92$	all	$\langle\Delta\rangle = 1.1 \pm 1.1$	all	$\langle\Delta\rangle = 1.1 \pm 1.1$
1	0.052 ± 0.032	1	0.042 ± 0.028	1	0.048 ± 0.028
2	0.040 ± 0.023	2	0.037 ± 0.018	2	0.034 ± 0.012
3	0.048 ± 0.019	3	0.042 ± 0.025	3	0.043 ± 0.024
4	0.025 ± 0.020	4	0.031 ± 0.028	4	0.045 ± 0.023
5	0.048 ± 0.019	5	0.053 ± 0.019	5	0.13 ± 0.038
6	0.017 ± 0.0085	6	0.020 ± 0.012	6	0.016 ± 0.0072
8	0.32 ± 0.14	8	0.32 ± 0.13	8	0.33 ± 0.14
9	0.036 ± 0.021	9	0.020 ± 0.0038	9	0.018 ± 0.010

Chapter 3

Sensitivity and Error Analysis of nf-HEDM

3.1 General Approach

The lack of uniqueness of the reconstructed microstructure given fixed input data motivates the careful experimenter to understand the reconstruction's dependence on $\delta\mathbf{E}$ as well as the fundamental limits of the technique. Understanding this dependence requires careful analysis of the how the reconstructed microstructure varies as a function of perturbations in the various components of $\mathbf{E}$. To perform such an analysis with precision, these perturbations must be exactly determined and the physically manifest $\mathbf{E}$ known exactly. For this reason, a simulated experiment was used to examine this sensitivity.

First a synthetic polycrystalline microstructure was created to serve as the 'ground truth' specimen for this work. Readers familiar with the image processing concept of a phantom will recognize this synthetic microstructure as a phantom for the nf-HEDM FMM reconstruction. From this phantom microstructure, Bragg diffraction was simulated using known experimental parameters and detector geometry. This simulated scattering was used to create simulated experimental data of the same form that might be taken from a synchrotron experiment. These data were then processed in the same manner as is typical for nf-HEDM reconstruction, complete with image segmentation. Reconstructions were performed following perturbations of the various components of $\mathbf{E}$, after which each reconstruction was characterized. These characterizations were then compared and conclusions drawn about each component's ability to influence reconstruction fidelity or precision. First the theoretical underpinnings of this analysis will be discussed, after which the details of the synthetic microstructure creation, scattering simulation, and resulting reconstruction will be covered. Following these topics, the sensitivity results will be discussed and conclusions drawn.

3.2 Theory

To examine the sensitivity of the FMM reconstruction to perturbations of its input parameters, error analysis will be used on the effective action of the reconstruction. We will begin by building a single variate case for intuition and then building the full multivariate expressions. Our simulation will utilize two sample-to-detector distances, (L_0 and L_1), so ignoring relative tilts of the detector, we have

$$\mathbf{E} = \{j_0, k_0, L_0, j_1, k_1, L_1\}, \tag{3.1}$$

a total of six constituent elements for $\mathbf{E}$.

3.2.1 Single Variate Case

First, we will examine a case where the FMM reconstruction takes only one parameter, E, and acts as a function on that parameter, namely,

$$f_{\text{FM}}(E) = \{u_0, u_1, .., u_N\} \tag{3.2}$$

where u_i represents the value of some objective function that quantifies the fidelity of the reconstruction with respect to its actual physical manifestation. For example, one possible choice of objective function could be root mean square error of the boundary center of mass (COM) position, such that

$$u_i = \sqrt{[\mathbf{r}_i - \tilde{\mathbf{r}}_i]^2}, \tag{3.3}$$

where $\mathbf{r}$ is the reconstructed boundary COM and $\tilde{\mathbf{r}}$ is the physical boundary COM. Other choices of objective function are possible, and indeed, various objective functions may be combined to piece together the components of the u-tuple. We will require, however, that if E_0 represents the physical experimental parameter space that actually created the scattering to be reconstructed, then

$$f_{\text{FM}}(E_0) = \{0, 0, ..., 0\} \tag{3.4}$$

and the reconstruction should reproduce a true and physical representation of the microstructure at the various minima of the chosen objective functions. Let us assume that the components of the u-tuple can be considered separately, *i.e.*

$$f_i(E) = u_i. \tag{3.5}$$

Say that during a reconstruction, perfect reproduction of E_0 was not possible, but one was close, to within some $E = E_0 + \delta E$, with δE a small displacement. In one dimension, this permits a Taylor expansion around E_0 for each component f_i, such that

$$f_i(E_0 + \delta E) = f(E_0) + (\delta E) f'(E_0) + \frac{1}{2}(\delta E)^2 f''(E_0) + ... \tag{3.6}$$

By construction, $f_i(E_0) = 0$, so $f(E_0)$ disappears leaving

$$f_i(E_0 + \delta E) = (\delta E) f'(E_0) + \frac{1}{2}(\delta E)^2 f''(E_0) + ... = u_i. \tag{3.7}$$

Taking only the linear terms, we recover

$$|f_{\rm FM}(E_0 + \delta E)| = |\vec{u}| = \left[\sum_i \left[(\delta E) \frac{\partial f_i(E)}{\partial E}\bigg|_{E=E_0} \right]^2 \right]^{\frac{1}{2}}, \tag{3.8}$$

the elementary quadrature of errors formula, for the special case that the components of u have the same units and form a vector space. In theory then, knowing the $\partial f_i/\partial E$s should be sufficient for the computation of u_i if δE is known. In reality, δE is *not* known, but we leave aside this complication for now, as it may be possible to estimate it.

3.2.2 Multivariate Case

Now we consider the higher dimensional case, where $f_{\rm FM}$ is a function of all detector geometry parameters explicitly, *i.e.*

$$f_{\rm FM}(j_0, k_0, L_0, j_1, k_1, L_1). \tag{3.9}$$

Applying the multivariate Taylor expansion for each component then gives

$$f_i(j_0{+}\delta j_0, k_0{+}\delta k_0, \ldots) = \delta j_0 \frac{\partial f_i}{\partial j_0} {+} \delta k_0 \frac{\partial f_i}{\partial k_0} {+} \ldots {+} \frac{1}{2} \begin{bmatrix} \delta j_0 & \delta k_0 & \ldots \end{bmatrix} \mathbf{H}^i \begin{bmatrix} \delta j_0 & \delta k_0 & \ldots \end{bmatrix}^{\mathbf{T}} {+} \ldots \tag{3.10}$$

with $\mathbf{H}$, the Hessian matrix, given by

$$\mathbf{H}^i_{\alpha\beta} = \partial_\alpha \partial_\beta f_i(j_0, k_0, L_0, j_1, k_1, L_1) \tag{3.11}$$

for $\alpha, \beta \in \{j_0, k_0, L_0, j_1, k_1, L_1\}$. Defining

$$\vec{x} = j_0 \hat{j_0} + k_0 \hat{k_0} + L_0 \hat{L_0} + j_1 \hat{j_1} + k_1 \hat{k_1} + L_1 \hat{L_1} \tag{3.12}$$

and

$$\delta\vec{x} = \delta j_0 \hat{j_0} + \delta k_0 \hat{k_0} + \delta L_0 \hat{L_0} + \delta j_1 \hat{j_1} + \delta k_1 \hat{k_1} + \delta L_1 \hat{L_1} \tag{3.13}$$

allows for writing the above a bit more succinctly as

$$f_i(\vec{x} + \delta\vec{x}) = \delta\vec{x} \cdot \vec{\nabla} f_i + \frac{1}{2} \delta\vec{x}\, \mathbf{H}^i\, \delta\vec{x}^{\,\mathbf{T}} + \ldots \tag{3.14}$$

To second order we expect errors associated with the detector to be of magnitude

$$|f_i(\vec{x} + \delta\vec{x})| = |\vec{u}| = \left[\sum_i \left(\delta\vec{x} \cdot \vec{\nabla} f_i + \frac{1}{2} \delta\vec{x}\, \mathbf{H}^i\, \delta\vec{x}^{\,\mathbf{T}} \right)^2 \right]^{\frac{1}{2}}. \tag{3.15}$$

3.2.3 Physical Basis

While the approach outlined above makes sense from a practitioner's point of view, the basis set $E = \{j_0, k_0, L_0, j_1, k_1, L_1\}$ doesn't explicitly capture the effects of changing relative positions between the two detectors, a quantity thought to influence reconstruction quality. The diffracted beams from the sample radiate in straight rays - any difference in the relative positions of the detectors will influence the intersection point of these rays relative to experimentally measured peaks. The forward model optimizes peak overlap and will compensate by changing orientation and boundary position. Define the projection of the vector from the forward model's origin to the projection of the rotation axis on a given detector plane

$$\vec{r_i} = (j_i, k_i) \tag{3.16}$$

for $i \in \{0, 1, ..., N\}$ where $N + 1$ is the total number of detector distances. For two detector distances then, we may describe the system totally by further defining the detector center of mass vector to be

$$\vec{R} = \left(\frac{1}{2}(j_0 + j_1), \frac{1}{2}(k_0 + k_1), \frac{1}{2}(L_0 + L_1)\right) \tag{3.17}$$

and the relative displacements

$$\Delta\vec{r} = r_1 - r_0 = (j_1 - j_0, k_1 - k_0, L_1 - L_0). \tag{3.18}$$

We then characterize the action of the forward model by

$$f_{\mathrm{FM}}(\vec{x}), \tag{3.19}$$

for $\vec{x} = (R_j, R_k, R_L, \Delta r_j, \Delta r_k, \Delta r_L)$ using this basis. To function within this framework, we must estimate values for the six first order derivatives of f_i,

$$\frac{\partial f_i}{\partial R_j}, \frac{\partial f_i}{\partial R_k}, ..., \frac{\partial f_i}{\partial(\Delta r_L)} \tag{3.20}$$

as well as the matrix of partials making up the second order contributions,

$$\mathbf{H}^i = \begin{pmatrix} \frac{\partial^2 f_i}{(\partial \Delta r_j)^2} & \frac{\partial^2 f_i}{\partial(\Delta r_j)\partial(\Delta r_k)} & \frac{\partial^2 f_i}{\partial(\Delta r_j)\partial(\Delta r_L)} & \frac{\partial^2 f_i}{\partial(\Delta r_j)\partial R_j} & \frac{\partial^2 f_i}{\partial(\Delta r_j)\partial R_k} & \frac{\partial^2 f_i}{\partial(\Delta r_j)\partial R_L} \\ & \frac{\partial^2 f_i}{\partial(\Delta r_k)^2} & \frac{\partial^2 f_i}{\partial(\Delta r_k)\partial(\Delta r_L)} & \frac{\partial^2 f_i}{\partial(\Delta r_k)\partial R_j} & \frac{\partial^2 f_i}{\partial(\Delta r_k)\partial R_k} & \frac{\partial^2 f_i}{\partial(\Delta r_k)\partial R_L} \\ & & \frac{\partial^2 f_i}{\partial(\Delta r_L)^2} & \frac{\partial^2 f_i}{\partial(\Delta r_L)\partial R_j} & \frac{\partial^2 f_i}{\partial(\Delta r_L)\partial R_k} & \frac{\partial^2 f_i}{\partial(\Delta r_L)\partial R_L} \\ & & & \frac{\partial^2 f_i}{\partial R_j^2} & \frac{\partial^2 f_i}{\partial R_j \partial R_k} & \frac{\partial^2 f_i}{\partial R_j \partial R_L} \\ & & & & \frac{\partial^2 f_i}{\partial R_k^2} & \frac{\partial^2 f_i}{\partial R_k \partial R_L} \\ & & & & & \frac{\partial^2 f_i}{\partial R_L^2} \end{pmatrix}. \tag{3.21}$$

This matrix is symmetric, so only the upper triangular elements are filled in. We then must define objective functions f_i to form each component u_i. Because the 'fidelity' of a boundary is poorly defined mathematically, we need to employ some common sense metrics. A reconstructed boundary is of high fidelity if it is in the same physical location as its real-life manifestation, is of the same scale and curvature, and is concretely defined with minimal noise. To these points we choose the following interpretations for the components u_i, recognizing that by mixing the units of its components, $|\vec{u}|$ has no meaning:

$$u = \{\delta x_{\text{FM}}, \delta y_{\text{FM}}, \alpha, \nu\}. \tag{3.22}$$

For one reconstructed boundary, the first two components describe the displacement of the center of mass position for the reconstructed boundary relative to its proper position, $u_{i\in(0,1)} = \mathbf{r}_i - \tilde{\mathbf{r}}_i$. The subscripted FM is just a reminder that these quantities are measured in the reconstruction space of the forward model. α represents the deviation between measured and proper curvature, $\kappa - \tilde{\kappa}$. ν describes the noise of the reconstructed boundary position; one choice is $l - \tilde{l}$, the difference in total boundary length between the reconstructed boundary and proper configuration. If there are N

boundaries reconstructed, the definitions of $(\delta x_{\mathrm{FM}}, \delta y_{\mathrm{FM}}, \alpha, \nu)$ may be generalized to

$$\langle \delta x_{\mathrm{FM}} \rangle = \frac{1}{N} \sum_{i}^{N} r_x^i - \tilde{r}_x^i \tag{3.23}$$

$$\langle \delta y_{\mathrm{FM}} \rangle = \frac{1}{N} \sum_{i}^{N} r_y^i - \tilde{r}_y^i \tag{3.24}$$

$$\langle \alpha \rangle = \left[\frac{1}{N} \sum_{i}^{N} (\kappa_i - \tilde{\kappa_i})^2 \right]^{\frac{1}{2}} \tag{3.25}$$

$$\langle \nu \rangle = \left[\frac{1}{N} \sum_{i}^{N} (l_i - \tilde{l}_i)^2 \right]^{\frac{1}{2}} \tag{3.26}$$

though there is no reason to believe that boundaries with arbitrary orientation are impacted by $\delta\vec{x}$ in the same way, *i.e.* $f_i(\vec{x}+\delta\vec{x})$ is a function of boundary orientation. It is necessary then, to measure $\vec{\nabla} f_i$ and $\mathbf{H}$ over a range of boundary orientations. We choose these forms for δx_{FM} and δy_{FM} rather than some squared-norm metric because the information about about the direction of average boundary motion is valuable for its physical interpretation with respect to the detector geometry. Later, we will use the results from the reconstructed phantom to numerically evaluate the terms of Eq 3.21 using these definitions.

3.3 Microstructural Phantom

A phantom microstructure was first created to provide the test structure. Depicted in Fig.3.1, this structure was designed to have simple, regular features but also to challenge the reconstruction with its grains of effectively variable size. There are also regions of comparatively high and low competition between orientations, as well as a sufficient number of orientations to distribute diffracting reciprocal lattice vectors over the unit sphere, but not so many grains as to make the phantom difficult for the eye to interpret. The phantom was designed to be of average size and simple sample geometry; specifically it is a cross section of a cylinder with 200 μm radius. The cylinder center is centered on the rotation axis. The orientations populating the various regions of the RGB colormap depicted in Fig. 3.1 are tabulated in Table 3.1. This microstructure was generated on a triangular '.mic' grid standard to nf-HEDM FMM reconstructions as implemented in [15]. The voxel sidewidth of this grid was chosen to be $\sim$ 700 nm, smaller than the spatial resolution of the measurement, to eliminate discretization artifacts from the simulated scattering.

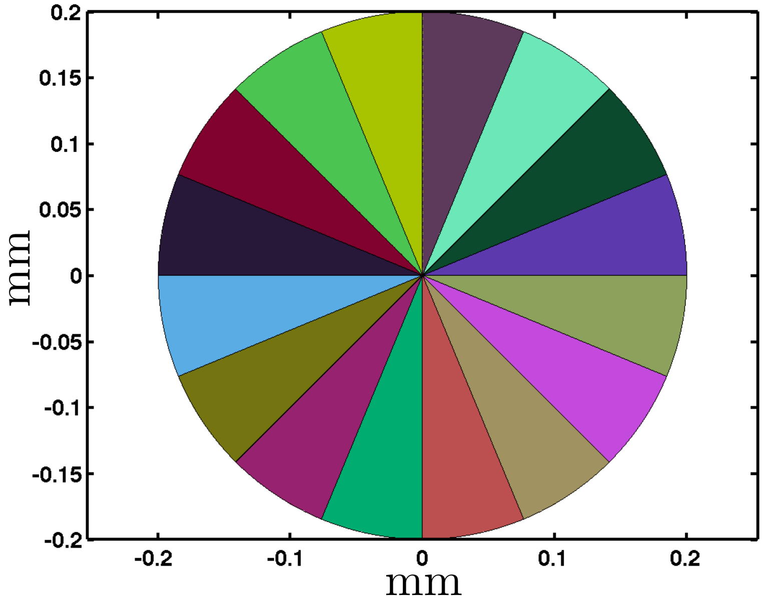

Figure 3.1: Phantom microstructure used to probe the sensitivity of the FMM reconstruction to input detector geometry. Grains vary in size from approximately 50 μm to < 1 μm. Regular geometric features also provide easily computable ground truth spatial features. Grains are numerous enough to be significant, but not so numerous as to overwhelm powers of individual *ad hoc* observation.

Table 3.1: The specific orientations used to populate the phantom microstructure's orientation field.

Grain #	Euler Angles (ZXZ) [°]
1	(26.4016, 15.733, 322.144)
2	(39.7653, 28.2655, 279.215)
3	(68.0573, 14.5046, 278.419)
4	(110.348, 37.2366, 271.913)
5	(117.029, 31.0065, 227.383)
6	(144.482, 18.9241, 251.756)
7	(156.061, 43.0288, 198.642)
8	(189.771, 42.6375, 140.165)
9	(203.782, 5.98192, 117.541)
10	(219.236, 45.5514, 115.848)
11	(236.416, 27.0513, 110.714)
12	(253.19, 26.6194, 124.717)
13	(257.729, 41.6495, 73.2265)
14	(284.478, 33.5856, 69.6385)
15	(315.943, 28.4711, 26.5919)
16	(339.842, 30.7226, 54.5223)

3.4 Creation of Synthetic Tiff Files

Before reconstructions of the phantom microstructure can be performed, simulated diffraction images must be created. To accomplish this, the IceNine software package was used to simulate scattering from the phantom microstructure using the parameters and detector geometry enumerated in Table 3.2. Gold was chosen as the simulated material due to its historical significance as the *de facto* calibration standard for nf-HEDM and the particularly simple form of its structure factor given its face-centered cubic (FCC) crystal structure. The beam energy, 65.351 keV, corresponds to the Hf k-edge and was chosen due to its common use as a working energy for nf-HEDM. The rotation axis projections were chosen to align at the center of the bottom of the near-field CCD detector, again consistent with historical precedent. Also consistent with historical choices, an angular integration interval of $\Delta\omega = 1°$ was chosen for the simulated diffraction data. Peaks up to Q_{max} of 10 Åwere simulated, as might be used for reconstruction historically. This work is meant not only to inform future experimental choices, but also to evaluate the sometimes arbitrary choices of the past.

The simulation used projects the diffraction originating from each voxel element onto a simulated detector and then counts the number of projected voxels that land in each pixel, reporting that count as an 'intensity,' associated with a particular lit pixel. These intensities reflect only the geometry of the diffracting grains and the structure factor of the underlying FCC lattice, and do not incorporate the atomic

Table 3.2: Parameters used to simulate scattering from the phantom microstructure.

Parameter	Value
Material	Gold (Au)
Lattice Parameter	4.08 Å
Crystal Symmetry	FCC
Beam Energy	65.351 keV
j_0	1024 p
k_0	2030 p
L_0	5.00 mm
j_1	1024 p
k_1	2030 p
L_1	6.50 mm

form factor, the Debye-Waller factor, and the Lorentz factors discussed in Chapter 1. Nevertheless this geometry is sufficient to explain the intensity variation on a peak by peak basis. Using these intensities, and the peak locations synthetic tiff files were generated, in identical form to those collected typically during collection of nf-HEDM data. An example of one such image is shown in Fig. 3.2(a). Of course, the image of the direct beam is missing from this image, as it contains only simulated diffraction.

In an effort to improve correspondance to the physical experiment, an empirically measured Gaussian point spread function was applied to each synthetic diffraction image. This point spread function was measured by examining the direct beam at normal incidence at the center of the detector, and comparing its apparent vertical extent with the vertical extent measured from the fluorescence measurement described in Chapter 2. The full width at half max (FWHM) of the vertical beam profile as measured on the nf-HEDM detector was 3.0 pixels, or 4.44 μm at the nf-HEDM pixel pitch of 1.48 μm per pixel. This FWHM corresponds to a Gaussian $\sigma_{\text{obs}} = 1.89\mu$m for the observed beam profile. Using the properties of Gaussian convolution, we know that the observed beam variance

$$\sigma_{\text{obs}}^2 = \sigma_0^2 + \sigma_{\text{psf}}^2 \tag{3.27}$$

where $\sigma_0^2 = (7.55 \times 10^{-4})^2$ is the variance of the vertical beam profile measured in Chapter 2, and σ_{psf}^2 is the variance of the point-spread function. Solving, it is found that

$$\sigma_{\text{psf}} = 1.73\,\mu\text{m} \tag{3.28}$$

for a Gaussian kernel. Here, we assume the size of the horizontal point-spread kernel is equal to the vertical kernel, and that the point spread function does not vary too strongly with incident beam angle or position on the detector. As a first pass toward treating these effects, these assumptions are probably reasonable. A Gaussian kernel with $\sigma_{\text{psf}} = 1.727\,\mu$m was then convolved with the synthetic 'measured' diffrac-

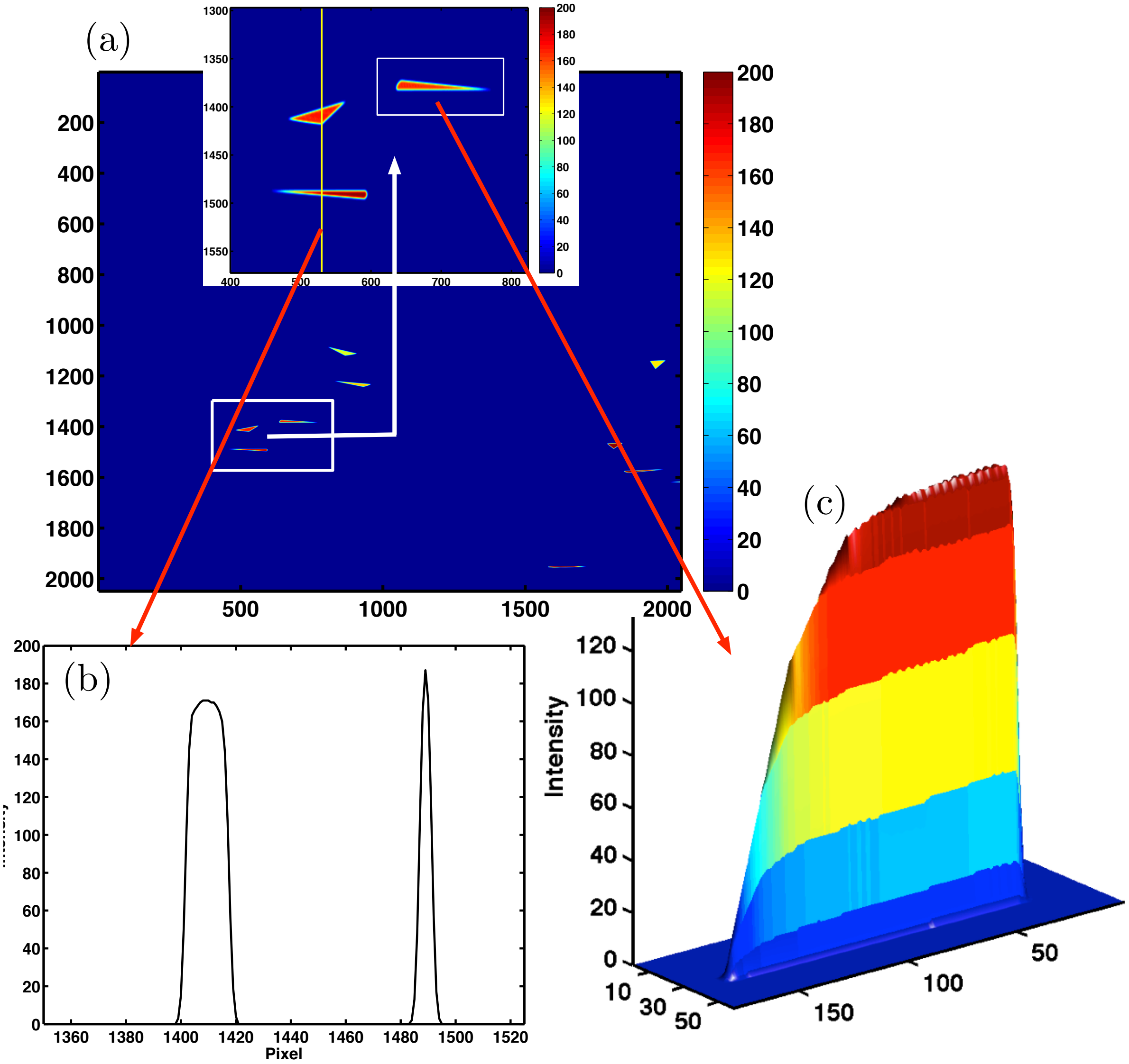

Figure 3.2: (a) An example of the synthetic image file produced used the scattering simulated from the phantom microstructure. The wedge-shaped projections reflect the shapes of the scattering grains. Within the zoomed in region, there is the lined out pixel row depicted in yellow. The intensity of this pixel row is plotted in (b), with higher intensities observed for grains with more compressed geometries. This higher intensity reflects the number of projected voxels landing within a given pixel. The boxed grain within the zoomed-in region is plotted in three dimensions in (c), where the geometric dependence on intensity is again evident.

tion peaks. These images served as the basis for the beginning of the conventional reconstruction pipeline.

3.5 Binarization of the synthetic diffraction data

Before reconstruction of raw data can commence, peaks must be segmented and binarized. For our purposes here, we again utilized Lind's method [1]. While this method is not extremely sensitive to choices of input parameters, variations do occur, so we sought to eliminate arbitrariness from the decision of choosing these parameters. A matrix of the Peak Height Ratio (percentage of maximum peak intensity at which to contour the connected peak) and σ (kernel size of the Gaussian smoothing kernel utilized by the Laplacian of Gaussian filter) parameters was constructed, and at each entry in the matrix, a cost was calculated based on a reconstruction performed with those binarized filed, at the nominal $\mathbf{E_0}$. Because these parameters primarily impact grain boundary geometry, the cost computed used the minimum point to point boundary distance, in a form similar to those used in Chapter 2,

$$\mathcal{C} = \frac{1}{N}\sum_{i=1}^{N}\min_{j}[(\vec{r}_i - \vec{r'}_j)^2]^{\frac{1}{2}}, \tag{3.29}$$

for boundary centroids at reconstructed position $\vec{r}_i$ and theoretical position $\vec{r'}_j$. The cost minimum of this optimization was shallow, representing the weak dependence on the segmentation results on the input parameters. The minimum was found at PHR = 0.13 and σ = 0.9 pixels. These values are reasonable for experimentally collected data. The segmentation of synthetic diffraction images used for subsequent reconstructions utilized these parameters. The boundaries from the reconstruction obtained using the reduced files with these parameters at $\mathbf{E}$ is shown in Fig. 3.3 in red, overlaid on the black boundaries from the as-generated phantom. Some minor discrepancies exist on the boundaries and some noise exists, too; it is the opinion of this experimenter that this effect is due to over-fitting at the boundaries. Because the simulated signal is noiseless, applying the point-spread function has the potential to leave multiple orientation solutions around the grain boundaries. The PHR parameter of the segmentation was designed to mitigate this effect, but there may be additional sources of noise inherent to experimental data collection not captured by the steps taken in the simulation which contribute to this over-fitting.

3.6 Reconstruction and Calculation of the First Order Terms

With the segmented images in hand, reconstruction using perturbed detector geometries can commence. Taking the detector geometries listed in Table 3.2 as $\mathbf{E_0}$,

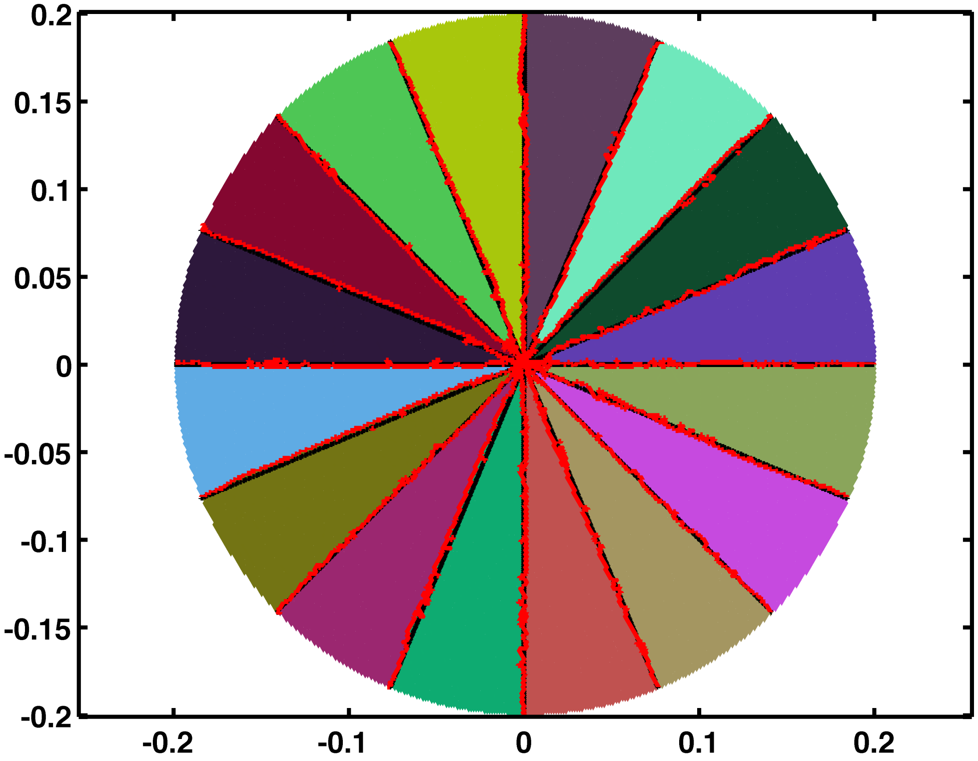

Figure 3.3: Boundaries (red) from the reconstruction utilize the optimum segmentation parameters determined. In black, the boundaries from the as-generated phantom. All dimensions pictured are in mm.

reconstructions were performed with perturbations made to the physically relevant basis described in Section 3.2.3, $E = \{R_j, R_k, R_L, \Delta r_j, \Delta r_k, \Delta r_L\}$. The ranges for these perturbations were determined through a mix of trial and error and prior experience in performing reconstructions. Voxels with 1.5 μm sidewidth were used and reconstructions were performed at $Q_{\max} = 10$ Å to mirror historically average reconstruction conditions. All of the following results are expected to be dependent on $Q_{\max}$. One could imagine constructing calibration curves by automating the analysis procedures that produced the following data, thereby establishing reconstruction sensitivities as a function of the number of peaks fit.[1] Due to computational constraints, 10 Å was chosen as the most generally applicable parameter. Some examples of segmented boundaries from these reconstructions are shown in Fig 3.4. For each re-

---

[1] A word here about computational cost: for the data presented in this section, each reconstruction took approximately 1,500 CPU hours. A total of 43 reconstructions were used to collect data for this section totaling 6.5×10^4 CPU hours for this section alone.

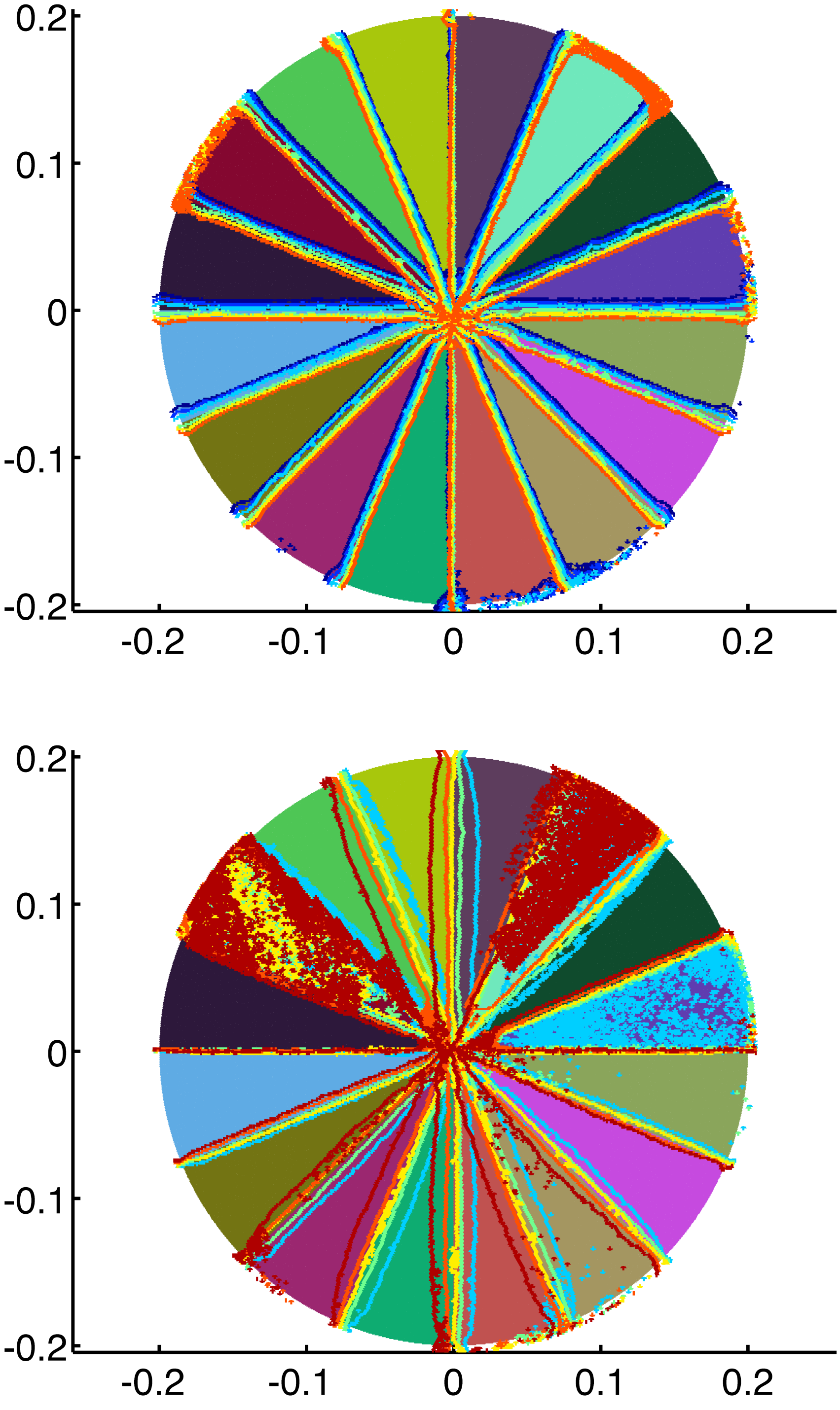

Figure 3.4: Top, grain boundaries reconstructed as R_j is varied over the range $[-8.88, 8.88]$ μm. Bottom, grain boundaries reconstructed as R_k is varied over the range $[-4.44, 4.44]$ μm. Grain boundary segments separate voxels with $\geq 5°$ misorientation. All dimensions pictured are in mm.

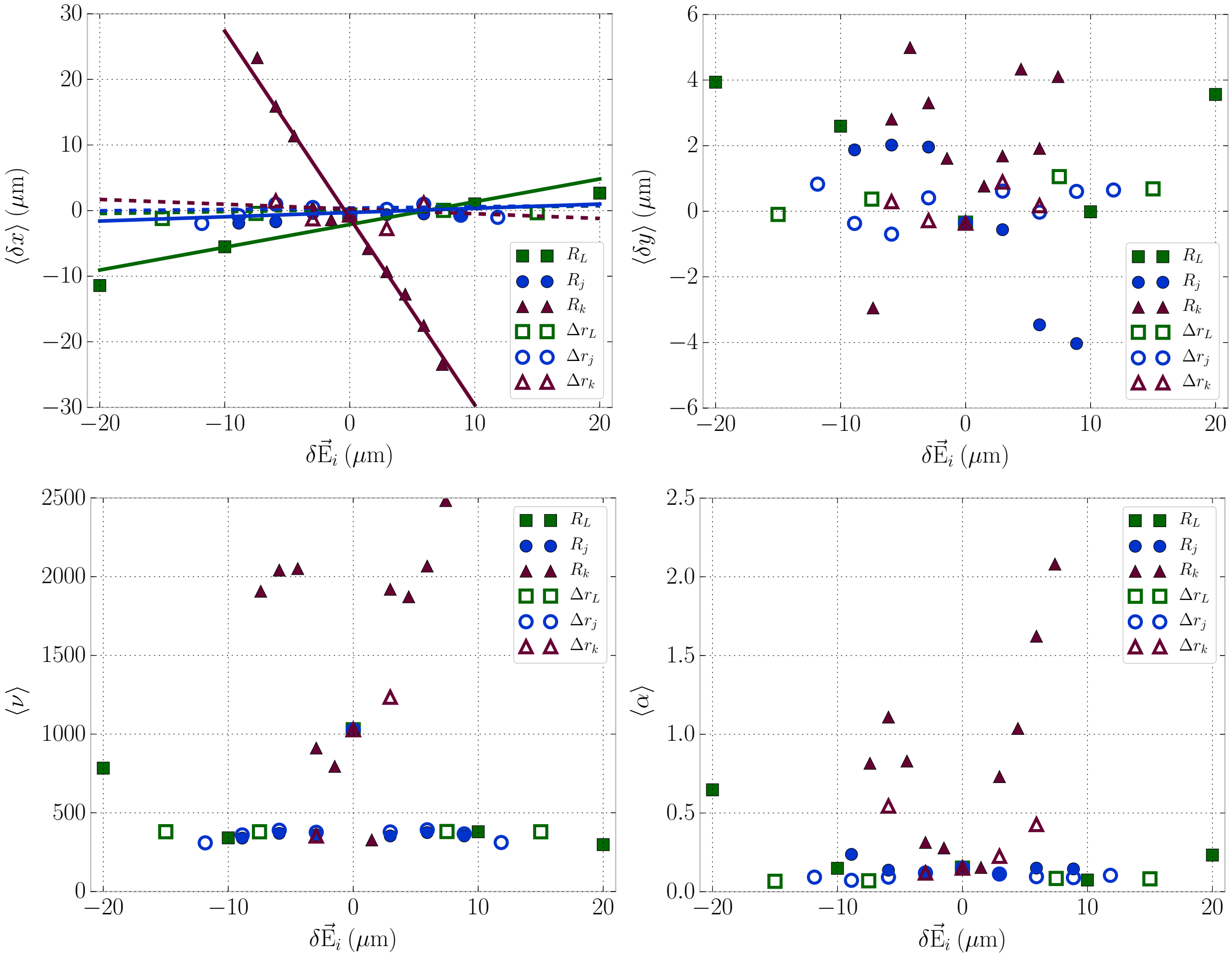

Figure 3.5: Plots showing the results from perturbations of the components of **E** in the objective function spaces defined by Eq. 3.23.

construction, the u-tuple is computed from Eq. 3.23. These results are shown in Fig. 3.5. For each reconstruction, the objective functions were evaluated and the resulting values associated with the magnitude of the perturbation. At zero perturbation, the value of each objective function is evaluated using the reconstruction obtained by using an unperturbed detector geometry, *i.e.* the one with boundaries depicted in Fig. 3.3. The units of $\langle x \rangle$ and $\langle y \rangle$ are μm and measure the average response of the boundary locations in reconstruction space coordinates to perturbations of the detector geometry. The units of $\langle \alpha \rangle$ and $\langle \nu \rangle$ are both dimensionless and measure the extent to which the reconstructed boundaries develop curvatures and noise respectively.

To compute $\langle \alpha \rangle$, a qualitative curvature metric was employed. Each boundary in a given reconstruction was centered at the origin and then fit to a quadratic function constrained to have no linear term. The absolute value of the quadratic coefficient was retained and averaged over all boundaries in a reconstruction. $\langle\alpha\rangle$ then measures the average of this coefficient for all boundaries in a reconstruction which corresponds to a measure of average curvature, but one cannot interpret it as the mathematically rigorous average curvature. Regarding, $\langle\nu\rangle$, we measure the boundary length l by counting the integer number of voxel sidewidths separating two voxels with misorientation $> 5°$. The total extra 1D interface in the 2D cross section from an increase noise is $\langle\nu\rangle \times w$ where w is voxel sidewidth.

To establish comparable values for $\langle x\rangle$ and $\langle y\rangle$, linear fits were performed on the objective function outputs for each reconstruction. Linear fits for $\langle x\rangle$ are plotted in Fig 3.5, but not for $\langle y\rangle$ where they obscure the data. For $\langle\alpha\rangle$, the collection of costs is defined in a relatively symmetrical way with a minimum at $\delta\mathbf{E} = 0$. Ignoring the unknown underlying functional form that this distribution follows, we choose to characterize these curves at lowest order by fitting them to parabolas. The quadratic coefficient will be used to compare the relative effects of each component of E_i. Despite the interesting behavior of $\langle\nu\rangle$ around $\delta\mathbf{E} = 0$, we adopt the same approach for this metric. Given a parabola fixed to be centered at zero, the outlying point at $\delta\mathbf{E} = 0$ will cause deviation of the intercept term, which we will ignore. The noise associated with this point is associated with the overfitting, discussed previously.

The results from these fits and their standard errors are reported in Table 3.3. These terms reflect the fact that certain geometric parameters are more important to reconstruction fidelity. Those most critical are highlighted in yellow and their effects are an order of magnitude or two greater than the others. The detector center of mass coordinates, R_j, R_k, and R_L have the most impact on the value of the objective functions relating to boundary motion. In fact, it appears that the detector relative motions (Δr_i) do not change boundary positions much at all. The effects of Δr_j are small in every objective function space, while perturbations to Δr_k are seen to cause

Table 3.3: Values for the first derivatives of f with respect to the various components of E_i.

Term	$\langle\delta x_{\mathrm{FM}}\rangle$	$\langle\delta y_{\mathrm{FM}}\rangle$	$\langle\alpha\rangle$	$\langle\nu\rangle$
$\frac{\partial f}{\partial R_j}$	$(6.5 \pm 4.2) * 10^{-2}$	$-(3.8 \pm 1.8) * 10^{-1}$	$(8.6 \pm 4.7) * 10^{-4}$	$(1.6 \pm 2.1) * 10^{-1}$
$\frac{\partial f}{\partial R_k}$	$(-2.85 \pm 0.97) * 10^{0}$	$(1.6 \pm 1.6) * 10^{-1}$	$(2.4 \pm 0.6) * 10^{-2}$	$(3.5 \pm 0.98) * 10^{1}$
$\frac{\partial f}{\partial R_L}$	$(3.5 \pm 2.1) * 10^{-1}$	$(-3.4 \pm 7.3) * 10^{-2}$	$(8.8 \pm 5.8) * 10^{-4}$	$(1.4 \pm 0.92) * 10^{0}$
$\frac{\partial f}{\partial \Delta r_j}$	$(2.0 \pm 4.6) * 10^{-2}$	$(2.1 \pm 2.6) * 10^{-2}$	$(-2.2 \pm 1.4) * 10^{-4}$	$(3.4 \pm 9.8) * 10^{-2}$
$\frac{\partial f}{\partial \Delta r_k}$	$(-7.2 \pm 2.1) * 10^{-2}$	$(3.1 \pm 6.2) * 10^{-2}$	$(1.1 \pm 0.2) * 10^{-2}$	$(8.8 \pm 1.9) * 10^{1}$
$\frac{\partial f}{\partial \Delta r_L}$	$(3.0 \pm 2.2) * 10^{-2}$	$(3.0 \pm 2.8) * 10^{-2}$	$(2.0 \pm 1.8) * 10^{-4}$	$(-5.7 \pm 9.9) * 10^{-2}$

both noise and curvature of the grain boundaries. The large impact associated with the k-containing perturbations reflect the compressed projection geometry in the vertical direction. Curiously, shears of the rotation-axis-to-detector distances, Δr_L, are not associated with particularly severe effects. This is surprising because shearing in this direction was thought to make the linear system connecting the scattering origin and the observed peaks inconsistent. More curiously, in two cases, the sign of these first order components seems to be counter intuitive, reflecting improvements in the reconstructed microstructures associated with $\delta \mathbf{E}$ perturbations. One such case is the effect of Δr_L on $\langle \nu \rangle$, but for this case, the uncertainty in the size of the coefficient is larger than the coefficient. A case with less uncertainty is that of perturbations of Δr_j and the resulting effects on $\langle \alpha \rangle$. While only a speculative explanation, it might appear that shearing the detectors along this dimension removes some of the tendency to overfit at the grain boundaries, resulting in straighter, less noisy boundaries.

The effects of terms $\frac{\partial f}{\partial R_j}$ and $\frac{\partial f}{\partial R_L}$ have straightforward physical interpretations. For positive motions of R_j, the detector, which sits in the yz plane in reconstruction-space coordinates, moves in the $-\hat{y}$ direction in reconstruction space. The sign of $\frac{\partial f}{\partial R_j}|_{\langle \delta y \rangle}$ is negative, reflecting the manner in which the entire structure translates along $-\hat{y}$, essentially translating the reconstructed voxels to continuing to overlap simulated scattering with observed scattering. Positive motions of R_L occur in the $+\hat{x}$ direction in reconstruction space and the sign and magnitude of $\frac{\partial f}{\partial R_L}|_{\langle \delta x \rangle}$ reflects a structure consistent with observed scattering may be obtained by translating the original microstructure toward $+\hat{x}$. The action of positive motions of R_k, (due to its definition, which corresponds to the pixel rows of the detector) however, defies simplistic analysis; these motions occur in the $-\hat{z}$ direction, which would require lowering the Bragg angles for diffracted beams originating from initial voxel positions. One might expect a translation of the reconstructed microstructure in the $+\hat{x}$ direction to preserve the original Bragg angles, but this does not occur. Instead the motion is in $-\hat{x}$.

Notably, motions of R_k have deleterious effects on reconstructions which reflect themselves in all components of the u-tuple. This argues for capturing the projection of the rotation axis on the detector by physically imaging the direct beam. While the beam can be skew with respect to the detector (thus creating a difference between the image of the direct beam and the vertical projection of the rotation axis on the detector) this skew is generally small. Care should also be taken to properly determine R_j and R_L, the former by either capturing the specimen's precession about the rotation axis or careful calibration and the later through the use of careful calibration.

3.7 Second Order Terms

While understanding the first order effects is a good step forward toward understanding the sensitivities of the FMM reconstruction to various perturbations of the components of $\mathbf{E}$, due to to coupling between the rotation-axis-to-detector distance and both j and k components of an observed diffraction peak, second order coupling between errors in $\mathbf{E}$ are expected to play an important role in explaining the reconstruction space errors observed. To quantify the terms in Eq. 3.21, we must make several approximations. Because each reconstruction is time consuming (at this resolution and $Q_{\max}$, approximately 1,500 CPU hours/cross section) collecting sufficient data to allow for polynomial fitting in the neighborhood of $\delta\mathbf{E} = 0$ is unfeasible. By limiting to linear regressions of f (fitting lines to the data points corresponding to $\frac{\partial f}{\partial E_i}$), we enforce the condition that all unmixed second order derivatives are strictly zero, *i.e.* $\frac{\partial^2 f}{(\partial E_i)^2} = 0$ by construction. This dramatically simplifies our evaluation of Eq. 3.21, where by setting all diagonal elements to zero, we need to compute only 15 out of the original 21 elements.

The following method was used to compute these remaining 15 terms. For each matrix element in Eq. 3.21, 16 reconstructions were performed at a matrix of values of δE_i and δE_j and combined with the first order reconstructions that contained no E_j perturbation *i.e.* for

$$\begin{pmatrix} \delta E_{i,0}\delta E_{j,0} & \delta E_{i,0}\delta E_{j,1} & \delta E_{i,0} & \delta E_{i,0}\delta E_{j,2} & \delta E_{i,0}\delta E_{j,3} \\ \delta E_{i,1}\delta E_{j,0} & \delta E_{i,1}\delta E_{j,1} & \delta E_{i,1} & \delta E_{i,1}\delta E_{j,2} & \delta E_{i,1}\delta E_{j,3} \\ \delta E_{i,2}\delta E_{j,0} & \delta E_{i,2}\delta E_{j,1} & \delta E_{i,2} & \delta E_{i,2}\delta E_{j,2} & \delta E_{i,2}\delta E_{j,3} \\ \delta E_{i,4}\delta E_{j,0} & \delta E_{i,4}\delta E_{j,1} & \delta E_{i,3} & \delta E_{i,4}\delta E_{j,2} & \delta E_{i,4}\delta E_{j,3} \end{pmatrix}. \tag{3.30}$$

Linear fits to the values of the objective functions were performed reading down the rows to yield four slope values corresponding to each column of the matrix above. An example is shown for the computation of the term $\frac{\partial^2 f}{\partial R_j \partial R_k}$ for $\langle \delta x \rangle$ in Fig. a. These slopes and their errors were fit using weighted linear least squares regression, assuming no covariance between the errors in first order terms. (This is also only an approximation.) This is shown for the same case in Fig. b. The slope of this last linear regression is reported in Table 3.4.

For $\langle \alpha \rangle$ and $\langle \nu \rangle$, again we expect a minimum in the objective function at the column-wise fit with no δE_j and for additional δE_j errors to increase the cost given by the objective function regardless of their sign. Fitting linearly does not make sense given we expect this minimum at $\delta E_j = 0$, so again we fit a parabola and take the quadratic coefficient as the value of $\frac{\partial^2 f}{\partial E_i \partial E_j}$. In the space of $\langle \alpha \rangle$, we can interpret $\frac{\partial^2 f}{\partial E_i \partial E_j}$ as a number that characterizes how much the quadratic coefficients given by $\frac{\partial f}{\partial E_i}$ change as E_j is varied. Similarly, for $\langle \nu \rangle$, $\frac{\partial^2 f}{\partial E_i \partial E_j}$ characterizes how the quadratic coefficients describing the increase in noise vary, but the change in this coefficient is not the same is the change in the underlying physical quantity, *i.e* the noise. Thus, second order terms describing the $\langle \nu \rangle$ and $\langle \alpha \rangle$ spaces should be compared only between various E_i, E_j combinations within those spaces. As for the first order terms, the magnitudes of the second order terms vary widely with the terms including R_k and δr_k again taking a starring role. Terms most affecting the reconstruction results

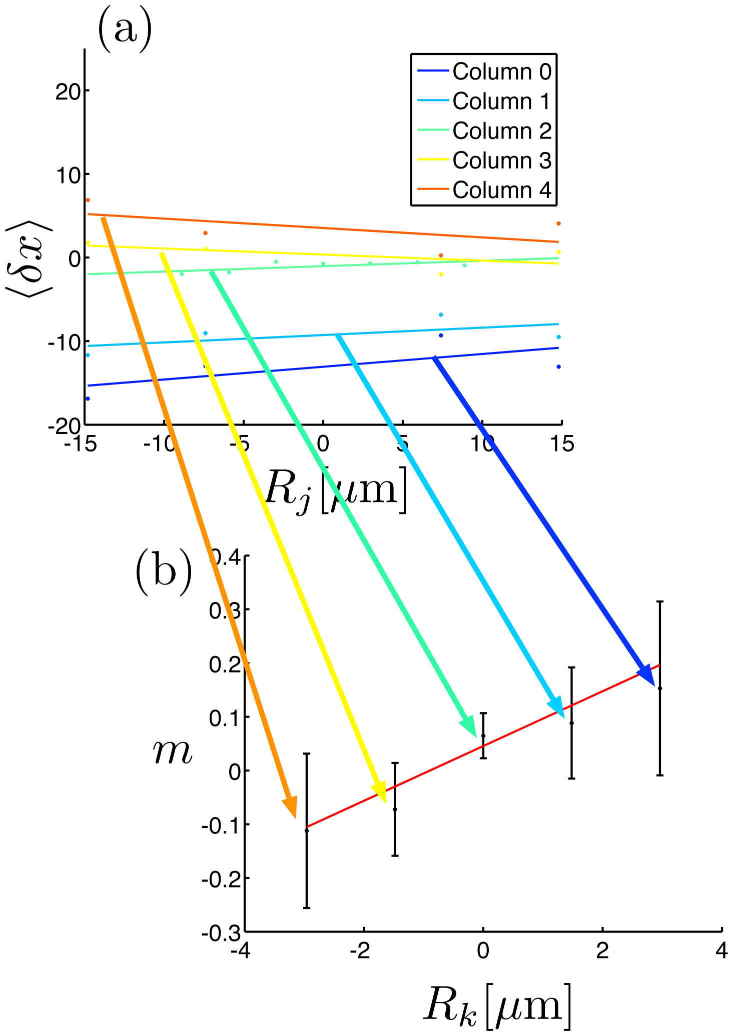

Figure 3.6: Illustration of the calculation of the second order term for $\frac{\partial^2 f}{\partial R_j \partial R_k}$. After computing linear regressions down the rows of 3.30, another linear regression is performed on the collected slope values. This is the value used as the second order term.

Table 3.4: Results for the second order terms giving the magnitude of the coupling between $\delta\mathbf{E_i}$ errors.

Term	$\langle \delta x_{\mathrm{FM}} \rangle$	$\langle \delta y_{\mathrm{FM}} \rangle$	$\langle \alpha \rangle$	$\langle \nu \rangle$
$\frac{\partial^2 f_i}{\partial R_j \partial R_k}$	$(5.10 \pm 1.29) * 10^{-2}$	$-(8.17 \pm 30.4) * 10^{-3}$	$(-1.76 \pm 6.58) * 10^{-5}$	$(1.29 \pm 0.764) * 10^{-1}$
$\frac{\partial^2 f_i}{\partial R_j \partial R_L}$	$(-6.87 \pm 2.11) * 10^{-3}$	$(1.91 \pm 5.16) * 10^{-3}$	$(0.241 \pm 1.17) * 10^{-6}$	$(8.82 \pm 5.26) * 10^{-3}$
$\frac{\partial^2 f_i}{\partial R_k \partial R_L}$	$(-0.534 \pm 2.04) * 10^{-3}$	$(4.10 \pm 6.32) * 10^{-3}$	$(1.31 \pm 0.381) * 10^{-4}$	$(2.53 \pm 1.68) * 10^{-1}$
$\frac{\partial^2 f_i}{\partial \Delta r_j \partial R_j}$	$(-0.706 \pm 1.27) * 10^{-3}$	$(2.04 \pm 1.03) * 10^{-3}$	$(1.71 \pm 2.52) * 10^{-6}$	$(2.88 \pm 1.24) * 10^{-2}$
$\frac{\partial^2 f_i}{\partial \Delta r_j \partial R_k}$	$(-0.206 \pm 1.18) * 10^{-2}$	$(-1.67 \pm 2.22) * 10^{-2}$	$(4.20 \pm 2.54) * 10^{-5}$	$(4.03 \pm 2.07) * 10^{-1}$
$\frac{\partial^2 f_i}{\partial \Delta r_j \partial R_L}$	$(1.15 \pm 1.47) * 10^{-3}$	$(8.92 \pm 4.68) * 10^{-4}$	$(1.93 \pm 1.06) * 10^{-6}$	$(5.77 \pm 1.64) * 10^{-3}$
$\frac{\partial^2 f_i}{\partial \Delta r_j \partial \Delta r_L}$	$(-1.08 \pm 0.340) * 10^{-3}$	$(0.549 \pm 2.53) * 10^{-4}$	$(4.03 \pm 4.20) * 10^{-7}$	$(5.36 \pm 5.86) * 10^{-4}$
$\frac{\partial^2 f_i}{\partial \Delta r_j \partial \Delta r_k}$	$(7.77 \pm 4.15) * 10^{-3}$	$(3.45 \pm 4.52) * 10^{-3}$	$(2.02 \pm 1.19) * 10^{-5}$	$(4.76 \pm 3.05) * 10^{-2}$
$\frac{\partial^2 f_i}{\partial \Delta r_k \partial R_L}$	$(3.07 \pm 1.52) * 10^{-2}$	$(7.55 \pm 1.75) * 10^{-3}$	$(5.91 \pm 6.97) * 10^{-5}$	$(2.84 \pm 1.05) * 10^{-1}$
$\frac{\partial^2 f_i}{\partial \Delta r_k \partial R_j}$	$(0.197 \pm 2.05) * 10^{-2}$	$(-4.68 \pm 2.12) * 10^{-3}$	$(-5.13 \pm 1.81) * 10^{-5}$	$(2.75 \pm 0.734) * 10^{-1}$
$\frac{\partial^2 f_i}{\partial \Delta r_k \partial R_k}$	$(-3.11 \pm 9.18) * 10^{-2}$	$(1.91 \pm 0.343) * 10^{-1}$	$(-1.11 \pm 0.114) * 10^{-3}$	-3.77 ± 4.70
$\frac{\partial^2 f_i}{\partial \Delta r_k \partial \Delta r_L}$	$(-2.41 \pm 1.68) * 10^{-6}$	$(-7.66 \pm 3.33) * 10^{-6}$	$(1.98 \pm 0.711) * 10^{-11}$	$(2.86 \pm 1.03) * 10^{-8}$
$\frac{\partial^2 f_i}{\partial \Delta r_L \partial R_j}$	$(3.17 \pm 8.23) * 10^{-4}$	$(-1.59 \pm 0.749) * 10^{-3}$	$(3.32 \pm 1.91) * 10^{-7}$	$(3.63 \pm 2.83) * 10^{-3}$
$\frac{\partial^2 f_i}{\partial \Delta r_L \partial R_k}$	$(0.411 \pm 2.27) * 10^{-2}$	$(0.542 \pm 4.21) * 10^{-3}$	$(4.56 \pm 3.57) * 10^{-5}$	$(2.95 \pm 1.08) * 10^{-1}$
$\frac{\partial^2 f_i}{\partial \Delta r_L \partial R_L}$	$(0.571 \pm 1.55) * 10^{-3}$	$(9.35 \pm 5.13) * 10^{-4}$	$(0.206 \pm 8.17) * 10^{-7}$	$(1.88 \pm 0.984) * 10^{-3}$

are again highlighted in yellow. Intuition for these terms is difficult to come by, but a few general comments can be made. First, the magnitude of the terms highlighted is generally about one order lower than their corresponding first order terms. This means that while the coupling can be strong for certain combinations of parameters, these terms are of sub-dominant importance. Secondly, the uncertainties reflected in the standard errors of these coefficients is comparatively larger. This reflects the challenges of using few data points, though one should again be cognizant to note the significant computational challenges inherent in computing these metrics. Each of the 15 terms required 16 reconstructions, plus the first order reconstructions, totaling about 5×10^6 CPU hours in all. Even terms with high uncertainty were paid for.

Again, a few anomalies are highlighted in blue, notably, the sign of $\frac{\partial^2 f}{\partial \Delta r_k R_k}|_{\langle \nu \rangle}$. The uncertainty of this term is also very high, and examination of the underlying data shows poor argreement with any quadratic form, as the point at $\delta R_k = 0$ is not a minimum. A similarly strange effect takes place for $\langle \alpha \rangle$, though without the noise. More work is needed to identify exactly the cause of this anomaly. The abnormally small magnitudes associated with the $\frac{\partial^2 f}{\partial \Delta r_k \Delta r_L}$ terms are also interesting; here, examination shows the reconstructions to be of very high quality despite the detectors being significantly sheared. It seems that these dimensions have some sort of offsetting mechanism that achieves this effect, but this mechanism is not well understood either.

3.8 Conclusions

Evaluating and digesting the results from this suite of simulations is a formidable task with no clear end. That said, there are some definitive conclusions one can draw from examination of these data.

- R_k and Δr_k are the most important detector geometry parameters; errors in these quantities can change the formations of grains and grain boundaries in deleterious and profound ways. Fortunately, these errors are also the easiest to spot, because reconstruction quality deteriorates rapidly as perturbations to these parameters become larger. To remedy the possibility of small errors that can move the relative position of grain boundaries on the order of microns, it is recommended to keep an image of the direct beam on the detector.

- Perturbations to R_j and R_L cause mostly rigid body translation of the reconstructed microstructure. Combined with errors in other parameters, these perturbations can cause relative motions that should be avoided at all costs.

- Shearing of the detector system can cause inconsistencies in the scattering solution landscape that lead to noise in the reconstructions.[2]

- Again, all of these sensitivities depend on $Q_{\max}$. Increasing $Q_{\max}$ should more tightly constrain the reconstructed structure around solutions representing its physical realization, but this approach requires refining $\mathbf{E}$ and increases computational complexity.

- Most perturbations of the detector geometry can safely be ignored if the right errors are contained!

---

[2] Indeed, surprising or intermittent noise in the reconstruction can be used to diagnose the presence of beam instability at the synchrotron, *ex post.* No proof given.

3.9 Moving Forward: Containing Errors without Monte Carlo

3.9.1 Iterative Approach

Relying on naive Parameter Monte Carlo for optimization in a in a high dimensional space is an unsatisfying and time consuming way to find a good approximation for **E**. In light of this, driven forward by the previous work, a new method has been developed to perform this optimization which relies on integrating detector intensities. The basic idea is that if a very rough approximation for **E** can be obtained through ray-tracing or some other method, and a FMM implementation is able to use this rough approximation for **E** to identify spatially resolved orientations, a bootstrapping method can be applied to further refine the parameters in a way that converges to the true value for $\mathbf{E_0}$. The bootstrapping method itself involves maximizing the convolution of the intensities between simulated scattering and raw observed scattering over various relative image translations of the datasets. By maximizing intensity overlap, a correction to **E** may obtained and the reconstruction performed again to improve its quality. Following the additional reconstruction, another correction can be computed from which another improved reconstruction can be performed, and so on.

The advantages of this approach are manifold. First, this method is grounded physically; in theory, the **E** that maximizes intensity overlap is $\mathbf{E_0}$. Further, by using the intensity information, each diffracted peak contributes more information than with a binary approach. A higher degree of precision should thus be possible. The computational time associated with running the Parameter Monte Carlo is also greatly reduced. While an iterative approach utilizes more reconstruction steps, these reconstructions would be performed to check the output of the Monte Carlo anyway, so nothing is lost. The intensity convolution raster also takes minutes of CPU time rather than the hours required for the Monte Carlo. Lastly, the application of this method has the potential for real convergence, in the sense that after a sufficient number of iteration steps, the differences between reconstructed microstructures should be discretization noise and the computed corrections should be close to zero.

3.9.2 Implementation and Validation

We first note the feasibility of modeling intensity variations within peak geometries has already been established in [10]. This is easily corroborated anecdotally by examining a few diffraction peaks and comparing them to simulated scattering generated from a reconstruction of the grains that produced the scattering. One such case is shown in Fig. 3.7. In Fig. 3.7(c) a reconstruction of a bicrystalline gold wire sample is shown. Scattering was simulated from the dark green grain and compared to the raw diffraction images collected. Pictured in Fig. 3.7(a) and 3.7(b) is the observed

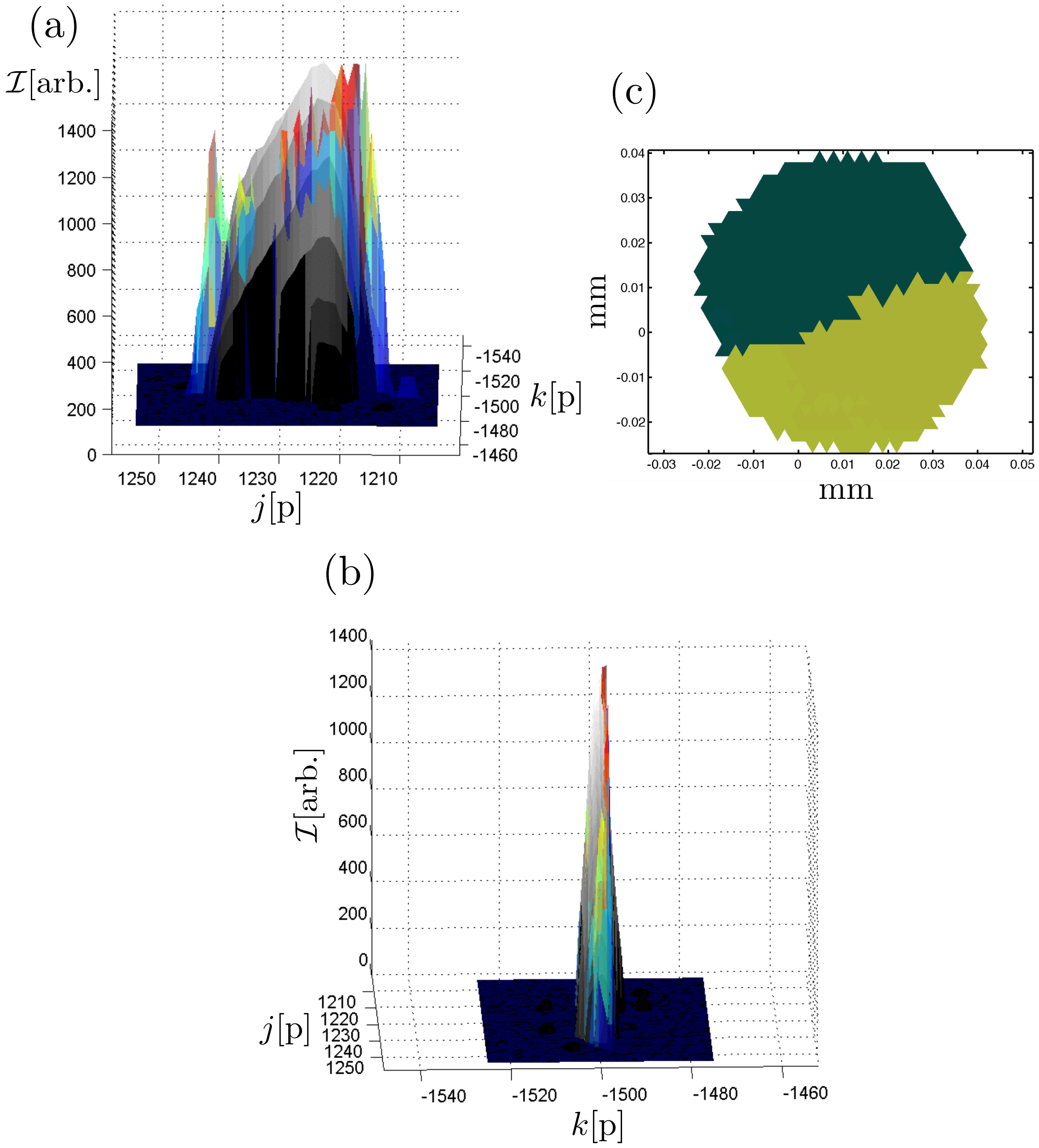

Figure 3.7: Anecdotal illustration that variation in projected grain geometry is sufficient to explain the intensity variations of observed experimental diffraction, up to a constant scale factor. In (a), a side-on view of one simulated Bragg peak (jet colormap) overlaid with experimentally observed raw diffraction (gray colormap) at that detector location. (b), an orthogonal projection of the same system. (c), the reconstructed microstructure from which the simulated scattering was generated, reconstructed using the collection of segmented diffraction peaks belonging to the same data set as the raw peak shown.

diffraction in the gray colorscale plotted simultaneously with the simulated diffraction in the jet colorscale. The maximum intensity value of the simulated scattering has been scaled to correspond to the maximum observed in the raw dataset. The shape of the raw diffraction signal is well reflected in the simulation, with the exception of some noise associated with the fairly large 2.5 μm voxel size used for the reconstruction. The outlying peak at $j \approx 1243$ is likely due reconstructed orientations or boundaries not being completely optimized.

Taking this one peak as a representative example, one would implement the intensity convolution raster by summing the convolution of these two overlapping images S and R (simulated and raw, respectively),

$$\mathcal{I} = \sum_j \sum_k S_{j,k} \circ R_{j,k}, \tag{3.31}$$

where $A \circ B$ denotes the Hadamard (or element-wise) product of two matrices A and B. Here the detector notation (j, k) is used to refer to the matrix indices commonly labeled (i, j). The raster takes place by constructing a matrix of $\mathcal{I}$ values computed by

$$\mathcal{I}_{n,m} = \sum_j \sum_k S_{j+n-n_0,k+m-m_0} \circ R_{j,k} \tag{3.32}$$

for $n \in \{1, 2, \ldots, N\}$, $m \in \{1, 2, \ldots, M\}$, and initial integer offsets n_0 and m_0. Computing the correction to deviations in detector deviations in j or k then amounts to finding the indices of the maximum element of $\mathcal{I}_{n,m}$. In reality, this is done for every diffraction peak simultaneously by rastering and integrating the entire detector at one time. One use tricks to prevent implementation level bugs like overflows etc., but at the core, this technique is straightforward. Having followed this procedure one may obtain images corresponding $\mathcal{I}_{n,m}$ like Fig. 3.8(a). In this figure, a scaled integrated intensity $\tilde{\mathcal{I}}$ is computed at each element of $\mathcal{I}_{n,m}$. The scaling is purely for readability and is meaningless. There is a maximum in the integrated convolution corresponding to a relative image shift of the simulated data of ≈ -3 pixels. That data point represents the computed correction to an applied known perturbation of $+6$ pixels in R_j, which illustrated in Fig. 3.9 and discussed later. One important consideration not yet discussed is that because each detector's geometric parameters must be optimized independently using this method, the detector center-of-mass basis is not as useful here. This basis is used in the validation steps that follow for consistency with the rest of the work, but in practice corrections to each detector's geometry should be computed seperately in the (j_i, k_i, L_i) basis. Moreover, determining an optimum value for L_i using this method requires simulating scattering onto detectors at incrementally varied L_i values and choosing the maximum $\mathcal{I}_{n,m,l}$, where l runs over the number of L_i distances simulated. Curves showing the variation of three such examples $\mathcal{I}_{n,m,0}, \mathcal{I}_{n,m,1}, \mathcal{I}_{n,m,2}$ are shown in Fig. 3.8.

To validate this procedure, the intensity convolution raster was performed on the scattering simulated from the reconstructions used to deduce $\frac{\partial f}{\partial R_j}$ and $\frac{\partial f}{\partial R_k}$ onto the

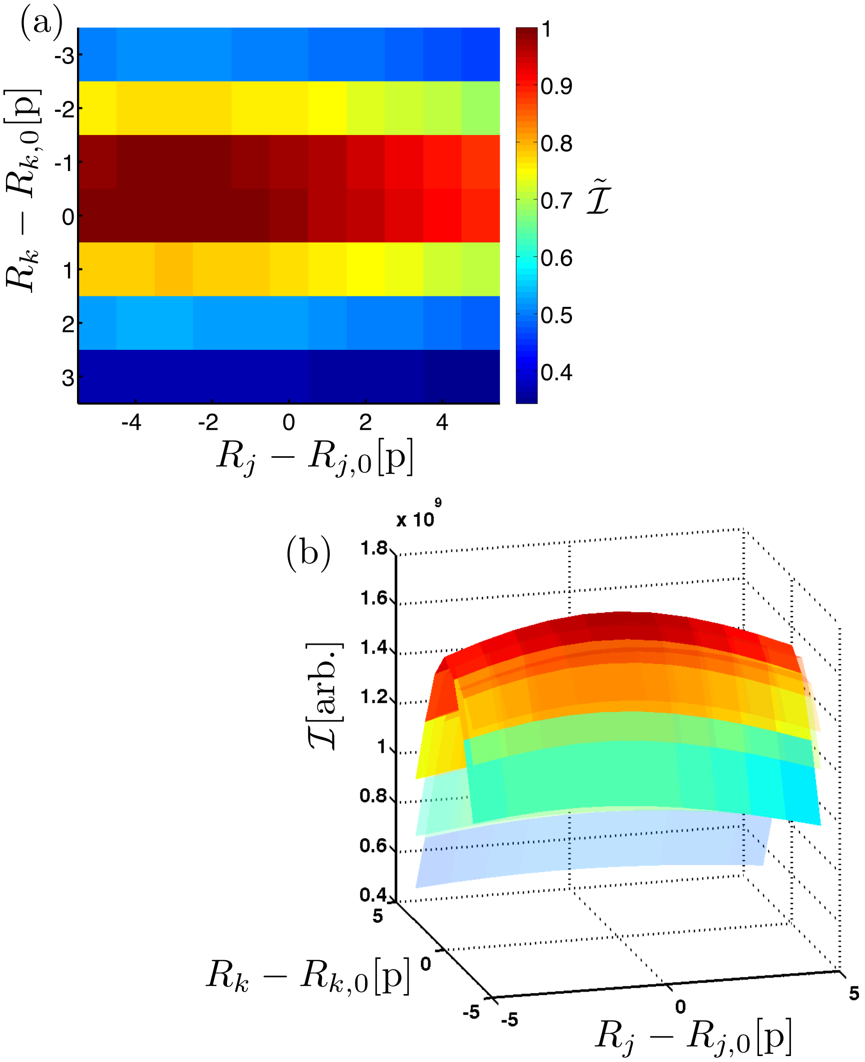

Figure 3.8: Illustration of the value of the integrated intensity convolution, as a function of the relative translations between simulated and synthetic raw image datasets. (a), the maximum in the image represents the computed correction of R_j for the last data point in 3.9a. Using this method, to identify the proper R_L, intensity convolution rasters of R_j and R_k must be performed at various Li distances, and the maximum integrated intensity retained to complete the experimental geometry parameter set. (b) shows three such surfaces, where each surface represents a computation as in (a), but for a different value of L_i.

first detector (L_0) at its proper rotation-axis-to-detector distance. Simulations were performed at $Q_{\max} = 13$Å. Corrections were computed at various perturbations of R_j and R_k, and those corrections were compared to the actual perturbations. In this implementation, the raw data used were the synthetic raw images used to perform the sensitivity analysis. Corrections were computed for all the peaks on each 1° wide angular integration in $\Delta\omega \in [-180, 180]$, and then the results were combined, but only implementation-level details prevent this process from being performed with one raster step. The results are shown in Figs. 3.9 and 3.10. The computed corrections are shown in blue in each case and are compared to the theoretically proper correction. Error bars reflect the standard deviation of the correction computed from each angular integration. Computed corrections do pass through the origin indicating that this process is convergent to $\delta\mathbf{E} = 0$ for deviations in only one component of $\mathbf{E}$ at a time. Examining Fig. 3.9 first, the slope the computed corrections is only half of its theoretical value. It remains unclear why this is true, but this curve can function as a calibration curve for future calculations. There should be no modification suggested to R_k, and we see that this is true, subject to some discretization errors. Including more simulated diffraction peaks could help achieve more resolution.

Examining Fig. 3.10, within the range of "reasonable" deviations in R_k (< 4 pixels or so) the intensity convolution raster admirably computes the appropriate corrections to R_k. These corrections also converge to the unperturbed value. The desirable R_j is rightly found to be zero, though there is much more noise, because as previously noted, R_k has the ability to dramatically change grain shapes at large perturbation values. This illustration is convincing enough to this experimenter to call for the additional development work required to implement this technique in a robust and automated way to achieve reliable determination of $\mathbf{E_0}$.

3.9.3 Improvement: Intensity Modeling

Applying the intensity convolution raster method to real experimental is complicated by the fact that the intensity variation from peak to peak includes not only the geometry of the diffracting grains, but also the atomic form, Debye-Waller, and Lorentz factors previously discussed in Chapter 1. Performing the convolution raster calculation on a single image (or a collection of images) is then biased by peaks with comparatively high intensity, namely lower order scattering peaks with smaller values of $|Q|$. To compare each peak's contribution's equally (or even implement a customized weighting scheme), one must normalize away these factors. (Alternatively, one could compute $\mathcal{I}_{n,m,l}$ for each peak separately after scaling its intensity to the raw data and the combine these separate results. This represents unnecessary computational complexity and computationally inefficient. The elegant approach is to normalize away non-geometric intensity variations.)

The beginning steps toward modeling these intensity variations should involve checking whether existing models, when combined, reproduce data taken during syn-

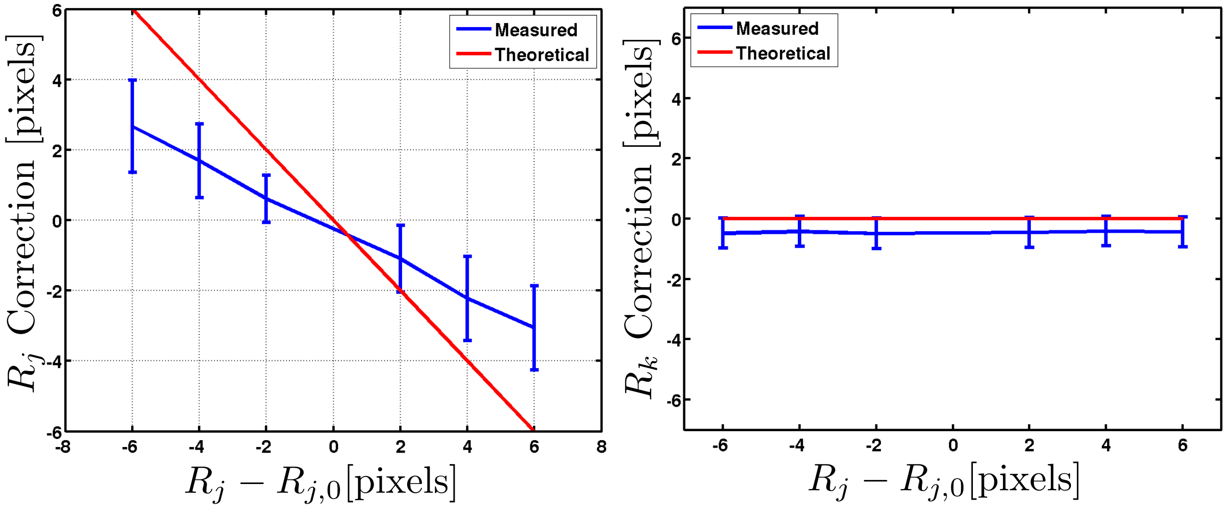

(a) (b)

Figure 3.9: Calibration curves illustrating that maximizing the convolution between simulated scattering and synthetic raw data gives a corrections to modified detector geometry that converge to the true values of E_0. (a), the computed corrections to R_j to a perturbation of R_j by an amount given on the horizontal axis. The red line marking the line $y = -x$ is the theoretical correction for each value, while computed values are plotted in blue. Error bars reflect the standard deviations of this quantity as computed from each 1° wide image in $\Delta\omega \in [-180°, 180°]$. (b) the corrections to a perturbation of R_k given a perturbation of R_j. Theoretically, a correction of zero should be computed for this case.

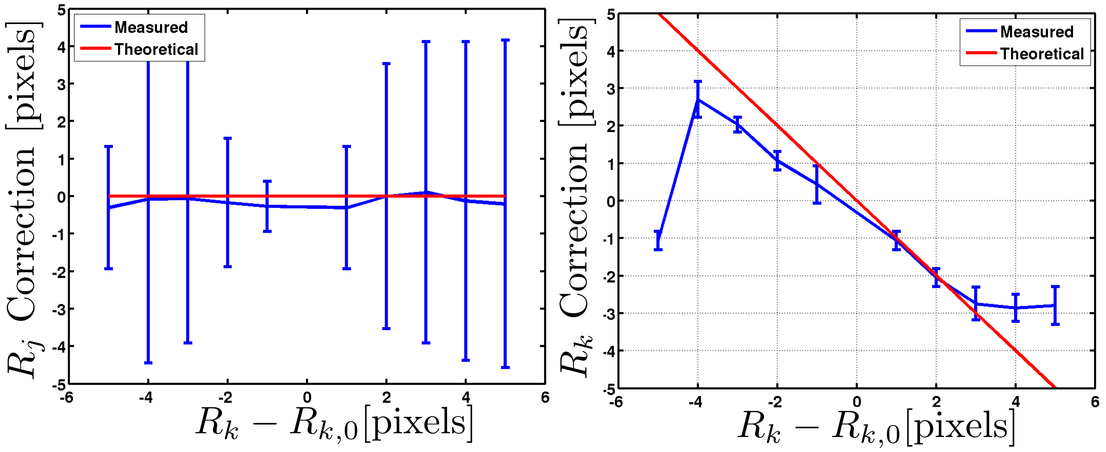

(a) (b)

Figure 3.10: (a), the computed corrections to R_j to a perturbation of R_k by an amount given on the horizontal axis. Theoretically, a correction of zero should be computed for this case. Error bars reflect the standard deviations of this quantity as computed from each 1° wide image in $\Delta\omega \in [-180°, 180°]$. (b), the corrections to a perturbation of R_k given a perturbation of R_k. The red line marking the line $y = -x$ is the theoretical correction for each value, while computed values are plotted in blue.

chrotron experiments. We seek this confirmation by examining the scattering from the bicrystalline gold wire structure shown previously in Fig. 3.7. Diffraction from this gold wire was collected in the usual way, using 0.25° angular integration steps and beam energy of 65.351 keV. Following reconstruction of the microstructure from this data, scattering was simulated from the reconstructed microstructure. This simulated scattering contained information on each Bragg peak's reciprocal lattice vector, $\vec{G_{\mathrm{hkl}}}$ in addition pixel-by-pixel information on its projected extent on the detector. The segmented peaks used for the reconstruction were then associated with this additional information. Each binarized peak, when combined with the reconstructed orientation for the original reconstructed grain was associated with η, 2θ, and $|Q|$ values, variables not precisely observable in the near field regime with finite sample extent. Care was taken to merge single peaks appearing neighboring angular integration intervals due to mosaic spread or Lorentz broadening (the tendency for grains near $\eta = 0$ that have slowly precessing $\vec{G_{\mathrm{hkl}}}$ vectors to fulfill the Laue condition over longer intervals).

The atomic form factor, plotted in Chapter 1, was first divided from the intensity of each peak.[3] Neglecting x-ray absorption through the small cylindrical sample, the remaining intensity variation is associated with the Lorentz and Debye-Waller factors. First, groups of peaks at fixed $|Q|$ were examined to determine whether the simple

$$L(2\theta, \eta) \propto \frac{1}{\sin(2\theta)\sin(\eta)} \tag{3.33}$$

model of Lorentz factor adequately modeled variations across fixed $|Q|$. A single scale factor, applied to all peaks, brought good agreement as shown in Fig. 3.11. Given the good agreement, this factor was then divided from the intensity of each diffraction peak and the intensity of the results plotted against Q to examine whether the remaining variation is due to the Debye-Waller factor. This result is plotted in Fig. 3.12. There appears to be a bifurcation of the data. With proper scaling, either branch could possibly describe the Debye factor variation, though the shape of the lower branch seems to be a better match. No combination of variables tried so far, including η, direction of $\vec{Q}$, and $\Delta\omega$ interval can explain the separation between these branches. The effect is not due to the differing orientations of two crystals evaluated, as shown by Fig. 3.12(b). The closest thing to an explanation comes from examining the spatial arrangement of these peaks on the detector; after arbitrarily choosing a value on which to delineate the 'upper branch', population 'A', from the lower branch, population 'B', it seems perhaps population A forms preferentially along particular detector axes, as in Fig. 3.13. The spacing and angle of these axes appears to be regular. One possible model would be to assign some probability of a higher intensity response for the peaks landing in these regions. That said, much work is still necessary to determine whether this effect is caused by the CCD, some exotic experimental failure like slit scattering, or some other yet unknown effect. Performing

---

[3] While the form factor is a function of beam energy, these corrections will be small away from the K-shell absorption edge at 81 keV.

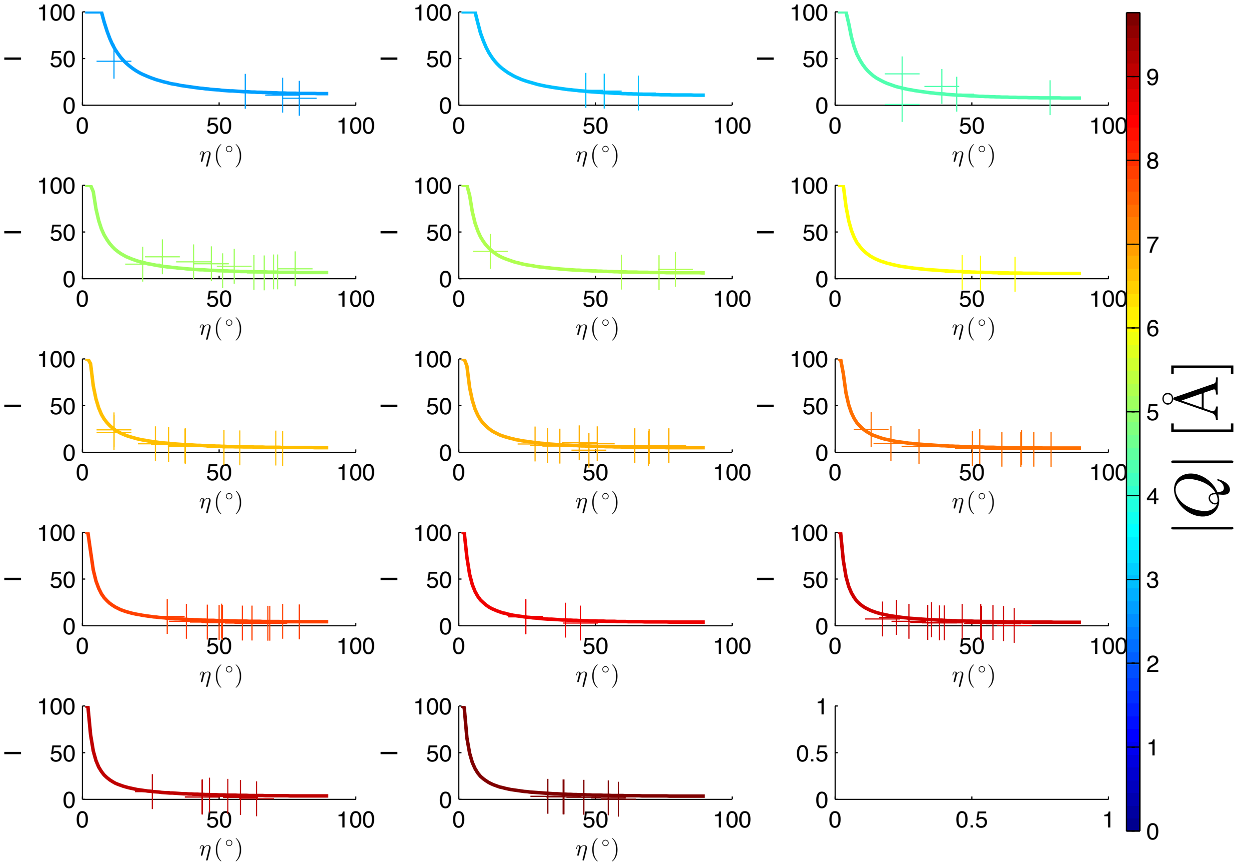

Figure 3.11: Plot illustrating that Eq. 3.33 models intensity variations well for groups of peaks at fixed $|Q|$. Peaks < 10 Å were examined for the two grains shown in Fig. 3.7(c).

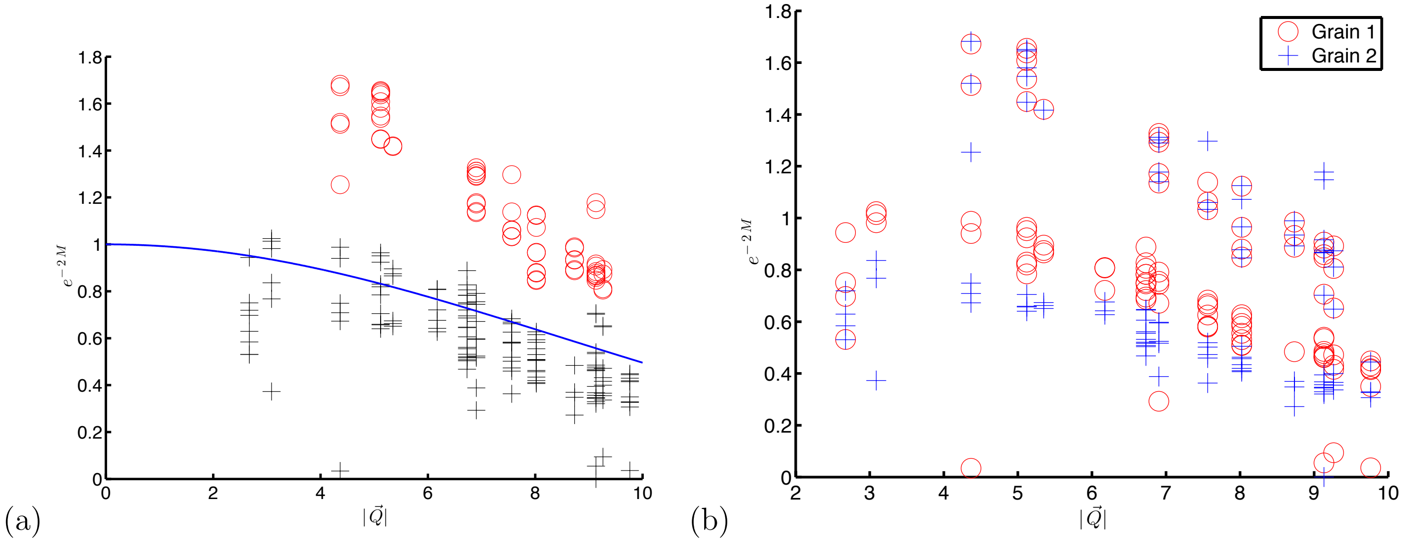

Figure 3.12: The remaining intensity variation cannot be described by the Debye Waller effect alone. (a), the two branches of the bifurcation are arbitrarily defined and given different colors and markers. The theoretical Debye-Waller factor for gold at room temperature is plotted in blue in (a). (b), this effect is not separated by considering each grain's scattering differently.

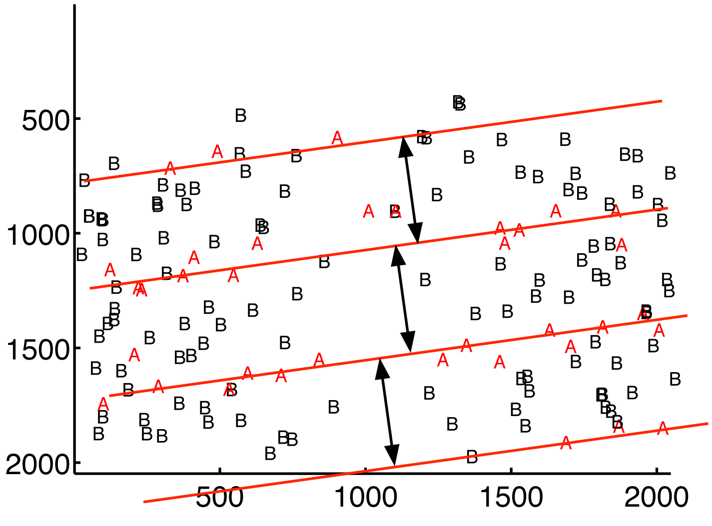

Figure 3.13: A possible explanation of the origin of the two branches of the bifurcation in the Deybe-Waller factor intensity variation. Peaks in the upper branch appear to form along regularly spaced parallel axes on the detector. More work is needed to determine whether this is a persistent effect.

a careful experiment with the express purpose of performing this modeling carefully might be in order.

Chapter 4

Case Study: Spall Voids in Shocked Copper

The following case study illustrates an application of the nf-HEDM technique that relies on accurate spatial resolution of grain boundaries and microstructural interfaces. The heuristics developed in the previous two chapters, which were shown to promote reliable reconstruction, were strictly adhered to for the following analysis. The remainder of this chapter reproduces a manuscript that is published in the Journal of Applied Physics and is available at doi:10.1063/1.4947270.

4.1 Introduction

Understanding the plastic response of materials has been a longstanding goal for scientists who desire to engineer them for specific applications [51, 52, 53]. Recent advances in non-destructive characterization have allowed for some of the first direct comparisons between quasi-static models of plasticity in polycrystals[54, 55, 56, 57] and experiment.[58, 59, 60] With the goal of linking to dynamic models[61, 62, 63, 64, 65] we leverage these advances to study high strain-rate plasticity through shock loading of coarse-grained copper and discuss the first non-destructive characterization of dynamic damage nucleation in the bulk.

Many experiments have studied shock loading and void formation using gas gun driven flyer plates to impact a specimen and cause spallation [66, 67, 68, 69, 70, 71, 72, 73, 74, 75, 76]. These studies have shown that relative orientation of constituent grains plays a role in determining where voids form,[69, 77, 78, 71, 72, 79] that the structure of the grain boundary also plays a role,[80] and that the geometry of the loading direction *vis-a-vis* these features is also important [73]. Novel modeling and simulation efforts have confirmed that grain boundaries with different character behave differently under high rate dynamic compression[65, 74] and demonstrated success in elucidating the void growth regime [81].

In this work, we use synchrotron-based near-field High Energy Diffraction Microscopy (nf-HEDM)[7, 10] to map the microstructure of a mm^3-sized, well-annealed copper sample. The specimen was shock loaded using an experimental setup tuned to form micro-scale voids. The shocked microstructure was then remapped, and micro-computed tomography (μCT) was performed to image the void field. All three data sets were then registered to provide fully 3D, before and after information on the sample's orientation and void fields.

A total of 485 voids are resolved with 87% being found close to observed grain boundaries. The distribution of void locations is non-uniform within the spall plane, implying either some asymmetry in the loading or a microstructural origin. It is found that the spalled region does have a distinct microstructure: its volume is dominated by large grains with complex topologies with a significant fraction of the volume being occupied by unusually large Σ-3 related domains (Σ3D). These configurations do not extend to regions where voids did not form in large numbers. A significant fraction of the voids are close to boundaries within the Σ3Ds. Thus, voids may be preferentially nucleated on boundaries of large grains or they may tend to occur within Σ3Ds. Within the somewhat skewed statistics of the spalled region, there is no statistically significant preference for the voids to form on any particular type of boundary. We conclude that systematic, non-destructive, before and after measurements hold the possibility of sorting out these questions and that it is now possible to perform dynamic loading on fully characterized microstructures so that, for example, one can avoid including or purposely include exceptional microstructural populations in the region to be spalled.

4.2 Experimental Methods

A half-hard plate of 99.997% pure polycrystalline oxygen free electrolytic C101 copper was machined and annealed in vacuum at 450°C for 30 minutes. Bingert *et al.* performed electron backscatter diffraction (EBSD) microscopy on a characteristic free surface of the material and determined the mean grain size to be approximately 30 μm, excluding annealing twins. Including these features resulted in a mean grain size of 14 μm, though the authors note large variation in the grain sizes with some grains as large as 100-200 μm. A subvolume of the 1.2 mm^2 $\times$ 2.8 mm cylindrical sample's microstructure was mapped using nf-HEDM at Sector 1-ID at Argonne National Laboratory's Advanced Photon Source (APS 1-ID). The sample was illuminated with a monochromatic 65.384 keV x-ray beam plane-focused to approximately 1.4 mm $\times$ 2 μm. Bragg-diffracted beams were collected on a CCD detector optically coupled to a thin scintillation screen by rotating the sample about its axis of symmetry. Volumetric data were acquired by translating the sample parallel to its symmetry axis such that successive planar cross sections were illuminated. Images corresponding to 170 layers spaced at 4 μm were collected for a mapped volume of ≈ 0.8 mm^3.

The measured volume was micromachined out of the sample and embedded in a copper target assembly. Radial momentum trapping rings fabricated from the same material were utilized to prevent lateral release processes from affecting the uniaxial loading state. This assembly was shock loaded at 300 m·s^{-1} with a copper impact plate 360 μm in thickness, using a modified 7.6 mm-diameter gas-driven Taylor gun.[75] After shock loading, soft capture of the sample was employed to mitigate further damage. The shocked sample was remapped at APS 1-ID, where 136 layers of diffraction were collected in the manner previously described. This 1.2 mm^2 × 544 μm volume was centered around the anticipated spall plane of the specimen and included both highly damaged and less damaged regions. While certain especially damaged regions were not completely reconstructable (see Fig. 4.1f), sufficient volume from the less damaged region was reconstructed so as to allow for registration of the two datasets and examination of microstructural evolution. In regions with the most damage, based on comparison with prior quasi-static measurements on copper,[60] we estimate inhomogenous local plastic strains on the order of 10-20%.

Parallel-beam absorption μCT images were collected to image the void field within the post-shocked sample. Using 65.384 keV x-rays, the sample was illuminated with an unfocused beam of dimension 1.5 mm × 1 mm. The sample was fully rotated about its axis of symmetry, and radiographs were collected every 0.1°. These radiographs were reconstructed with the GridRec algorithm to yield 625 cross-sectional images at 1.48 μm resolution [22, 24].

4.3 Data Analysis and Results

Post-processing of the reconstructed μCT data was required to segment the void field. The 3D image stack represents the material density in 1.7×10^8 volume elements (voxels) within a 0.544 mm^3 volume. Voids are recognized as connected voxels with reduced density compared to that of the fully dense material. An intensity threshold was applied to extract these features. To remove reconstruction artifacts, these segmented regions were examined for connectivity and accepted if they were independently reconstructed in adjacent cross-sections. Lastly, any remaining reconstruction artifacts, *e.g.* rings from hot or dead detector pixels, were manually removed. Following void extraction, 485 unique voids were found with mean diameter $\bar{d}_{void} = 4.4$ μm. The void field extracted was then transformed into the pre-shocked reference frame, as discussed below.

To reconstruct the nf-HEDM data, the IceNine program[15] was used to optimize peak overlap between simulated diffraction from reconstruction space sample voxels and the observed diffraction [10]. Reconstructed voxels from each plane were integrated into 3D volumes representing the pre- and post-shocked orientation fields. These states were reconstructed using equilateral triangular voxels of sidewidth 5.6 μm and 2.8 μm respectively. Features of interest including grains, grain boundaries, N-lines (lines connecting $N \geq 3$ distinct grains), and M-nodes (points connecting $M \geq 4$ grains) were then extracted directly from each volume; three or more contiguous voxels with crystallographic misorientation $\leq 5°$ were defined as grains, only

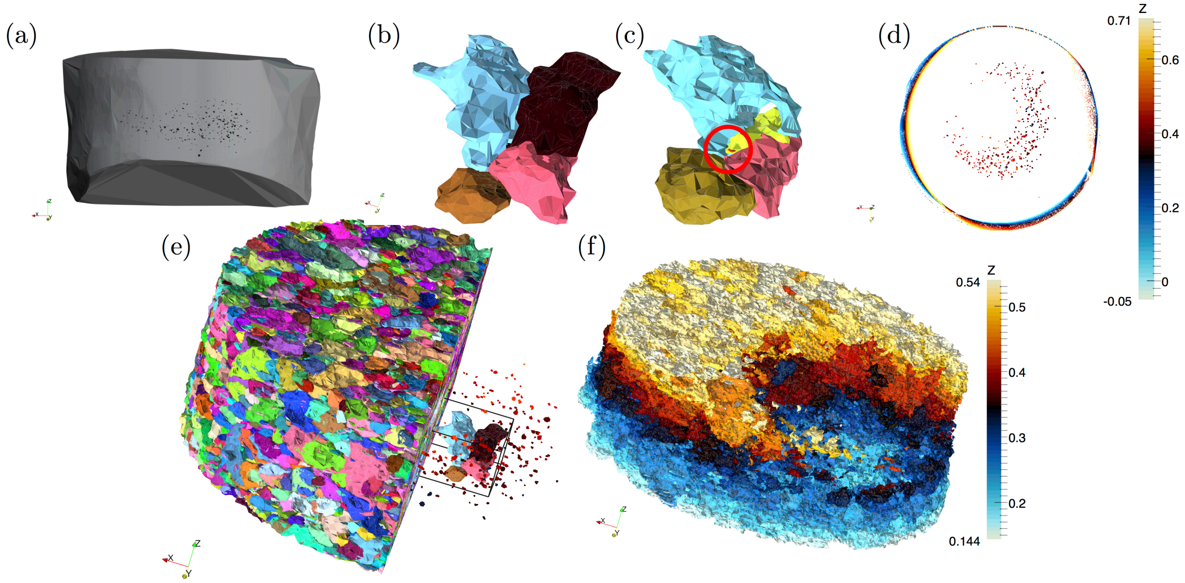

Figure 4.1: A summary of the experimental data collected. (a), a cutaway view of the μCT measured post-shocked sample. The voids are shown at actual size in black near the mid-plane. (b), a four-grain system from the pre-shocked state, colored by mapping Rodrigues orientation vectors to RGB values. (c), the same four-grain system extracted from the registered post-shocked state. Color differences illustrate bulk lattice rotations of the constituent grains. In the case of the maroon grain of (b) this lattice rotation crosses a periodic boundary condition within the color map producing the yellow grain of (c). Highlighted with the red circle is a void formed at the $M = 4$ node connecting the four grains extracted. (d), a top down view of the sample edges segmented from μCT of the post-shock sample includes the spall-void field created by the flyer plate impact. Voids lie in a crescent-shaped region and are slightly enlarged for visibility. Colors represent the z-coordinate normal to the figure. (e), a cutaway view of the pre-shocked reconstructed orientation field, colored by orientation. In (f), the reconstructed post-shocked sample, with grains colored by center of mass distance along the loading direction ($\hat{z}$). The missing region in the right foreground is due to severe plastic deformation which prevents reliable reconstruction, though material does exist here.

$N = 3$ (triple) lines were segmented, and M-nodes were defined to be points where two or more triple lines terminated within the resolution of one voxel. Average grain orientations are computed over each set of associated voxels.

To analyze the pre-shocked state, a 1.2 mm^2 × 420 μm region of interest (ROI) was extracted from the total of 1.2 mm^2 × 680 μm measured. From this ROI, 16,996 grains were segmented with mean and standard deviation sphere-equivalent diameter $\bar{d}_{pre} = 23 \pm 20$ μm. Many were significantly larger, and in fact the largest 100 grains account for 25% of the ROI volume; the largest 1000 account for over 90%. Comparison of the reconstructed pre-shocked microstructure with the EBSD image of the same sample (though not the same region) in Bingert *et al.* reveals the absence of certain thin, flat grains in the nf-HEDM reconstruction. Identified as the FFC annealing twins, these grains have misorientation $60°\langle 111\rangle$ (coincident site lattice (CSL) boundary Σ-3[35]) and share $\sim 1/3$ of the same Bragg peaks. For cases where the grain boundary inclination plane is also $\langle 111\rangle$, the boundary is called a coherent twin. The ability to differentiate parent and embedded twins depends on optimal experimental conditions; in this case, during collection of the pre-shocked diffraction images, conditions were compromised by beam instability. Combined with sub-optimal beam-block placement which partially attenuated diffracted beams with small Bragg angles, this prevents resolution of small twin features. (For an illustration in which nf-HEDM is used successfully to track annealing twins, see Lin *et al.*)

A 1.2 mm^2 × 400 μm ROI was extracted from the post-shock measurement, with 26,269 grains of $\bar{d}_{post} = 13 \pm 15$ μm. The large standard deviation reflects the shape of the size distribution, which again has large positive skew. The difference in the number of grains found before and after shock treatment is ascribed to the combination of grain-breakup events and a resolution effect associated with reconstructing the post-shock volume with smaller voxels. Both the pre- and post-shocked ROIs are centered around the spall plane of the post-shocked sample state and correspond to largely the same sample volume.

A registration procedure was followed to map the two data sets into one reference frame. The optimal registration was obtained by minimizing integrated misorientation angle[56, 50] under rigid body rotations and translations. Higher order corrections to this registration could be computed on a grain-by-grain basis by allowing optimization within the full affine space. While this additional procedure would account for local shape change due to grain plasticity, the initial registration produced sufficient correspondence between states that further refinement was not necessary. Both the post-shock HEDM and the voids were transformed in the same way into the reference frame of the pre-shock HEDM data set, and the void field was compared to this data set. The void field was not used in determining the registration of states.

The distribution of voids along the loading direction is centered at the sample mid-plane. Looking down the loading axis, as in Fig. 4.1(d), while voids are concentrated near a single radius, the azimuthal distribution is crescent shaped. We discuss possible causes for this below. The shock compression caused some lateral expansion

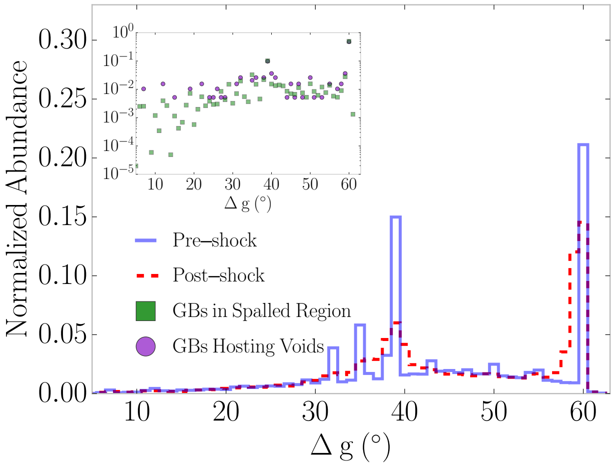

Figure 4.2: A normalized, number-weighted histogram of the misorientation angle between all nearest-neighbor grains in the pre-shocked (blue) and post-shocked (red) states. Histogram bins are centered on integer values between $[5°, 62°]$. Inset, boundary area weighted misorientation histograms for all boundaries in the spalled region (green squares) of the pre-shocked state and just those boundaries found to be associated with voids (purple circles). Histogram values are represented by the symbols and are plotted on a log scale to emphasize differences between the distributions. Bins are again centered on integer values between $[5°, 62°]$.

Table 4.1: Summary of void locations relative to the pre-shocked microstructure. Voids in one category do not appear in another.

Void Locations	Abundance
Within resolution of M $\geq$ 4 Node	$10/485 \approx 2\%$
Within resolution of a triple line	$126/485 \approx 26\%$
Within resolution of a boundary	$196/485 \approx 40\%$
$\leq$ 10 μm from an interface	$91/485 \approx 19\%$
$>$ 10 μm from an interface	$62/485 \approx 13\%$
Total	$485/485 = 100\%$

of the sample, as is shown in Fig. 4.1(a), a cutaway view of the μCT volume. Voids are small and sparse in the average sense: the porosity over the volume of the sample is $\sim 0.006\%$.

Most voids nucleate on interfaces, namely grain boundaries, triple lines and M-nodes. As seen in Table 4.1, 68% of voids form within one voxel of these interfaces. This is as expected from previous work [69, 82, 70, 78, 73, 76, 72]. About 19% of voids form between voxel resolution and 10 μm from one of these interfaces; these voids may well have formed at boundaries that moved during the dynamic deformation and therefore are not precisely at pre-shock boundary locations. Some voids (13%) appear to form within grains (≥ 10 μm from an interface). This finding has precedent,[77] but may also be the result of unresolved twins.

4.4 Discussion

The microstructural environment

Fig. 4.2 shows number weighted histograms of the cross boundary lattice misorientation angle between neighboring grains before and after shock loading. Examination of the axes of misorientation in these distributions reveals that the sharp peaks at 60°, 39°, 35°, and 32° correspond to the 'special' CSL boundaries Σ-3, Σ-9 ($38.9°\langle 110\rangle$), Σ-27β ($35.4°\langle 210\rangle$), and Σ-27α ($31.6°\langle 110\rangle$) respectively. The widths of these peaks are broadened considerably in the post-shocked state. This finding is consistent with the average orientation of each grain being individually perturbed by the shock loading. It is also observed that the dispersion of orientations within grains increases significantly after the shock, much as is observed in quasi-static loading measurements [58].

There are some differences in the microstructure local to the voided region relative to the unvoided regions of microstructure. A subregion of the ROI was used to evaluate these differences by first forming a Laplacian surface that enclosed all the voids, then expanding this surface isotropically by 100 μm. The resultant crescent-shaped mask partitions points within the ROI into nominally voided and nonvoided regions, with the voided region occupying the region within the mask. Grains within this voided region form a Σ-3 related domain that blankets the void field. Using three large void-hosting grains as seeds, we examine grains connected to these seeds by Σ-3 boundaries and expand to their Σ-3 connected neighbors. To limit the growth of this Σ3D, connected grains must be members of the largest 500 grains within the ROI. The resulting domains contain 46 grains, make up 10% of the ROI, and span the void field. These large domains are characteristic of the voided region. Relative to outside, the voided region contains twice the boundary area fraction of Σ-3 connected grains belonging to domains with ≥ 13 constituents. The mean domain size for the region outside the voided region is 6.7 Σ-3 connected neighbors; within it is 9.0. These differences are highlighted in Fig. 4.3.

While there is a difference in Σ3D size within the voided region, there is no statistically significant variation in local misorientation distribution between the voided and unvoided regions. Area-weighted misorientation distributions for grain boundaries within randomly placed spheres of radius r were computed at the spall plane. The distributions obtained did not differ significantly across length scales at $r = 50\,\mu$m, $r = 100\,\mu$m, $r = 150\,\mu$m, or $r = 200\,\mu$m as would be expected if local grain boundary character were to explain the shape of the void field.

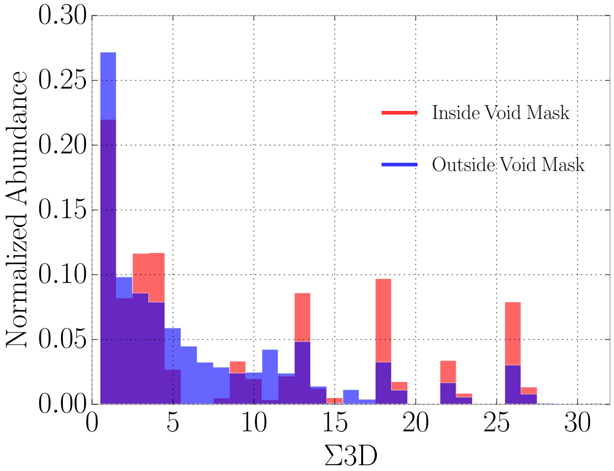

Figure 4.3: Area-normalized histogram of the Σ-3 connected domain size, Σ3D. The red distribution represents boundary area within the spalled region, while the blue distribution represents boundaries that are outside. The horizontal axis indicates the number of grains within a domain.

Void location statistics

The $N_v = 196$ voids on grain boundaries are on boundaries of only 112 unique grains, which are in general large, together comprising 25% of the pre-shock ROI. The misorientation angles of these boundaries are shown in the inset of Fig 4.2 in purple; in green, the boundary-area weighted misorientation distribution of all boundaries in the voided region is shown for comparison. Of interest is how the probability of void formation, $P[v]$, depends on a particular misorientation angle, Δg. The measured misorientation distribution in purple in Fig. 4.2 is the probability of observing a particular misorientation, given that that boundary has a void, $P[\Delta g|v]$. Application of Bayes' Theorem allows for the reversal of the conditional,

$$P[v|\Delta g] = \frac{P[\Delta g|v]}{P[\Delta g]} P[v] \tag{4.1}$$

which allows us to evaluate $P[v|\Delta g]$, the probability of forming a void given Δg, modulo the overall constant factor of $P[v]$ about which we are not concerned. The ratio of the distributions in the inset of Fig. 4.2 gives Fig. 4.4. Marked horizontally in yellow is the line at which $P[\Delta g|v]/P[\Delta g] = 1$, the case of statistical independence between v and Δg. The overlap of the error bars with $P[\Delta g|v]/P[\Delta g] = 1$ indicates that there is no evidence that misorientation angle promotes or inhibits void formation among various boundary populations, special CSL or otherwise. The two peaks at the low limit of Δg may be misleading since they are based on the formation of only two and three voids respectively. While we have marginalized over the rotation

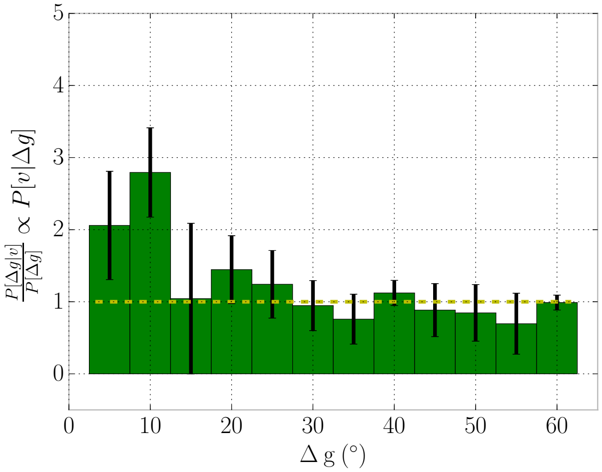

Figure 4.4: A histogram proportional to $P[v|\Delta g]$, the probability of void formation given a certain boundary misorientation angle, Δg. N_v=196. See text for details. The error bars are propagated Poisson errors from the distributions in the inset in Fig. 4.2.

axis and boundary inclination degrees of freedom, these are strongly coupled to Δg for the special CSL cases. Due to the large area fraction of Σ-3 boundary within this region, the remaining $\approx$ 100 voids that are on other, general high angle boundaries are not numerous enough to statistically resolve nucleation preferences among generalized high angle boundary types.

Resolving the relative void nucleation preference between the coherent twin boundary and general Σ-3 boundary types could further validate simulations [65]. For reasons discussed above, many of the coherent grain boundaries are missing from our analysis. Utilizing a regularized smoothing algorithm to remove discretization noise[40] of the Σ-3 grain boundaries observed, we calculate $< 1\%$ of the Σ-3 boundary area within the voided region is within 10° of the coherence criterion; the expected fraction is substantially larger than this [38]. As such, we cannot draw conclusions about nucleation preferences among this class of boundary from the current data set.

Void distribution

While the distribution of voids along the loading direction is centered at the sample mid-plane, the azimuthal distribution is nonuniform, as is clear from Fig. 4.1d. This distribution may be caused by either the microstructure of the voided region itself or by loading asymmetry.

The underlying microstructural may cause this azimuthal variation. The microstructure within the voided region contains unusually large Σ3Ds comprised of usually large grains. The implication is that the size of the constituent Σ3D may play some role in localizing the stresses that cause incipient void formation. Grain size may play a contributing role. Comparing the stresses within these regions using the far-field HEDM technique (ff-HEDM)[9, 17, 19, 20, 21] could be illuminating.

On the other hand, some facts argue for asymmetry in the loading condition as the primary cause of this distribution. As mentioned, there is no variation in the local misorientation distribution within and outside of the voided region as would be expected if local grain boundary character explained the shape of the void field. Further, the spatial variation in void location is smooth; if there were localized microstructural features associated with spots of preferential nucleation, these features would have to be non-homogeneously distributed within the microstruture, which is unlikely for a conventionally processed specimen. Under perfectly uniaxial loading conditions, by symmetry, there should be no azimuthal strain variation from the impact. Triaxiality due to asymmetric plate impact or non-ideal lateral momentum confinement can both cause release waves which are not along the nominal loading direction. These waves, when superposed with waves along the nominal loading axis are capable of modifying the regions of tension and compression. Notably, voids form in regions of tension, but from the data collected, one cannot determine the local strain states in the material. Indeed, mapping these states with ff-HEDM could assist in the resolution of questions like these.

3D grain morphology characterization

Grains forming the Σ3Ds have non-convex and re-entrant shapes, with protrusions that span hundreds of microns [83]. The complex grain conformations and the large sizes of some of the grains within the volume cannot be inferred from planar cross sections. To show this, planar slices normal to the loading axis of the 500 largest grains in the ROI are examined. For each of these grains, a sphere equivalent volume, $V_{2D,XY}$, is determined using the cross-sectional area equivalent circle diameter and compared to the 3D measured volume from the nf-HEDM measurement, V_{3D}. Taking the ratio of these quantities gives an estimate for accuracy of the naive stereographic assumption. Figure 4.5(a) plots this quantity as a function layer index, spanning the number of 4 μm spaced layers of HEDM data over which each grain persists. The black overlay represents an 80 μm perfectly spherical grain, with a $V_{\mathrm{2D,XY}}/V_{\mathrm{3D}}$ ratio of unity at the cross section at the equator of the sphere. For the largest grains, each grain's true volume is underestimated, and significant deviations from the equiaxed case show the formation of narrow protrusions from the bodies of the grains. These protrusions, however, do not appear to form isotropically; Fig. 4.5(b) shows the same metric computed from slices in a perpendicular plane and indicates overestimation of grain volume. Grain protrusions or long axes extend preferentially along the loading direction. Neither cross section accurately estimates grain volume for the larger grains in the measured region. Smaller grains exhibit apparent volume estimates more consistent with equiaxed, more spherical shapes. The Σ3D connected grains within the voided region are large (46 of these grains comprise 10% of the

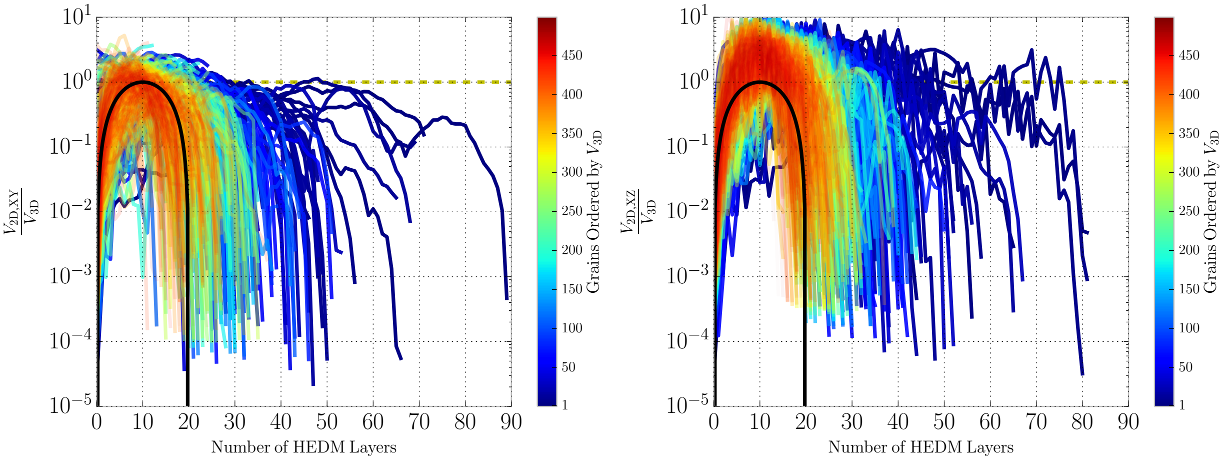

(a) (b)

Figure 4.5: Plots of the ratio between sphere equivalent volume and the actual measured volume for the largest 500 grains, ordered from largest (grain 1) to smallest (grain 500). Note, the vertical axis is scaled logarithmically. Sphere equivalent volumes are calculated by finding the sphere equivalent area of a given 2D slice in (a) the XY plane or (b) the XZ plane. Overlayed in black is the ratio plotted for a spherical grain of radius 80 μm. While the smallest grains are reasonably spherical, large grains are elongated; this is seen by noting the deviations from the black curve's shape in the curves corresponding to the larger grains. (Deviations between the horizontal extent of the black curve and the colored curves represent differences in grain size only.) Excepting the start and end points of each curve, regions where the computed ratio differs from unity represent cross-sections where simple stereographic estimates of grain size are misleading.

volume of the entire $\sim 1.7\times10^5$ grain ROI) and include the grains with these extending protrusions. These re-entrant shapes may also play some contributory role in void formation.

4.5 Conclusion

This work demonstrates a new methodology for studying shock loading that allows 3D, before and after measurements. Void observations are interpreted in the context of the surrounding initial state microstructure, *i.e.* the microstructure that received the shock. Such a pre-shock measurement was not possible prior to the development of HEDM and related high energy x-ray grain mapping methods. Three dimensional information is found to significantly affect interpretation. For example, in the present case, large networks of Σ3Ds that are specific to the voided region limit statistical statements about the grain boundary character dependence of the susceptibility to void formation. On the other hand, the prevalence of voiding within this region raises questions as to a possible role of large grains, complex grain topologies, and/or Σ3Ds.

In future work, it will be possible to fully characterize samples prior to shock loading experiments and to select specific microstructural sites of interest. Adding non-destructive strain state characterization using far-field HEDM before and after loading will yield substantially more detailed information with which to test computational models. Even in the current data set, a wealth of information (*e.g.*, grain rotation, break-up, and internal misorientation development) remains to extracted. Avenues for further work on the current data set include analyses of changes in grain morphology and of intragranular damage accumulation through observed orientation variations. More broadly, the methodology can be employed to study myriad shock loading scenarios and specimens.

Chapter 5

Case Study: Thermally Induced Porosity in a Sintered Ni-base Superalloy

Like the last chapter, this chapter follows a case which demonstrates an application of the nf-HEDM technique that requires accurate localization of microstructural interfaces. Here, the location and position of grain triple junction lines influence the interpretation of the mechanism for thermal porosity growth. The manuscript below is currently under review.

5.1 Introduction

A variety of methods have been developing over the past 10 years that use the penetration power of high energy x-rays to address internal microstructural issues in polycrystalline materials [7, 45, 9, 10, 84, 85]. The non-destructive nature of x-rays in hard materials allows the tracking of thermal [86, 87, 88] and mechanical [50, 89, 21, 59, 90, 58, 60] responses; these techniques can be extended to many additional sample treatments, types, and states. Synchrotron beams can be tuned to convenient energies for a broad range of sample materials [91] and can be used in a variety of focusing configurations. Recent work by a large collaboration involving the present authors and others has moved in the direction of combining multiple measurement modalities so as to gain a more complete picture of sample states and heterogeneous responses[21] as well as developing sophisticated sample environments [92]. Here, we describe integrated micro-computed absorption tomography (μCT) measurements of internal void distributions and near-field High Energy Diffraction Microscopy (nf-HEDM) mapping of grain shapes and orientations.

Following considerable development, powder metallurgy has become one of the most common processing routes for nickel-base superalloys used in turbine engine applications, as the process is a cost-effective means to control both alloy composition and microstructure [93, 94, 95, 96]. One downside to this pathway, however, is the tendency to form thermally induced porosity (TIP) which can have significant deleterious impacts on materials performance [97]. Powder processed nickel-base superalloys are particularly prone to TIP, as subsequent heat treatments near the high solvus temperature of the strengthening γ' phase causes expansion of entrapped gas from the atomization process and consequent nucleation of pores [98, 99, 100]. Analogous effects are present in some additive manufactured metallic materials [101, 102]. For the powder case, gas may also become entrapped by leakage during hot isostatic pressing (HIP) processing [103, 100]. The formation of TIP must be mitigated, as the pores can act as fatigue crack initiation sites and thus limit the overall mechanical performance of the alloy [97].

A nickel-base superalloy [104] sample was purposely treated to induce a significant population of thermally induced pores [99, 100]. The data are shown to reliably reproduce the expected correlations between specific microstructural features and void positions, thus validating the measurements and analysis procedures. This work then sets the stage for future work correlating density inhomogeneities of multiple origins (voids, cracks, second phase inclusions, etc) to underlying microstructure and microstructural responses. Indeed, a similar analysis may be adapted to study the interplay between microstructure and porosity in additive manufactured metals.

Crystalline grains are joined at quasi-two dimensional interfaces or grain boundaries. The boundaries are regions of excess energy density relative to the energy density in crystalline volumes;[2] the structural disorder leading to this increased energy extends over a finite thickness at the atomic scale [105]. Due to the atomic disorder, boundary regions are typically associated with a slightly reduced material density and, thus, may allow for increased diffusion rates relative to those in single crystals. Boundaries can also be sinks for impurities and in some materials have been associated with distinct structural phases [106]. The edges of grain boundaries occur at junctions where three grains meet; these are typically linear junctions known as triple lines. These linear defects can serve as pipes for atomic diffusion. Triple lines, in turn, end at four grain junctions which are essentially points, called quadruple nodes. While fortuitous alignment of grains can generate triple planes and quadruple lines, these are extremely rare and, in most cases, accidental. Triple lines and quadruple nodes, of course, can also be expected to be sinks for diffusing species and therefore can be preferred locations for TIP formation [107]. As such, we would expect pores to form at these interfaces as opposed to intragranular regions.

5.2 Experiment

5.2.1 Sample

The nickel-base superalloy sample was prepared at the Air Force Research Lab (AFRL). The as-received material was a powder processed polycrystalline nickel-base superalloy with a subsolvus heat treatment and starting grain size of approximately 5 μm . The initial volume fraction of porosity was measured in the as-received sample by automated serial sectioning SEM analysis[108] to be approximately 0.25%. The material was subsequently subjected to a supersolvus heat treatment at 1215° C for 48 hours, followed by an oil quench. This was expected to cause argon gas, which was present in solution in the matrix after the powder processing, to coalesce and form a distribution of pores throughout the material. The final measured volume fraction of porosity in the region characterized here is 5.9%, as calculated from the μCT reconstruction of the sample described below. The sample was electric discharge machined (EDM) so as to have a measured gauge section of 1 mm by 1 mm square and a length of 5 mm. Two small gold fiducial markers, approximately 30 μm × 30 μm × 50 μm in size, were affixed to the sample surface with micro-manipulators with one millimeter between the centers [44]. These markers are easily visible in tomographic images and are reconstructed from the nf-HEDM data as well so they are useful in registration of the data sets. Single layers of nf-HEDM data were collected from the sample cross-sections at the midpoints of the markers while 55 contiguous layers are collected from a volume between the markers, as described below.

5.2.2 Measurements

μCT was conducted concurrently with a nf-HEDM measurement at the 1-ID beamline at the Advanced Photon Source at Argonne National Laboratory. The combined use of these techniques provides a 3D spatially-resolved orientation field, and a map of the locations and shapes of pores larger than a few microns in diameter. The common measured volume is shown in Fig. 5.1.

Tomography

A large "box" beam, 1 mm in the vertical direction by 1.5 mm horizontally, defined by slits upstream of the sample, illuminates the entire sample cross-section and the entire region between and including the gold fiducial markers. The chosen beam energy of 65 keV is well matched to the sample cross-section dimension since the absorption length in nickel at this energy is approximately one millimeter. Images of the transmitted intensity pattern are collected with the same high resolution imaging detector as used in the nf-HEDM measurement. Spatial resolution is isotropic and is defined by the pixel pitch of 1.5 μm . Images are collected at fixed sample rotation positions, ω (the ω axis is orthogonal to the beam and vertical in the hutch), at 0.1° intervals spanning a 180° range. The counting time per image is 0.2 seconds. The μCT data volume was reconstructed using the GridRec algorithm implemented in code available at the beamline [22, 24, 23].

HEDM

The nf-HEDM measurement[9, 8, 7] again uses 65 keV x-rays, now focused in the vertical direction by silicon sawtooth refractive lenses to ~2 μm vertical × 1.5 mm horizontal. This beam illuminates a cross-section of the sample and diffraction images are collected using the same detector as described above. In this measurement, diffraction images were collected in $\delta\omega = 1^\circ$ integration intervals spanning $\Delta\omega = 180^\circ$ range. The counting time per image was 0.8 seconds and the sample rotated continuously as images were collected. As is typical, two rotation axis-to-detector distances were sampled, in this case at $L = 4.2$ and 6.2 millimeters from the rotation axis. Fifty-five such layer data sets were collected with 4 μm spacing between them so the data set spans 220 μm along the sample axis. The forward modeling computational method (FMM) [8] implemented in the IceNine software package [10] was used to reconstruct the microstructure. Each measured sample cross-section is meshed with small triangular elements (voxels), here with ~ 2.5 μm sides. This voxel size strikes a balance between computational overhead and the limiting spatial resolution of the detector which is ≈ 1.5 μm .

The lattice orientation in each voxel is independently optimized to generate maximal overlap with experimentally observed scattering over the entire image set. The 3D orientation field is constructed by integrating the reconstructed orientation fields of these 2D cross-sections. Orientation resolution of the resulting map is ~0.1° [10, 109]. The spatial resolution referred to here is specifically relevant to locations of grain boundaries. Neighboring orientations are, in effect, compared through a "confidence" or completeness measure based on the fraction of simulated Bragg peaks that are matched in the experimental data set [8, 10]. This comparison of lattice orientations is not available at the edges of the sample or in the neighborhood of voids or pores, and for this reason the nf-HEDM method has a broader resolution width with respect to locating such features. Large pores are observed through reduced values of the confidence metric but small pores are not resolved. We therefore employ the μCT data to establish clear, high resolution 3D definition of the pores.

In addition to the nf-HEDM orientation mapping and μCT density mapping, far-field high energy diffraction microscopy (ff-HEDM)[9, 17] data were also collected. These data, using a more efficient but lower resolution detector placed $\gtrsim 1$ m downstream of the sample, are used here to resolve the presence of minor phases (more conventionally, ff-HEDM is used to determine lattice orientations, elastic strains and grain centers-of-mass [9, 21]). Analysis of the raw far field diffraction images shows fundamental peaks with contributions from both the FCC matrix γ phase and the coherent $L1_2$ precipitate γ' phase and superlattice peaks with contributions from only the γ' phase. Diffracted peak intensity observed from both the matrix and the coherent precipitate is consistent with the lack of significant texture in the orientation distribution deduced from the data of Fig. 5.1a. A limited number of peaks not associated with the γ matrix phase or the γ' precipitate phase are also present, suggesting the possibility of additional phases within the alloy material. The scattering

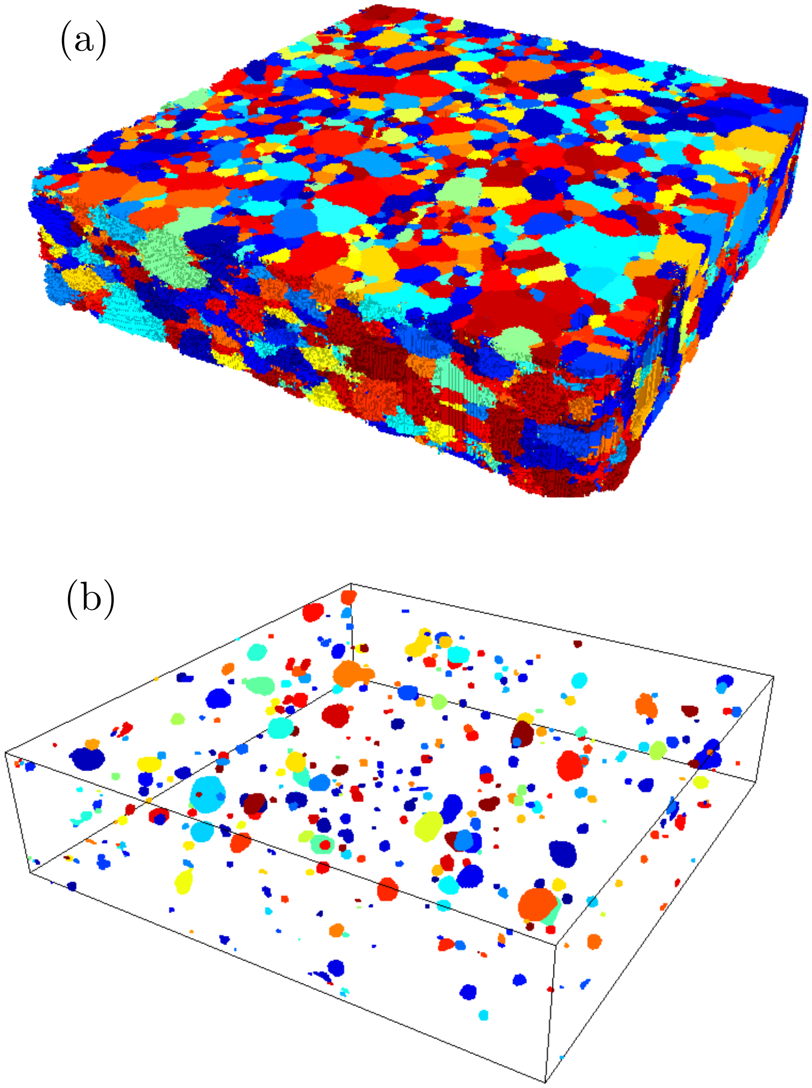

Figure 5.1: (a) The measured orientation field. Distinct colors represent distinct grains. Grains are defined as contiguous sets of ≥ 3 voxels with disorientation $< 5°$. The total measured volume is ~ 1 mm $\times$ 1mm $\times$ 220 μm and contains $\sim 17,500$ such grains. Colors are coded by grain ID numbers. (b) Pores segmented from the μCT within the volume common to the μCT measurement and the 55 layer nf-HEDM volume, mapped into the coordinate frame of the orientation field of (a). Distinct pores (~ 250) are given distinct, but arbitrary, colors.

from these phases is weak and sparse, which indicates these scatterers are small and rare and should not impact the following analysis.

5.3 Characterizations

Pores are extracted from the tomography data set by segmenting at a threshold reconstructed density level characteristic of the pore features. Excluding apparent pore features smaller than two tomography voxels, the number of pores is 264 and the average and standard deviation radius is found to be $\bar{r}_p = 6.5 \pm 4.6\ \mu\text{m}$ (sphere equivalent radius, $r = (\frac{3}{4\pi}V)^{\frac{1}{3}}$, where V is the sum of included voxel volumes) with the distribution of radii shown in Fig. 5.2a. The nf-HEDM data contain a rich set of microstructural information. To quantify the differences in the relative orientation of neighboring grains, we employ the disorientation angle, the minimum angle required to rotate a crystal's orientation or one of its symmetry equivalents about the appropriate axis to obtain the orientation of the neighboring crystal. Grains are defined here to be sets of three or more contiguous voxels with disorientations of $< 5^\circ$. This yields an average and standard deviation sphere equivalent grain radius of $\bar{r}_g = 12.1 \pm 8.4$ μm . Roughly 17,500 distinct grains are found in the 0.220 mm^3 measured volume. Figure 5.2a compares the distributions of grain and pore radii normalized by the average grain radius $\tilde{R} = r/\bar{r}_g$. These are plotted against the log of the normalized frequency and show almost two decades of pore sizes and three decades of grain sizes. Pores are, in general, smaller than the grains that make up the bulk of the volume thus allowing the association of pores with particular microstructural features.

The analysis of nearest-neighbor grain pairs shown in Fig. 5.2b, based on the $\sim 17,500$ grain network, reveals a smooth Mackenzie-like distribution associated with random orientations,[3] modulated by a comparatively large population of boundaries with 60° lattice rotations; this peak is common to low stacking fault energy fcc materials such as nickel and its alloys, and in this case are thought to be annealing twins grown during heat treatment [88]. The vast majority of the boundaries at 60° have the $\Sigma 3$ disorientation (60° rotation about the $\langle 111 \rangle$ axis). In contrast to nf-HEDM data sets in well-annealed, pure nickel[109, 88] and copper[58, 83] the current sample lacks significant peaks at $\Sigma 9$ and/or $\Sigma 27$ disorientations. This distinction may be related to the powder origin of this sample in contrast to casting or forging processing pathways.

5.4 Microstructure-pore correlation

The reconstructed μCT and nf-HEDM data sets, both shown in Fig. 5.1, are registered by hand to within the spatial resolution of the orientation field. This registration is based on both the gold fiducial markers (not depicted in Fig. 5.1) and on the

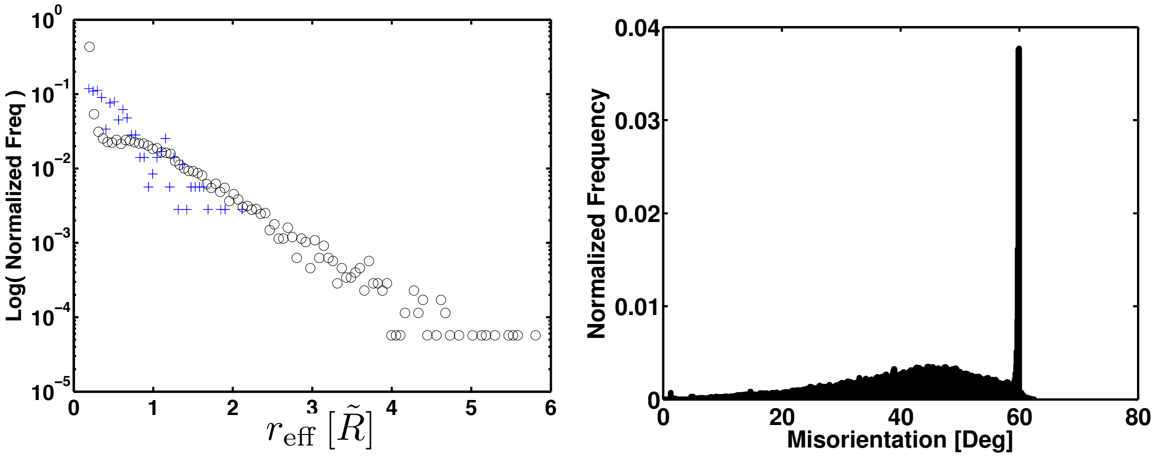

(a) (b)

Figure 5.2: Microstructure statistics. (a) Log-scaled normalized histogram of grain and pore sizes, plotted as a function of reduced sphere equivalent radius. Grain sizes are shown in black circles, pore sizes in blue pluses. The reduced radius is defined as the radius of the object divided by the average *grain* radius, $\bar{r}_g = 12.6\ \mu\text{m}$. The bin width is 0.05 in reduced units. In each case, the largest features have only one or zero occurrence per bin. (b) Normalized disorientation angle distribution for all unique nearest-neighbor grain pairs. The peak at 60° is characteristic of low stacking fault, face centered cubic metals; [2] the vast majority of these neighbor pairs have the $\Sigma 3$ disorientation, corresponding to a 60° rotation about a $\langle 111 \rangle$ axis. The otherwise essentially smooth distribution is characteristic of randomly oriented cubes [3]. Bins are 0.1° wide.

Table 5.1: Summary of statistics for triple lines. All units of distance measured in $\tilde{R} := r/\bar{r}_g$. The column labeled Δ is the difference of the two preceding columns. COM refers to center of mass, NTL to nearest triple line, NQN to nearest quadruple node, and RP to random points.

Feature	$\langle \mid \mathbf{r}_{RP,NTL} \mid \rangle$	$\langle \mid \mathbf{r}_{\text{Pore},NTL} \mid \rangle$	Δ
Pore COM to NTL	0.68	0.44	0.25
All Pore Voxels to NTL	0.68	0.36	0.32

pore structures which are resolved by both of the measurements (i.e., relatively large pores).

To facilitate analysis of pore proximity to microstructural features, triple lines and quadruple nodes were extracted directly from the voxelized orientation field by identifying and connecting discrete points connecting neighboring grain triples. Grain orientations are not smoothed during this process, but one nearest-neighbor mean-position filter was applied to smooth the extracted triple lines. Quadruple nodes were defined to be the points terminating these lines. Anecdotal examination of typical pore-orientation field topologies shows myriad cases in which a pore has formed in close proximity to either a triple line or quadruple node. Prototypical examples are pictured in Fig. 5.4. We use the term “close proximity” due to the finite (and different) measurement resolutions of the HEDM and μCT techniques. Figure 5.4a depicts a triple line in black formed by the intersection of three grains. Only two cross sections of the 3D orientation field are plotted, but volumetric orientation information from the adjacent layers was used to extract the entire triple line shown. A triangulation of a segmented pore is plotted in light blue, and the triple line, at the intersection of the same three grains, can be seen to extend to one side of the pore and resume at the other side. This is a typical arrangement for a pore that has nucleated on or near a triple line and implies the morphology of the line itself is important in determining the ultimate morphology and location of the pore. Figure 5.4b depicts a side view of this same system.

Figure 5.4c shows a typical arrangement for a pore nucleating close to or on a quadruple node. Several triple lines formed by the intersection of nearby grains terminate in quadruple nodes on the boundary of a single grain (dark brown in the figure); thus the pore has formed within close proximity to many of these features. While there exist some pores that appear to be near the centers of grains, these are rare by comparison to the morphologies illustrated here.

The computational extraction of large numbers of voids, triple lines and quadruple nodes allows a statistical analysis of the spatial correlations between these features. It is expected that the average distance from a random point in the microstructure to the nearest triple line or quadruple node will be of the order of the grain radius. If pores nucleate at random positions, we expect this same result. If pores nucleate preferentially at or near these features, then the distribution of distances should be

Table 5.2: Summary of statistics for quadruple nodes. Abbreviations are the same as in Table 5.1.

Feature	$\langle \mid \mathbf{r}_{RP,NQN} \mid \rangle$	$\langle \mid \mathbf{r}_{\text{Pore},NQN} \mid \rangle$	Δ
Pore COM to NQN	0.88	0.63	0.25
All Pore Voxels to NQN	0.88	0.52	0.36

compressed to smaller values. For each pore, the minimum perpendicular distance to each feature type is calculated. Distributions using both the pore centers of mass and all points within the pores are shown in Fig. 5.5. Also shown are distributions obtained by finding the minimum distance from $N \approx 4 \times 10^5$ randomly generated points to the triple lines and quadruple nodes. The pore-associated points indeed do occur closer to the origin than the peaks for the ensemble of random points. The data in Fig. 5.5a are noisy due to the limited number of $\sim$250 pores within the volume. The pores contain on average $\sim$340 μCT voxels. Using the ensemble of these points gives the distribution in Fig. 5.5b. The fact that the relatively smooth solid curves in Fig. 5.5b are consistent with the noisy distributions in Fig. 5.5a implies that most voids have isotropic shapes. We will discuss exceptions to this observation below.

After generating the random points, we calculate the average distance to the nearest triple line, $\langle \mid \mathbf{r}_{RP,NTL} \mid \rangle$, and the average distance to the nearest quadruple node, $\langle \mid \mathbf{r}_{RP,NQN} \mid \rangle$. We then may compare these distances to the averages for the pore-associated points, from either the pore center of mass or all pore constituent points to the nearest triple line or quadruple node. Results for triple lines are summarized in table 5.1 and results for quadruple nodes are summarized in table 5.2. For a given set of pore-associated points and either the nearest triple line (NTL) or nearest quadruple node (NQN), the column of the table labeled Δ represents the difference of the first two columns, and indicates that voids are substantially closer, by both center-of-mass or volume point measures, to these microstructural features than are random points.

While the correlations described are qualitatively convincing, we next test these results for statistical significance. Because we are comparing empirical distributions, we employ non-parametric tests to perform confidence testing. Two such tests used to differentiate between distributions are the Wilcoxon rank-sum (WRS) test[110] and the Kolmogorov-Smirnov (K-S) test [111, 112, 113, 114]. These tests differ in their implementation but are each used to establish whether collected observations from two separate distributions come from the same underlying distribution. Performing the WRS and K-S tests comparing the collection of $\left|\mathbf{r}_{\text{Pore},NTL}\right|$ and $\left|\mathbf{r}_{\text{Pore},NQN}\right|$ distributions with the corresponding $\left|\mathbf{r}_{RP,NTL}\right|$ and $\left|\mathbf{r}_{RP,NQN}\right|$ distributions shows statistical significance at vanishing p levels, with p being the probability that the two distributions are drawn from the same population. Figure 5.6 shows the cumulative distributions associated with the distributions in Fig. 5.5b, and illustrates clearly that pores are found closer to quadruple nodes and triple lines than random points.

In addition to examining pore location within the grain network, the correlation

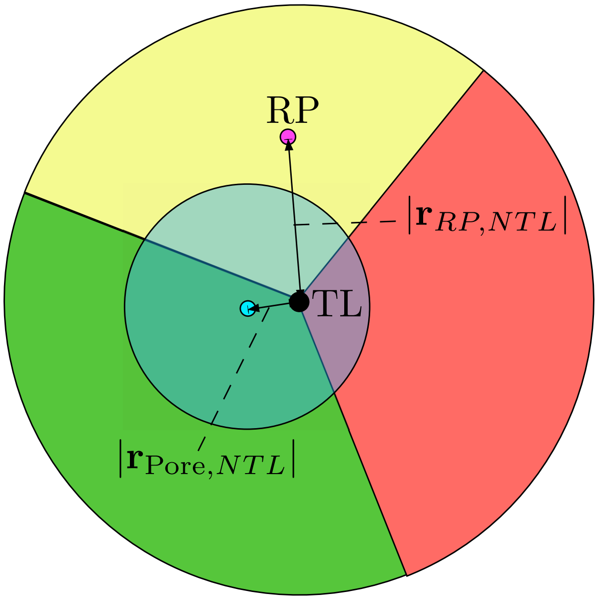

Figure 5.3: A 2D grain schematic illustrating the statistical used for analysis. The green, red, and yellow regions represent grains; pictured is the cross section of an imaginary tricrystalline cylindrical sample. These grains are joined by a triple line orientated along the axis of the cylinder, depicted in black. A pore is depicted transparent cyan, with its center of mass in darker cyan. The distance between this center of mass and the triple line is $|\mathbf{r}_{\text{Pore},NTL}|$. If there were another triple line in the sample, the nearest would be chosen to compute this quantity. A random point is shown in magenta. The distance between this point and the nearest triple line is then $|\mathbf{r}_{RP,NTL}|$.

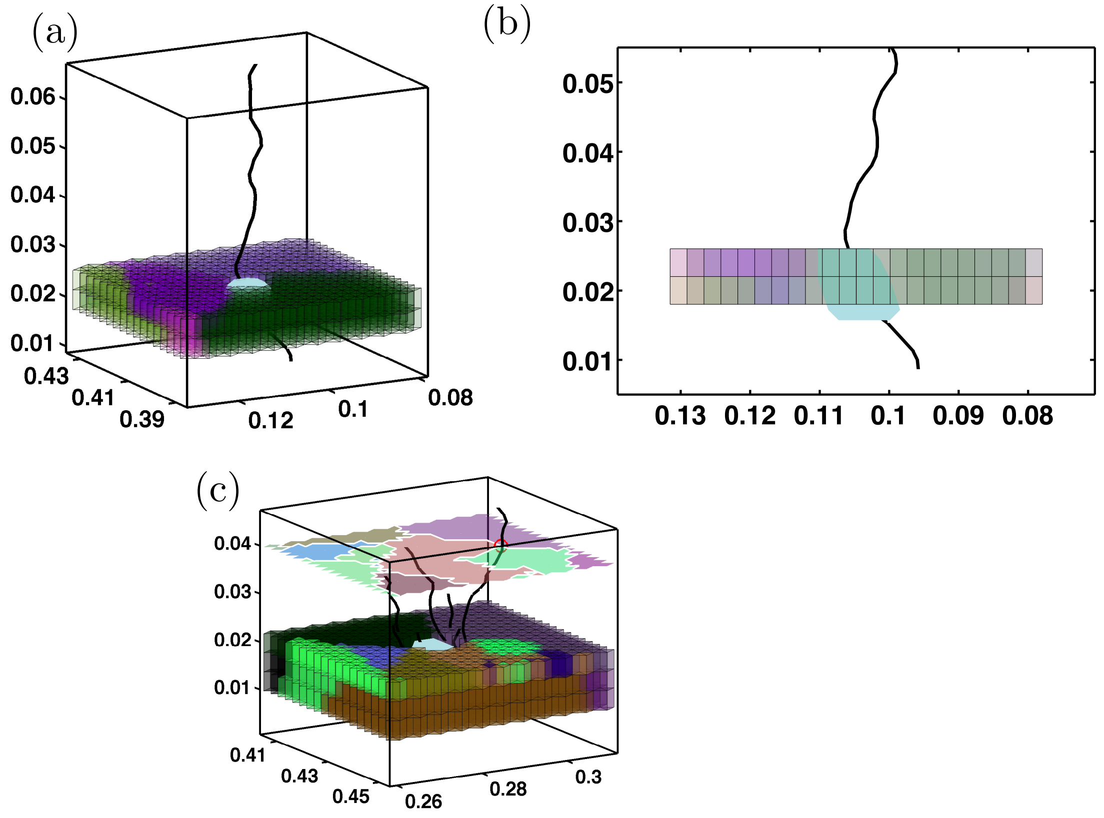

Figure 5.4: Typical grain–pore topologies. In each figure, a triangulation of pore points is shown in light blue together with neighboring grain orientations. Orientations are colored by mapping Rodrigues orientation vectors to red-green-blue color vectors. (a) A pore formed on a triple line (black). The triple line is formed by the intersection of the dark green, light purple, and dark purple grains. While the entire pore volume is shown, only two layers of the measured orientations are shown in order to make the pore visible; the same three grains enclose the pore and intersect along the entire length of triple line shown. (b) shows the same pore-grain system as in (a), depicted from a side view with the orientation information made partially transparent to allow visualization of the pore. The orientation of the triple line appears correlated with the longer axis of the anisotropic void shape. (c) A pore located at a quadruple node; in fact, several near-by triple lines terminate on the darker brown grain in the foreground of the lower orientation layers, which is orientationally distinct from the grains above it. A 2D representation of the orientation field approximately 20 μm above the shown 3D structure illustrates the triple line's intersection–marked with the red circle–with this plane. The statistical significance of these examples is discussed in the text. All dimensions are in millimeters.

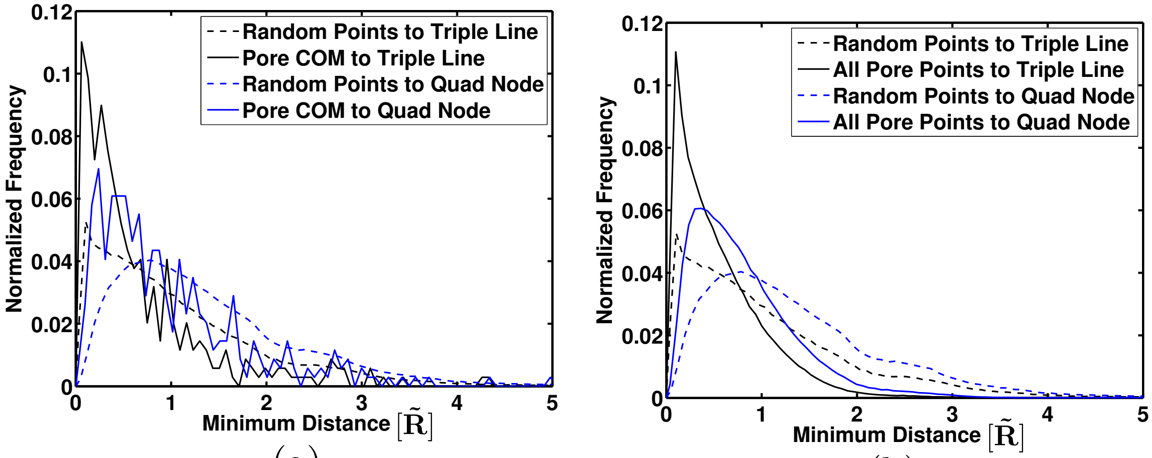

(a) (b)

Figure 5.5: The minimum distance from each pore to the nearest quadruple node and triple line compared to the minimum distance from random points within the microstructure to the same set of quadruple nodes and triple lines. The abscissa is in dimensionless multiples of the average grain radius, $\bar{r}_g = 12.6\mu$m. We call this unit $\tilde{R}$. (a) uses the pore center of mass as a proxy for pore location; (b) uses all points segmented from the tomography as pore constituents.

between crystallographic orientation and pore location was probed by examining the grains adjacent to the segmented pores. The pairwise disorientation between triples of crystals adjacent to the pores was computed and classified by both coincident site lattice number and disorientation angle. The distribution of these quantities in grains adjacent to pores showed no discernible difference with the disorientation distribution shown in Fig. 5.2b. Further, no significant correlation existed among the groups of triples.

Pore-grain morphologies such as that shown in Fig. 5.4b suggest that anisotropic pores form with their long axis aligned with a parent triple line. Here, we demonstrate that the statistics support this observation. After triple line segments that are interrupted by a pore are connected by linear interpolation, the end-to-end vector, $\vec{v}$, defining the local triple line direction is computed. Inertia tensors are computed for the pore and diagonalized as a metric for anisotropy. Taking the ratio of the largest eigenvalue to the smallest eigenvalue defines an aspect ratio, c/a, for all pores of usable size for comparison to a nearby triple line. The median $c/a = 1.5$ is used as a cutoff to select anisotropic cases, and the $N = 100$ pores above this threshold are examined. An alignment coefficient, $A = |\vec{v} \cdot \vec{e}|$, is computed for each pore, where $\vec{e}$ is the principle axis as computed from the inertia tensor. If multiple lines bridge the pore, these contributions are averaged on a pore-by-pore basis. Results are histogrammed in Fig. 5.7. Uniformly distributed random normals on the unit sphere

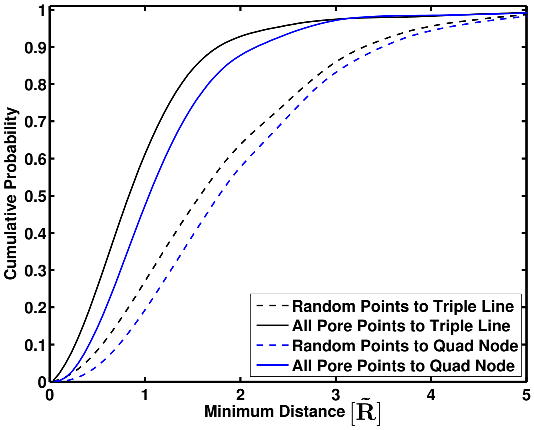

Figure 5.6: The cumulative distribution functions (CDFs) for the data shown in Fig. 5.5, obtained by integration. The CDFs for the minimum distance from pore centers of mass to a triple line and for the minimum distance from pore centers of mass to a quad node are always greater than their counterparts using random points.

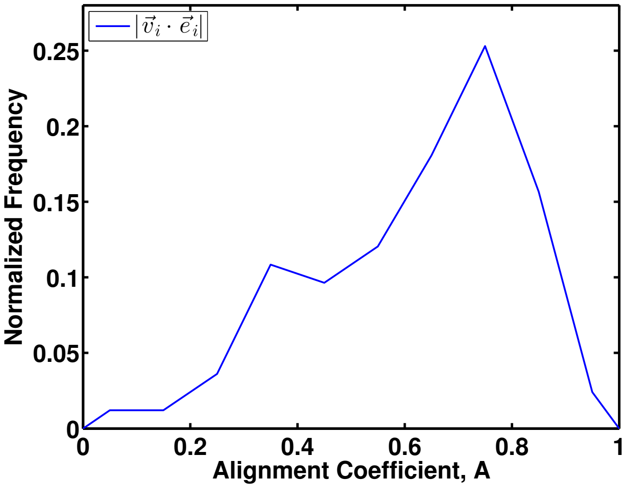

Figure 5.7: The distribution of the alignment coefficient (cosine of the angle) between the principle axis of anisotropic pores and the orientation of the nearest triple line.

would result in a flat distribution. The peak at $A \approx 0.75$ indicates the pore principle axes are more aligned with nearby triple lines than would be expected if the principle axes were randomly oriented.

5.5 Discussion

Statistical analysis shows both that pores are found on average to be 0.32 $\tilde{R}$ closer to triple lines and 0.36 $\tilde{R}$ closer to quadruple nodes than random points and also that the long axes of anisotropic pores tend to be correlated with the direction of nearby triple lines. The preferential nucleation of pores with these morphologies at microstructural interfaces points to possible mechanisms for their formation. The observations are consistent with thermally induced pores being a result of either trapped gas diffusing along the triple lines and collecting at a point or coarsening grains squeezing existing trapped gas along a triple line.

Gas that remains trapped in the microstucture following the initial processing treatments will undergo thermally activated diffusion during subsequent heat treatment. This diffusion is accelerated at regions of high free volume; within the bulk of the sample these regions exist at the interfaces between grains, with the highest free volume occurring at triple lines and quadruple nodes. It is possible that trapped gas that initially starts on or diffuses to a triple line will diffuse preferentially along the line, coalescing into a pore as more gas accumulates, and expanding at high temperature.

A similar mechanism involves the coarsening of grains during heat treatments. Gas trapped during initial atomization will be localized between atomized particles.

Subsequent heat treatments will cause fusing and densification of these particles and coarsening of grains in the sample. This process will necessarily displace the trapped gas, which will again flow along triple lines toward quadruple nodes. The data collected, unfortunately, do not allow for differentiation of these cases with respect to the sample discussed. *In-situ* or multi-state studies are necessary to resolve these questions. What we show here, however, is clear correlation between regions of high free volume and the location of thermally induced pores. In addition, we demonstrate a capability that will allow sequences of states to be characterized.

5.6 Conclusions

Multimodal, high energy x-ray measurements, here primarily nf-HEDM and μCT, allow for the collection of statistical microstructural information or analysis of critical events within polycrystals with full 3D localization of the events and the surrounding microstructural neighborhoods. The combined strengths of these techniques were leveraged to extract complete 3D information on the microstructure of a nickel-base superalloy sample exhibiting significant thermally induced porosity. Triple lines and quadruple nodes were then extracted from the orientation field; the grain network was also analyzed. The spatial locations of the thermally induced pores were cataloged and compared to the locations of the nearest triple lines and quadruple nodes. We find that the statistical ensemble of pores is found closer to triple lines and quadruple nodes than are random points. These results have been found to be statistically significant. No evidence is currently present to suggest that there are groups of crystallographic orientations around triple lines and quadruple nodes that preferentially nucleate these pores. These pores may form by the diffusion of trapped gas along the triple lines or by coarsening grains displacing existing trapped gas along the triple lines.

As previously discussed, porosity significantly impacts material properties both in materials sintered from powder and in additive manufactured materials. While powder metallurgists have characterized factors that influence porosity in that processing pathway, much less is known about how porosity forms during the various additive manufacturing processing routes. Hard x-ray techniques like those described have proven to be a time-efficient and nondestructive way to interrogate bulk polycrystalline volumes and should be considered for studies of macroscopic structures with large gradients in thermal history. Similarly, these methods are recommended whenever crystallography and material density must be jointly interrogated as in cases of *in situ* or *ex situ* damage nucleation or propagation, during the coarsening of porous structures, or during the active development of porosity. Combined with full ff-HEDM analysis, this suite of techniques creates a spatially resolved field of stress, orientation, and density values from which full mesoscopic analysis is possible. Clearly, these techniques are most powerful when employed concurrently.

This work also serves to highlight the challenges and rewards of handling large, 3D, multi-parameter data sets. While examples of particular phenomena can be located by direct, human searching, statistical significance must be determined through automated characterizations that require the development of computer codes and appropriate data structures, as has been done here. The wealth of information in these data sets requires one to focus on one or two specific aspects and leave many additional characterizations for future work.

Chapter 6

Conclusion and Directions for Future Work

6.1 Recapitulation

This work has sought to the identify fundamental limitations and characteristics of the forward modeling method of reconstruction. The FMM is challenging to characterize from a conceptual standpoint by nature of the optimization processes integral to its implementation. To find the core limits of the technique in its current form, significant effort focused on comparing a precisely performed nf-HEDM measurement with a 'ground truth' surface EBSD measurement. The FMM reconstruction of the experimental data was heavily constrained by using many peaks to optimize the reconstruction of each voxel's orientation. Performed in this way, the spatial accuracy of the reconstructed grain boundaries was found to be within the limits imposed by the discretization of the underlying reconstruction grid and the effective pixel size of the nf-HEDM CCD detector. The orientation resolution was found to depend linearly on the size of the angular integration interval, but was found to be $< 0.05°$ for the conventionally utilized experimental values of of 0.5-1°.

Neither orientation resolution nor grain boundary fidelity is found to depend strongly on the L_i chosen, though the number and spacing of detectors used was found to influence subtle features of the reconstruction in understandable ways. The necessity of iteratively improving a reconstruction by bootstrapping between increasing $Q_{\max}$ and improving $\mathbf{E}$–even when good initial estimates for $\mathbf{E}$ were obtained–was made evident. It has been demonstrated that reconstructions of reasonable to good fidelity may be obtained through reconstruction with sparsely populated signal. Most importantly, a calibration sample was fully characterized non-destructively; this sample can serve as a round robin calibration for new non-destructive imaging techniques or a test bed for exotic and novel reconstruction methods.

The sensitivity of the FMM reconstruction to the detector geometry of the virtual experiment was extensively evaluated. The responses of four objective functions, each characterizing grain boundary fidelity, were measured when subjected to perturbations around the equilibrium point in the 6D detector position space. Perturbations to R_k, R_j, and R_L were found to most significantly impact reconstructed boundary positions, while shears of the detectors in the vertical direction, Δr_k, were associated with accumulation of significant noise at grain boundary and the development of artificial boundary curvatures. The strength of the coupling between perturbations in different dimensions was found to be of highly variable magnitude, with some coupling weak enough to be safely ignored. Strong coupling between detector center of mass terms influenced boundary positions, while coupling between many terms contributed to noise development.

A new approach to optimizing the components of $\mathbf{E}$, intensity convolution, was proposed to replace naive Monte Carlo and was shown to converge to $\mathbf{E_0}$ in a controlled simulation case devoid of non-geometric peak intensity variations. Some measure of success in modeling these intensity variations was demonstrated, with high comparative success exhibited for the Lorentz factor and some comparative setbacks evident for modeling of Debye-Waller intensity variation. These computations will serve a reasonable springboard, should an interested experimenter desire to advance techniques utilizing intensity modeling or simulation.

Following these developments, two cases utilizing proper application of nf-HEDM spatial resolution were illustrated. In the first, a true *tour-de-force* involving the efforts of many, the results of three experiments were synthesized to examine the microstructural affectors of voiding in a shocked copper sample. While no preference with respect to grain boundary character was discovered, voids were found to be localized in a region of microstructure with features dominated by large, topologically complex networks of Σ-3 related grains. In the second case, tomographic and orientation field data were combined to examine the microstructural features influencing the presence of thermally induced porosity in a nickel-base superalloy. Pores were found to be statistically associated with microstructural interfaces and elongated along triple lines. Each of these examples illustrates results with interpretations that depend critically on high fidelity spatial information and would be unattainable without careful adherence to disciplined reconstruction principles.

6.2 Lessons Learned

Work performed in Chapters 2 and 3 point toward guidelines for data collection and reconstruction that accurately reproduces physically present features within the microstructure. The vertical profile of the beam should be made as narrow as possible with the focusing optics, both to minimize finite beam width effects and to collect the highest order scattering possible. One should be aware that by placing the line-focused beam at the bottom of the detector, a very good approximation to k_i may be imaged directly, an especially useful feature when seeking to the control the deleterious errors shown in Chapter 3. Further, in this configuration, the total number of diffraction peaks collected is generally greater than a configuration in which data collection is performed with the beam in the center of the detector. This is due to the cubic dependence between $Q_{\max}$ and the total number of peaks observed. (The relevant comparison involves examining the tradeoff between collecting twice as many peaks at half the $Q_{\max}$ by including the lower half plane scattering. This tradeoff only becomes worth considering when the high order scattering is too weak to be viewed on the detector.) There do not appear to be significant differences in the fidelity of the reconstructed microstructure for 'reasonable' choices of L_i, provided a good approximation for $\mathbf{E}_0$ is found. Shrinking the angular integration interval has been shown to linearly improve the angular resolution of the reconstructed microstructure. An experimenter can select the appropriate angular interval to achieve desired resolution.

To ensure the highest fidelity reconstructions, a practitioner of nf-HEDM should utilize as high a $Q_{\max}$ as possible for reconstruction, ideally > 14 Å. Enforcing this condition requires good optimization of $\mathbf{E}$, and essentially shrinks the size of the region of the parameter space in which any reconstruction can be found at all. Colloquially, reconstruction via the FMM becomes more 'difficult' (requirements are more precise), but the results are more accurate. If spatial features are not of critical importance, high $Q_{\max}$ is not necessary; good approximations to the physical microstructure may also be obtained through sparse sampling within the angular space.

6.3 Prospects for Future Work

6.3.1 Au Calibration Specimen

While much has been learned from characterization of the calibrant, further worthwhile endeavors include:

- Investigating in detail the decline in reconstruction quality at 0.2° angular integration steps and below and its cause. Following completion of this step, examining the orientation resolution of the nf-HEDM reconstruction at and below this limit;
- performing misorientation space analysis of the grain network as a function of various parameter modifications;
- comparing voxel-by-voxel orientation variations between EBSD and nf-HEDM data sets and characterizing intragranular orientation variations in detail; and,
- reconstructing the bulk layers and hosting the data publicly.

6.3.2 Technique Development

Other extensions for the simulation suites and intensity convolution could include:

- illustrating predictive power of the partial derivatives computed by propagating known perturbations and comparing the output with a reconstruction at that perturbation;
- extending to objective functions that include metrics that characterize the reconstructed orientations; and,
- conducting a dedicated experiment to carefully measure non-geometric intensity variations.

6.3.3 Shocked Copper

Given the wealth of pre-processed data from the shocked copper experiment, one could imagine:

- characterizing orientation gradients that develop as a result of the shock loading;
- examining grain shape change;
- computing some measure of dislocation content (Nye Tensor or otherwise) to quantify damage accumulation; and,
- perform a far-field HEDM experiment on the post-shocked state to map the strain field of the sample.

Each of these research thrusts represents a significant investment in time and energy; hopefully, amid the fray associated with scrambling toward ever more novel measurements, some of these questions can be answered.

6.4 Looking Forward

The prospects for researchers desiring to continue to develop HEDM have never looked better. Within the materials community, there is ever increasing interest in leveraging the significant advancements in non-destructive characterization techniques made over the past 10 (and prior) years to create multimodal datasets of scale and dimension never before attained. For example, the herculean task of collecting, reconstructing, and registering nf-HEDM spatial orientation information, ff-HEDM stress/strain information, phase and absorption contrast tomography information reflecting material density, and digital image correlation-based extensometry, while still herculean, is now commonplace. *Tours-de-force* are the new norm. At the same time, real-time feedback is becoming necessary for the next generation of measurements.

Two concurrent thrusts must be balanced going forward, if access to these novel data sets is going to spread. The first involves engineering and maintenance of the systems currently implemented. Updates and patches to fundamental code infrastructure must be developed in order to improve the usability and effectiveness of the tools which allowed such pioneering expansion. These code bases should be refactored and streamlined not because they are ineffective but because maintenance and support of these systems has become a serious constraint on man-hours better spent on further innovation or science. Pipelines which automatically log and archive metadata must be implemented in a robust manner, again to lessen the transaction costs and ease the learning curves associated with identifying and storing experimentally critical information. Each of these tasks could easily occupy a team of professional developers for a time, and in part, these issues are of concern because such monumental non-scientific tasks currently occupy the attentions of graduate students who are also trying to achieve scientific results and further innovation. These challenges will likely remain until funding bodies recognize the potential gains of explicitly facilitating collaboration between scientists and professional-grade developers.

The second critical research thrust involves further innovation on the part of scientists implementing these techniques. Continuing to develop existing technologies and algorithms with an eye toward multi-modal integration will enable the creation of even more intricate and high dimensional data sets. To this point, learning to model and simulate diffracted intensities is a critical first step toward voxel-by-voxel strain resolution. Elaborate bootstrapping and optimization techniques may be possible by integrating nf-HEDM and ff-HEDM into a comprehensive diffraction microscropy experiment that directly gives spatially resolved orientation and strain fields at the microscale, without the need for time consuming and piecemeal reconstruction and registration techniques. Those multi-modal reconstruction and registration techniques which facilitated the case studies of Chapters 4 and 5 have the potential to hinder further science when viewed as a necessary component of the measurement paradigm of the future.

While balancing engineering and optimization of existing systems with further innovation can be challenging, productive multidisciplinary collaborations (like those which facilitated this work) have the best hope of advancing the bounds of knowledge in this domain and beyond.

Appendix A

HEDM-EBSD Surface Registration

Algorithm 2: GetCost($\{r_{\text{EBSD}}\}$, z_{surface}) gives optimum registration and lowest cost to register boundary sets.

```
Data: $z_{\text{surface}}$, EBSD surface boundaries $\{r_{\text{EBSD}}\}$
Result: $\epsilon$, the smallest mean error for $z_{\text{surface}}$ and $R$, the corresponding
        registration to $\{r_{\text{EBSD}}\}$
begin
    $b_{\text{HEDM}} \leftarrow$ GetBoundaries($z_{\text{surface}}$) ;
    $\epsilon_{min} \leftarrow \infty$;
    $R_{\text{best}} \leftarrow \mathbb{I}$;
    $x_{\text{best}}, y_{\text{best}} \leftarrow 0$;
    for $\theta \leftarrow \theta_{low}$ to $\theta_{high}$ do
        for $x \leftarrow x_{low}$ to $x_{high}$ do
            for $y \leftarrow y_{low}$ to $y_{high}$ do
                $\epsilon' \leftarrow 0$;
                $R \leftarrow$ Rotation($\theta$);
                $b'_{\text{HEDM}} \leftarrow (R * b_{\text{HEDM}}) + (x, y)$;
                for $b'_i \in b'_{HEDM}$ do
                    $\epsilon' \leftarrow \epsilon' + \min_j \sqrt{(b'_i - r_{j,\text{EBSD}})^2}$;
                end
                $\epsilon' \leftarrow \epsilon' / (\sum i)$;
                if $\epsilon' < \epsilon_{\text{best}}$ then
                    $R_{\text{best}} \leftarrow R$;
                    $x_{\text{best}} \leftarrow x$;
                    $y_{\text{best}} \leftarrow y$;
                    $\epsilon_{\text{best}} = \epsilon'$;
                end
            end
        end
    end
    return ($R_{\text{best}}, x_{\text{best}}, y_{\text{best}}, \epsilon_{\text{best}}$);
end
```

Bibliography

[1] J. Lind, *In-situ High-Energy Diffraction Microscopy Study of Zirconium Under Uni-axial Tensile Deformation.* PhD thesis, Carnegie Mellon University, 2013.

[2] D. L. Olmsted, S. M. Foiles, and E. A. Holm, "Survey of computed grain boundary properties in face-centered cubic metals: I. grain boundary energy," *Acta Materialia*, vol. 57, no. 13, pp. 3694 – 3703, 2009.

[3] J. Mackenzie, "Second paper on the statistics associated with the random disorientation of cubes," *Biometrika*, vol. 45, no. 1-2, pp. 229–240, 1958.

[4] Group on Advanced Materials, "Materials genome initiative for global competitiveness," 2011.

[5] J. von Neumann, *Metal Interfaces.* Cleveland: American Society for Metals, 1952.

[6] R. D. MacPherson and D. J. Srolovitz, "The von neumann relation generalized to coarsening of three-dimensional microstructures," *Nature*, vol. 446, pp. 1053–1055, Apr. 2007.

[7] H. F. Poulsen, *Three-Dimensional X-Ray Diffraction Microscopy: Mapping Polycrystals and their Dynamics.* Springer Tracts in Modern Physics, 2004.

[8] R. M. Suter, D. Hennessy, C. Xiao, and U. Lienert, "Forward modeling method for microstructure reconstruction using x-ray diffraction microscopy: Single-crystal verification," *Review of Scientific Instruments*, vol. 77, no. 12, 2006.

[9] U. Lienert, S. F. Li, C. M. Hefferan, J. Lind, R. M. Suter, J. V. Bernier, N. R. Barton, M. C. Brandes, M. J. Mills, M. P. Miller, B. Jakobsen, and W. Pantleon, "High-energy diffraction microscopy at the Advanced Photon Source," *JOM*, vol. 63, no. 7, pp. 70–77, 2011.

[10] S. F. Li and R. M. Suter, "Adaptive reconstruction method for three-dimensional orientation imaging," *Journal of Applied Crystallography*, vol. 46, pp. 512–524, Apr 2013.

[11] N. Ashcroft and N. Mermin, *Solid State Physics.* Saunders College, 1976.

[12] C. Kittel, *Introduction to Solid State Physics.* John Wiley & Sons, Inc., 6th ed., 1986.

[13] S. Shastri, K. Evans-Lutterodt, R. Sheffield, A. Stein, M. Metzler, and P. Kenesei, "Kinoform lens focusing of high-energy x-rays (50 - 100 keV)," in *SPIE Proceedings*, 2014.

[14] L. Renversade, R. Quey, W. Ludwig, D. Menasche, S. Maddali, R. M. Suter, and A. Borbély, "Comparison between diffraction contrast tomography and high-energy diffraction microscopy on a slightly deformed aluminium alloy," *IUCrJ*, vol. 3, Jan 2016.

[15] S. F. Li, "IceNine." https://github.com/FrankieLi/IceNine.

[16] J. Lind, A. D. Rollett, R. Pokharel, C. M. Hefferan, S. F. Li, U. Lienert, and R. M. Suter, "Image processing in experiments on, and simulations of plastic ddeformation of polycrystals," in *Proceedings of IEEE International Conference on Image Processing*, IEEE, 2014.

[17] J. V. Bernier, N. R. Barton, U. Lienert, and M. P. Miller, "Far-field high-energy diffraction microscopy: a tool for intergranular orientation and strain analysis," *The Journal of Strain Analysis for Engineering Design*, vol. 46, no. 7, pp. 527–547, 2011.

[18] J. K. Edmiston, N. R. Barton, J. V. Bernier, G. C. Johnson, and D. J. Steigmann, "Precision of lattice strain and orientation measurements using high-energy monochromatic X-ray diffraction," *Journal of Applied Crystallography*, vol. 44, pp. 299–312, Apr 2011.

[19] J. Oddershede, B. Camin, S. Schmidt, L. P. Mikkelsen, H. O. Soerensen, U. Lienert, H. F. Poulsen, and W. Reimers, "Measuring the stress field around an evolving crack in tensile deformed Mg AZ31 using three-dimensional x-ray diffraction," *Acta Materialia*, vol. 60, no. 8, pp. 3570 – 3580, 2012.

[20] A. Beaudoin, M. Obstalecki, W. Tayon, M. Hernquist, R. Mudrock, P. Kenesei, and U. Lienert, "In situ assessment of lattice strain in an Al-Li alloy," *Acta Materialia*, vol. 61, no. 9, pp. 3456 – 3464, 2013.

[21] J. C. Schuren, P. A. Shade, J. V. Bernier, S. F. Li, B. Blank, J. Lind, P. Kenesei, U. Lienert, R. M. Suter, T. J. Turner, D. M. Dimiduk, and J. Almer, "New opportunities for quantitative tracking of polycrystal responses in three dimensions," *Current Opinion in Solid State and Materials Science*, vol. 19, no. 4, pp. 235 – 244, 2014.

[22] Y. Wang, F. De Carlo, I. Foster, J. Insley, C. Kesselman, P. Lane, G. von Laszewski, D. Mancini, I. McNulty, M. Su, and B. Tieman, "Quasi-real-time x-ray microtomography system at the advanced photon source," in *SPIE Proceedings*, vol. 3772, p. 318, 1999.

[23] F. De Carlo, P. Albee, Y. Chu, D. Mancini, B. Tieman, and S. Wang, "High-throughput real-time x-ray microtomography at the advanced photon source," in *SPIE Proceedings*, vol. 4503, 2002.

[24] B. Dowd, G. Campbell, R. Marr, V. Nagarkar, S. Tipnis, L. Axe, and D. Siddons, "Developments in synchrotron x-ray computed microtomography at the national synchrotron light source," in *SPIE Proceedings*, vol. 3772, 1999.

[25] B. Warren, *X-Ray Diffraction.* Dover, 1990.

[26] C. Chantler, K. Olsen, R. Dragoset, J. Chang, A. Kishore, S. Kotochigova, and D. Zucker, "Detailed tabulation of atomic form factors, photoelectric absorption and scattering cross section, and mass attenuation coefficients for Z = 1-92 from E = 1-10 eV to E = 0.4-1.0 MeV," 1995, 1996, 2001.

[27] J. Als-Nielsen and D. McMorrow, *Elements of Modern X-ray Physics.* Wiley, second ed., 2011.

[28] R. Suter, "Unpublished." 2016.

[29] I. Robinson and R. Harder, "Coherent x-ray diffraction imaging of strain at the nanoscale," *Nat Mater*, vol. 8, no. 4, pp. 291–298, 2009.

[30] G. Xiong, J. N. Clark, C. Nicklin, J. Rawle, and I. K. Robinson, "Atomic diffusion within individual gold nanocrystal," *Scientific Reports*, vol. 4, pp. 6765–, Oct. 2014.

[31] A. Ulvestad, A. Singer, J. N. Clark, H. M. Cho, J. W. Kim, R. Harder, J. Maser, Y. S. Meng, and O. G. Shpyrko, "Topological defect dynamics in operando battery nanoparticles," *Science*, vol. 348, no. 6241, pp. 1344–1347, 2015.

[32] A. Ulvestad, J. N. Clark, R. Harder, I. K. Robinson, and O. G. Shpyrko, "3D imaging of twin domain defects in gold nanoparticles," *Nano Letters*, vol. 15, no. 6, pp. 4066–4070, 2015. PMID: 25965558.

[33] N. Metropolis, A. W. Rosenbluth, M. N. Rosenbluth, A. H. Teller, and E. Teller, "Equation of State Calculations by Fast Computing Machines," *Journal of Physical Chemistry*, vol. 21, pp. 1087–1092, 1953.

[34] M. Kronberg and F. Wilson, "Secondary recrystallization in copper.," *Trans. Met. Soc. AIME*, vol. 185, pp. 501–514, 1949.

[35] D. Brandon, "The structure of high-angle grain boundaries," *Acta Metallurgica*, vol. 14, no. 11, pp. 1479 – 1484, 1966.

[36] A. Sutton and R. Balluffi, "On geometric criteria for low interfacial energy.," *Acta Materialia*, vol. 35, pp. 2177–2201, 1987.

[37] E. A. Holm, D. L. Olmsted, and S. M. Foiles, "Comparing grain boundary energies in face-centered cubic metals: Al, Au, Cu and Ni," *Scripta Materialia*, vol. 63, no. 9, pp. 905 – 908, 2010.

[38] E. A. Holm, G. S. Rohrer, S. M. Foiles, A. D. Rollett, H. M. Miller, and D. L. Olmsted, "Validating computed grain boundary energies in fcc metals using the grain boundary character distribution," *Acta Materialia*, vol. 59, no. 13, pp. 5250 – 5256, 2011.

[39] V. V. Bulatov, B. W. Reed, and M. Kumar, "Grain boundary energy function for fcc metals," *Acta Materialia*, vol. 65, no. 0, pp. 161 – 175, 2014.

[40] S. Maddali and R. Suter, "A topology-faithful nonparametric smoothing technique for bulk interface networks," *arXiv:1601.04699*, 2016.

[41] G. S. Rohrer, D. M. Saylor, B. E. Dasher, B. L. Adams, A. D. Rollett, and P. Wynblatt, "The distribution of internal interfaces in polycrystals," *MEKU*, vol. 95, no. 4, pp. 197–214, 2004.

[42] C. M. Hefferan, *Measurement of Annealing Phenomena in High Purity Metals with Near-field High Energy X-ray Diffraction Microscopy*. PhD thesis, Carnegie Mellon University, 2012.

[43] S. Maddali, *Computational mining of meso-scale physics from high-energy X-ray data sets*. PhD thesis, Carnegie Mellon University, 2016.

[44] P. A. Shade, D. B. Menasche, J. V. Bernier, P. Kenesei, J.-S. Park, R. M. Suter, J. C. Schuren, and T. J. Turner, "Fiducial marker application method for position alignment of in situ multimodal x-ray experiments and reconstructions," *Journal of Applied Crystallography*, pp. n/a–n/a, 2016.

[45] W. Ludwig, S. Schmidt, E. M. Lauridsen, and H. F. Poulsen, "X-ray diffraction contrast tomography: a novel technique for three-dimensional grain mapping of polycrystals. i. direct beam case," *Journal of Applied Crystallography*, vol. 41, no. 2, pp. 302–309, 2008.

[46] M. Syha, W. Rheinheimer, M. Baeurer, E. Lauridsen, W. Ludwig, D. Weygand, and P. Gumbsch, "Three-dimensional grain structure of sintered bulk strontium titanate from x-ray diffraction contrast tomography," *Scripta Materialia*, vol. 66, no. 1, pp. 1 – 4, 2012.

[47] A. Merkle, C. Holzner, M. Feser, S. McDonald, P. Withers, W. Harris, E. Lauridsen, P. Reischig, H. Poulsen, and L. Lavery, "3D crystallographic imaging using laboratory-based diffraction contrast tomography (dct)," *Microscopy and Microanalysis*, vol. 21, pp. 603–604, 8 2015.

[48] W. Yang, B. Larson, J. Tischler, G. Ice, J. Budai, and W. Liu, "Differential-aperture x-ray structural microscopy: a submicron-resolution three-dimensional probe of local microstructure and strain," *Micron (Oxford, England : 1993)*, vol. 35, no. 6, pp. 431–439, 2004.

[49] G. Nolze, "Image distortions in sem and their influences on EBSD measurements," *Ultramicroscopy*, vol. 107, pp. 172 – 183, 2007.

[50] S. F. Li, J. Lind, C. M. Hefferan, R. Pokharel, U. Lienert, A. D. Rollett, and R. M. Suter, "Three-dimensional plastic response in polycrystalline copper *via* near-field high-energy X-ray diffraction microscopy," *Journal of Applied Crystallography*, vol. 45, pp. 1098–1108, Dec 2012.

[51] T. Mashimo, Y. Hanaoka, and K. Nagayama, "Elastoplastic properties under shock compression of Al_2O_3 single crystal and polycrystal," *Journal of Applied Physics*, vol. 63, no. 2, pp. 327–336, 1988.

[52] D. Jia, Y. M. Wang, K. T. Ramesh, E. Ma, Y. T. Zhu, and R. Z. Valiev, "Deformation behavior and plastic instabilities of ultrafine-grained titanium," *Applied Physics Letters*, vol. 79, no. 5, pp. 611–613, 2001.

[53] Q. Wei, D. Jia, K. T. Ramesh, and E. Ma, "Evolution and microstructure of shear bands in nanostructured Fe," *Applied Physics Letters*, vol. 81, no. 7, pp. 1240–1242, 2002.

[54] S. R. Kalidindi, A. Bhattacharyya, and R. D. Doherty, "Detailed analyses of grain–scale plastic deformation in columnar polycrystalline aluminium using orientation image mapping and crystal plasticity models," *Proceedings of the Royal Society of London A: Mathematical, Physical and Engineering Sciences*, vol. 460, no. 2047, pp. 1935–1956, 2004.

[55] R. A. Lebensohn, Y. Liu, and P. P. Castaneda, "On the accuracy of the self-consistent approximation for polycrystals: comparison with full-field numerical simulations," *Acta Materialia*, vol. 52, no. 18, pp. 5347 – 5361, 2004.

[56] R. A. Lebensohn, R. Brenner, O. Castelnau, and A. D. Rollett, "Orientation image-based micromechanical modelling of subgrain texture evolution in polycrystalline copper," *Acta Materialia*, vol. 56, no. 15, pp. 3914 – 3926, 2008.

[57] A. D. Rollett, R. A. Lebensohn, M. Groeber, Y. Choi, J. Li, and G. S. Rohrer, "Stress hot spots in viscoplastic deformation of polycrystals," *Modelling and Simulation in Materials Science and Engineering*, vol. 18, no. 7, p. 074005, 2010.

[58] R. Pokharel, J. Lind, A. K. Kanjarla, R. A. Lebensohn, S. F. Li, P. Kenesei, R. M. Suter, and A. D. Rollett, "Polycrystal plasticity: Comparison between grain - scale observations of deformation and simulations," *Annual Review of Condensed Matter Physics*, vol. 5, no. 1, pp. 317–346, 2014.

[59] J. Lind, S. F. Li, R. Pokharel, U. Lienert, A. D. Rollett, and R. M. Suter, "Tensile twin nucleation events coupled to neighboring slip observed in three dimensions," *Acta Materialia*, vol. 76, no. 0, pp. 213 – 220, 2014.

[60] R. Pokharel, J. Lind, S. F. Li, P. Kenesei, R. A. Lebensohn, R. M. Suter, and A. D. Rollett, "In-situ observation of bulk 3D grain evolution during plastic deformation in polycrystalline Cu," *International Journal of Plasticity*, vol. 67, no. 0, pp. 217 – 234, 2015.

[61] E. T. Seppälä, J. Belak, and R. E. Rudd, "Effect of stress triaxiality on void growth in dynamic fracture of metals: A molecular dynamics study," *Phys. Rev. B*, vol. 69, p. 134101, Apr 2004.

[62] S. Case and Y. Horie, "Modelling the shock response of polycrystals at the mesoscale," *AIP Conference Proceedings*, vol. 845, no. 1, pp. 307–310, 2006.

[63] S.-N. Luo, T. C. Germann, D. L. Tonks, and Q. An, "Shock wave loading and spallation of copper bicrystals with asymmetric $\Sigma\langle 110\rangle$ tilt grain boundaries," *Journal of Applied Physics*, vol. 108, no. 9, pp. –, 2010.

[64] Q. An, W. Z. Han, S. N. Luo, T. C. Germann, D. L. Tonks, and W. A. Goddard, "Left-right loading dependence of shock response of (111)//(112) Cu bicrystals: Deformation and spallation," *Journal of Applied Physics*, vol. 111, no. 5, pp. –, 2012.

[65] S. J. Fensin, E. K. Cerreta, G. T. Gray III, and S. M. Valone, "Why are some interfaces in materials stronger than others?," *Sci. Rep.*, vol. 4, Jun 2014.

[66] A. Mishra, M. Martin, N. Thadhani, B. Kad, E. Kenik, and M. Meyers, "High-strain-rate response of ultra-fine-grained copper," *Acta Materialia*, vol. 56, no. 12, pp. 2770 – 2783, 2008.

[67] J. F. Bingert, V. Livescu, and E. K. Cerreta, "Characterization of shear localization and shock damage with EBSD," in *Electron Backscatter Diffraction in Materials Science* (A. J. Schwartz, M. Kumar, B. L. Adams, and D. P. Field, eds.), ch. 22, Springer, 2nd ed., 2009.

[68] J. N. Johnson, G. T. Gray III, and N. K. Bourne, "Effect of pulse duration and strain rate on incipient spall fracture in copper," *Journal of Applied Physics*, vol. 86, no. 9, pp. 4892–4901, 1999.

[69] L. Wayne, K. Krishnan, S. DiGiacomo, N. Kovvali, P. Peralta, S. Luo, S. Greenfield, D. Byler, D. Paisley, K. McClellan, A. Koskelo, and R. Dickerson, "Statistics of weak grain boundaries for spall damage in polycrystalline copper," *Scripta Materialia*, vol. 63, no. 11, pp. 1065 – 1068, 2010.

[70] D. Dennis-Koller, J. P. Escobedo-Diaz, E. K. Cerreta, C. A. Bronkhorst, B. Hansen, R. A. Lebensohn, H. Mourad, B. M. Patterson, and D. Tonks, "Controlled shock loading conditions for microstructural correlation of dynamic damage behavior," in *APS Shock Compression of Condensed Matter Meeting Abstracts*, p. 5005, June 2011.

[71] J. P. Escobedo, E. N. Brown, C. P. Trujillo, E. K. Cerreta, and G. T. Gray III, "The effect of shock-wave profile on dynamic brittle failure," *Journal of Applied Physics*, vol. 113, no. 10, pp. –, 2013.

[72] J. P. Escobedo, E. K. Cerreta, D. Dennis-Koller, C. P. Trujillo, and C. A. Bronkhorst, "Influence of boundary structure and near neighbor crystallographic orientation on the dynamic damage evolution during shock loading," *Philosophical Magazine*, vol. 93, no. 7, pp. 833–846, 2013.

[73] S. J. Fensin, J. P. Escobedo-Diaz, C. Brandl, E. K. Cerreta, G. T. Gray III, T. C. Germann, and S. M. Valone, "Effect of loading direction on grain boundary failure under shock loading," *Acta Materialia*, vol. 64, no. 0, pp. 113 – 122, 2014.

[74] W. Han, E. Cerreta, N. Mara, I. Beyerlein, J. Carpenter, S. Zheng, C. Trujillo, P. Dickerson, and A. Misra, "Deformation and failure of shocked bulk cu-nb nanolaminates," *Acta Materialia*, vol. 63, no. 0, pp. 150 – 161, 2014.

[75] J. F. Bingert, R. M. Suter, J. Lind, S. F. Li, R. Pokharel, and C. P. Trujillo, "High-energy diffraction microscopy characterization of spall damage," in *Dynamic Behavior of Materials, Volume 1: Proceedings of the 2013 Annual Conference on Experimental and Applied Mechanics* (B. Song, D. Casem, and J. Kimberley, eds.), vol. 1, ch. 48, Springer, 2014.

[76] R. Abbasi, K. Dzieciol, and A. Borbly, "Three-dimensional analysis of creep voids in copper by serial sectioning combined with large field ebsd," *Materials Science and Technology*, vol. 31, no. 5, pp. 540–546, 2015.

[77] A. G. Perez-Bergquist, E. K. Cerreta, C. P. Trujillo, F. Cao, and G. T. Gray III, "Orientation dependence of void formation and substructure deformation in a

spalled copper bicrystal," *Scripta Materialia*, vol. 65, no. 12, pp. 1069 – 1072, 2011.

[78] E. K. Cerreta, J. P. Escobedo, A. G. Perez-Bergquist, D. Dennis-Koller, C. P. Trujillo, G. T. Gray III, C. Brandl, and T. C. Germann, "Early stage dynamic damage and the role of grain boundary type," *Scripta Materialia*, vol. 66, no. 9, pp. 638 – 641, 2012.

[79] Y. Yang, P. Zhi-qiang, C. Xing-zhi, G. Zhao-liang, T. Tie-gang, H. Hai-bo, and Z. Qing-ming, "Spall behaviors of high purity copper under sweeping detonation," *Materials Science and Engineering: A*, vol. 651, pp. 636 – 645, 2016.

[80] A. G. Perez-Bergquist, J. P. Escobedo, C. P. Trujillo, E. K. Cerreta, G. T. Gray III, C. Brandl, and T. C. Germann, "The role of the structure of grain boundary interfaces during shock loading," *AIP Conference Proceedings*, vol. 1426, no. 1, pp. 1359–1362, 2012.

[81] R. A. Lebensohn and R. Pokharel, "Interpretation of Microstructural Effects on Porosity Evolution Using a Combined Dilatational/Crystal Plasticity Computational Approach," *JOM - Journal of the Minerals, Metals and Materials Society*, vol. 66, pp. 437–443, Mar. 2014.

[82] J. P. Escobedo, D. Dennis-Koller, E. K. Cerreta, B. M. Patterson, C. A. Bronkhorst, B. L. Hansen, D. Tonks, and R. A. Lebensohn, "Effects of grain size and boundary structure on the dynamic tensile response of copper," *Journal of Applied Physics*, vol. 110, no. 3, pp. –, 2011.

[83] B. Reed, B. Adams, J. Bernier, C. Hefferan, A. Henrie, S. Li, J. Lind, R. Suter, and M. Kumar, "Experimental tests of stereological estimates of grain boundary populations," *Acta Materialia*, vol. 60, pp. 2999 – 3010, 2012.

[84] H. Toda, "3D/4D analyses of damage and fracture behaviours in structural materials via synchrotron x-ray tomography," *Microscopy*, vol. 63, no. suppl 1, pp. i3–i4, 2014.

[85] H. Simons, A. King, W. Ludwig, C. Detlefs, W. Pantleon, S. Schmidt, F. Stöhr, I. Snigireva, A. Snigirev, and H. F. Poulsen, "Dark-field x-ray microscopy for multiscale structural characterization," *Nature Communications*, vol. 6, Jan 2015. Article.

[86] C. M. Hefferan, J. Lind, S. F. Li, U. Lienert, A. D. Rollett, and R. M. Suter, "Observation of recovery and recrystallization in high-purity aluminum measured with forward modeling analysis of high-energy diffraction microscopy," *Acta Materialia*, vol. 60, no. 10, pp. 4311 – 4318, 2012.

[87] I. McKenna, S. Poulsen, E. Lauridsen, W. Ludwig, and P. Voorhees, "Grain growth in four dimensions: A comparison between simulation and experiment," *Acta Materialia*, vol. 78, pp. 125 – 134, 2014.

[88] B. Lin, Y. Jin, C. Hefferan, S. Li, J. Lind, R. Suter, M. Bernacki, N. Bozzolo, A. Rollett, and G. Rohrer, "Observation of annealing twin nucleation at triple lines in nickel during grain growth," *Acta Materialia*, vol. 99, pp. 63 – 68, 2015.

[89] T. R. Bieler, L. Wang, A. J. Beaudoin, P. Kenesei, and U. Lienert, "In situ characterization of twin nucleation in pure ti using 3d-xrd," *Metallurgical and Materials Transactions*, vol. 45, pp. 109–122, 01 2014.

[90] H. Abdolvand, M. Majkut, J. Oddershede, J. P. Wright, and M. R. Daymond, "Study of 3-d stress development in parent and twin pairs of a hexagonal close-packed polycrystal: Part i, in-situ three-dimensional synchrotron x-ray diffraction measurement," *Acta Materialia*, vol. 93, pp. 246 – 255, 2015.

[91] D. W. Brown, S. F. Li, L. Balogh, D. Byler, C. M. Hefferan, J. Lind, S. R. Niezgoda, R. M. Suter, J. F. Hunter, and P. Kenesei, "Demonstration of near field high energy x-ray diffraction microscopy on high-z ceramic nuclear fuel material," in *Mechanical Stress Evaluation by Neutrons and Synchrotron Radiation VII*, vol. 777 of *Materials Science Forum*, pp. 112–117, Trans Tech Publications, 4 2014.

[92] P. A. Shade, B. Blank, J. C. Schuren, T. J. Turner, P. Kenesei, K. Goetze, R. M. Suter, J. V. Bernier, S. F. Li, J. Lind, U. Lienert, and J. Almer, "A rotational and axial motion system load frame insert for in situ high energy x-ray studies," *Review of Scientific Instruments*, vol. 86, no. 9, 2015.

[93] C. Sims, "A history of superalloy metallurgy for superalloy metallurgists," *Superalloys*, pp. 399–419, 1984.

[94] D. Chang, D. Krueger, and R. Sprague, "Superalloy powder processing, properties and turbine disk application," *Superalloys*, pp. 245–273, 1984.

[95] D. Furrer and H. Fecht, "Ni-based superalloys for turbine discs," *JOM*, vol. 51, no. 1, pp. 14–17, 1999.

[96] A. Banik, K. Green, M. Hardy, D. Mourer, and R. T., "Low cost powder metal turbine components," *Superalloys*, 2004.

[97] R. L. Dreshfield and R. V. Miner Jr., "Effects of thermally induced porosity on an as-HIP powder metallurgy superalloy," 1980. Prepared for the Annual Meeting of the American Institute of Mining, Metallurgical and Petroleum Engineers.

[98] H. Fiedler, T. Sawyer, R. Kopp, and A. Leatham, "The spray forming of superalloys," *JOM*, vol. 39, no. 8, pp. 28–33, 1987.

[99] R. L. Dreshfield, "Defects in nickel-base superalloys," *JOM*, vol. 39, no. 7, pp. 16–21, 1987.

[100] E. S. Huron, R. L. Casey, M. F. Henry, and D. P. Mourer, "The influence of alloy chemistry and powder production methods on porosity in a P/M nickel-base superalloy," pp. 667–676, 1996.

[101] B. A. Szost, S. Terzi, F. Martina, D. Boisselier, A. Prytuliak, T. Pirling, M. Hofmann, and D. J. Jarvis, "A comparative study of additive manufacturing techniques: Residual stress and microstructural analysis of CLAD and WAAM printed Ti-6–Al-4–V components," *Materials & Design*, pp. –, 2015.

[102] H. D. Carlton, A. Haboub, G. F. Gallegos, D. Y. Parkinson, and A. A. MacDowell, "Damage evolution and failure mechanisms in additively manufactured stainless steel," *Materials Science and Engineering: A*, vol. 651, pp. 406 – 414, 2016.

[103] E. S. Huron, "Method for reducing thermally induced porosity in a polycrystalline nickel-base superalloy article," December 1996. US Patent 5,584,948.

[104] T. M. Pollock and S. Tin, "Nickel-based superalloys for advanced turbine engines: Chemistry, microstructure and properties," *Journal of Propulsion and Power*, vol. 22, pp. 361–374, Mar. 2006.

[105] Z. Shan, E. A. Stach, J. M. K. Wiezorek, J. A. Knapp, D. M. Follstaedt, and S. X. Mao, "Grain boundary-mediated plasticity in nanocrystalline nickel," *Science*, vol. 305, no. 5684, pp. 654–657, 2004.

[106] P. R. Cantwell, M. Tang, S. J. Dillon, J. Luo, G. S. Rohrer, and M. P. Harmer, "Grain boundary complexions," *Acta Materialia*, vol. 62, pp. 1 – 48, 2014.

[107] T. J. Garosshen, T. D. Tillman, and G. P. McCarthy, "Effects of B, C, and Zr on the structure and properties of a P/M nickel base superalloy," *Metallurgical Transactions A*, vol. 18, no. 1, pp. 69–77, 1987.

[108] M. Uchic, M. Groeber, M. Shah, P. Callahan, A. Shiveley, M. Scott, M. Chapman, and J. Spowart, *An Automated Multi-Modal Serial Sectioning System for Characterization of Grain-Scale Microstructures in Engineering Materials*, pp. 195–202. 1 International Conference on 3D Materials Science, John Wiley & Sons, Inc., 2012.

[109] C. M. Hefferan, S. F. Li, J. Lind, U. Lienert, A. D. Rollett, P. Wynblatt, and R. M. Suter, “Statistics of high purity nickel microstructure from high energy x-ray diffraction microscopy.,” *Computers, Materials and Continua*, vol. 14, no. 39, pp. 209–219, 2009.

[110] F. Wilcoxon, “Individual comparisons by ranking methods,” *Biometrics Bulletin*, vol. 1, no. 6, pp. pp. 80–83, 1945.

[111] A. N. Kolmogorov, “Sulla determinazione empirica di una legge di distribuzione,” *Giornale dell’Istituto Italiano degli Attuari*, vol. 4, pp. 83–91, 1933.

[112] N. V. Smirnov, “On the estimation of the discrepancy between empirical curves of distribution for two independent samples,” *Bull. Math. Univ. Moscou*, vol. 2, no. 2, 1939.

[113] N. Smirnov, “Table for estimating the goodness of fit of empirical distributions,” *The Annals of Mathematical Statistics*, vol. 19, no. 2, pp. pp. 279–281, 1948.

[114] F. Massey Jr., “The Kolmogorov-Smirnov test for goodness of fit,” *Journal of the American Statistical Association*, vol. 46, no. 253, pp. pp. 68–78, 1951.